University of Naples “Federico II”

Doctorate in
STRUCTURAL, GEOTECHNICAL ENGINEERING
AND SEISMIC RISK
XXXI CYCLE

Microstructure and mechanical behaviour of cemented soils lightened by foam

Domenico De Sarno

Supervisors

Prof. Gianfranco Urciuoli
Prof. Claudio Mancuso

PhD Coordinator

Prof. Luciano Rosati

Acknowledgments

The whole research wouldn’t have been possible without the wisdom and help of Prof. Gianfranco Urciuoli, to whom I am very grateful. I would like to express my great appreciation to Prof. Claudio Mancuso, especially for his patience and comprehension.

I owe special thanks to Prof. Marco Valerio Nicotera, which has been extremely helpful in the interpretation of data, and Dr. Raffaele Papa, who was the first to believe in me, along with TERRE LEGGERE that provided all the materials.

I am very grateful to Prof. Giacomo Russo and Dr. Enza Vitale which have been fundamental in the whole part of the thesis devoted to microstructural and mineralogical analyses, in both tests and interpretation of data. Furthermore, the assistance provided by Enza in these years has been very valuable. I wish also to acknowledge the help provided by Dr. Dimitri Deneele in SEM observations.

Domenico De Sarno

Summary

List of symbols

- Soil slurry
    - W_{slurry} weight of soil slurry;
    - V_{slurry} volume of soil slurry;
    - $\gamma_{slurry} = \frac{W_{slurry}}{V_{slurry}}$ bulk density of soil slurry;
    - $w_s = \frac{W_{ws}}{W_s^s}$ water content of soil slurry;
  - Solid
    - W_s^s weight of dry soil;
    - V_s^s absolute volume of soil;
    - $\rho_s = \frac{W_s^s}{V_s^s}$ specific weight of soil;
  - Liquid
    - W_{ws} weight of water in soil slurry;
    - ρ_w specific weight of water;
- Cement paste
    - W_c weight of cement paste;
    - V_c volume of cement paste;
    - $W_{c,h}$ weight of hydrated cement;
    - $V_{c,h}$ volume of hydrated cement;
    - $V_{c,p}$ total volume of pores in cement paste;
    - $V_{cap\ pores}$ total volume of capillary pores;
    - $\alpha = \frac{W_{wc,n-ev}}{W_{c,a,h}}$;
    - $\beta \cong 0.746$ parameter that takes account for shrinkage of non-evaporable water in cement paste;
    - ${}^{w_c}/_{c} = \frac{W_{wc}}{W_{c,a}}$ gravimetric water to cement ratio;
  - Solid
    - $W_{c,a}$ weight of anhydrous (dry) cement (as a powder);
    - $W_{c,a,h}$ weight of the portion of initial anhydrous cement ($W_{c,a}$) that is hydrated at a certain curing time, i.e. “anhydrous hydrated cement”;
    - $x = \frac{W_{c,a,h}}{W_{c,a}}$ gravimetric portion of anhydrous cement hydrated at a certain curing time;
    - $V_{c,a}^s$ absolute volume of anhydrous (dry) cement;

        - $\rho_{c,a} = \frac{W_{c,a}}{V_{c,a}^s}$ specific weight of anhydrous (dry) cement;
        - $W_{c,unh}$ weight of unhydrated cement at certain curing time;
        - $V_{c,unh}^s$ absolute volume of unhydrated cement;
        - $W_c^s = W_{c,h}^s + W_{c,unh}$ weight of solid cement paste;
        - V_c^s absolute volume of solid cement paste;
        - $W_{c,h}^s$ weight of solid products of hydration;
        - $V_{c,h}^s$ absolute volume of solid products of hydration;
        - $W_{wc,ch}$ weight of chemically combined water;
        - $W_{wc,n-ev}$ weight of non-evaporable water in cement paste;
        - $V_{wc,n-ev} = \frac{W_{wc,n-ev}}{\rho_w}$ volume of non-evaporable water;
    - Liquid
        - W_c^l weight of liquid phase in cement paste;
        - V_c^l volume of liquid phase in cement paste;
        - W_{wc} weight of water added to cement paste;
        - V_{wc} volume of water added to cement paste;
        - $W_{w\ cap\ pores}$ weight of water in capillary pores;
        - $W_{wc,ev}$ weight of evaporable water in cement paste;
        - $V_{w\ cap\ pores}$ volume of capillary pores filled with water;
        - $W_{gel\ water}$ weight of gel water;
        - $V_{gel\ water}$ volume of gel water;
    - Gas
        - V_c^g volume of gas phase in cement paste;
        - $V_{e\ cap\ pores}$ volume of empty capillary pores;
- Foam
        - V_f volume of foam;
        - W_f total weight of foam;
        - $\gamma_f = \frac{W_f}{V_f}$ bulk density of foam;
    - Solid
        - W_f^s weight of solid phase in foam;
    - Liquid
        - W_f^l weight of liquid phase in foam;
        - $\rho_{solution}$ density of surfactant solution used to produce the foam;

        - V_f^l volume of liquid phase in foam;
    - Gas
        - $V_{air,foam}$ volume of air in foam;
- Lightweight cemented soil
        - W weight of lightweight cemented soil;
        - V volume of lightweight cemented soil;
        - w gravimetric water content of lightweight cemented soil;
        - V_p volume of pores of lightweight cemented soil;
        - n porosity of lightweight cemented soil;
        - e void ratio of lightweight cemented soil;
        - $\frac{c}{s} = \frac{W_{c,a}}{W_s^s}$; $e_f' = \frac{V_f}{V_{soil\,slurry}+V_{grout}}$; $n_f = \frac{V_f}{V}$;
        - $e_b = \frac{V_{ch}}{V^s}$ void ratio of bonds
        - $\frac{\gamma_{dry}(n_f)}{\gamma_{dry}(n_f=0)} = \frac{\gamma_{dry}}{\gamma_{dry,0}}$ relative dry density
    - Solid
        - W^s weight of solid phase in lightweight cemented soil
        - V^s volume of solid phase in lightweight cemented soil
        - $\rho^s = \frac{W^s}{V^s}$ specific weight of solid phase of lightweight cemented soil
    - Liquid
        - W^l weight of liquid phase in lightweight cemented soil;
        - V^l volume of liquid phase in lightweight cemented soil;
        - $W_{w,ev}$ weight of evaporable water in lightweight cemented soil;
        - $V_{w,ev}$ volume of evaporable water in lightweight cemented soil;
    - Gas
        - V^g volume of gas phase in lightweight cemented soil;
        - $V_{air\,voids}$ volume of air in lightweight cemented soil.

List of figures

1. Introduction

The management of large amounts of excavated soil is a primary problem in civil engineering, often due to not suitable mechanical properties for its reuse as a construction material. Italian legislation defines the excavated soil and rocks (DPR 120/17) as the excavated soil deriving from activities aimed to a construction project such as excavations (construction excavations, foundations, trenches), bores, piles, soil improvement, infrastructural projects (tunnels, streets), removal and levelling of soil constructions. They can also contain concrete and cementitious mixtures, bentonite, PVC, fiberglass, and admixtures for mechanised excavations if pollutant concentration is below specific threshold. When the excavated soil is qualified as a waste, its disposal after a temporary storage must be considered in site management and high costs can derive. However, if the excavated soil can be reused as a material in the same construction project (or in a different one) for backfilling, trench reinstatement, soil embankments or substituting quarrying material in productive processes, it can be qualified as by-product with clear advantages in terms of environmental and economic costs.

A suitable solution for reuse of excavated soil is the addition of cement and foam to produce lightweight cemented soils (LWCS). Lightweight cemented soil is prepared by mixing soil with water, cement and an air foam. The aim of this technique is to obtain a material with high workability in the fresh state (so that it can be transferred by pumping from batch plant to the construction site and poured) improved mechanical properties of the hardened paste given by the binding agent (as cement) and a specific low density (varying from 6 to 15 kN/m^3) thanks to the addition of a foam. The fresh paste is self-levelling and no compaction is required, thus reducing construction time. The method can be theoretically applied to any kind of soil except for very coarse particles which can segregate in the fresh paste. However, the necessity of such a method often arise for fine grained soil, especially clayey and silty soil, whose mechanical properties are generally not suitable for construction purposes or require high compaction efforts.

The treatment of soil by means of binding agents is nowadays very common in engineering practice. Well established soil improvement techniques as deep mixing, jet grouting and lime stabilization are based on mixing binding agents as cement and lime to improve soil mechanical performances. The former two are

grouped in the category of *soil mixing*, which is referred to as soil improvement and conditioning techniques in which soil is disrupted and mixed with binding agents via rotating utensils to obtain a "geomaterial" with specific geotechnical performances directly on site (Marzano, 2017). They are often used for columnar treatments, but also trench mixing techniques exist. A similar soil improvement technique is the permeation grouting, that is based on deep injection of cementitious mixtures at low pressure. It differs from soil mixing because no mixing of soil happens and a very little disturbance to soil fabric occurs (Flora and Lirer, 2011). In these cases, soil is not excavated. Conversely, cement and lime treatment (stabilization) techniques, as well as the lightweight cemented soil method, are used to improve soil mechanical properties to reuse it as a construction material. Cement and lime are the most commonly used binding agents in soil mixing, but others like fly ash and blast furnace slag, or the innovative geopolymers, can be used to substitute them, partially or wholly (Kaniraj and Havanagi, 1999; Wild et al., 1998; Zhang et al., 2013). In the LWCS method, the most common binding agent is cement, but also other binding agents have been efficiently used (S. Horpibulsuk et al., 2014).

A foam is a dispersion of bubbles in a liquid. In geotechnical engineering, foams are commonly used as a soil conditioner in Earth Pressure Balance (EPB) mechanized tunnelling technology. The addition of a foam has various purposes. It is used to make the soil almost impermeable and to reduce abrasive behaviour of some soils; it acts on consistency giving the soil a pseudoplastic state, to help muck circulation from excavation to its storage; in a fine grained soil, it is used to reduce clogging potential of clays and avoid overconsolidation under the action of the cutting edge of the screw (Quebaud et al., 1998). The effect of foam conditioning on soil properties related to EPB mechanised is widely studied (Borio et al., 2008; Milligan, 2000; Plötze et al., 2013; Sebastiani et al., 2017; Thewes et al., 2011; Zumsteg et al., 2012). In civil engineering, foam is also used to produce foam concrete (foamed concrete, foamcrete) that is a cellular concrete obtained by mixing a preformed foam with grout (like lightweight cemented soil method). It differs from gas-concrete, which is a cellular concrete usually obtained by adding aluminium powder to the paste. Foam concrete is a lightweight concrete whose density can go down to 300 kg/m^3 along with strength which reduces as well; it is defined as a low density controlled low strength material and used for various applications such as backfills, void filling, insulation fills and pavement bases (Ramme, 2005). To avoid confusion, it is

worth noting that the term "foam" is also used to define dispersion of gas in solids, such as porous materials, cellular concrete and polymer foams, thus the lightweight cemented soil can be defined as a "foam" as well. However, in the following, the term foam will only refer to a gas dispersion in liquid.

The lightweight cemented soil method or lightweight treated soil method has been studied by various authors and efficiently applied on dredged soil in port construction in Japan (Tsuchida and Egashira, 2004), or suggested as a construction material for constructions on soft clays (Horpibulsuk et al., 2012b). The method requires that soil is diluted at a water content, w_s, above the liquid limit, w_l, to obtain a soil slurry, a suspension. The binding agent can be either added as a powder or mixed with water at a certain water to cement ratio by weight, w_c/c. These two procedures are defined as *dry* and *wet* in soil mixing, respectively. By this way, a cemented soil can be obtained. The amount of binding agent is usually defined as the ratio by weight of anhydrous cement to dry soil, *c/s*, or to the volume of material produced. Foam is usually added as the last component. The amount of foam can be defined in different ways; in some cases, the volume of foam is related to the volume of soil slurry (Teerawattanasuk et al., 2015), in other cases to the total volume of soil slurry and foam (Horpibulsuk et al., 2012b). A diagram of the mixing method used in this study is represented in Figure 1-1.

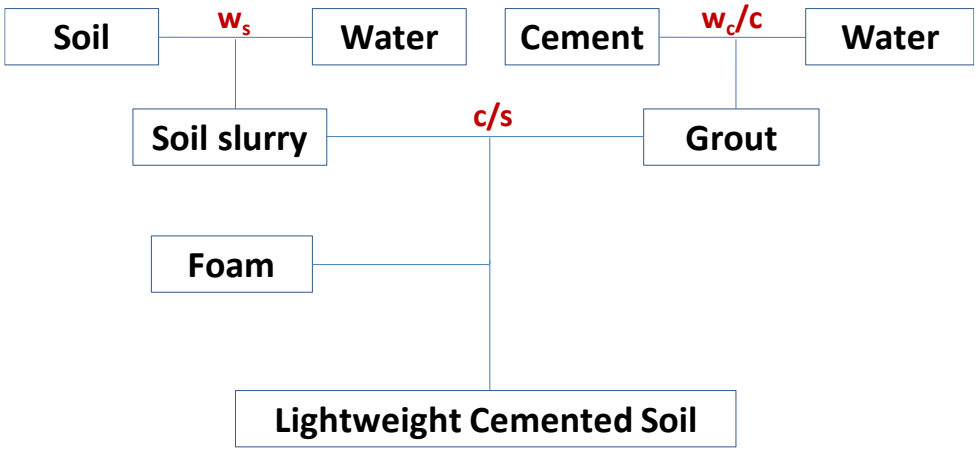

Figure 1-1. Diagram of lightweight cement soil method.

In this experimental study, the influence of addition of cement and foam to soil on mineralogical and microstructural features is presented. Time dependent mineralogical and microstructural changes have been monitored at increasing curing time by means of X Ray Diffraction (XRD), Thermogravimetric Analysis

(TGA), Scanning Electron Microscopy (SEM) and Mercury Intrusion Porosimetry (MIP). Mechanical behaviour of treated soil has been investigated by means of oedometric and direct shear tests. Tests are briefly described in Appendix B.

In the following chapter a brief description of the main clay minerals, along with their structure and mineralogy, is presented. Then, clay-water interaction and rheological behaviour of clay suspensions, i.e., soil slurry, are shown. The 3rd chapter is about cement and foam. Cement classification, chemistry and rheology of the fresh cement paste are briefly summarized. A short description of foam properties and stability is given. In these chapters, the phases of each component (soil slurry, cement paste and foam) will be identified. The superscripts "s", "l" and "g" will be used to specify respectively the solid, liquid and gas phases, the subscripts "s", "c" and "f" will refer respectively to soil, cement and foam.

In the 4th chapter a literature review on the mechanical behaviour of cemented soils and lightweight cement soils is presented.

In the 5th chapter a description of materials and methods used in this study is given. The relations between the phases of the produced material in dependence of initial amounts of material are derived, starting from equations in Chapters 2 and 3 for each component.

The results of mineralogical and microstructural tests are presented in the 6th chapter. Direct shear test and oedometric test results are discussed in 7th chapter; in Appendix C, results of all the performed tests are shown.

References

Borio, L., Peila, D., Oggeri, C., Pelizza, S., 2008. Effects of foam on soil conditioned behaviour 1–8.

DPR 120/17: Regulation about the simplified discipline of the management of excavated soil and rocks, 13/06/2017 n° 120.

Flora, A., Lirer, S., 2011. Interventi di consolidamento dei terreni: tecnologie e scelte di progetto, in: AGI (Ed.), XXIV Convegno Nazionale Di Geotecnica Su "Innovazione Tecnologica Nell'Ingegneria Geotecnica".

Horpibulsuk, S., Suddeepong, A., Chinkulkijniwat, A., Liu, M.D., 2012. Strength and compressibility of lightweight cemented clays. Appl. Clay Sci. 69, 11–21. https://doi.org/10.1016/j.clay.2012.08.006

Horpibulsuk, S., Wijitchot, A., Nerimitknornburee, A., Shen, S.L., Suksiripattanapong, C., 2014. Factors influencing unit weight and strength of lightweight cemented clay. Q. J. Eng. Geol. Hydrogeol. 47, 101–109. https://doi.org/10.1144/qjegh2012-069

Kaniraj, S.R., Havanagi, V.G., 1999. Compressive strength of cement stabilized fly ash-soil mixtures. Cem. Concr. Res. 29, 673–677. https://doi.org/10.1016/S0008-8846(99)00018-6

Marzano, I.P., 2017. Soil Mixing. Tecnologie esecutive, applicazioni, progetto e controlli, Argomenti di ingegneria geotecnica. Hevelius.

Milligan, G., 2000. Lubrication and soil conditioning in tunnelling, pipe jacking and microtunnelling. A state-of-the-art review. Rev. Lit. Arts Am. 44, 1–46.

Plötze, M., Zumsteg, R., A.M. Puzrin, 2013. Effects of dispersing foams and polymers on the mechanical behaviour of clay pastes. Géotechnique 63, 920–933. https://doi.org/10.1680/geot.12.P.044

Quebaud, S., Sibai, M., Henry, J.P., 1998. Use of chemical foam for improvements in drilling by earth-pressure balanced shields in granular soils. Tunn. Undergr. Sp. Technol. 13, 173–180. https://doi.org/10.1016/S0886-7798(98)00045-5

Ramme, B.W., 2005. ACI 229R-99 Controlled Low-Strength Materials 99, 1–15.

Sebastiani, D., Di Giulio, A., Miliziano, S., 2017. La gestione del condizionamento del terreno nello scavo meccanizzato di una galleria con TBM-EPB: risultati di una attività sperimentale, in: IARG - Incontro Annuale Ricercatori Geotecnica.

Teerawattanasuk, C., Voottipruex, P., Horpibulsuk, S., 2015. Mix design charts for lightweight cellular cemented Bangkok clay. Appl. Clay Sci. 104, 318–323. https://doi.org/10.1016/j.clay.2014.12.012

Thewes, M., Budach, C., Bezuijen, A., 2011. Foam conditioning in EPB tunnelling. Geotech. Asp. Undergr. Constr. Soft Gr. - 7th Int. Symp. 127–135. https://doi.org/10.1201/b12748-19

Tsuchida, T., Egashira, K., 2004. The Lightweight Treated Soil Method: New Geomaterials for Soft Ground Engineering in Coastal Areas. CRC Press - Taylor & Francis Group, London.

Wild, S., Kinuthia, J.M., Jones, G.I., Higgins, D.D., 1998. Effects of partial substitution of lime with ground granulated blast furnace slag (GGBS) on the strength properties of lime-stabilised sulphate-bearing clay soils 51, 37–53.

Zhang, M., Guo, H., El-Korchi, T., Zhang, G., Tao, M., 2013. Experimental feasibility study of geopolymer as the next-generation soil stabilizer. Constr. Build. Mater. 47, 1468–1478. https://doi.org/10.1016/j.conbuildmat.2013.06.017

Zumsteg, R., Plötze, M., Puzrin, A. M., 2012. Effect of Soil Conditioners on the Pressure and Rate-Dependent Shear Strength of Different Clays. J. Geotech. Geoenvironmental Engineering 138, 1138–1146.

2. Soil

The lightweight cemented soil method can be applied to any kind of soil, except for coarse particles which can segregate from bulk. In this study attention was given to clayey soils, characterised by an amount of clay higher than 12% and non-negligible plasticity (ASTM, 2006). The behaviour of a clayey soil and its interaction with water are strictly related to mineral composition. Indeed. mineral composition and nature of constituent pore fluid can affect significantly some properties of a clayey soil, such as plasticity and residual strength (Di Maio and Fenelli, 1994, 1997). Due to this, clay minerals are briefly presented. Then, clay-water interaction and rheological behaviour of clay suspensions are shown, due to their importance in the treatment method which requires a dilution of clayey soil to obtain a slurry to be mixed with other components.

2.1. Clay and clay minerals

In geotechnics, the term clay refers to particles with diameter lower than 2 μm (A.G.I., 1963), but in a more general definition, the term clay implies a "natural, earthy, fine-grained material which develops plasticity when mixed with a limited amount of water" (Grim, 1968). The plasticity is the property that a substance, continuously deformed under a finite force, has to maintain its shape after the force is removed or reduced (Andrade et al., 2011). Chemical analyses showed that clay minerals are composed essentially of silica, alumina, and water, with amounts of iron, alkalis and alkaline earths (Grim, 1968). The upper limit is dependent on the tendency of clay minerals to be concentrated in a size less than 2 μm (Grim, 1968).

Clay minerals refer to a group of hydrous aluminosilicates that predominate the clay-sized (<2 μm) fraction of soils (Barton and Karathanasis, 2002). The nomenclature and classification of these minerals have been discussed for many years (Grim, 1968). A classification is proposed by "The Clay Minerals Society" (Martin et al., 1991). A discussion about clay minerals classification goes beyond the purposes of the thesis; however, due to its importance, a brief description of clay minerals has been reported in Appendix A.

Table 1. Classification of planar hydrous phyllosilicates.

Layer type	Interlayer material[1]	Group	Octahedral character	Species
1:1	None or H_2O only ($x \sim 0$)	Serpentine-kaolin	Trioctahedral	Lizardite, berthierine, amesite, cronstedtite, nepouite, kellyite, fraipontite, brindleyite
			Dioctahedral	Kaolinite, dickite, nacrite, halloysite (planar)
			Di-trioctahedral	Odinite
2:1	None ($x \sim 0$)	Talc-pyrophyllite	Trioctahedral	Talc, willemseite, kerolite, pimelite
			Dioctahedral	Pyrophyllite, ferripyrophyllite
	Hydrated exchangeable cations ($x \sim 0.2$–0.6)	Smectite	Trioctahedral	Saponite, hectorite, sauconite, stevensite, swinefordite
			Dioctahedral	Montmorillonite, beidellite, nontronite, volkonskoite
	Hydrated exchangeable cations ($x \sim 0.6$–0.9)	Vermiculite	Trioctahedral	Trioctahedral vermiculite
			Dioctahedral	Dioctahedral vermiculite
	Non-hydrated monovalent cations ($x \sim 0.6$–1.0)	True (flexible) mica	Trioctahedral	Biotite, phlogopite, lepidolite, etc.
			Dioctahedral	Muscovite, illite, glauconite, celadonite, paragonite, etc.
	Non-hydrated divalent cations ($x \sim 1.8$–2.0)	Brittle mica	Trioctahedral	Clintonite, kinoshitalite, bityite, anandite
			Dioctahedral	Margarite
	Hydroxide sheet (x = variable)	Chlorite	Trioctahedral	Clinochlore, chamosite, pennantite, nimite, baileychlore
			Dioctahedral	Donbassite
			Di-trioctahedral	Cookeite, sudoite
2:1	Regularly interstratified (x = variable)	Variable	Trioctahedral	Corrensite, aliettite, hydrobiotite, kulkeite
			Dioctahedral	Rectorite, tosudite

[1] x is net layer charge per formula unit.

Table 2. Classification of non-planar hydrous phyllosilicates.

Layer type	Modulated component	Linkage configuration	Unit layer, c sin β value	Traditional affiliation	Species
A. Modulated structures					
1:1 layer	Tet. Sheet	Strips	7 Å	Serpentine	Antigorite, bementite
		Islands	7 Å	Serpentine	Greenalite, caryopilite, pyrosmalite, manganpyrosmalite, feropyrosmalite, friedelite, mcgillite, schallerite, nelenite
		Other		None	None
2:1 layer	Tet. Sheet	Strips	9.5 Å	Talc	Minnesotaite
			12.5 Å	Mica	Ganophyllite, eggletonite
		Islands	9.6–12.5 Å	Mica/complex	Zussmanite, parsettensite, stilpnomelane, ferrostilpnomelane, ferristilpnomelane, lennilenapeite
		Other	12.3 Å	None	Bannisterite
			14 Å	Chlorite	Gonyerite
	Oct. Sheet	Strips	12.7–13.4 Å	Pyribole	Sepiolite, loughlinite, falcondoite, palygorskite, yofortierite
B. Rolled and spheroidal structures					
1:1 layer	None	Trioctahedral	–	Serpentine	Chrysotile, pecoraite
		Dioctahedral	–	Kaolin	Halloysite (nonplanar)

Figure 2-1. Nomenclature and classification of clay minerals, Copyright "The Clay Minerals Society"(Martin et al., 1991)

2.2. Clay-water interaction

The peculiar behaviour of clay when mixed with water depends on clay minerals structure and the high surface area of particles. As already shown in 2.1, the surface of clay minerals is composed of oxygen atoms or hydroxyl groups and excess electrons can arise from cations substitution in lattice (Grim, 1968). By this way, hydrogen covalent bonds can form between particle surface and water molecules, due to polarity of water. The totality of the negative electrical layer on the surface particles and the positive electrical layer in the adsorbed water is called electrical double layer.

2.2.1. Diffuse layer models and clay particle associations

In the simplest model, electrical double layer can be represented as composed of only two planes where all the electrical potential nullifies, proposed by Helmholtz as reported by Paunovic and Schlesinger (2006) (Figure 2-2a). However, due to counter-ions adsorption on particle surface, the counter-ions concentration is higher on the surface and lower in the bulk of solution. This causes a diffusive force of counter-ions towards the bulk solution, so that concentration of counter-ions is maximal near particle surface and decreases with distance. Moreover, due to electrostatic repelling force of surface, there is a deficiency of ions of the same sign of the surface charge around the layer. This is called diffuse layer model, called Gouy-Chapman model as reported by Paunovic and Schlesinger (2006) and it's represented schematically in Figure 2-2b.

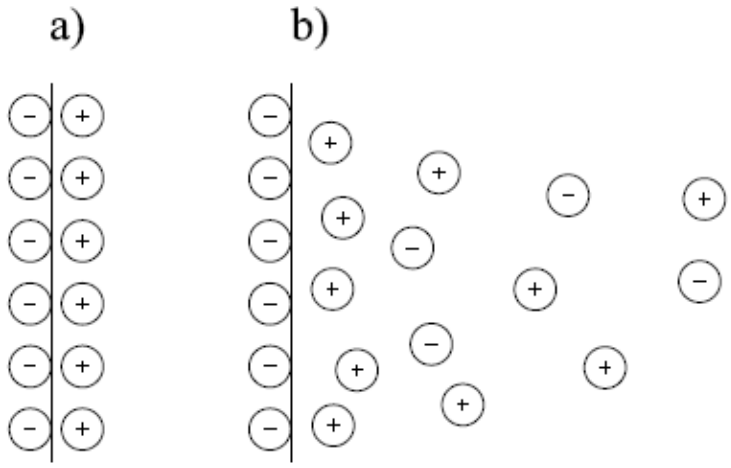

Figure 2-2. Diagrammatic sketch of electrical double layer. (a) Helmholtz model; (b) diffuse layer model.

The exact distribution of ions as a function of distance from the particle can be derived from electrostatic and diffusion theory. As concentration, the electric potential is maximum at the surface and decreases exponentially with distance. If the double layer is created by adsorption of potential-determining ions then the electrical potential, Φ, is expressed by Nernst equation (2-1) and, at a certain temperature T, it depends only on concentration of these ions in bulk solution, c, and the valence of ions, v:

$$\Phi_0 = \frac{k_B T}{ve} \ln\left(\frac{c}{c_0}\right) \Rightarrow \mathrm{c} = \mathrm{c}_0 \exp\left(\frac{ve\Phi_0}{k_B T}\right) \qquad (2\text{-}1)$$

where k_B is the Boltzmann constant and c_0 is the concentration at zero point of charge when Φ=0 (van Olphen, 1977). As reported by van Olphen (1977), for small potentials at surface, the distribution of electric potential, Φ, with distance, x, from particle surface can be expressed as:

$$\Phi = \Phi_0 \exp(-kx) \qquad (2\text{-}2)$$

where k is a constant inversely proportional to dielectric constant of the medium. These equations show that higher the counter-ion valences and concentration, lower is the electric potential and the diffuse layer is more compressed.

When two particles approach, due to their diffuse counter-ions, there is a repulsive force between them and work is required to move close two particles. However, also attractive forces exist, and flocculation demonstrate their existence. These forces are van der Waals attraction forces. According to van Olphen (1977), these forces are equal to the sum of all the attractive forces between every atom of one particle and every atom of the other particle and this summation lead to a less rapid decay with distance. Indeed, while van der Waals attractive force between two atoms is inversely proportional to the seventh power of the distance, it is inversely proportional to the third power of distance between two spherical particles (van Olphen, 1977). The attractive force is basically independent on solution, while repulsive forces depend on ion concentration and ion valence. As ion concentration decreases, as shown Figure 2-3 from a to c, suspension behaviour changes. In case a, which refers to a high ion concentration, if two particles come in contact, attractive forces are dominant, and flocculation occurs. In case c, at high distances, repulsive forces are dominant, and particles don't flocculate; however, at much lower distances, attractive forces can be dominant, and coagulation takes place. Indeed, the sections that represent long-range repulsions are called "energy barriers" and particles that has passed the "barrier" are said to have "jumped over the barrier" (van Olphen, 1977). Case b represents an intermediate and unstable state.

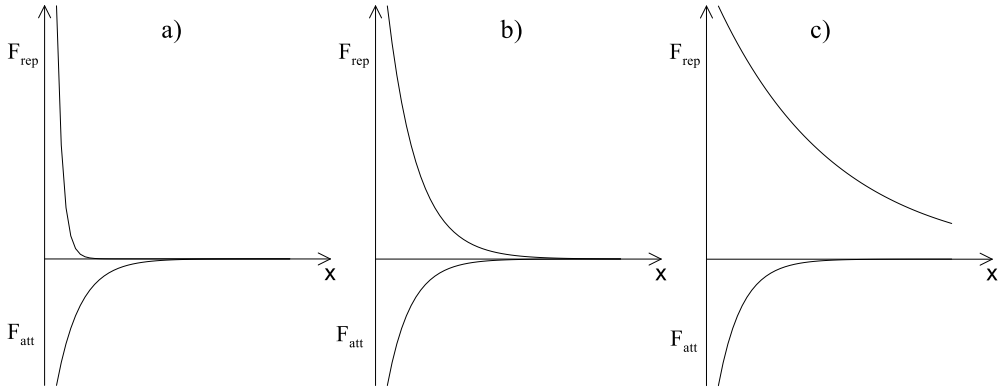

Figure 2-3. Representation of double layer repulsive forces (F_{rep}) and attractive van der Waals forces (F_{att}) with distance.

A more complex model for diffuse layer is the Stern model, that is a combination of Helmholtz and Gouy-Chapman models (Paunovic and Schlesinger, 2006). It assumes that some ions are restricted to a very small plane close to the particle surface (as the Helmholtz model) which cause a strong reduction of electric potential, while other ions are distributed in the solution, as Gouy-Chapman model.

The models shown in 2.2.1 can be applied to all suspensions. In the case of clay, the electric double layer structure is more complex due to clay mineral morphology. On the flat surface, a net negative charge due to ion substitution occurs. The compensating cations between unit-layers try to diffuse away in presence of water due to lower concentration, while they are attracted electrostatically to the charged lattice. These compensating cations act as counter-ions of the double layer, they are exchangeable for other cations and are confined in a narrow space between unit-layer surfaces. Due to the large adsorption force between lattice and counter-ions, conversely to other suspensions, a large portion of counter-ions is located on the surface while a smaller one is in the diffuse layer, with a better accordance to Stern model. On the edge surface, due to the abrupt disruption of tetrahedral and octahedral sheets, primary bonds are broken. It is likely that a positive double layer is created also on the edge surface.

Because of the plate-like morphology, when particles flocculate, three different particle associations may occur: Face to Face (FF), Edge to Face (EF) and Edge to Edge (EE).

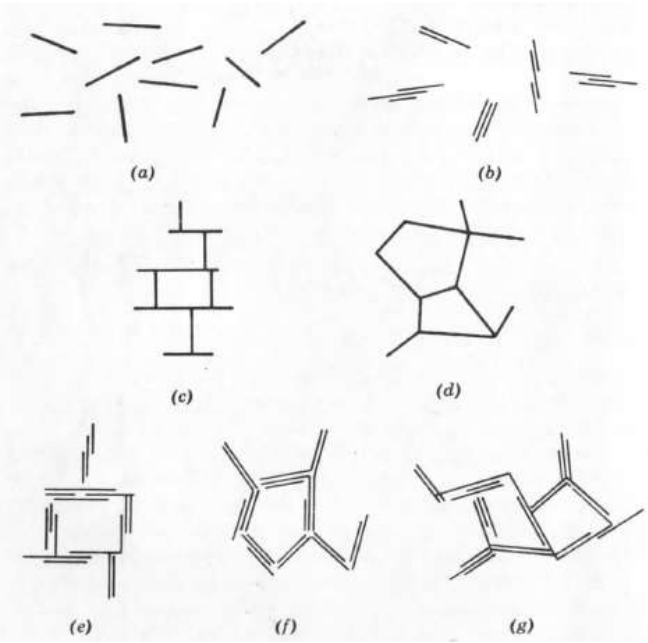

Figure 2-4. Schematic representation of types of clay particle associations: (a) Deflocculated and dispersed; (b) Deflocculated and aggregated; (c) EF flocculated and dispersed; (d) EE flocculated and dispersed (e) EF flocculated and aggregated (f) EE flocculated and aggregated (g) EE and EF flocculated and aggregated. (van Olphen, 1977).

Due to different double layers, their interaction changes in dependence of the kind of particle association. At the same time, due to different geometry, summation of van der Waals forces changes and, by consequence, the attractive force. As reported by van Olphen (1977), EE and EF associations lead to agglomerates that can be called "flocs", while FF association can be called "aggregate"; dissociation of EE and EF particles is called "deflocculation", while FF separation in thinner flakes can be called "dispersion". This means that a suspension can be flocculated and dispersed or aggregated but deflocculated (Figure 2-4). Modes of clay particle association affect rheological behaviour of clay suspensions. In the following section, a brief explanation of rheological behaviour of suspensions and the influence of flocculation will be presented.

2.2.2. Rheological properties of clay suspensions

Given a unit cube of matter with a fixed lower surface named reference surface, if a shear stress τ is applied on the top surface, there is movement of the top layer in the same direction. The layer below moves in the same direction with a lower velocity and so on, which results in a velocity gradient in normal direction respect to shear stress direction. This gradient is called rate of shear, D, measured in sec^{-1}. The rheological behaviour can be described by a relationship between shear stress and the rate of shear. When they are related by a linear relationship passing through origin, the fluid is called Newtonian (2-3). The constant of

proportionality is called coefficient of viscosity or briefly *viscosity*, η, whose physical unit, in the International System, is Poiseuille (Pl), equal to 1·Pa·sec. Water viscosity at 20 °C is 10^{-3} Pl, equal to 0.01 poise, another commonly used unit.

$$\tau = \eta D \qquad (2\text{-}3)$$

Dilute suspensions behave as Newtonian fluids. The ratio between suspension viscosity, η, and liquid medium viscosity, η_0, is called *relative viscosity of suspension*, η_r, and can be related to the amount of dispersed solids with a theoretical relation derived by Einstein, as reported by van Olphen (1977):

$$\eta_r = 1 + k_{\eta_r} C_s \qquad (2\text{-}4)$$

where C_s is the concentration of solids by volume and k_{η_r} is a constant equal to 2.5 for spheres but it is much larger if particles are anisometric as plates or rods. The relation is valid only for suspension dispersed enough so that particles (large compared to molecules of medium) don't influence one each other.

If solid concentration is high enough that interaction cannot be neglected, these formulas are no longer valid. Indeed, concentrated suspensions behave as non-newtonian fluids. Examples of non-newtonian behaviours are represented in Figure 2-5. In such systems, at each point, the *apparent viscosity*, τ/D, and *differential viscosity* (or *plastic viscosity*), dτ/dD, can be defined.

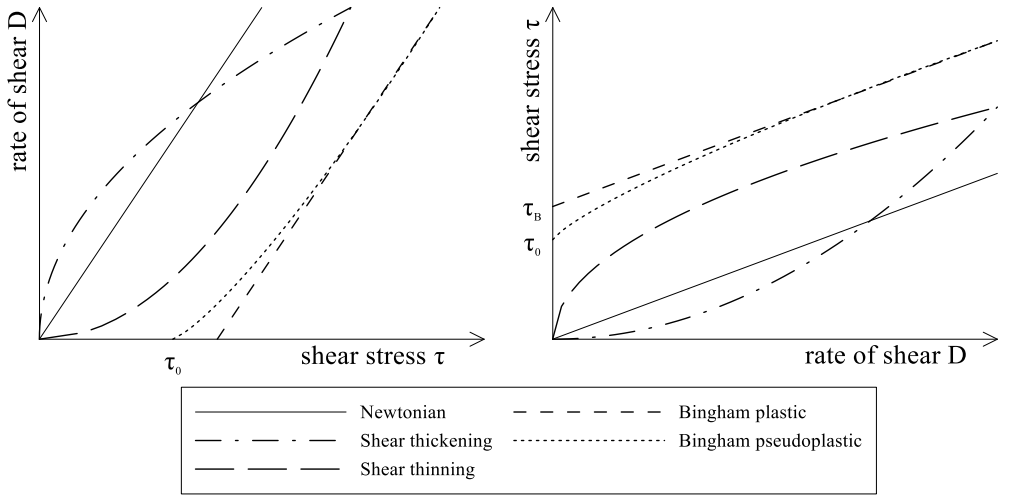

Figure 2-5. Rheological behaviour in laminar flow.

When both apparent and differential viscosity increase with shear stress, the flow is defined as *dilatant* or *shear thickening*. In the opposite, when both apparent and differential viscosity decrease with shear stress, it is defined as

shear thinning. Thickening and thinning behaviours can be described by a power law model (2-5), where K and n are two constants. If n < 1, it is shear thinning, with n > 1 it is shear thickening.

$$\tau = KD^n \quad (2\text{-}5)$$

If no flow occurs below a threshold shear stress τ_0, defined as *yield stress*, and differential viscosity decrease till a constant value where τ-D relation becomes linear, it is called *Bingham pseudoplastic flow*. Extrapolating the straight line to low shear rates, an ordinate τ_B (called *Bingham yield stress*) is obtained. This linear behaviour is called *ideal plastic flow* or *Bingham plastic flow*, described by equation (2-6).

$$\tau = \tau_B + \eta D \quad (2\text{-}6)$$

$$\tau = \tau_0 + KD^n \quad (2\text{-}7)$$

A shear thinning behaviour with an initial yield stress, τ_0, it's also possible and there are different models which can describe this behaviour, as the Herschel-Bulkley which simply adds a yield stress to power model (2-7). It is worth noting that this representation of rheological behaviour is only valid in laminar flow, whereas turbulent flow occurs at high shear rates and behaviour is also determined by inertia forces.

These properties can be also dependent on shear history and shearing time. When apparent viscosity decreases with shearing time, it is called *thixotropic*; at the opposite, if apparent viscosity increases with shearing, it is called *rheopectic*.

Some models can be used to predict the viscosity of a concentrated suspension, as the Einstein model for dilute suspensions (2-4). An example is the Krieger-Dougherty model (Krieger and Dougherty, 1959), in which $C_{s,\,max}$ is the maximum solid concentration by volume, while [η] is the intrinsic viscosity of suspension. As reported by Struble and Sun (1995), it takes account for the effect of individual particle on viscosity.

$$\eta_r = \left(1 + \frac{C_s}{C_{s,max}}\right)^{-[\eta]C_{s,max}} \quad (2\text{-}8)$$

2.2.2.1. Rheological behaviour of clay suspensions

The flow behaviour of dilute and concentrated clay suspensions is of the Newtonian and Bingham type, respectively. Indeed, flocculated particles are

linked together, thus a certain yield stress is developed. The behaviour can also be thixotropic.

Particle association presented in 2.2.1 affects the behaviour of a clay suspension. In a dilute clay suspension, viscosity increases if flocs are formed by EE and EF association, while it decreases when FF association occurs. In concentrated clay suspension, the continuous card-house structure given by EE and EF associations within the total volume leads to a Bingham behaviour. However, yield stress is reduced when FF association occurs simultaneously due to the lower links in the card-house structure.

In a pure water suspension, double layers are developed enough to prevent particle association by van der Waals attraction but, thanks to the opposite charge of edge and faces that exceeds the FF repulsion, EF association occurs with a T shape, leading to relatively high viscosity in dilute systems and high yield stress in concentrated systems. Salinity of water does affect the association and, by consequence, rheological properties. A low concentration of NaCl can lead to a compression of the double layer, diminishing both EF attraction and FF repulsion, leading to the breakage of the card-house structure and a reduction in yield stress and viscosity, respectively in concentrated and dilute clay suspensions. However, at higher salt concentration, due to further compression of double layer, van der Waals attraction forces between EE and EF association enhance and the card-house structure is more likely to occur, leading to an increase in viscosity and yield stress. At very high concentrations, yield stress can decrease again, maybe due to FF association by which card structure links are reduced. However, these effects depend on clay mineralogy and salt. By this way, flocculation or deflocculation can be fostered. There are cases in which a suspension must be fluid enough to be poured, but with a rather high concentration. In such a case, a lower viscosity and yield stress can be obtained by deflocculating the system by breaking EE and EF associations. This can be achieved by reversing positive-edge charge, determining an EE and EF repulsion (van Olphen, 1977).

In soil science, clay-water interaction is simply defined via Atterberg limits, which represent conventional boundary water content, w, between solid-plastic state, *plastic limit* w_p, and plastic-liquid state, *liquid limit* w_l, whose difference is defined as *plasticity index* $I_p=w_l-w_p$. These index properties are determined by means of standard procedures and are used for classification of fine grained soils (ASTM, 2006, 2005). The state is defined via the *consistency index* $I_c=(w_l-w)/I_p$,

and *liquidity index* $I_l=(w-w_p)/I_p$. Even if the liquid limit is conventionally defined via Casagrande method, it has been shown that it can be related to a specific undrained shear strength, that is the water content at which undrained shear strength, s_u, of the remoulded soil is equal to 2 kPa (ASTM, 2005). Indeed, the liquid limit can be obtained also via the fall cone test, which allow to determine the undrained shear strength of a soil and it is standardized and preferred in many countries (Houlsby, 1982; Koumoto and Houlsby, 2001). Liquid limit can be assumed as the water content at which a 60°, 60 g cone penetrates 10 mm, corresponding to s_u=2 kPa. Indeed, undrained shear strength, s_u, can be determined as:

$$s_u = \frac{KW}{h^2} \tag{2-9}$$

Where h is the penetration depth, W is the weight of the cone and K is the fall cone factor, as defined by Hansbo (1957), which depends on cone geometry and roughness, as shown by Koumoto and Houlsby (2001), and it is equal to 0.30 for a 60° semi-rough cone. The relation between water content and undrained shear strength is nonlinear, as shown by Koumoto and Houlsby (2001) which propose the relation (2-10), linear in log(w)-log(s_u) plane, where p_a is the atmospheric pressure.

$$w = a\left(\frac{s_u}{p_a}\right)^{-b} \tag{2-10}$$

They also suggest a fall cone undrained shear strength at the liquid limit equal to 1.4 kPa. The liquidity index and the undrained shear strength can be related to rheological properties of clay suspensions. Indeed, Locat and Demers (1988) show that a good relation exists between viscosity and liquidity index for different clays. They observe both Bingham and Bingham pseudoplastic behaviour; as expected, an increase in I_L leads to a reduction of viscosity and yield stress. The authors identify a good relation between viscosity (in 10^{-3} Pl) and I_L, proposing equation (2-11). About yield stress, not a unique relationship with I_L seems to exist (converging at lower liquid index), but they only identify a range. However, for each soil, Locat and Demers (1988) find a linear relationship between log τ_0 – log s_u. They also propose a relationship between s_u and I_L (2-12), whose expression is similar to (2-10).

$$\eta = \left(\frac{9.27}{I_L}\right)^{3.33} \tag{2-11}$$

$$s_u = \left(\frac{19.8}{I_L}\right)^{2.44} \quad (2\text{-}12)$$

2.3. Bulk properties of soil slurry

The soil, in its initial state, is a multiphase material composed of solid, liquid and gas phases. However, in the production process of the lightweight cemented soil, it is mixed with water at high water content, above liquid limit, to obtain a slurry. The initial structure of the soil is disrupted, particles are diluted, and a suspension is obtained; thus, slurry properties are, at least theoretically, independent of initial condition. If there is no air entrapped, then there is no gas phase. The subscript "s" refers to soil, while the superscript "s" refers to the solid phase of soil. With W_s^s and V_s^s respectively the weight and the volume of solid soil and W_{ws} the weight of water in the slurry:

$$\rho_s = \frac{W_s^s}{V_s^s} \quad (2\text{-}13)$$

$$w_s = \frac{W_{ws}}{W_s^s} \quad (2\text{-}14)$$

where w_s is the water content of soil slurry. W_{ws} is the sum of initial water in soil and the water added to obtain a specific w_s. Hence:

$$W_{slurry} = (1 + w_s)W_s^s \quad (2\text{-}15)$$

If the absence of voids and air entrapped is assumed, then:

$$V_{slurry} = V_s^s + V_{ws} = \frac{W_s^s}{\rho_s} + \frac{W_{ws}}{\rho_w} = \frac{W_s^s}{\rho_s} + \frac{w_s W_s^s}{\rho_w} = W_s^s\left(\frac{1}{\rho_s} + \frac{w_s}{\rho_w}\right) \quad (2\text{-}16)$$

$$\gamma_{slurry} = \frac{W_{slurry}}{V_{slurry}} = \frac{1 + w_s}{\frac{1}{\rho_s} + \frac{w_s}{\rho_w}} \quad (2\text{-}17)$$

where ρ_w is the density of water. Figure 2-6 shows the percentages of mass and volumes in a soil slurry for w_s=140% and ρ_s=2.59 g/cm^3.

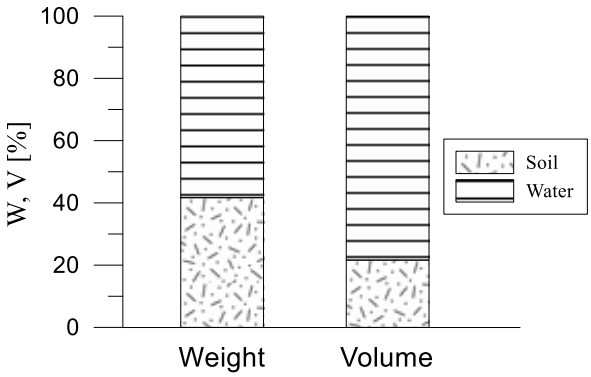

Figure 2-6. Percentages of mass and volume in soil slurry for w_s=140% and ρ_s=2.59 [g/cm^3]

2.4. Summary

The behavior of clayey soil suspensions, the main constituent of the lightweight cemented soil, has been described in this section. The clay-water interaction strongly depends on clay mineralogy, which has been briefly described in Appendix A; the interaction between water and clay particles can be modelled by means of diffuse layer theory; at macroscale, the behavior can be modeled as a Bingham fluid. Depending on clay minerals, dilution (i.e. water content) and salts concentration different particle associations can occur, thus affecting the rheological behavior of clayey suspensions. Rheological properties (i.e. yield stress and viscosity) can be related to properties and state parameters commonly used in soil science, such as liquid limit and liquidity index.

References

A.G.I., 1963. Nomenclatura geotecnica e classifica delle terre.

Andrade, F.A., Al-Qureshi, H.A., Hotza, D., 2011. Measuring the plasticity of clays: A review. Appl. Clay Sci. 51, 1–7. https://doi.org/10.1016/j.clay.2010.10.028

ASTM, 2006. Standard Practice for Classification of Soils for Engineering Purposes (Unified Soil Classification System), ASTM Standard Guide. https://doi.org/10.1520/D2487-11.

ASTM, 2005. Standard Test Methods for Liquid Limit, Plastic Limit, and Plasticity Index of Soils, Report. https://doi.org/10.1520/D4318-10.

Barton, C.D., Karathanasis, A.D., 2002. Clay Minerals. Encycl. Soil Sci. 187–192. https://doi.org/10.1081/E-ESS-120001688

Di Maio, C., Fenelli, G.B., 1997. Influenza delle interazioni chimico-fisiche sulla deformabilità di alcuni terreni argillosi. Riv. Ital. di Geotec. 695–707.

Di Maio, C., Fenelli, G.B., 1994. Residual strength of kaolin and bentonite: the influence of their constituent pore fluid. Géotechnique. https://doi.org/10.1680/geot.1994.44.2.217

Grim, R.E., 1968. Clay mineralogy, International series in the earth and planetary sciences. McGraw-Hill.

Hansbo, S., 1957. A new approach to the determination of the shear strength of clay by the fall-cone test, in: Swedish Geotechnical Institute Proceedings. pp. 1–59.

Houlsby, G.T., 1982. Theoretical analysis of the fall cone test. Géotechnique 32, 111–118. https://doi.org/10.1680/geot.1982.32.2.111

Koumoto, T., Houlsby, G.T., 2001. Theory and practice of the fall cone test. Géotechnique 51, 701–712. https://doi.org/10.1680/geot.2001.51.8.701

Krieger, I.M., Dougherty, T.J., 1959. A Mechanism for Non-Newtonian Flow in Suspensions of Rigid Spheres. Trans. Soc. Rheol. https://doi.org/10.1122/1.548848

Locat, J., Demers, D., 1988. Viscosity, yield stress, remolded strength, and liquidity index relationships for sensitive clays. Can. Geotech. J. 25, 799–806. https://doi.org/10.1139/t88-088

Martin, R.T., Bailey, S.W., Eberl, D.D., Fanning, D.S., Guggenheim, S., Kodama, H., Pevear, D.R., Środoń, J., Wicks, F.J., 1991. Report of the clay minerals society nomenclature committee: Revised classification of clay materials, Clays and Clay Minerals. https://doi.org/10.1346/CCMN.1991.0390315

Paunovic, M., Schlesinger, M., 2006. Fundamentals of Electrochemical Deposition, The ECS Series of Texts and Monographs. Wiley.

Struble, L., Sun, G.K., 1995. Viscosity of Portland cement paste as a function of concentration. Adv. Cem. Based Mater. 2, 62–69. https://doi.org/10.1016/1065-7355(95)90026-8

van Olphen, H., 1977. An introduction to clay colloid chemistry : for clay technologists, geologists, and soil scientists. New York.

3. Cement and foam

The lightweight cemented soil method requires the addition of two additives to soil slurry: cement and foam. The former is the binding agent, required to have the hardening of the paste, i.e. to gain strength. A summary of cement classification is reported below. Then, the main chemical compounds and reactions are presented. Finally, the structure and the different phases in the cement paste are widely discussed due to their considerable importance on lightweight cemented soil bulk properties. Foam is a dispersion of bubbles in a surfactant solution. It is added to lower the density, thanks to bubbles entrapped in the fresh paste during mixing, and to enhance workability. The main properties of foam and mechanisms of foam stability are discussed in this section.

3.1. Cement

Portland cement, named for resemblance of hardened paste to the Portland stone (a limestone near Dorset), was patented by Joseph Aspdin in 1824, but the prototype of modern cement was made in 1845 by Isaac Johnson (Neville, 2011). Nowadays, Portland cement represents the category defined as CEM I, in which its percentage has to be higher than 95%. Cements classified as CEM II are blend of Portland cement (which is the main constituent) with other materials, such as blast furnace slag, silica fume, pozzolana, fly ash, limestone. More generally they can be referred to as blended Portland cements. Blastfurnace cements, pozzolanic cements and composite cements are classified as CEM III, CEM IV and CEM V, respectively. They differ from blend cements in terms of percentages; for example, if blastfurnace slag percentage is below 35%, it is classified as CEM II Portland slag, if above, it is classified as CEM III Blastfurnace cement. The threshold in pozzolanic cements is 11%. Composite cements are composed of different materials. A letter, such as A, B or C, indicates that the amount of added material is within a specific range, while (for CEM II) a letter specifies the additional material, such as P for pozzolana and L or LL for limestone.

Cements are also classified in terms of minimum compressive strength in MPa at 28 days, which gives the name to the class: 32.5, 42.5, 52.5. These classes are subdivided in sub-classes depending on early stage strength whose minimum value depends on the resistance class. Cements with ordinary early stage strength are classified as *Normal hardening* and denoted by letter N, while cements with higher early age are classified as *Rapid hardening cements* and denoted by letter R.

3.1.1. Chemical composition and hydration reactions

The cement is manufactured primarily by burning up to 1450 °C a mix of calcareous material, such as limestone or chalk, and alumina and silica found as clay or shale and grinding the resulting clinker. These raw materials consist mainly of lime, silica, alumina and iron oxide.

The main components of cement are summarized in the following list. The name of compound, composition and abbreviation are reported. In cement chemistry, the following abbreviations are commonly used: CaO=C, SiO_2=S, Al_2O_3=A, Fe_2O_3=F, H_2O=H.

- Tricalcium silicate - $3CaO \cdot SiO_2 \equiv C_3S$
- Dicalcium silicate $2CaO \cdot SiO_2 \equiv C_2S$
- Tricalcium aluminate $3CaO \cdot Al_2O_3 \equiv C_3A$
- Tetracalcium auminoferrite $4CaO \cdot Al_2O_3 \cdot Fe_2O_3 \equiv C_4AF$

It is worth noting that C_2S can have at least three forms: α, β and γ. The former, α-C_2S, inverts to β-C_2S at 1450° C. This form, that is the one hydraulically active, is preserved in commercial cements, otherwise it further changes to γ-C_2S at 670° C. The composition of cement can vary a lot, but the first two compounds usually constitute around 70% by weight. They can contain some oxides and impurities. In this case, the "impure" calcium silicates are defined as alite and belite, respectively.

Minor compounds, in terms of quantity, such as K_2O, Na_2O, MgO, TiO_2, Mn_2O_3 constitute usually no more than a few per cent, but they can be of interest. The first two are known as "alkalis" and they have been found to react with some aggregates leading to disintegration of concrete and its rate of gain of strength (Neville, 2011). Gypsum ($CaSO_4 \cdot 2H_2O$) is also present; it is fundamental for workability of fresh past that is related to hydration of tricalcium aluminates.

The setting time is defined as the time at which the cement paste changes from a fluid to a rigid state, losing workability. This stiffening process is called "setting". Initial and final setting time are two arbitrarily conditions that can be determined via the Vicat needle (ASTM, 2008). Hardening, which must be distinguished by setting, is the gain of strength of a set cement paste. Setting and hardening of cement paste depends on the hydration of these compounds, primarily C_3S and C_2S, and their products (*products of hydration*) that are insoluble in water.

The hydration process develops in time and its rate decreases continuously. The rate of hydration of the main compounds differ considerably. Calcium aluminates reactions are faster than calcium silicates. Calcium silicate hydration reactions can be assumed as the following, where $C_3S_2H_3$ is a lower basicity calcium silicate and lime is separated as calcium hydroxide (*portlandite*), $Ca(OH)_2$.

$$2C_3S + 6H \rightarrow C_3S_2H_3 + 3Ca(OH)_2 \quad (3\text{-}1)$$

$$2C_2S + 4H \rightarrow C_3S_2H_3 + Ca(OH)_2 \quad (3\text{-}2)$$

The hydration of C_3S is faster than C_2S; rate of reaction can be defined as moderate and slow, respectively. The product $C_3S_2H_3$ is usually referred as C-S-H gel. Indeed, there are uncertainties about the actual C:S ratio, and it is likely that products of C_2S and C_3S are slightly different, so the reactions above are derived by an assumption about CSH composition. The CSH is referred to as gel because it appears as amorphous, but electron microscopy shows a crystalline character. Its structure is very disordered and can appear often as composed of fibrous or flattened particles as some clay minerals, as suggested by Taylor (1950). In initial state of hydration, calcium hydroxide forms thin hexagonal plates of tens of micrometres. Later, the plates merge into a massive deposit constituting up to 25% of hardened paste.

Portlandite particles produced by hydration of calcium silicates, due to the limited solubility, are formed within interstitial space and, with a continuing supply of moisture, can react with silica thus producing additional hydration products of a fine pore structure (Newman and Choo, 2003). As reported by Bergado (1996), portlandite can react in soil-cement stabilization, and reactions, namely pozzolanic reactions, can be summarized by the following equations:

$$Ca(OH)_2 + SiO_2 \rightarrow CSH \quad (3\text{-}3)$$

$$Ca(OH)_2 + Al_2O_3 \rightarrow CAH \quad (3\text{-}4)$$

These reactions depend on solubility of silicates and aluminates in soil; however, as stated by Bergado (1996), primary products of hydration (3-1, 3-2), are much stronger than the secondary ones, which produce a further additional cementing substance enhancing the bond strength between particles.

As already pointed out, the hydration of tricalcium aluminate is faster than calcium silicates. If sulphates are absent, its hydration leads to initial formation of calcium aluminium hydrate, C_4AH_{19}, and subsequently C_3AH_6 (Black et al., 2006); the chemical reaction can be assumed as the following:

$$C_3A + 6H \rightarrow C_3AH_6 \qquad (3\text{-}5)$$

In absence of gypsum, this reaction would be very violent, producing heat due to the exothermic nature of reaction, leading to the *flash set*, that is the immediate stiffening of the paste. Carbonation of calcium aluminium hydrate leads to formation of calcium hemicarbonaluminate, $C_8A_2\overline{C}H_{24}$, and calcium monocarboaluminate, $C_4A\overline{C}H_{11}$, (where $\overline{C}$ is the abbreviation for CO_3) observed by Black et al. (2006) characterized by peaks in X-Ray diffraction[1] at 10.75° and 11.65°, respectively.

When gypsum is present, C_3A reacts with water and SO_4^{-2} forming a calcium trisulphate aluminate $3CaO{\cdot}3CaSO_4{\cdot}32H_2O$ (3-6), the *ettringite*, which acts as a coating on C_3A. When SO_4^{-2} goes through it, an expansion occurs, the coating is disrupted, and another coating is formed; this process goes on till exhaustion of SO_4^{-2}. When all the sulphate has been consumed, the remaining C_3A reacts with ettringite forming $3CaO{\cdot}CaSO_4{\cdot}12H_2O$ (3-7), known as monosulphate, which can reverse again in ettringite if it comes in contact with other sulphates in solution (Marchese, 2003; Newman and Choo, 2003). Hydration of C_4AF is believed to be analogues to C_3A, but slower.

$$C_3A + 3CaSO_4 + 32H \rightarrow 3(C_3A \cdot C\bar{S} \cdot 32H) \qquad (3\text{-}6)$$

$$C_3A \cdot 3C\bar{S} \cdot 32H + 2C_3A + 4H \rightarrow 3(C_3A \cdot C\bar{S} \cdot 12H) \qquad (3\text{-}7)$$

It is worth noting that the presence of C_3A is undesirable in cement, but necessary in the manufacturing process because it acts as a flux, reducing the burning temperature of clinker and facilitating the combination of lime and silica. In the hardened paste, it gives a negligible contribute to strength, and if attacked by sulphates, the expansion due to ettringite formation can cause the disruption of the hardened paste.

Setting is due to the compounds which react first, i.e., C_3A and C_3S. Due to gypsum, C_3S sets before; conversely, a porous framework of calcium aluminate hydrate would form, in which the remaining compounds would hydrate affecting negatively the strength characteristics. Sometimes the "*false set*" occurs at early mixing time. It can be due to dehydration of gypsum during the manufacturing of cement, which leads, when mixed with water, to formation of crystals of gypsum causing a loss in workability. However, without adding any water, workability can be improved by remixing the concrete.

[1]The XRD analysis is described in Appendix B.

3.1.1.1. Temperature effects on products of hydration

The progress of hydration of the cement paste can be studied via thermogravimetric analyses and x-ray diffraction, especially in the early stage (Neville, 2011). These methods are briefly explained in Appendix B. As reported by Alarcon-Ruiz et al. (2005), many authors have described reactions occurring at different ranges of temperature. From 30 to 105 °C, almost all the evaporable water and part of the bound water escapes. It is considered that a temperature of 120 °C is required to remove all the evaporable water. In the range of temperature that goes from 110 to 300 °C, the loss of water combined in hydrates take place. More specifically, between 110-170 °C, decomposition of gypsum and ettringite and part of carbo-aluminate hydrates occur. Decomposition of C-S-H and the remaining carbo-aluminate hydrates take place between 180 and 300 °C. Decomposition of portlandite usually occurs between 450 and 550 °C, as reported by Alarcon-Ruiz et al. (2005), but Lothenbach et al. (2007) observed a slightly lower range on CEM II/A-LL 42.5 R (with $w_c/c=0.5$) with a peak at 450°C. Lothenbach et al. (2007) also observe, on the same cement paste, dissolution of calcium monocarboaluminate at 650 °C. Finally, between 700 and 900 °C, $CaCO_3$ decarbonation takes place.

3.1.2. Hardening and hardened paste structure

Hardening is the development of strength in a set paste and it is due to the almost total reaction of cement compounds in hydrated forms (Marchese, 2003). Cement paste is constituted of a matrix composed of very small (in the order of nanometres) interlocking crystals of calcium silicate hydrates, which can be described as gel, in which other compounds such as portlandite, aluminates and alumina-ferrites, minor components and unhydrated cement are submerged. The cement paste is porous due to voids left by hydrated water and the water-filled spaces. Thus, these *capillary pores* can be either empty or filled with water. The gel matrix itself is porous (porosity of gel is around 28%), and the interstitial voids are called *gel pores*, with a nominal diameter of 3 nm while capillary pores are one or two orders of magnitude larger.

It is worth noting that because of the colloidal dimension of products of hydration the surface area of the solid phase increases enormously, and a large amount of free water becomes adsorbed on this surface. Indeed, a fraction of water is *chemically combined water*, a portion is held between the surfaces of gel sheets and it is called *interlayer or zeolitic water* and another fraction is held by surface forces and it is called *adsorbed water*. This water is not free water so, if the material is seal cured (i.e. no outward or inward water flow occurs) cement

compounds use up the mixing water and water content decreases; this phenomenon is known as *self-desiccation*. If the available water is not enough (a water to cement ratio by weight lower than 0.5, approximately), hydration rate in a seal cured paste is lower than a moist cured paste. A much higher water to cement ratio leads to a much porous paste, decreasing the strength.

The actual source of the strength of cement gel, which includes also portlandite crystals and gel pores, has not been fully understood yet, but it is probably related to two different cohesive forces (Neville, 2011). The first one is a physical attraction due to van der Waals forces between the particles that have a very large surface area. The second one is due to chemical bonds between particles.

3.1.2.1. Rapid hardening cements

Rapid hardening cements differ from normal hardening because of the relatively higher early stage strength. Rapid hardening must not be confused with high rate of setting which is usually the same of normal hardening cements. The increase rate of hardening is obtained by a higher amount of C_3S, up to 70% and by a higher fineness (Neville, 2011). Higher strength usually persists at 28 days and it equalizes at 2 or 3 months. Later, the strength becomes lower than coarser cements. It shouldn't be used in large construction due to high rate of heat development related to the faster rate of hydration. Ultra-high early strength cements are also manufactured but they are not standardized.

3.1.3. Effect of alkalis

As already pointed out, the minor compounds can affect significantly the cement paste. In first place, they affect alkalinity of fresh cement paste, which has normally a pH above 12.5 but it is higher in cements with high alkali content.

They also affect the development of strength. These effects are not fully understood yet, but generally the presence of alkali increases the strength at early ages (around 3 days) but decreases the long-term strength, as shown in some tests at 28 days curing.

Alkali can also react with some aggregates, as with silica and carbonates. The former is the most common. Alkaline hydroxides in pore water react with siliceous minerals in aggregates forming an alkali-silicate gel, with a rate that depend on aggregate size. This process is enhanced by the high pH which increase silica minerals solubility. The gel can constitute a plane of weakness in the aggregate, or it can be a coating on the aggregate, altering the bonds between

the surrounding cement paste and the aggregate surface and by consequence weakening the structure. Moreover, being a swelling gel under imbibition, its expansion can lead to cracks and disruption in the hardened paste due to the consequent internal pressure. These reactions seem to occur only in presence of Ca^{+2} ions, so they can be prevented by adding pozzolana in the mix which removes $Ca(OH)_2$. Conversely, a large water availability, high permeability and wetting-drying cycles accelerate the process. The other phenomenon, alkali-carbonate reaction, occurs when alkalis react with some dolomitic limestones; the volume of gel produced is lower than original and then it is subject to swelling under humid conditions. This leads to a breakage of bonds between aggregate and cement paste. However, reactive carbonate rocks are not very widespread, and this phenomenon is not likely to occur.

3.1.4. Fillers and limestone Portland cement

Fillers are fine-ground material with uniform properties and fineness (about the same as cement) which can be added up to a certain maximum content to gain beneficial effects on some properties of concrete such as workability, density, permeability, bleeding or cracking tendency. They are usually chemical inert, but if no harm derives from their reactions, there is no disadvantage by using them. They can be either naturally occurring or processed inorganic mineral materials.

One of the most common filler is limestone and, differently from other fillers (usually limited to 5%), it can be added up to 35%. This cement is known as Portland limestone cement (for example CEM II/A L, CEM II/B-LL). The $CaCO_3$ has to be the main constituent of the limestone, above 75%, while clay content has to be lower than 1.2 g/ 100 g (Newman and Choo, 2003). Carbonate calcium is not chemically inert. As reported by Neville (2011), Zielinska (1972) showed that it reacts with C_3A and C_4AF to produce $3CaO{\cdot}Al_2O_3CaCO_311H_2O$. Limestone fillers can also be used in self-compacting concrete to aid cohesion in fresh concrete.

3.1.5. Rheology of fresh paste

The rheology of fresh concrete is an important topic in concrete technology because it is strictly related to workability and consistency, which have qualitative meaning. The ACI Committee (2008) defined workability as the "property of freshly mixed concrete or mortar that determines the ease with which it can be mixed, placed, consolidated, and finished to a homogenous condition", while consistency is defined as the "degree to which a freshly mixed concrete, mortar, grout, or cement paste resists deformation" and it can be

normal, plastic and wettest stable. Other words are used to describe flow properties of concrete such as stability and mobility. These properties are obviously related to rheological properties but, according to Ferraris (1999), this terminology should be discarded in favour of parameters which have physical meaning, as viscosity and yield stress (2.2.2). Indeed, the rheological behaviour of concrete is often assumed as a Bingham flow, described with Bingham plastic model which requires two parameters. However, the most common tests measure only one factor which is related to these properties. A few tests can give two parameters which are not necessarily directly related to yield stress and viscosity. They are more expensive and not easy to perform, so they are not commonly used. A summary of these tests is reported by Ferraris (1999).

The rheological properties of cement paste can be also related to the concentration of the suspension. Indeed, the fresh cement paste is a highly concentrate suspension of solid particles in water (Banfill, 1991), whose behaviour, at initial stage, is very similar to unreactive silica suspensions (Chougnet et al., 2008); as well known, workability increases with increasing w/c ratio, i.e. decreasing concentration, thus decreasing yield stress and viscosity. As observed by Struble and Sun (1995), the behaviour tends to be Newtonian in dilute suspension and pseudoplastic or Bingham pseudoplastic in concentrated suspensions, so that viscosity decreases also with shear stress. In their experimental work, Struble and Sun (1995) find the strain rate – stress relationship to be best fitted by a power law (2-5) and they suggest that viscosity, at a specific strain rate, can be fitted by the Krieger-Dougherty model (2-8) with $C_{s,max}$ varying from 0.64 to 0.8 and $[\eta]$ varying from 4.7 to 0.8 at increasing shear rate. They also find that viscosity varies from 5 to 0.01 Pl, depending on water to cement ratio by weight (w_c/c), type of cement, additives and strain rate. Chougnet et al. (2008) find that viscosity decreases with shear strain, varying from 10 to 0.03 Pl for $w_c/c=0.5$ and from 60 to 0.3 for $w_c/c=0.3$. They also find that the yield stress (assuming a Bingham plastic behaviour) ranges from 200 to 40 Pa at increasing w_c/c. However, assuming a non-linear model to fit data, they find τ_0 to be one order of magnitude lower (Figure 2-5). These ranges are in agreement to the values reported by Banfill (1991), that is 10-100 Pa for yield stress and 0.01-1 Pl for viscosity.

3.1.6. Bulk properties of cement paste

The weight and absolute volume of anhydrous cement (i.e. the cement added to the mix as a powder) will be termed $W_{c,a}$ and $V^s_{c,a}$, respectively. The "s" superscript implies that the volume refers to the volume of the solid phase. The

superscript "s" is not used for the terms that refer to unhydrated and anhydrous cement because they already refer to a "dry" state. Referring to volumes, being the cement a powder, the superscript "s" will be used to specify if symbol refers to the volume of the solid phase. Hence, the specific weight of the cement powder is defined as:

$$\rho_{c,a} = \frac{W_{c,a}}{V_{c,a}^{s}} \tag{3-8}$$

Given the water to cement ratio by weight, $\frac{w_c}{c} = \frac{W_{wc}}{W_{c,\,a}}$, with W_{wc} the water initially added to cement, if air entrapped is neglected, the weight and volume of cement suspension, respectively W_c and V_c, are:

$$W_c = W_{c,a} + W_{wc} = \left(1 + \frac{w_c}{c}\right) W_{c,a} \tag{3-9}$$

$$V_c = V_{c,a}^{s} + V_{wc} \tag{3-10}$$

where V_{wc} is the volume of water added to grout.

In the mixture, at a generic time, t, a portion x of the anhydrous cement, $W_{c,a}$, combines with water and it's hydrated. The solid products of hydration, whose weight is $W_{c,\,h}^{s}$, can be assumed as the sum of the water chemically combined, whose weight is $W_{wc,\,ch}$, and the portion of anhydrous cement that is hydrated. This portion x of the total anhydrous cement can be defined as "anhydrous hydrated cement", whose weight is $W_{c,a,h}$. The residual part is the unhydrated cement, $W_{c,unh}$:

$$W_{c,h}^{s} = W_{c,a,h} + W_{wc,ch} \tag{3-11}$$

$$W_{c,a,h} = xW_{c,a};\ W_{c,unh} = (1-x)W_{c,a}; \tag{3-12}$$

$$W_{c,a} = W_{c,a,h} + W_{c,unh} \tag{3-13}$$

It is worth noting that, conversely to unhydrated cement, water chemically combined and anhydrous hydrated cement are not actually present in the cement paste, but only their products of hydration exist. In terms of volumes:

$$V_{c,unh}^{s} = W_{c,unh}/\rho_{c,a} \tag{3-14}$$

$$V_{c,a}^{s} = V_{c,a,h}^{s} + V_{c,unh}^{s} \tag{3-15}$$

When a portion of cement is hydrated, the cement paste is composed of unhydrated cement, hydrated cement and capillary pores:

$$V_c = V^s_{c,unh} + V_{c,h} + V_{cap\ pores} \quad (3\text{-}16)$$

The term $V^s_{c,\ unh}$ refers to volume of the solid phase of the cement that is still not hydrated. The term $V_{cap\ pores}$ refers to the volume of capillary pores in the cement paste. The term $V_{c,\ h}$ is the volume of the hydrated cement and it is composed of water and cement. Indeed, as reported by Neville (2011), only a portion of water can be regarded as free water, beyond the range of surface force, while another amount is held in varying states. A fraction is chemically combined water whereas another amount of water is held between the surfaces of the gel sheets and it's called "interlayer" or "zeolitic" water. Another fraction is held by surface forces and it's called adsorbed water. Moreover, the water held in the cement paste is denser than free water, occupying a lower volume than the volume occupied before chemical reactions began. Given that, the hydrated cement can be considered as composed of solid products of hydration and gel water:

$$V_{c,h} = V^s_{c,h} + V_{gel\ water} \quad (3\text{-}17)$$

$$W_{c,h} = W^s_{c,h} + W_{gel\ water} \quad (3\text{-}18)$$

From (3-11):

$$W_{c,h} = W_{c,a,h} + W_{wc,ch} + W_{gel\ water} \quad (3\text{-}19)$$

The remaining water is within capillary pores (which can be either filled with water or empty) or held as gel water:

$$V_{cap\ pores} = V_{w\ cap\ pores} + V_{e\ cap\ pores} \quad (3\text{-}20)$$

$V_{cap\ pores}$, $V_{w\ cap\ pores}$ and $V_{e\ cap\ pores}$ are respectively the volume of capillary pores, the volume of capillary pores occupied by water and the volume of empty capillary pores. Hence, the balance of mass and volume become:

$$W_c = W_{c,unh} + W_{c,h} + W_{w\ cap\ pores} = \\ = W_{c,unh} + W_{c,a,h} + W_{wc,ch} + W_{gel\ water} + W_{w\ cap\ pores} \quad (3\text{-}21)$$

$$V_c = V^s_{c,unh} + V_{c,h} + V_{cap\ pores} = \\ = V^s_{c,unh} + V^s_{c,h} + V_{gel\ water} + V_{w\ cap\ pores} + V_{e\ cap\ pores} \quad (3\text{-}22)$$

An example, given by Neville (2011), is shown in Figure 3-1.

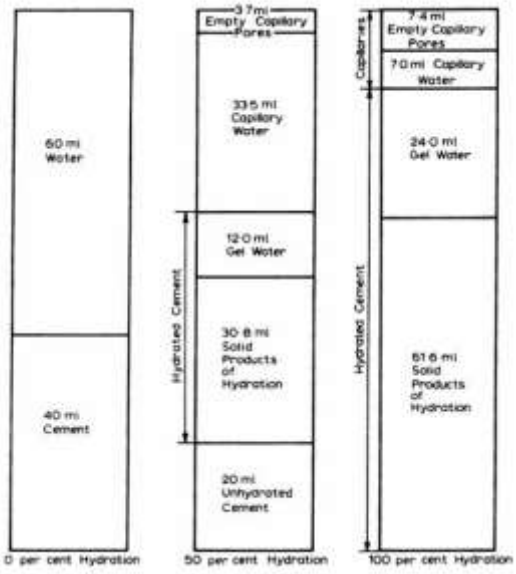

Figure 3-1. Cement paste composition at different hydration states for V_c=40 ml and V_{wc}=60 ml (Neville 2011).

These amounts are not easy to determine. Therefore, as suggested by Neville (2011), it's more convenient to divide the water of the cement paste in "evaporable water" and "non-evaporable water". According to Neville (2011), the "non-evaporable water" in a cement paste is composed of almost all of the chemically combined water and some water not held by chemical bonds. The "evaporable water" can be regarded as free water and it represents the liquid phase of cement paste; the "non-evaporable water" can be considered as part of solid phase. This division is implicitly assumed when water content is determined based on laboratory standard procedure, in which samples are oven dried at a specific temperature. Non-evaporable water can be related to the weight of hydrated (anhydrous) cement $W_{c,\,a,\,h}$ via a coefficient α:

$$W_{wc,n-ev} = \alpha W_{c,a,h} = \alpha x W_{c,a} = \frac{\alpha x W_{wc}}{w_c/c} \qquad (3\text{-}23)$$

$$W_{wc} = W_{wc,ch} + W_{gel\ water} + W_{w\ cap\ pores} = W_{wc,n-ev} + W_{wc,ev} \qquad (3\text{-}24)$$

$$W_{wc,ev} = W_{wc} - W_{wc,n-ev} = W_{wc}\left(1 - \frac{\alpha x}{w_c/c}\right) \qquad (3\text{-}25)$$

The coefficient α depends on the degree of hydration. In a well hydrated cement, α is around 18 % while in a full hydrated cement is around 23 %.

If $W_{wc,\ n\text{-}ev}$ is assumed as part of solid products of hydration, then:

$$W_{c,h}^{s} \cong W_{c,a,h} + W_{wc,n-ev} = W_{c,a,h} + \alpha W_{c,a,h} = (1+\alpha)W_{c,a,h} = x(1+\alpha)W_{c,a} \quad (3\text{-}26)$$

$$W_{c}^{s} = W_{c,h}^{s} + W_{c,unh} = W_{c,a} + (1-x)W_{c,a} = (1+\alpha x)W_{c,a} \quad (3\text{-}27)$$

This means that if x=0, the solid phase of cement is equal to the initial amount of cement powder added to the paste, while the solid phase of hydrated cement is equal to zero. When x>0, they both increase due to the amount of water combined.

It is worth noting that the amount of non-evaporable water has a considerable significance. It is representative of the progress of hydration, and the measurement in time of this quantity can be used as a measure of the degree of hydration in the cement paste, which is strictly related to the gain in strength. As reported by Neville (2011), Powers (1958) and then Khalil and Ward (1973) found a linear relationship between the heat of hydration and the amount of non-evaporable water. By this way, knowing the heat of hydration, it is possible to estimate the amount of non-evaporable water. The amount of non-evaporable water can be indirectly derived by measuring the amount of evaporable water in a sample. Finally, if non-evaporable water is assumed as the amount of water in gel, it can be assumed as the loss of water in the range of temperature 105-350 °C (3.1.1.1) and derived from the interpretation of a thermogravimetric analysis.

The balance of mass becomes:

$$W_c = W_{c,unh} + W_{c,a,h} + W_{wc,n-ev} + W_{wc,ev} \quad (3\text{-}28)$$

The volume occupied by the solid products of hydration, $V_{c,h}^{s}$, is equal to the sum of volumes of anhydrous cement and water less 0.254 of the volume of non-evaporable water (Neville, 2011). With β= (1-0.254):

$$V_{c,h}^{s} = V_{c,a,h}^{s} + (1-0.254)V_{wc,n-ev} = V_{c,a,h}^{s} + \beta V_{wc,n-ev} \quad (3\text{-}29)$$

$$V_c = V_{c,unh}^{s} + V_{c,h}^{s} + V_{e\ cap\ pores} = V_{c,unh}^{s} + V_{c,a,h}^{s} + \beta V_{wc,n-ev} + V_{wc,ev} + V_{e\ cap\ pores} = V_{c,a}^{s} + \beta V_{wc,n-ev} + V_{wc,ev} + V_{e\ cap\ pores} \quad (3\text{-}30)$$

This simply states that the volume of cement is the sum of solid volume of initially added cement, the volume of non-evaporable water multiplied by β (to take account of the reduced occupied volume), the evaporable water and the empty capillary pores developed during hydration. This also means that the volume of pores in the cement paste, $V_{c,\,p}$, is:

$$V_{c,p} = V_{e\ cap\ pores} + V_{wc,ev} \tag{3-31}$$

The unhydrated cement, the anhydrous hydrated cement and the non-evaporable water constitute the solid phase of the cement paste. The evaporable water is the liquid phase. The empty capillary pores constitute the volume filled with gas phase.

If shrinkage is neglected and the material is seal cured, then the volume is constant and equal to the initial volume of cement suspension (3-10):

$$V_c = V_{c,a}^s + V_{wc} = V_{c,unh}^s + V_{c,a,h}^s + \beta V_{wc,n-ev} + V_{wc,ev} + V_{e\ cap\ pores} \tag{3-32}$$

Given (3-15) and (3-32), the volume of empty capillary pores can be expressed as:

$$\begin{aligned} V_{e\ cap\ pores} &= V_{c,a}^s + V_{wc} - \left(V_{c,unh}^s + V_{c,a,h}^s\right) - \beta V_{wc,n-ev} - V_{wc,ev} \\ &= V_{wc} - \beta V_{wc,n-ev} - V_{wc,ev} \end{aligned} \tag{3-33}$$

Dividing equation (3-24) by ρ_w:

$$V_{wc} = V_{wc,ev} + V_{wc,n-ev} \tag{3-34}$$

$$\begin{aligned} V_{e\ cap\ pores} &= V_{wc,ev} + V_{wc,n-ev} - \beta V_{wc,n-ev} - V_{wc,ev} \\ &= (1-\beta)V_{wc,n-ev} = \frac{(1-\beta)}{\rho_w}\frac{\alpha x W_{wc}}{w_c/c} \end{aligned} \tag{3-35}$$

This means that if no shrinkage occurs, the volume no more occupied by water (due to hydration) becomes an empty capillary space occupied by gas phase. This is enough to divide the phases in a cement paste at different hydration degrees, represented by x, that is a function of time.

A comparison between the two balances, given by (3-22) and (3-30), is carried out for a better understanding of the relations between the terms. The volume of gel water can be calculated, according to Neville (2011), as a porosity of hydrated cement (3-17), $n_{gel\ w}$, approximately equal to 28 %:

$$V_{gel\,water} = \left(\frac{n_{gel\,w}}{1-n_{gel\,w}}\right)V_{c,h}^{s} = \frac{n_{gel\,w}}{1-n_{gel\,w}}\left(V_{c,a,h}^{s} + V_{wc,ch}\right) = \frac{n_{gel\,w}}{1-n_{gel\,w}}\left(V_{c,a,h}^{s} + V_{wc,n-ev}\right) \quad (3\text{-}36)$$

The graphical representation of volumes in cement paste for 100 g of anhydrous cement and $w_c/c=0.5$ is reported in Figure 3-2.

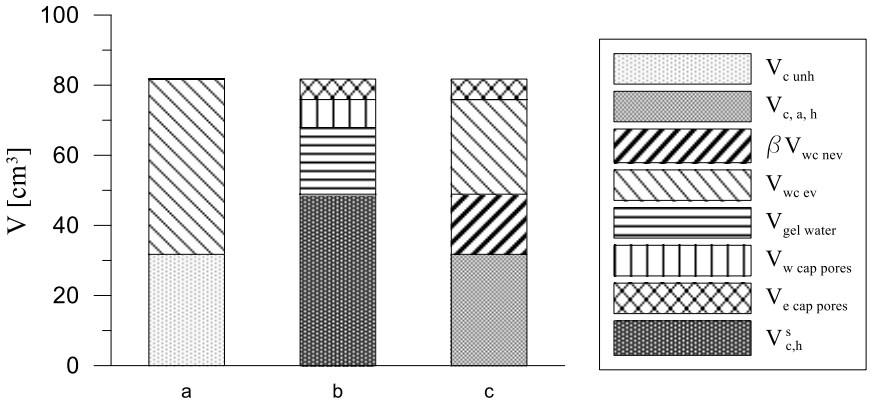

Figure 3-2. Graphical representation of volumes in cement paste for 100 g of anhydrous cement and $w_c/c=0.5$ assuming $V_{wc,n-ev}=V_{wc\,ch}$; a) x=0, $V_{c,a}=V_{c,unh}$ and $V_{wc}=V_{wc,ev}$; b) x=1, $V_{c,h}=V_c$ volume balance given by (3-22); c) x=1, $V_{c,h}=V_c$ volume balance given by equation (3-30).

When x=0 (a) (and no air is entrapped) all the cement is unhydrated and all the added water is "evaporable" water. When x=1 (b and c) the volume occupied by solid products of hydrated cement is composed of the volume of anhydrous cement and part of the water added, the non-evaporable water, multiplied by β. The evaporable water, that is the liquid phase, is composed of the gel water and the water held in capillary pores. Finally, due to the lower volume occupied by water chemically combined, the volume initially occupied by water (a) is reduced and if no shrinkage occurs this gap is covered by empty capillary pores.

In the following, the weights and volume of the solid, liquid and gas phase, expressed in function of α, β, x and w_c/c and initial amounts of cement and water ($W_{c,a}$ and W_{wc}) are summarized:

$$W_c^s = W_{c,unh} + W_{c,a,h} + W_{wc,n-ev} = (1+\alpha x)W_{c,a} \quad (3\text{-}37)$$

$$V_c^s = V_{c,unh}^s + V_{c,h}^s = V_{c,unh}^s + V_{c,a,h}^s + \beta V_{wc,n-ev} = V_{c,a}^s + \beta V_{wc,n-ev} = \frac{1}{\rho_c}W_{c,a} + \frac{1}{\rho_w}\alpha x\beta W_{c,a} = W_{c,a}\left(\frac{1}{\rho_c} + \frac{\alpha x\beta}{\rho_w}\right) = \left(1+\alpha x\beta\frac{\rho_c}{\rho_w}\right)\frac{W_{c,a}}{\rho_c} \quad (3\text{-}38)$$

$$W_c^l = W_{wc,ev} = W_{wc}\left(1 - \frac{\alpha x}{w_c/c}\right) \quad (3\text{-}39)$$

$$V_c^l = V_{wc,ev} = \frac{W_{wc}}{\rho_w}\left(1 - \frac{\alpha x}{w_c/c}\right) \quad (3\text{-}40)$$

$$V_c^g = V_{e\ cap\ pores} = \frac{(1-\beta)}{\rho_w}\frac{\alpha x W_{wc}}{w_c/c} \quad (3\text{-}41)$$

In Figure 3-3, two bar charts that show the mass and balance for $W_{c,a}$=100 g are presented.

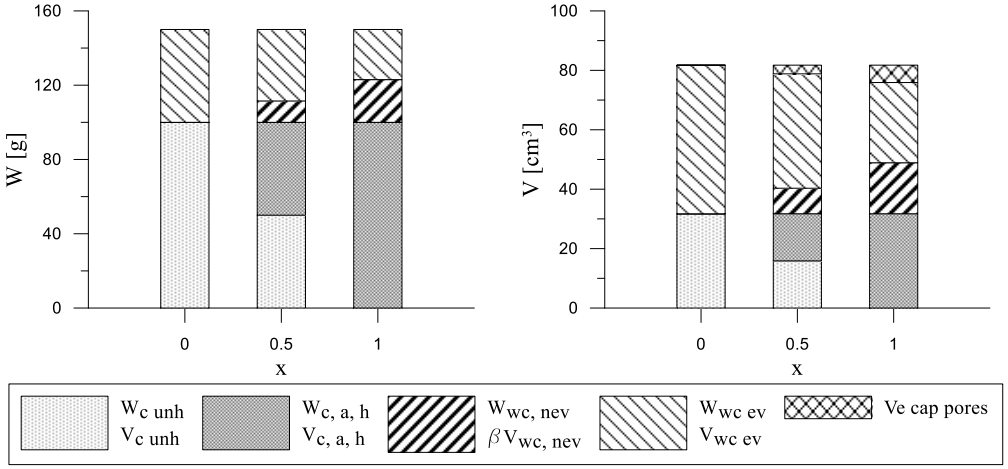

Figure 3-3. Representation of weights and volumes in the cement paste for $W_{c,a}$=100 g and w_c/c=0.5.

3.2. Foam

A foam is a dispersed system of bubbles separated by liquid layers. When the gas content is low, it can be called emulsion and bubbles have spherical shape; when gas content goes above 50%, bubbles become polyhedral. Different methods exist to generate foams. In condensation methods, gas bubbles are generated by reducing external pressure, increasing temperature or via chemical reactions. In dispersion methods, gas can be either injected directly into the foaming solution through capillaries, porous plates and gauzes or blown through gauzes wetted with surfactant solution. In some cases, solution and gas simultaneously flow to produce foam, in which also gas can be pressurized via a compressor. However, also other different methods exist (Ekserova and Krugli͡akov, 1998).

The most important parameters characterising a polyhedral foam are the *Foam Expansion Ratio* (FER), foam dispersity and foam stability. The former is defined as the ratio between the volume of foam, V_f, and the volume of the liquid content, V_f^l:

$$FER = \frac{V_f}{V_f^l} = \frac{V_f^g + V_f^l}{V_f^l} \qquad (3\text{-}42)$$

where V_f^g is the gas content of foam. This parameter represents the foaming ability of the solution from which the foam is derived. If the weight of gas phase, W_f^g, is negligible respect to the weight of the liquid phase, W_f^l, the weight of foam W_f is equal to the weight of the liquid phase, so that:

$$FER = \frac{V_f}{V_f^l} = \frac{W_f}{\gamma_f}\frac{\gamma_{sol}}{W_f^l} \cong \frac{\gamma_{sol}}{\gamma_f} \qquad (3\text{-}43)$$

where γ_{sol} and γ_f are the unit weight of solution and foam, respectively. Knowing both, it's possible to determine the foam expansion ratio. The density of liquid solution is usually almost equal to the density of water; thus, FER depends only on density of foam and the lower it is, the higher the foam expansion ratio, which can go up to 1000. However, for very high FER, the assumption that the weight of gas phase is negligible fails and other methods should be used to measure this parameter.

Foam dispersity determines many of foam properties. The kinetic of changes in foam dispersity indicates the rate of inner destruction of bubbles. It can be identified by bubble size distribution (which reveals completely the foam

dispersity), the average bubble size or the specific foam surface ε, defined as the ratio of total surface area of all liquid/gas interfaces in foam to the volume of foam (ε_f), the volume of gas phase (ε_g) or the volume of liquid phase (ε_l).

The ability of a foam to maintain the expansion ratio and dispersity constant with time is referred to as foam stability. The simplest measure of foam stability is the foam lifetime. Indeed, a foam is thermodynamically unstable due to the increased interfacial area and, by consequence, interfacial free energy; thus, sooner or later, it is destroyed. Foams with a considerable lifetime (which can be measured also in days) are called metastable, while they are defined as unstable if the lifetime is a matter of seconds.

It is worth noting that no foam can be produced from pure water, because if a bubble is introduced in it, it bursts almost immediately, as soon as liquid has drained away (Pugh, 1996). The presence of a "*surface active agent*" (i.e. a *surfactant*) in the solution is required to produce a foam.

3.2.1. Surfactants

A surfactant molecule is composed of polar head groups, which are the hydrophilic (lipophobic, oleophobic) part and non-polar tail groups, the hydrophobic (lipophilic, oleophilic) part. Both structure and shape affect their properties. The simplest one is composed of a tail and head (as soaps), as shown in Figure 3-4, but they can also have one head and two tails, two heads and one tail or more complex structures.

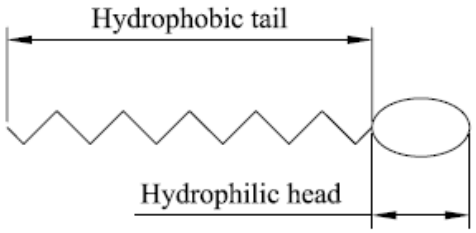

Figure 3-4. Surfactant molecule sketch.

Classification of surfactants is based on the hydrophilic group, and they can be anionic, cationic, non-ionic and amphoteric. The former two dissociate in water in a negative and a positive charged ion and the hydrophilic head is negatively (anion) or positively (cation) charged, respectively. Anionic surfactants are the most common and inexpensive. Non-ionic surfactants do not dissociate in water and the head has a neutral charge. The amphoteric ions can show all the behaviours above, depending on pH.

The hydrophobic tail is generally composed of hydrocarbon chains, synthesised from animal fats, natural vegetable oils or petrochemicals. The hydrocarbon chains synthesised from natural sources contain even number of hydrocarbon chains because their structures is built up from ethylene (Farn, 2008). Rarely, they are fluorocarbon and silicone chains which have excellent properties, but their usage is limited due to the higher cost.

3.2.2. Surface tension and surfactant effect

A compound is called surfactant when it shows surface activity when added to a liquid, that is, it is able to adsorb on the surface or interface of the system to reduce surface or interfacial excess free energy (Farn, 2008). The surface tension, γ, is a thermodynamic property which can be defined as the amount of work dW required to have a unit area expansion, dA; at a liquid-air interface it is the free energy per unit area of the surface. It can be also defined as the force acting normal to the interface per unit length of the surface at equilibrium.

$$dW = \gamma dA \qquad (3\text{-}44)$$

Surface tension of water at 20°C is 72.8 mN/m. The surface tension is due to the different interaction between molecules in the bulk fluid and at the interface. In the bulk liquid, the molecules are subjected to uniform attractive forces in all directions with a zero net force, but at the interface the molecules on the gas side are widely spread and the molecular interactions are mainly between surface molecules and subsurface liquid molecules. This leads to a non-zero net force which gives to the molecules on the surface an excess free energy respect to the molecules in the bulk liquid; this free energy is the surface tension (Farn, 2008).

Conversely, the interfacial tension, γ_{AB}, is the tension at the interface between two immiscible phases, A and B. Given γ_A and γ_B the surface tension of A and B, and ψ_{AB} the interaction energy of the two phases per unit area, the interfacial energy is:

$$\gamma_{AB} = \gamma_A + \gamma_B - \psi_{AB} \qquad (3\text{-}45)$$

The interfacial tension is small (and ψ is large) if the two molecules are similar, such as water and ethanol. At a water-gas interface, the molecules of gas are widely spaced so that compared to condensed phase (A), the interaction in the gas phase (B) and between gas phase and condensed molecules is negligible. Because of this, at a gas-liquid interface $\gamma_{AB}=\gamma_A$.

A minimum amount of work is required to have the expansion of an interface, because bulk molecules should move from bulk to surface; this work per unit area

is given by the interfacial tension. When the surfactant is added, surfactant molecules move towards the interface, with the hydrophilic head oriented to the liquid and the hydrophobic tail towards the gas phase (Figure 3-5c) replacing the polar and non-polar molecules at the interface and destroying the cohesive forces between them. Then, the interaction at the interface is between hydrophilic head and polar (liquid) molecules and between hydrophobic tail and non-polar (gas) molecules. These interactions are stronger, thus decreasing significantly the interfacial tension and by consequence the work required to expand the interface.

The surface tension decreases non-linearly with surfactant bulk concentration till a critical value, that is defined as the *critical micelle concentration* (CMC) that is the concentration above which the surfactant molecules start forming aggregates called micelles. If concentration is higher than CMC no more reduction in surface tension occurs because interface (or surface) is saturated with surfactant monomers, while a further increase of concentration affects only micelles which have no effect on surface tension. At very low surfactant concentration, instead, surfactant molecules lie flat on the surface.

3.2.2.1. Surfactant effects on solid surface

Surfactants can also adsorb on solid phase, at a solid-liquid interface, due to different causes, such as hydrophobic bonding and electrostatic interaction. The former occurs between hydrophobic tails and hydrophobic surfaces (tail down adsorption). Hydrophobic bonding between tails of surfactant molecules adsorbed head down on hydrophilic solid surface and tails of surfactant molecules in liquid phase can occur, leading to a bilayer structure. When the solid surface is composed of strongly charged sites, the adsorption depends mainly on the electrostatic interaction between solid surface and oppositely charged head groups, while orientation of surfactant monomers makes the solid surface hydrophobic, reducing the electric potential of diffuse layer. At higher concentrations the adsorption increases, and a bilayer structure can occur, which reverse the potential to the surfactant head group sign. These effects depend on surfactant type and concentration, on the solid phase and other conditions such as temperature; their presence can indeed affect fine grained soil behaviour. Recent studies show the effects of surfactant on soil properties as plasticity (Akbulut et al., 2012; Jones et al., 2016; Park et al., 2006; Rahman et al., 2013), but it goes beyond the aim of this study.

3.2.2.2. Surfactant effect in foams

When foam is formed, bubbles are dispersed and separated by thin films of liquid called lamellae, whose intersection lines form capillaries called *Plateu borders* (Figure 3-5) constituting a continuous network within the foam. Rather than a flow from film to film, the fluid is conveyed in the Plateu borders due to the lower pressure respect to the pressure in the adjoining lamella and, by consequence, the thinning of film between bubbles occurs. As the thinning continues, a pressure in lamella due to electrostatic and steric repulsion forces between the adsorption layers on the surfaces, termed disjoining pressure, arises till an equilibrium is reached and drainage stops.

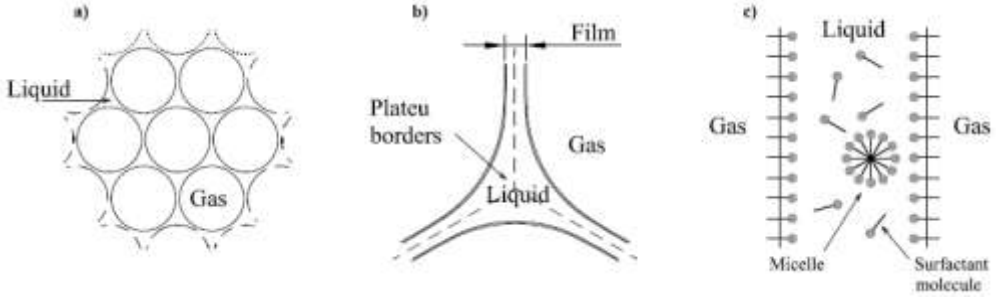

Figure 3-5. Diagrammatical sketch of (a) bubbles in foam, (b) plateau borders and (c) foam lamella.

If surfactant concentration is not too low, surfactant molecules move towards the interface between gas bubbles and liquid, so that the hydrophilic head points towards the liquid while other molecules and micelles (if concentration is above CMC) are dispersed in bulk (Figure 3-5c). When the liquid drains from the film to borders, the lamella is stretched, thus surfactant molecules concentration in the stretched, thinner zone lowers. This causes an increase in surface tension in the thinner zone and, by consequence, a surface tension gradient arises along the surface which is equivalent to surfactant adsorption gradient. This gradient causes a surfactant mass transfer with a diffusion flow from the bulk to the film surface and a surface flow in direction of the concentration gradient along the surface, dragging along a layer of hydrate water in the bulk phase (Ekserova and Krugliakov, 1998; Farn, 2008). This beneficial, self-healing effect of surfactants on the thin zone is referred to as Marangoni effect and it is an essential stabilising effect in foams. However, this effect is beneficial when compensation occurs via the surface flow, and not by a diffusion of molecules from the bulk phase.

3.2.3. Foam drainage and internal collapse

Foam stability is related to foam drainage and internal collapse. The former is the loss of liquid volume in time, ΔV_L, due to the excess liquid content respect to the hydrostatic equilibrium. As soon as the foam is formed the liquid starts to

drain out in Plateu borders and through them in lower layers of foam, governed by gravity. As reported by Ekserova and Kruglìakov (1998), many equations have been proposed to describe the foam drainage, as (3-46):

$$\Delta V_L = \frac{V_{L,0}\,\tau}{\frac{V_{L,0}}{w_0} + \tau} \qquad (3\text{-}46)$$

In the equation above, $V_{L,0}$ and w_0 are two parameters. The former can be assumed equal to the initial liquid volume in a foam, while w_0 characterises the initial volumetric flow rate referring to a unit cross-sectional foam area.

Foam drainage depends on many factors, such as viscosity, FER, surfactant type and concentrations etc. When the other conditions are the same, the ratio of foam drainage w_0 is inversely proportional to viscosity of foaming solution. Increasing the FER (i.e. lowering the density of foam) at constant dispersity, the foam drainage rate decreases because of the thinner radius of Plateau borders and w_0 is proportional to the square of FER. Foam dispersity also affects foam drainage rate, which seems to be proportional to the square of average radius. An increase in surfactant concentration decreases foam drainage rate.

Internal foam collapse is the internal destruction of foams, that is the separation of liquid from gas. It affects foam dispersity and it results from two phenomena: diffusion bubble expansion and bubble coalescence. The prevailing one depends on surfactant type and time from foam formation. The former occurs in polydisperse foams, due to the different gas pressure within bubbles of different size. There is a diffusion mass transfer of gas from the smaller bubbles to the larger ones. Average-sized bubbles receive gas from smaller ones and transfer gas to larger ones. Coalescence is the fusion of two bubbles due to the rupture of thin films separating them, which occurs when the films are very unstable. In both cases, the specific foam area decreases during process of internal foam collapse.

It is worth noting that these phenomena (foam drainage, internal collapse) which affect stability and lifetime of a foam occurs “naturally” due to the intrinsic thermodynamic instability. External actions as vibration or mixing with other suspensions (as in the lightweight cemented soil method) can also affect foam stability in different ways.

3.2.4. Bulk properties

The foam is a dispersion of bubbles in a liquid solution of water and surfactants. The solid phase corresponds to surfactants and residual solid of water (if not distilled). However, the residual solid in foam is negligible, thus it can be regarded as composed of liquid and gas phases, i.e. the solution and the air entrapped in bubbles. If the weight of gas in bubbles can be neglected, the weight of foam is:

$$W_f = W_f^s + W_f^g + W_f^l \cong W_f^l \qquad (3\text{-}47)$$

The volume of foam, V_f, can be assumed as the sum of the volume of air bubbles in the foam, $V_{air\ foam}$, and the volume of solution, V_f^l:

$$V_f = V_f^l + V_{air,foam} = V_f^l + V_f^g \qquad (3\text{-}48)$$

Hence:

$$V_f^g = V_{air,foam} = V_f - V_f^l = W_f\left(\frac{1}{\gamma_f} - \frac{1}{\rho_{solution}}\right) \approx W_f\left(\frac{1}{\gamma_f} - \frac{1}{\rho_w}\right) \qquad (3\text{-}49)$$

where density of solution has been assumed equal to density of water.

3.3. Summary

Cement and foam, the two additives required to produce lightweight cemented soil, have been described in this chapter. Cement main compounds and hydration reactions of cement, related to hardening of cement paste, i.e. gain of strength, have been shown. The rheological behaviour of fresh paste, that is mixed with soil suspension in the approach adopted in this study (section 5.3.5), has been discussed and it can be modelled as a Bingham fluid. Solid, liquid and gas phases of cement paste and their time evolution have been identified based on a literature approach; the results of this analysis will be used to determine bulk properties of lightweight cemented soil in section 5.1. The air foam is made of bubbles dispersed in a surfactant solution; it is a thermodynamically unstable system and a surface-active agent (i.e. the surfactant) is required to produce it. The main mechanisms of foam stability (i.e. foam drainage and internal collapse), the stabilizing effect of surfactant (Marangoni effect) and foam properties have been discussed in this section. Foam stability increases at increasing surfactant concentration up to critical micelle concentration above which no significant improvements can be observed.

References

ACI Committee 238, 2008. Report on Measurements of Workability and Rheology of Fresh Concrete.

Akbulut, S., Kurt Nese, Z., Arasan, S., 2012. Surfactant modified clays' consistency limits and contact angles. Earth Sci. Res. J. 16, 13–19.

Alarcon-Ruiz, L., Platret, G., Massieu, E., Ehrlacher, A., 2005. The use of thermal analysis in assessing the effect of temperature on a cement paste. Cem. Concr. Res. 35, 609–613. https://doi.org/10.1016/j.cemconres.2004.06.015

ASTM, C., 2008. 191-08. Standard test methods for time of setting of hydraulic cement by Vicat needle, American Society for Testing and Materials, Annual Book of ASTM Standards. https://doi.org/10.1520/C0191-18.2

Banfill, P.F.G., 1991. Rheology of Fresh Cement and Concrete. https://doi.org/10.4324/9780203473290

Bergado, D.T., 1996. Soft ground improvement in lowland and other environments. ASCE Press, New York, N.Y.

Black, L., Breen, C., Yarwood, J., Deng, C.S., Phipps, J., Maitland, G., 2006. Hydration of tricalcium aluminate (C3A) in the presence and absence of gypsum - Studied by Raman spectroscopy and X-ray diffraction. J. Mater. Chem. 16, 1263–1272. https://doi.org/10.1039/b509904h

Chougnet, A., Palermo, T., Audibert, A., Moan, M., 2008. Rheological behaviour of cement and silica suspensions: Particle aggregation modelling. Cem. Concr. Res. 38, 1297–1301. https://doi.org/10.1016/j.cemconres.2008.07.001

Ekserova, D.R., Kruglı̂akov, P.M., 1998. Foam and foam films: theory, experiment, application, Studies in interface science. https://doi.org/10.1016/S1383-7303(98)80004-5

Farn, R.J., 2008. Chemistry and Technology of Surfactants. Wiley.

Ferraris, C.F., 1999. Measurement of the rheological properties of high performance concrete: State of the art report. J. Res. Natl. Inst. Stand. Technol. 104, 461. https://doi.org/10.6028/jres.104.028

Jones, N., Lourenço, S.D.N., Paul, A., 2016. Testing surfactants as additives for clay improvement: compaction and suction effects 13006, 3–6. https://doi.org/10.1051/e3sconf/20160913006

Khalil, S.M., Ward, M.A., 1973. Influence of a lignin based admixture on the

hydration of portland cements. Cem. Concr. Res. 3, 677–688. https://doi.org/https://doi.org/10.1016/0008-8846(73)90003-3

Lothenbach, B., Winnefeld, F., Alder, C., Wieland, E., Lunk, P., 2007. Effect of temperature on the pore solution, microstructure and hydration products of Portland cement pastes. Cem. Concr. Res. 37, 483–491. https://doi.org/10.1016/j.cemconres.2006.11.016

Marchese, B., 2003. Tecnologia dei materiali e chimica applicata. Lezioni per gli allievi ingegneri civili, 2nd ed.

Neville, A.M., 2011. Properties of concrete, 5th ed. Pearson Education Limited.

Newman, J., Choo, B.S., 2003. Advanced Concrete Technology 1: Constituent Materials. Elsevier Science.

Park, J., Vipulanandan, C., Kim, J.W., Oh, M.H., 2006. Effects of surfactants and electrolyte solutions on the properties of soil. Environ. Geol. 49, 977–989. https://doi.org/10.1007/s00254-005-0136-6

Powers, T.C., 1958. The physical structure and engineering properties of concrete, in: Portland Cement Assoc R & D Lab Bull. Chicago, p. 39.

Pugh, R.J., 1996. Foaming, foam films, antifoaming and defoaming. Adv. Colloid Interface Sci. 64, 67–142. https://doi.org/10.1016/0001-8686(95)00280-4

Rahman, Z.A., Sahibin, A.R., Lihan, T., Idris, W.M.R., Sakina, M., 2013. Effects of surfactant on geotechnical characteristics of silty soil. Sains Malaysiana.

Struble, L., Sun, G.K., 1995. Viscosity of Portland cement paste as a function of concentration. Adv. Cem. Based Mater. 2, 62–69. https://doi.org/10.1016/1065-7355(95)90026-8

Taylor, H.F.W., 1950. Hydrated calcium silicates. Part I. Compound formation at ordinary temperatures. J. Chem. Soc. 3682–3690. https://doi.org/10.1039/JR9500003682

Zielinska, E., 1972. The influence of carbonate calcium on the hydration process in some Portland cement constituents. Pr. Inst. Technol. i Organ. Prod. Bud.

4. Mechanical behaviour of cemented soils

The mechanical behaviour of soils with a bonded structure is similar to that of porous weak rocks (Leroueil and Vaughan, 1990). Differently from artificial cause (as the addition of a bonding agent), bonds can arise from natural causes, such as deposition of silica at particle contacts in sands, deposition of carbonates from solution, from re-crystallization of minerals during weathering (Leroueil and Vaughan, 1990).

The increase of strength obtained by the addition of cement and lime has been reported by several authors (Clough et al., 1981; Locat et al., 1990; Mitchell, 1981; Sariosseiri and Muhunthan, 2008). Consoli et al. (2007) investigated the effect of cementation on a compacted cemented silty sand; they observed that even a small addition of cement is enough to generate a significant gain in strength, with an approximately linear increase of Unconfined Compressive Strength (UCS) with cement content. They observed that increasing dry density, the effectiveness of cementation enhances due to the existence of a larger number of contacts; indeed, they found that UCS increases exponentially at decreasing cemented soil porosity.

The effect of cement addition on unconfined compressive strength of cemented high water content clays was studied by Horpibulsuk et al. (2003) by varying the cement factor on a wide range, from 5 to 200 %. They observed that at low cement factors, approximately below 10 %, the increase in strength was only marginal, due to the slight amount of available cement per intercluster site. At higher cement contents, up to approximately 40 %, they observed a significant increase in strength; in this range of cement contents it was supposed to exist a continuity in the clay fabric and discontinuity in the hardened structure of the cement paste. At very high cement contents (above 70 %), the authors assumed that a continuity in cement paste existed, with clay particles embedded in cement paste. In the transition zone between 40 and 70 %, a marginal increment in strength was observed.

4.1. Compressibility

The schematic representation of compressibility behaviour of a cemented soil, as reported by different authors (Cuccovillo and Coop, 1999; Lade and Trads, 2014; Leroueil and Vaughan, 1990) has been reported in Figure 4-1.

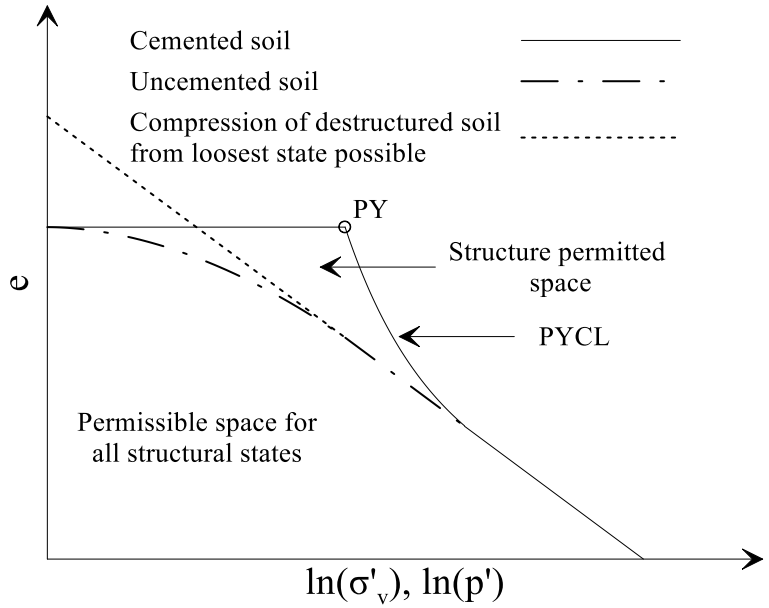

Figure 4-1. Schematic representation of compressibility behaviour of strongly cemented soil, after Leroueil and Vaughan (1990), Cuccovillo and Coop (1999)*; PY: Primary Yield, PYCL: Post-Yield Compression Line* (Rotta et al., 2003).

On the basis of experimental observations of the mechanical behaviour of artificially cemented carbonate sands, Cuccovillo and Coop (1999) stated that the effect of cementation was to increase both the size of the elastic domain in the stress space (i.e. the domain in which the strains are reversible) and the initial stiffness (i.e. the stiffness at small strain level), while larger strains were observed in post-yield state. Furthermore, they observed that the paths described in the tension-void ratio plane by the results of one-dimensional (i.e. k_0) or isotropic compression tests on cemented structured sand can reach points representing states that are impossible for a reconstituted uncemented sample of the same sand. Similar results were found by Pellegrino (1968, 1970) with reference to the behaviour in isotropic compression of Neapolitan yellow tuff, a porous weak rock; the stress-volumetric strain curves were characterized by a first segment with low strains, followed by a segment with much larger strains and finally the last segment with a decreasing gradient of the curve at increasing stress. This behaviour was interpreted as due to the high porosity and to some inhomogeneity of the material composing the matrix, which could lead, in singular points of the rock matrix itself, to a stress state characterized by tensile and shear stresses even during isotropic compression. Indeed, as stated by Lajtai (1969), the state of stress around a pore or void may vary from one of high tension to one of high compression even if the stresses applied at the sample boundaries are all compressive.

Rotta et al. (2003) studied the effect of curing stress on compacted cemented silty sands. They show that increasing the curing stress before cementation begins (simulating thus the curing of samples at different depths in a sedimentary deposit), the isotropic yielding stress increases. They also observed that after primary yield (Figure 4-1), the compression paths of all specimens at different initial void ratio followed a post-yield compression line (PYCL), that was unique for each specific cement content, and at high confining stresses (also above 30 MPa) converged towards the intrinsic compression line (ICL) of the uncemented soil. The PYCL expands and steepens at increasing cement content. The space between post-yield compression line and ICL is the zone of "structure permitted states", as defined by Leroueil and Vaughan (1990). Finally, they found that at decreasing initial void ratio (at same cement content), primary yield stress increases, while the relative effect of cementation decreases (increase in yield stress respect to uncemented yield stress).

Similar results are found for artificially cemented clays. Verástegui Flores and Van Impe (2009) show results on an artificially cemented kaolin starting from a slurry at a water content equal to 2 times the liquid limit (w_l); increasing the degree of cementation, the yield stress for k_0 compression increases, reaching states significantly above the intrinsic compression line of reconstituted soil, with a higher post-yield compressibility.

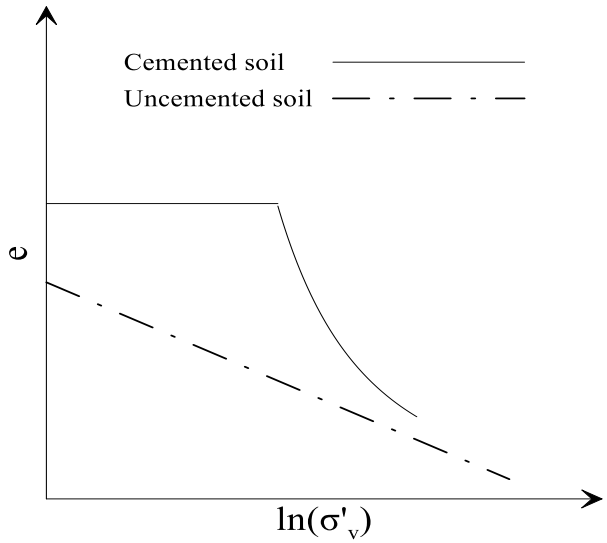

Figure 4-2. Schematic representation of compressibility behaviour of cemented clay, after Sasanian and Newson (2014).

As schematically shown in Figure 4-2, the void ratio at very low confining stress can be significantly above the one of the reconstituted soil. Similar results

were found by Sasanian and Newson (2014) on artificially cemented Ottawa clay, characterized by a bonded structure also in its natural state. Both undisturbed and artificially cemented clay (prepared at a water content of 80%, above limit liquid, and tested after 28 days of curing) show a higher initial void ratio and stiffness in pre-yield compression than reconstituted soil.

Horpibulsuk et al. (2004a) show the effect of water content on compressibility of cemented Bangkok and Ariake clays, by varying the liquidity index of slurry from 1 to 3. They show that the pre-yield deformation is negligible, and the yielding stress decreases with water content (after 28 days of curing). However, in post-yield, all the samples with the same cement content converge to the same line, for both soils. Horpibulsuk et al. (2004b) observe an increase of yield stress in isotropic compression on cemented Ariake clay at increasing cement content.

The effect of curing time has been shown by Xiao and Lee (2008), by testing different mixtures of cement treated marine clay; they show an increase in isotropic yield stress and a decrease in void ratio at increasing curing time, in all the cases.

4.2. Shear strength and triaxial compression behaviour

The behaviour of cemented soils in triaxial compression has been investigated by different authors. The behaviour of weakly cemented soils was studied by Maccarini (1987) via isotropically consolidated drained triaxial compression tests (CID). The artificial bonded soil was produced by firing a mixture of sand and kaolin slurry, hence bonds were given by the fired kaolin. At low confining stress, peak shear strength, corresponding to failure along a localized shear band, was reached before attaining the maximum dilation rate, indicating the bonded structure as responsible of the shear over-strength rather than dilatancy. However, the post-peak evolution of the compression tests showed a clear tendency of the material to reach a critical state, with a strongly dilative and brittle behaviour. At higher confining stresses, yield was observed before failure, which occurred at larger strains and was accompanied by significant contraction. Similar results were found also for natural soil (Saint-Vallier soft clay and oolitic limestone), as reported by Leroueil and Vaughan (1990), and by Consoli et al. (2002), which in particular studied the effect of curing pressure on a cemented silty sand.

Lade and Overton (1989), by studying a soil-cement mixture in triaxial compression, found that the peak shear strength and the value of the strain at

failure increased as the confining stress was raised; while cementation was still intact, the stress-strain relationship resulted to be almost linear, and a contractive behaviour was observed. After yielding, debonding occurred and the stress-strain behaviour was highly non-linear whereas, at increasing confining pressure, the behaviour became more contractive.

Similar observations were reported by Schnaid et al. (2001) with reference to mechanical tests on artificially cemented sand; they showed that increasing the cement content, stiffness and peak strength increased and maximum deviatoric stress tended toward a constant value independent on cementation. The volumetric behaviour was characterized by an initial contraction followed by a strong expansion and the maximum rate of dilation was shown right after reaching the peak strength. They also observed an increase of the values of both the friction angle and the cohesion at increasing cement content with respect to those of the uncemented soil. The idealized behaviour of a cemented soil is represented in Figure 4-3.

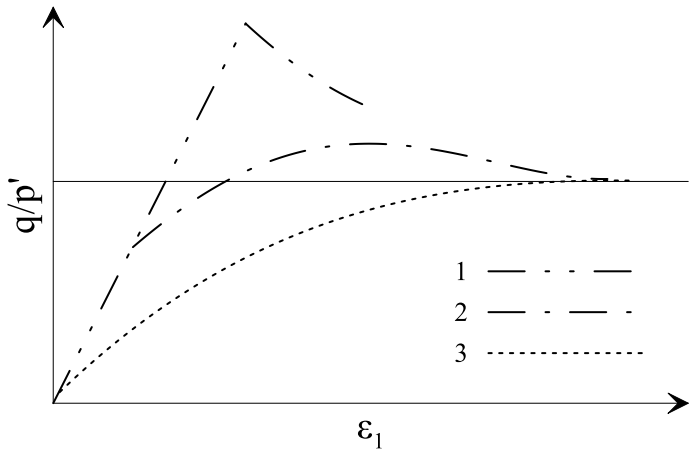

Figure 4-3. Idealized behaviour of cemented soil at different degree of cementation, after Cuccovillo and Coop (1999), Lade and Trads (2014).

Horpibulsuk et al. (2004b) studied the undrained behaviour of the cemented Ariake clay at different cement content. Samples were prepared at high initial water content (180 %). The stress-strain curves presented the typical behaviour of a cemented soil (behaviour 1 in Figure 4-3), characterized by a peak value of the stress deviator and a subsequent softening. They observed a negligible effect of confining stress on stress-strain curves, but a significant difference in pore-pressure development, which increased until peak deviator stress was achieved. At increasing confining pressure, higher pore water pressures were measured. After peak, a decrease in pore water pressure was observed. At higher cement content and low confining stresses, negative pore water pressures were measured,

showing a tendency to a dilative behaviour. They concluded that peak strength was mainly due to cementation, and not due to interlocking. Similar results were found by Verástegui Flores and Van Impe (2009) on a commercial kaolin.

Sariosseiri and Muhunthan (2008, 2009) studied the effect of cementation on two soils from the state of Washington, namely Aberdeen and Everett soils. Samples were prepared at maximum dry density and optimum water content. They observed an increase in peak shear strength at increasing confining stress regardless of cement content. At increasing cement content, they observed an increase in the peak of stress deviator achieved at lower strains. The stress strain curves were characterized by a significant softening; a decrease of post-peak deviator stress was observed at increasing cement content, accompanied by a higher brittleness. They also observed an increase in pore water pressure until peak strength was reached, which rose almost to the value of the total confining pressure, so that the effective confining pressure dropped to near zero. The authors suggested that this behaviour depends on cracks forming during split failure which transfer pressures immediately to pore water. After peak strength, a decrease in pore water pressure is observed, so that at low confining stresses slightly negative pore water pressure were measured.

4.3. Failure envelope and constitutive models

The adoption of Mohr-Coulomb criterion has been extensively used to characterize the failure of soils, but it led to some anomalies if applied to cement treated soils (Sariosseiri and Muhunthan, 2008). This is due to the likely curvature of failure envelope, as observed by some authors, which doesn't allow to define a unique friction angle to describe behaviour over a wide range of confining pressures. Lajtai (1969) suggested that, at increasing confining stresses, three mechanisms can be identified in direct shear tests on soft rocks: tensile failure, shear failure (both non-linear) and, at high confining stresses, ultimate strength failure (described by Mohr-Coulomb criterion with zero cohesion). However, this interpretation requires many tests in a wide range of confining stresses. As reported by Sariosseiri and Muhunthan (2008), other models have been proposed to describe the failure mechanism of geomaterials, such as Hoek and Brown, (Hoek, 1988) and Johnston (1985). The Griffith model (Griffith, 1924) has been proposed by Consoli et al. (2012) to describe the behaviour of a cemented sand. The Griffith criterion, in terms of normal stress acting on the failure surface, σ_n, and shear stress acting along the failure surface, τ, can be represented by the following equation:

$$\tau^2 = 4\sigma_t(\sigma_t - \sigma_n) \quad (4\text{-}1)$$

where σ_t is the tensile strength. However, under compressive stress conditions, closure of cracks can occur; if it happens before tensile stress at the crack tip is high enough to initiate fracture, the shear resistance resulting from the contact pressure between the crack faces has to be overcome before propagation of the crack can occur (Hoek and Bieniawski, 1965). To take account of this phenomenon, McClintock and Walsh (1962) modified the original theory of Griffith to take account of the compressive stress (while original criterion can be applied when normal stress is tensile) and a straight-line Mohr envelope resulted, namely Modified Griffith theory:

$$\tau = \mu\sigma_n - 2\sigma_t \quad (4\text{-}2)$$

where μ is the coefficient of internal friction. Hoek and Bieniawski (1965) compared the modified Griffith theory with a wide variety of materials finding a remarkable agreement. A good agreement was also found by Sariosseiri and Muhunthan (2008) on artificially cemented soils. A linear expression is also proposed by Schnaid et al. (2001).

Many constitutive models are available in literature to take account for structure in soils. The extension of Modified Cam Clay model (Roscoe and Burland, 1968) to structured soils has been proposed by some authors (Carter and Liu, 2005; Horpibulsuk et al., 2010; Liu and Carter, 2002; Suebsuk et al., 2011), namely Structured Modified Cam Clay. They assume an elliptical yield surface as the original model, while the effect of structure is considered by means of Δe, the difference between the void ratio of the structured soil and the void ratio of reconstituted soil at the same stress state. The failure surface is assumed parallel to non-treated soil and shifted by an intercept, as also suggested by Kasama et al. (2000). Nguyen et al. (2014) proposed a slightly different model, namely Cemented Cam Clay, to take account of non-linearity of failure envelope due to bonding degradation under isotropic compression. Constitutive models characterized by more than one surface, as the one proposed by Rouainia and Muir Wood (2000), are also available in literature. An extension to structured soils of the model introduced by Nova (1988, 1992) was proposed by Lagioia and Nova (1995), by means of p'_{t0}, that is the initial isotropic tensile strength, and p'_{m0}, that is related to the strength of the bonds in compression. Destructuration is related only to volumetric plastic strain. Similar models were proposed by Nova et al. (2003), Nova (2005), in which destructuration depends also on deviatoric plastic strains.

Pinyol et al. (2007) proposed a model for clayey rocks which took account for both cementation and suction effects, such as swelling/shrinkage behaviour due to wetting-drying cycles, by integrating into a common framework an elasto-plastic model for expansive materials and a damage model for the bond material. The degree of cementation is considered via the state parameters e_b, namely void ratio of bonds, defined as the ratio of volume of bonds (assumed non-porous) to the solid volume of clay matrix, and concentration of bonds, C_b, the ratio of volume of bonds to the total volume. The bond behaviour is modelled through isotropic damage theory by means of a scalar damage parameter, D. They adopt the function proposed by Carol et al. (2001) in which the damage evolution, r(L), is related to the damage variable L, that is a logarithmic function of D.

4.4. Governing parameters on behaviour of cemented soils

Some authors have tried to identify parameters which affect the mechanical properties of cemented soils. Schnaid et al. (2001) suggest that deviatoric stress at failure, q_f, can be expressed as a linear function of degree of cementation, represented by UCS (4-3). Indeed, they argued that the degree of cementation can be identified by UCS because it takes account for density, gradation, amount and nature of cement, and mineralogy of soil. In the hypotheses that peak strength envelopes are linear, the friction angles of cemented and uncemented soil have the same magnitude, the soil in uncemented condition is non-cohesive and frictional contribution is independent of cement content, the failure surface becomes:

$$q_f = \frac{2\sin\varphi}{1-\sin\varphi} p_i' + UCS \qquad (4\text{-}3)$$

where φ and $p_I^{'}$ are the friction angle and the initial mean effective stress, respectively. Consoli et al. (2007, 2009, 2011) identified a relationship between UCS and the ratio between porosity, n, and volumetric cement content, C_{iv}, defined as the ratio of absolute volume of cement to total volume:

$$UCS\ [kPa] = c_1 \left[\frac{n}{(C_{iv})^{c_2}}\right]^{-c_3} \qquad (4\text{-}4)$$

where c_1, c_2 and c_3 are three constants. They suggest that using the parameter $\frac{n}{(C_{iv})^{c_2}}$, one can design the amount of cement and the compaction effort necessary to obtain a mixture that meets the design strength. However, also c_2, the exponent of C_{iv}, varies depending on soil and cement used. Consoli et al. (2010, 2012) suggest that also tensile strength can be related to the ratio between porosity and

cement content; the relationship can be substituted in Griffith criterion (4-1) and a failure envelope depending on porosity and cement content can be derived.

Horpibulsuk et al. (2003, 2005, 2006) suggest the "water clay to cement ratio" ($w_s/\frac{c}{s}$ according to the adopted notation) as a governing parameter for compressive strength of cemented soils, proposing a relation based on the Abrams law (Abrams, 1918). By this way, they find a generalized relationship between strength, curing time and the water clay to cement ratio. It is worth noting that in admixed clay at high water content, the initial water content of soil slurry is strictly related to porosity. Indeed, being the saturation degree equal to one in a soil slurry, the void ratio is directly proportional to water content. In a subsequent study, Horpibulsuk et al. (2011a, 2011b, 2012a) proposed slightly different equations (4-5), (4-6), where A, B, c_1 and c_2 are four constants. According to the authors, A depends on type of clay, liquidity index and curing time while B is approximately 1.22~1.24.

$$UCS = \frac{A}{\left(w_s/\frac{c}{s}\right)^B} \tag{4-5}$$

$$\frac{UCS_{\left(w_s/\frac{c}{s}\right),\ t}}{UCS_{\left(w_s/\frac{c}{s}\right)_{ref},t=28d}} = \left[\frac{\left(w_s/\frac{c}{s}\right)_{ref}}{\left(w_s/\frac{c}{s}\right)}\right]^B (c_1 + c_2 \ln t) \tag{4-6}$$

Sasanian and Newson (2014) studied the behaviour of cemented clays at high water content. They investigated the undrained shear strength, c_u, at different curing times (up to 1200 days) by means of laboratory vane test; they observed that, also after 1000 days, the cemented soil continued to gain strength. Of course, strength increases with cement content and curing time since both contribute to production of cementing bonds. They also observed an increase in residual strength with curing time; however, it didn't increase with same rate of peak strength, so that higher brittleness and sensitivity were observed at increasing cementation. By normalizing undrained shear strength by c_u at a reference time, t_{ref}, of 28 days, they suggest the following expression for undrained shear strength:

$$\frac{c_u}{c_{u,t_{ref}}} = 0.96\left(\frac{t}{t_{ref}}\right)^{0.31} \tag{4-7}$$

They also studied the effect of $w_s/\frac{c}{s}$, as proposed by Horpibulsuk et al. (2003), on undrained shear strength; to take account of soil mineralogy on the gain in strength, the authors proposed a slightly different governing parameter, namely β, equal to the product of soil activity, A, to the power of 3.2 and the ratio $\frac{c}{s}/w_s$. According to authors, the undrained shear strength at 28 days, normalized respect to atmospheric pressure, is a second order polynomial function of β; they also observed the same dependency on yield stress in oedometric loading.

4.5. Lightweight cemented soil

The effects of foam addition on properties of cemented soils have not been widely investigated. Some results are reported by Tsuchida and Egashira (2004). The main purpose of these studies was the reuse of dredged soils in port constructions that are characterized by a significant water content, thus facilitating the treatment. Indeed, seawater was used in some laboratory tests to investigate properties of material, while density was kept higher than density of water so that slurry could be poured underwater. Full scale tests were also performed. Satoh et al. (2001) report the field test in Kumamoto port for the construction of a new quay wall to the depth of 10 m below the sea level; due to the low bearing capacity of the extremely soft marine clay of the seabed, namely Ariake clay, ground improvement techniques had to be considered. However, it was proved that the possible usage of LWCS as a backfill material would have reduced the construction costs by 20 ~ 25 %, by decreasing load and seismic earth pressure, thus allowing to reduce the width of concrete caisson and the scale of ground improvement techniques. The mixture was poured at 10 m below the sea level, thus wet density had to be higher than 10 kN/m^3; the measured UCS, at 28 and after 1 year, was approximately 1 MPa, much larger than the target value of 200 kPa. By using X-ray CT scanner, Otani et al. (2002) show that failure of these samples occurred with strain localization. The LWCS was used as a backfill material at the seawall in the reconstruction project of Kobe Port Island, after Kobe earthquake, and in the offshore expansion project of Tokyo International Airport, as reported by Watabe et al. (2009, 2011). In both cases, lightweight treated soil was covered by a layer of sand and a pavement. The air foam content was below 30%, with a target density around 11 kN/m^3 and minimum UCS target of 196 kPa. After almost ten years, the lightweight cemented soil was sampled in both sites. In Kobe Port Island, the density profile was almost constant and approximately equal to target density, except for larger values measured in the shallowest layer (around 300 mm) due to infiltration of rainwater. No cracks were detected; the UCS proved to be higher than target value along the entire depth

but characterized by a larger scatter compared to density vertical profile. Similar results were found in Tokyo International Airport.

Tsuchida and Egashira (2004) show that unconfined compressive strength of a LWCS grows almost linearly with cement content and decreases at increasing water content of soil slurry, as widely shown for cemented soil; the secant Young modulus at 50% of deviator, E_{50}, is approximately 100~200 times UCS. Tsuchida et al. (2007) show that lightened cemented soil exhibits considerable volumetric compression when subjected to shearing in triaxial compression, ascribing it to high compressibility of air foam. Larger strains were measured at increasing confining pressure. They also conducted K_0-consolidation tests via modified triaxial apparatus by controlling cell pressure so that lateral strain didn't exceed 0.02%. K_0 values declined up to 0.1 around axial strain of 0.5~1%, corresponding to consolidation yield points and implying a significant reduction of earth pressure. Permeability was studied by Kikuchi et al. (2005, 2006, 2011), which show that pores can be impermeable when air content is below 30 %; however, at higher air contents, a dramatic increase in permeability was observed.

Compressibility of lightweight cemented soil was investigated by Horpibulsuk et al. (2013); they observed that samples with larger void ratio (due to both water and air foam contents) were characterized by the lower yield stress and higher rate of destructuring. However, at high normal stresses, compression curves tend to converge. Similar results were found by Watabe et al. (2004) on two mixtures of lightweight cemented soil; they performed SEM and MIP analyses on samples subjected to K_0-loading at different confining stresses; along unloading paths, the change of void ratio was negligible. They observed that larger pores detected by SEM, with spherical shape and a diameter of 200 ~ 500 μm, were not detected by MIP, in which the largest pores observed were in the range of 20-60 μm. All these pores were associated to foam bubbles. At increasing normal stress, largest pores distorted into oblate spheres and then collapsed, so that at high confining pressures, not only compression curves but also pore size distribution coincided.

Some authors tried to identify parameters to describe the behaviour of lightweight cemented soil, as for non-lightened mixtures. Jongpradist et al. (2011) suggest to adopt the "effective void ratio", e_{st}, defined as:

$$e_{st} = w \ln\left(\frac{e_{ot}}{c/_S}\right) \qquad (4\text{-}8)$$

where e_{ot} and w are the void ratio and water content after-curing, respectively, as introduced by Lorenzo and Bergado (2004). Based on their investigation, they suggest that any mechanical characteristic normalized respect to atmospheric pressure, q', such as UCS and yield stress, can be identified by the following expression, where A and B are two constants:

$$q' = A\, exp(Be_{st}) \tag{4-9}$$

Horpibulsuk et al. (2012b) extended their approach on cemented clays (Horpibulsuk et al., 2011a) to lightweight cemented soils. They suggest, as a governing parameter, the ratio between the absolute volume of voids (sum of volumes of air and water) to the absolute volume of cement, V/C, as a key parameter to rule strength of lightweight cemented soil at a constant initial water content. However, to take account of the effect of water content, Horpibulsuk et al. (2014a) suggest the "water void to cement ratio", defined as the product of water content of soil slurry (defined in decimal) times V/C:

$$UCS = \frac{A}{\left(\frac{wV}{C}\right)^B} \tag{4-10}$$

$$\frac{UCS_{\left(\frac{w_s V}{C}\right),\ t}}{UCS_{\left(\frac{w_s V}{C}\right)_{ref}, t=28d}} = \left[\frac{\left(\frac{w_s V}{C}\right)_{ref}}{\left(\frac{w_s V}{C}\right)}\right]^B (c_1 + c_2 \ln t) \tag{4-11}$$

Teerawattanasuk et al. (2015) propose mix design charts to develop sustainable lightweight pavement materials, based on cement and air contents (related to the volume of wet soil). They varied the cement content from 100 to 250 kg/m^3 and the air content from 0 to 50 % and performed unconfined compressive tests. Each design chart is related to a specific cement content, while UCS decrease with foam content; thus, once cement content is chosen, based on the required UCS, the corresponding foam content can be derived.

4.6. Summary

A literature review on the mechanical behaviour of cemented soils has been shown in this section. Regardless of grain size distribution, an increase of degree of cementation determines an increase in yield stress in both isotropic and oedometric compression. Furthermore, an increase in peak strength and brittleness is observed, whereas a dilative behaviour can occur after right peak strength is reached. Different key parameters governing the strength of cemented soils have been proposed in literature and discussed in this section; they are

generally related to the amount of cementitious material and porosity; the latter has a negative effect on mechanical performances. Some studies on lightweight cemented soils have been presented. Despite not being widely investigated, it has been shown that the technique and resulting geomaterial can prove useful in engineering practice. Some approaches describing the strength of lightweight cemented soils have also been discussed.

References

Abrams, D.A., 1918. Design of Concrete Mixtures, Structural Materials, Research Laboratory. Lewis Institute, Chicago. Bulletin 1.

Carol, I., Rizzi, E., Willam, K., 2001. On the formulation of anisotropic elastic degradation. I. Theory based on a pseudo-logarithmic damage tensor rate. Int. J. Solids Struct. https://doi.org/10.1016/S0020-7683(00)00030-5

Carter, J.P., Liu, M.D., 2005. Review of the Structured Cam Clay Model. Soil Const. Model. Eval. Sel. Calibration . GSP 128 40771, 99–132. https://doi.org/10.1061/40771(169)5

Clough, G.W., Sitar, N., Bachus, R.C., 1981. Cemented Sands under Static Loading. J. Geotech. Eng. Div.

Consoli, N.C., Cruz, R.C., B.S., C., Maghous, S., 2012. Failure envelope of artificially cemented sand. Géotechnique 62, 543–547. https://doi.org/10.1680/geot.11.P.037

Consoli, N.C., da Silva Lopes, L., Foppa, D., Heineck, K.S., 2009. Key parameters dictating strength of lime/cement-treated soils. Proc. Inst. Civ. Eng. - Geotech. Eng. 162, 111–118. https://doi.org/10.1680/geng.2009.162.2.111

Consoli, N.C., Dalla Rosa, A., Corte, M.B., Da SIlva Lopes Jr, L., Consoli, B.S., 2011. Porosity-Cement Ratio Controlling Strength of Artificially Cemented Clays. J. Mater. Civ. Eng. https://doi.org/10.1061/(ASCE)MT.1943-5533.0000283.

Consoli, N.C., de Moraes, R.R., Festugato, L., 2013. Parameters Controlling Tensile and Compressive Strength of Fiber-Reinforced Cemented Soil. J. Mater. Civ. Eng. 25, 1568–1573. https://doi.org/10.1061/(ASCE)MT.1943-5533.0000555

Consoli, N.C., Foppa, D., Festugato, L., Heineck, K.S., 2007. Key Parameters for Strength Control of Artificially Cemented Soils. J. Geotech. Geoenvironmental Eng. https://doi.org/10.1061/(ASCE)1090-0241(2007)133:2(197)

Consoli, N.C., Rotta, G. V., Prietto, P.D.M., 2002. Influence of curing under stress on the triaxial response of cemented soils. Géotechnique 50, 99–105. https://doi.org/10.1680/geot.52.5.382.38705

Cuccovillo, T., Coop, M.R., 1999. On the mechanics of structured sands. Géotechnique 49, 741–760. https://doi.org/10.1680/geot.1999.49.6.741

Griffith, A., 1924. The theory of rupture, in: First Int. Cong. Appl. Mech. pp. 55–63.

Hoek, E., 1988. The Hoek-Brown failure criterion-a 1988 update, in: Proc. 15th Canadian Rock Mech. Symp. Toronto, Dept. Civil Engineering, University of Toronto, pp. 31–38.

Hoek, E., Bieniawski, Z.T., 1965. Brittle Rock Fracture Propagation In Rock Under Compression Brittle Rock Fracture Propagation in Rock Under Compression. Int. J. Fract. Mech. 1, 137–155. https://doi.org/10.1007/BF00186851

Horpibulsuk, S., Bergado, D.T., Lorenzo, G.A., 2004. Compressibility of cement-admixed clays at high water content. Géotechnique 54, 151–154. https://doi.org/10.1680/geot.2004.54.2.151

Horpibulsuk, S., Katkan, W., Sirilerdwattana, W., Rachan, R., 2006. Strength development in cement stabilized low plasticity and coarse grained soils: laboratory and field study. Soils Found. 117, 415–434. https://doi.org/10.1248/cpb.37.3229

Horpibulsuk, S., Liu, M.D., Liyanapathirana, D.S., Suebsuk, J., 2010. Behaviour of cemented clay simulated via the theoretical framework of the Structured Cam Clay model. Comput. Geotech. 37, 1–9. https://doi.org/10.1016/j.compgeo.2009.06.007

Horpibulsuk, S., Miura, N., Bergado, D.T., 2004. Undrained Shear Behavior of Cement Admixed Clay at High Water Content. J. Geotech. Geoenvironmental Eng. 130, 1236–1249. https://doi.org/10.1061/(ASCE)1090-0241(2004)130

Horpibulsuk, S., Miura, N., Nagaraj, T.S., 2005. Clay–Water/Cement Ratio Identity for Cement Admixed Soft Clays. J. Geotech. Geoenvironmental Eng. 131, 792–799. https://doi.org/10.1061/(ASCE)1090-0241(2005)131

Horpibulsuk, S., Nagaraj, T.S., Miura, N., 2003. Assessment of strength development in cement-admixed high water content clays with Abrams' law as a basis. Géotechnique 53, 439–444. https://doi.org/10.1680/geot.2003.53.4.439

Horpibulsuk, S., Phojan, W., Suddeepong, A., Chinkulkijniwat, A., Liu, M.D., 2012a. Strength development in blended cement admixed saline clay. Appl. Clay Sci. 55, 44–52. https://doi.org/10.1016/j.clay.2011.10.003

Horpibulsuk, S., Rachan, R., Suddeepong, A., 2011a. Assessment of strength development in blended cement admixed Bangkok clay. Constr. Build. Mater. 25, 1521–1531. https://doi.org/10.1016/j.conbuildmat.2010.08.006

Horpibulsuk, S., Rachan, R., Suddeepong, A., Chinkulkijniwat, A., 2011b. Strength Development in Cement Admixed Bangkok Clay: Laboratory and Field Investigations. Soils Found. 51, 239–251. https://doi.org/10.3208/sandf.51.239

Horpibulsuk, S., Rachan, R., Suddeepong, A., Liu, M.D., Du, Y.J., 2013. Compressibility of lightweight cemented clays. Eng. Geol. 159, 59–66. https://doi.org/10.1016/j.enggeo.2013.03.020

Horpibulsuk, S., Suddeepong, A., Chinkulkijniwat, A., Liu, M.D., 2012b. Strength and compressibility of lightweight cemented clays. Appl. Clay Sci. 69, 11–21. https://doi.org/10.1016/j.clay.2012.08.006

Horpibulsuk, S., Suddeepong, A., Suksiripattanapong, C., Chinkulkijniwat, A., Arulrajah, A., Disfani, M.M., 2014. Water-Void to Cement Ratio Identity of Lightweight Cellular-Cemented Material. J. Mater. Civ. Eng. 26, 1–10. https://doi.org/10.1061/(ASCE)MT.1943-5533.0001110.

Johnston, I.W., 1985. Strength of Intact Geomechanical Materials. J. Geotech. Eng. https://doi.org/10.1061/(ASCE)0733-9410(1985)111:6(730)

Jongpradist, P., Youwai, S., Jaturapitakkul, C., 2011. Effective Void Ratio for Assessing the Mechanical Properties of Cement-Clay Admixtures at High Water Content. J. Geotech. Geoenvironmental Eng. 137, 621–627. https://doi.org/10.1061/(ASCE)GT.1943-5606.0000462

Kasama, K., Ochiai, H., Yasufuku, N., 2000. On the stress-strain behaviour of lightly cemented clay based on an extended critical state concept. Soils Found. 33, 1660–1668. https://doi.org/10.3208/sandf.40.5_37

Kikuchi, Y., Nagatome, T., Mizutani, T.-A., Yoshino, H., 2011. The effect of air foam inclusion on the permeability and absorption properties of light weight soil. Soils Found. 51, 151–165. https://doi.org/10.3208/sandf.51.151

Kikuchi, Y., Nagatome, T., Otani, J., 2006. Visualization of permeability phenomena in lightweight treated soil mixed with air foam using micro-focus x-ray CT scanner. GeoCongress 2006 Geotech. Eng. Inf. Technol. Age. https://doi.org/10.1061/40803(187)48

Kikuchi, Y., Otani, J., Mukunoki, T., Yoshino, H., Nagatome, T., 2005. Permeability of lightweight treated soil mixed with air foam. Issmge2005 1721–1725. https://doi.org/10.3233/978-1-61499-656-9-1721

Lade, P. V., Overton, D.D., 1989. Cementation Effects in Frictional Materials. J. Geotech. Eng. https://doi.org/10.1061/(ASCE)0733-9410(1989)115:10(1373)

Lade, P. V., Trads, N., 2014. The role of cementation in the behaviour of cemented soils. Geotech. Res. https://doi.org/10.1680/gr.14.00011

Lagioia, R., Nova, R., 1995. An experimental and theoretical study of the behaviour of a calcarenite in triaxial compression. Géotechnique. https://doi.org/10.1680/geot.1995.45.4.633

Lajtai, E.Z., 1969. Strength of Discontinuous Rocks in Direct Shear. Géotechnique 19, 218–233. https://doi.org/10.1680/geot.1969.19.2.218

Leroueil, S., Vaughan, P.R., 1990. The general and congruent effects of structure in natural soils and weak rocks. Géotechnique 40, 467–488. https://doi.org/10.1680/geot.1990.40.3.467

Liu, M.D., Carter, J.P., 2002. A structured Cam Clay model. Can. Geotech. J. 39, 1313–1332. https://doi.org/10.1139/t02-069

Locat, J., Berube, M., Choquette, M., 1990. Laboratory investigations on the lime stabilization sensitive clays: shear strength development. Can. Geotech. J.

Lorenzo, G. a, Bergado, D.T., 2004. Fundamental Parameters of Cement-Admixed Clay — New Approach. J. Geotech. Geoenvironmental Eng. https://doi.org/10.1061/(ASCE)1090-0241(2004)130

Maccarini, M., 1987. Laboratory studies for a weakly bonded artificial soil.

McClintock, F.A., Walsh, J.B., 1962. Friction on Griffith cracks in rocks under pressure, in: Proc. 4th US Nat. Congr. Appl. Mech. pp. 1015–1022.

Mitchell, J.K., 1981. Soil improvement-state of the art report, in: Proc., 11th Int. Conf. on SMFE. pp. 509–565.

Nguyen, L.D., Fatahi, B., Khabbaz, H., 2014. A constitutive model for cemented clays capturing cementation degradation. Int. J. Plast. 56, 1–18. https://doi.org/10.1016/j.ijplas.2014.01.007

Nova, R., 2005. A simple elastoplastic model for soils and soft rocks. Soil Const. Model. https://doi.org/doi:10.1061/40771(169)16

Nova, R., 1992. Mathematical modelling of natural and engineered geomaterials.

General lecture 1st ECSM Munchen. Eur. J. Mech. A/Solids 11, 135–154.

Nova, R., 1988. Sinfonietta classica: an exercise on classical soil modelling. Const. Equations Granul. non-cohesive soils 501–519.

Nova, R., Castellanza, R., Tamagnini, C., 2003. A constitutive model for bonded geomaterials subject to mechanical and/or chemical degradation. Int. J. Numer. Anal. Methods Geomech. https://doi.org/10.1002/nag.294

Otani, J., Mukonoki, T., Kikuchi, Y., 2002. Visualization for engineering property of in-situ light weight soils with air foams. Soils Found. 42, 93–105. https://doi.org/10.1248/cpb.37.3229

Pellegrino, A., 1970. Mechanical behaviour of soft rocks under high stresses. Int. Soc. Rock Mech. Proc. 1.

Pellegrino, A., 1968. Compressibilità e resistenza a rottura del tufo giallo napoletano, in: IX Convegno Di Geotecnica. Genova.

Pinyol, N., Vaunat, J., Alonso, E.E., 2007. A constitutive model for soft clayey rocks that includes weathering effects. Géotechnique 57, 137–151. https://doi.org/10.1680/geot.2007.57.2.137

Roscoe, K.H., Burland, J.B., 1968. On the Generalised Stress-Strain Behaviour of "Wet" Clays, in: Engineering Plasticity.

Rotta, G. V., Consoli, N.C., Prietto, P.D.M., Coop, M.R., Graham, J., 2003. Isotropic yielding in an artificially cemented soil cured under stress. Géotechnique 53, 493–501. https://doi.org/10.1680/geot.53.5.493.37508

Rouainia, M., Muir Wood, D., 2000. A kinematic hardening constitutive model for natural clays with loss of structure. Géotechnique 50, 153–164. https://doi.org/10.1680/geot.2000.50.2.153

Sariosseiri, F., Muhunthan, B., 2009. Effect of cement treatment on geotechnical properties of some Washington State soils. Eng. Geol. https://doi.org/10.1016/j.enggeo.2008.09.003

Sariosseiri, F., Muhunthan, B., 2008. Interpretation of Geotechnical Properties of Cement Treated Soils, Washington State Department of Transportation.

Sasanian, S., Newson, T.A., 2014. Basic parameters governing the behaviour of cement-treated clays. Soils Found. 54, 209–224. https://doi.org/10.1016/j.sandf.2014.02.011

Satoh, T., Tsuchida, T., Mitsukori, K., Hong, Z., 2001. Field placing test of lightweight treated soil under seawater in Kumamoto port. Soils Found. 41, 145–154. https://doi.org/10.3208/sandf.41.5_145

Schnaid, F., Prietto, P.D.M., Consoli, N.C., 2001. Characterization of Cemented Sand in Triaxial Compression. J. Geotech. Geoenvironmental Eng. 0241, 857–868. https://doi.org/10.1061/(ASCE)1090-0241(2001)127:10(857)

Suebsuk, J., Horpibulsuk, S., Liu, M.D., 2011. A critical state model for overconsolidated structured clays. Comput. Geotech. https://doi.org/10.1016/j.compgeo.2011.03.010

Teerawattanasuk, C., Voottipruex, P., Horpibulsuk, S., 2015. Mix design charts for lightweight cellular cemented Bangkok clay. Appl. Clay Sci. 104, 318–323. https://doi.org/10.1016/j.clay.2014.12.012

Tsuchida, T., Egashira, K., 2004. The Lightweight Treated Soil Method: New Geomaterials for Soft Ground Engineering in Coastal Areas. CRC Press - Taylor & Francis Group, London.

Tsuchida, T., Tang, Y.X., Watabe, Y., 2007. Mechanical Properties of Lightweight Treated Soil Cured in Water Pressure. Soils Found. 47, 731–748. https://doi.org/10.3208/sandf.47.731

Verástegui Flores, R.D., Van Impe, W.F., 2009. Stress-strain behavior of artificially cemented Kaolin clay. Proc. 17th Int. Conf. Soil Mech. Geotech. Eng. Acad. Pract. Geotech. Eng. 1, 283–286. https://doi.org/10.3233/978-1-60750-031-5-283

Watabe, Y., Itou, Y., Kang, M.-S., Tsuchida, T., 2004. One-dimensional compression of air-foam treated lightweight geo-material in microscopic point of view. Soils Found. https://doi.org/10.3208/sandf.44.6_53

Watabe, Y., Saegusa, H., Shinsha, H., Tsuchida, T., 2011. Ten year follow-up study of airfoam-treated lightweight soil. Proc. Inst. Civ. Eng. Gr. Improv. 164, 189–200. https://doi.org/10.1680/grim.2011.164.3.189

Watabe, Y., Tanaka, M., Saegusa, H., Shinsha, H., Tsuchida, T., 2009. Long-Term Properties of Airfoam-Treated Lightweight Soil Made from Dredged Clay. J. ASTM Int. 6, 1–10. https://doi.org/10.1520/JAI102134

Xiao, H.W., Lee, F.H., 2008. Curing time effect on behavior of cement treated marine clay. Proc. World Acad. Sci. Eng. Technol. 33, 2070–3740.

5. Materials and methods

Materials and methods used in this study are described in this chapter. Relations between the amounts of soil, cement and foam used for the mixture and bulk properties of lightweight cemented soil, such as bulk density, water content and porosity, are determined. These equations can be used to design the mixture with specific properties that can also be related to mechanical strength of the resulting hardened material, as shown in chapter 4. Starting from these equations, it is also possible to determine the amounts of soil, cement and foam per unit volume, which can be useful in construction projects. The adopted mix design approach is presented after a brief description of methods used in literature. Finally, materials (soil, cement and foam) and mixtures investigated in this study are presented. Microstructural and mechanical tests are described in Appendix B.

5.1. LWCS bulk properties

The lightweight cemented soil is a mix of soil slurry, grout and foam. Each component is composed of solid, liquid and gas phases. Due to the binding agent and subsequent chemical reactions, these phases also evolve with time. In the following, the relations between the phases of the obtained material, starting from the initial amounts of soil, water, cement and foam, are derived. It will be assumed that no shrinkage occurs, that the material is seal cured (i.e. no water flow inward or outward occurs) and there is no air entrapped in soil and cement slurries. The superscripts "s", "l" and "g" will be used to specify respectively the solid, liquid and gas phases. The subscripts "s", "c" and "f" will refer respectively to soil, cement and foam. Some terms regarding water will not be indicated by any superscript for simplicity. Presence of gas and solid phases in water are neglected.

The mass balance of solid and liquid phase state that:

$$W_{LWCS}^{s} = W_{s}^{s} + W_{c}^{s} + W_{f}^{s} \cong W_{s}^{s} + W_{c}^{s} \quad (5\text{-}1)$$

$$W_{LWCS}^{l} = W_{ws} + W_{c}^{l} + W_{f}^{l} \cong W_{ws} + W_{c}^{l} + W_{f} \quad (5\text{-}2)$$

Substituting equations (3-37) and (3-39) in equations (5-1) and (5-2), the weight of solid and liquid phase and water content of lightweight cemented soil are:

$$W_{LWCS}^{s} = W_{s}^{s} + W_{c,a} + W_{wc,n-ev} = W_{s}^{s} + (1 + \alpha x) W_{c,a} \quad (5\text{-}3)$$

$$W_{LWCS}^{l} = W_{ws} + W_{wc} + W_f - W_{wc,n-ev} = W_{ws} + W_{wc}\left(1 - \frac{\alpha x}{w_c/c}\right) + W_f \quad (5\text{-}4)$$

$$w = \frac{W_{LWCS}^{l}}{W_{LWCS}^{s}} = \frac{W_{ws} + W_{wc}\left(1 - \frac{\alpha x}{w_c/c}\right) + W_f}{W_s^s + (1+\alpha x)W_{c,a}} \quad (5\text{-}5)$$

The volume balance of solid phase states that:

$$V_{LWCS}^{s} = V_s^s + V_c^s = V_s^s + V_{c,unh}^s + V_{c,a,h}^s + \beta V_{wc,n-ev} \quad (5\text{-}6)$$

From (3-38):

$$V_{LWCS}^{s} = V_s^s + \left(1 + \frac{\beta x \alpha \rho_{c,a}}{\rho_w}\right) V_{c,a}^s = \frac{W_s^s}{\rho_s} + \left(1 + \alpha x \beta \frac{\rho_{c,a}}{\rho_w}\right)\frac{W_{c,a}}{\rho_c} \quad (5\text{-}7)$$

$$\rho_{LWCS}^{s} = \frac{W_{LWCS}^{s}}{V_{LWCS}^{s}} = \frac{W_s^s + (1+\alpha x)W_{c,a}}{V_s^s + \left(1 + \frac{\beta x \alpha \rho_{c,a}}{\rho_w}\right) V_{c,a}^s} = \frac{W_s^s + (1+\alpha x)W_{c,a}}{\frac{W_s^s}{\rho_s} + \left(1 + \alpha x \beta \frac{\rho_{c,a}}{\rho_w}\right)\frac{W_{c,a}}{\rho_c}} \quad (5\text{-}8)$$

Equation (5-8) shows that the specific weight of a lightweight cemented soil is independent on the gravimetric water to cement ratio. However, if the water available for hydration of cement was not enough, then cement couldn't fully hydrate and that would affect the progress of hydration, represented by x.

The volume balance of liquid phase states that:

$$V_{LWCS}^{l} = V_{ws} + V_c^l + V_f^l = V_{ws} + V_{wc,ev} + V_f^l \quad (5\text{-}9)$$

$$V_{LWCS}^{l} \cong \frac{W_{ws}}{\rho_w} + \frac{W_{wc}}{\rho_w}\left(1 - \frac{\alpha x}{w_c/c}\right) + \frac{W_f}{\rho_w} = \frac{1}{\rho_w}\left[W_{ws} + W_{wc}\left(1 - \frac{\alpha x}{w_c/c}\right) + W_f\right] \quad (5\text{-}10)$$

Due to presence of cement paste, water in a lightweight cemented soil can be held in different states. Thus, the same approach adopted for cement paste (3.1.6) can be used for a cemented soil and liquid phase can be considered as the evaporable water at a specific temperature. This is implicitly assumed if water content is determined according to laboratory standard procedure. Hence, the volume of liquid phase:

$$V_{LWCS}^{l} = \frac{W_{w,ev}}{\rho_w} = V_{w,ev} \cong V_{ws} + V_{wc,ev} + V_f^l \qquad (5\text{-}11)$$

Where $W_{w,ev}$ and $V_{w,ev}$ are respectively the weight and volume of evaporable water from the lightweight cemented soil. The volume balance of the gas phase:

$$V_{LWCS}^{g} = V_{air\ voids} = V_c^g + V_f^g = \frac{(1-\beta)}{\rho_w}\frac{\alpha x W_{wc}}{w_c/_c} + W_f\left(\frac{1}{\gamma_f} - \frac{1}{\rho_w}\right) \qquad (5\text{-}12)$$

The volume of pores V_p is composed of the volume of liquid and air voids:

$$\begin{aligned} V_p = V_{LWCS}^{l} + V_{LWCS}^{g} &= V_{ws} + \left(V_{wc,ev} + V_c^g\right) + \left(V_f^l + V_f^g\right) \\ &= V_{ws} + V_{wc,ev} + V_{e\ cap\ pores} + V_f \end{aligned} \qquad (5\text{-}13)$$

$$V_p = \frac{W_{ws}}{\rho_w} + \frac{W_{wc}}{\rho_w}\left(1 - \frac{\alpha x}{w_c/_c} + \frac{\alpha x(1-\beta)}{w_c/_c}\right) + V_f \qquad (5\text{-}14)$$

Finally, the weight and volume of a lightweight cemented soil are:

$$\begin{aligned} W_{LWCS} &= W_{LWCS}^{s} + W_{LWCS}^{l} \\ &= W_s^s + W_{ws} + (1+\alpha x)W_{c,a} + W_{wc}\left(1 - \frac{\alpha x}{w_c/_c}\right) + W_f \\ &= W_s^s + W_{ws} + W_{c,a}^s + W_{wc} + W_f \\ &= W_{soil\ slurry} + W_{grout} + W_f \end{aligned} \qquad (5\text{-}15)$$

$$\begin{aligned} V_{LWCS} &= V_{LWCS}^{s} + V_{LWCS}^{l} + V_{LWCS}^{g} = \\ &= V_s^s + \left(1 + \frac{\beta\alpha x \rho_{c,a}}{\rho_w}\right)V_{c,a}^s + V_{ws} + V_f + V_{wc}\left(1 - \frac{\beta\alpha x}{w_c/_c}\right) \\ &= V_s^s + V_{ws} + V_{c,a}^s + V_{wc} + V_f \\ &= V_{soil\ slurry} + V_{grout} + V_f \end{aligned} \qquad (5\text{-}16)$$

These last two equations are quite trivial and simply state that the total weight and volume of the material are the sum of weights and volumes of soil slurry, grout and foam, respectively. Moreover, they are constant with time in the hypothesis assumed (no shrinkage and sealed material). If equation (5-15) does have to be true because it can also come from a mass balance, equation (5-16) could be contested. The sum of volumes is not necessarily equal to the sum of volumes of each component. It would be true only if the volume of each component didn't change during mix, that is, if no mutual penetration between soil slurry, grout and foam occurred. This happens when two liquids with no air entrapped are mixed.

Even if no foam is added ($V_f = 0$) and air is not entrapped in soil and cement suspensions during mix, equation (5-16) is still not necessarily true. The empty capillary pores produced during hydration reactions of cement can be filled by water that comes from soil slurry (i.e. mutual penetration of slurry and cement paste) and that could reduce the total volume. However, this phenomenon is complex and depends on both setting time and stiffness of mix, thus it will be neglected for simplicity. In a cemented soil, where no foam is added, equation (5-16) can give a good estimation of the volume of material produced.

More problems occur when foam is added, because it is a dispersion of air bubbles in a surfactant solution and air is entrapped for certain. The air bubbles can undergo collapse, so the volume of foam can decrease upon mechanical mixing. If the equation (5-16) is applied, the resulting volume is just a theoretical volume equal or lower than the actual volume produced. A better estimation of soil properties can be obtained if the volume of foam is substituted by a corrected volume of foam which takes account of the breakage of bubbles. An attempt will be shown in paragraph 5.2.1.1. Summarizing the equations above (the subscript "LWCS" is removed for simplicity):

$$W^s = W_s^s + W_{c,a}^s + W_{wc,n-ev} = W_s^s + (1 + \alpha x) W_{c,a} \tag{5-17}$$

$$\begin{aligned} W^l &= W_{ws} + W_{wc} + W_f - W_{wc,n-ev} \\ &= W_{ws} + W_{wc}\left(1 - \frac{\alpha x}{{w_c}/{c}}\right) + W_f \end{aligned} \tag{5-18}$$

$$W = W_{soil\ slurry} + W_{grout} + W_f = W_s^s + W_{ws} + W_{c,a} + W_{wc} + W_f \tag{5-19}$$

$$V^s = V_s^s + \left(1 + \frac{\beta x \alpha \rho_c}{\rho_w}\right) V_{c,a} = \frac{W_s}{\rho_s} + \left(1 + \frac{\beta x \alpha \rho_{c,a}}{\rho_w}\right) \frac{W_{c,a}}{\rho_{c,a}} \tag{5-20}$$

$$V^l = \frac{W_{w,ev}}{\rho_w} = \frac{1}{\rho_w}\left[W_{ws} + W_{wc}\left(1 - \frac{\alpha x}{{w_c}/{c}}\right) + W_f\right] \tag{5-21}$$

$$V^g = \frac{(1-\beta)}{\rho_w} \frac{\alpha x W_{wc}}{{w_c}/{c}} + W_f \left(\frac{1}{\gamma_f} + \frac{1}{\rho_w}\right) \tag{5-22}$$

$$V_p = V_{ws} + V_f + V_{wc}\left(1 - \frac{\beta \alpha x}{{w_c}/{c}}\right) = \frac{W_{ws}}{\rho_w} + \frac{W_{c,a}}{\rho_w}\left({w_c}/{c} - \beta \alpha x\right) + V_f \tag{5-23}$$

$$\begin{aligned} V = V^s + V_p &= V_s^s + V_{ws} + V_{c,a} + V_{wc} + V_f \\ &= V_{soil\ slurry} + V_{grout} + V_f \end{aligned} \tag{5-24}$$

The weight and volumes of each phase have been determined, thus bulk properties of a LWCS can be defined. However, it is convenient to relate these amounts to dry weight of soil. Given:

$$\frac{c}{s} = \frac{W_{c,a}}{W_s^s}; w_s = \frac{W_{ws}}{W_s^s}; \tag{5-25}$$

The equations (5-17) to (5-24) become:

$$W^s = W_s^s + (1+\alpha x)\left(\frac{c}{s}\right)W_s^s = W_s^s\left[1+(1+\alpha x)\left(\frac{c}{s}\right)\right] \tag{5-26}$$

$$\begin{aligned} W^l &= w_s W_s^s + W_s^s\left(\frac{w_c}{c}\right)\left(\frac{c}{s}\right)\left(1-\frac{\alpha x}{{}^{w_c}/_{c}}\right) + W_f \\ &= W_s^s\left[w_s + \left(\frac{c}{s}\right)\left(\frac{w_c}{c}-\alpha x\right)\right] + W_f \end{aligned} \tag{5-27}$$

$$\begin{aligned} W &= W_s^s + w_s W_s^s + \left(\frac{c}{s}\right)W_s^s + \left(\frac{w_c}{c}\right)\left(\frac{c}{s}\right)W_s^s{}_s + W_f \\ &= W_s^s\left[1+w_s+\left(1+\frac{w_c}{c}\right)\left(\frac{c}{s}\right)\right] + W_f \end{aligned} \tag{5-28}$$

$$\begin{aligned} V^s &= \frac{W_s^s}{\rho_s} + \left(1+\frac{\beta x\alpha\rho_{c,a}}{\rho_w}\right)\left(\frac{c}{s}\right)\frac{W_s^s}{\rho_{c,a}} \\ &= W_s^s\left[\frac{1}{\rho_s} + \left(\frac{1}{\rho_{c,a}}+\frac{\beta x\alpha}{\rho_w}\right)\left(\frac{c}{s}\right)\right] \end{aligned} \tag{5-29}$$

$$\begin{aligned} V^l = \frac{W_{w,ev}}{\rho_w} &= \frac{1}{\rho_w}\left[w_s W_s^s + W_s^s\left(\frac{c}{s}\right)\left(\frac{w_c}{c}-\alpha x\right) + W_f\right] \\ &= W_s^s\left[\frac{w_s}{\rho_w} + \frac{1}{\rho_w}\left(\frac{c}{s}\right)\left(\frac{w_c}{c}-\alpha x\right)\right] + \frac{W_f}{\rho_w} \end{aligned} \tag{5-30}$$

$$V_p = W_s^s\left[\frac{w_s}{\rho_w} + \frac{1}{\rho_w}\left(\frac{c}{s}\right)\left({}^{w_c}/_{c} - \beta\alpha x\right)\right] + V_f \tag{5-31}$$

$$V = V^s + V_p = W_s^s\left[\frac{1}{\rho_s} + \frac{w_s}{\rho_w} + \left(\frac{c}{s}\right)\left(\frac{1}{\rho_{c,a}} + \frac{{}^{w_c}/_{c}}{\rho_w}\right)\right] + V_f \tag{5-32}$$

By this way the volume and weights of solid, liquid and gas phase have been written in terms of weight of solid soil and foam (with $V_f = \gamma_f W_f$). Hence:

$$\rho^s = \frac{W^s}{V^s} = \frac{(1+\alpha x)\left(\frac{c}{s}\right)+1}{\frac{1}{\rho_s}+\left(\frac{1}{\rho_{c,a}}+\frac{\beta x\alpha}{\rho_w}\right)\left(\frac{c}{s}\right)} = \rho_s\frac{1+(1+\alpha x)\left(\frac{c}{s}\right)}{1+\left(\frac{\rho_s}{\rho_{c,a}}+\frac{\rho_s}{\rho_w}\beta x\alpha\right)\left(\frac{c}{s}\right)} \tag{5-33}$$

$$w = \frac{W^l}{W^s} = \frac{W_s^s\left[w_s + \left(\frac{c}{s}\right)\left(\frac{w_c}{c} - \alpha x\right)\right] + W_f}{W_s^s\left[(1+\alpha x)\left(\frac{c}{s}\right) + 1\right]} = \frac{w_s + \left(\frac{c}{s}\right)\left(\frac{w_c}{c} - \alpha x\right) + \frac{W_f}{W_s^s}}{(1+\alpha x)\left(\frac{c}{s}\right) + 1} \quad (5\text{-}34)$$

$$\gamma = \frac{W}{V} = \frac{W_s^s\left[1 + w_s + \left(\frac{c}{s}\right) + \left(\frac{w_c}{c}\right)\left(\frac{c}{s}\right)\right] + W_f}{W_s^s\left[\frac{1}{\rho_s} + \frac{w_s}{\rho_w} + \left(\frac{c}{s}\right)\left(\frac{1}{\rho_{c,a}} + \frac{{}^{w_c}/_{c}}{\rho_w}\right)\right] + V_f} = \frac{1 + w_s + \left(\frac{c}{s}\right) + \left(\frac{w_c}{c}\right)\left(\frac{c}{s}\right) + \frac{W_f}{W_s^s}}{\frac{1}{\rho_s} + \frac{w_s}{\rho_w} + \left(\frac{c}{s}\right)\left(\frac{1}{\rho_{c,a}} + \frac{{}^{w_c}/_{c}}{\rho_w}\right) + \frac{V_f}{W_s^s}} \quad (5\text{-}35)$$

$$n = \frac{V_p}{V} = \frac{\frac{w_s}{\rho_w} + \frac{1}{\rho_w}\left(\frac{c}{s}\right)\left({}^{w_c}/_{c} - \beta\alpha x\right) + \frac{V_f}{W_s^s}}{\frac{1}{\rho_s} + \frac{w_s}{\rho_w} + \left(\frac{c}{s}\right)\left(\frac{1}{\rho_{c,a}} + \frac{{}^{w_c}/_{c}}{\rho_w}\right) + \frac{V_f}{W_s^s}} \quad (5\text{-}36)$$

$$e = \frac{V_p}{V_{solid}} = \frac{\frac{w_s}{\rho_w} + \frac{1}{\rho_w}\left(\frac{c}{s}\right)\left({}^{w_c}/_{c} - \beta\alpha x\right) + \frac{V_f}{W_s^s}}{\frac{1}{\rho_s} + \left(\frac{1}{\rho_{c,a}} + \frac{\beta x \alpha}{\rho_w}\right)\left(\frac{c}{s}\right)} \quad (5\text{-}37)$$

$$\gamma_{dry} = \frac{W^s}{V} = \frac{W_s^s\left[1 + \left(\frac{c}{s}\right)(1+\alpha x)\right]}{W_s^s\left[\frac{1}{\rho_s} + \frac{w_s}{\rho_w} + \left(\frac{c}{s}\right)\left(\frac{1}{\rho_{c,a}} + \frac{{}^{w_c}/_{c}}{\rho_w}\right)\right] + V_f} = \frac{\left[1 + \left(\frac{c}{s}\right)(1+\alpha x)\right]}{\left[\frac{1}{\rho_s} + \frac{w_s}{\rho_w} + \left(\frac{c}{s}\right)\left(\frac{1}{\rho_{c,a}} + \frac{{}^{w_c}/_{c}}{\rho_w}\right)\right] + \frac{V_f}{W_s}} \quad (5\text{-}38)$$

$$\gamma_{sat} = \frac{W^s + \rho_w V_p}{V} = \frac{W_s^s\left[1 + w_s + \left(1 + \frac{w_c}{c} + (1-\beta)\alpha x\right)\left(\frac{c}{s}\right)\right] + \rho_w V_f}{W_s^s\left[\frac{1}{\rho_s} + \frac{w_s}{\rho_w} + \left(\frac{c}{s}\right)\left(\frac{1}{\rho_{c,a}} + \frac{{}^{w_c}/_{c}}{\rho_w}\right)\right] + V_f} \quad (5\text{-}39)$$

$$w_{max} = \frac{W_s^s \left[w_s + \left(\frac{c}{s}\right)\left(\frac{w_c}{c} - \beta\alpha x\right)\right] + \rho_w V_f}{W_s \left[1 + (1 + \alpha x)\left(\frac{c}{s}\right)\right]} = \frac{w_s + \left(\frac{c}{s}\right)\left(\frac{w_c}{c} - \beta\alpha x\right) + \frac{\rho_w V_f}{W_s^s}}{1 + (1 + \alpha x)\left(\frac{c}{s}\right)} \quad (5\text{-}40)$$

$$S_r = \frac{w}{w_{max}} = \frac{w\rho^s}{e\rho^w} = \frac{w_s + \left(\frac{c}{s}\right)\left(\frac{w_c}{c} - \alpha x\right) + \frac{W_f}{W_s^s}}{w_s + \left(\frac{c}{s}\right)\left(\frac{w_c}{c} - \beta\alpha x\right) + \frac{\rho^w V_f}{W_s^s}} \quad (5\text{-}41)$$

If only soil slurry is considered (W_f=V_f=c/s=0), equation (5-41) gives obviously 1 because it has been assumed that no air is entrapped. However, if c/s>0 and x>0, even if W_f=V_f=0 (cemented soil), saturation degree is slightly lower than 1. This is due to the empty capillary pores formed in the cement paste. If x=1, α=0.2, β=0.746, $\rho_{c,a}/\rho_w$=3.15 and ρ_s=26 kN/m^3 (ρ_{ca}=31.5 kN/m^3):

$$W^s = W_s^s \left[1.2\frac{c}{s} + 1\right] \quad (5\text{-}42)$$

$$\rho_{LWCS}^s = \frac{W^s}{V^s} \cong \rho_s \frac{1.2\left(\frac{c}{s}\right) + 1}{1 + 1.47\frac{\rho_s}{\rho_{c,a}}\left(\frac{c}{s}\right)} \cong \rho_s \frac{1.2\left(\frac{c}{s}\right) + 1}{1.22\left(\frac{c}{s}\right) + 1} \cong \rho_s \quad (5\text{-}43)$$

The equation (5-43) states that, regardless of *c/s*, if the cement is well hydrated, the specific weight of a cemented soil is approximately equal to the specific weight of the soil itself. Indeed, the cement paste is lightened by the presence of water combined.

In Figure 5-1 a graphical representation of equations above is shown at varying x, from 0 (no hydration) to 1 (100 % of the cement hydrated). The bar charts show on the left column the amounts of solid, liquid and gas phase in LWCS and on the right column their composition.

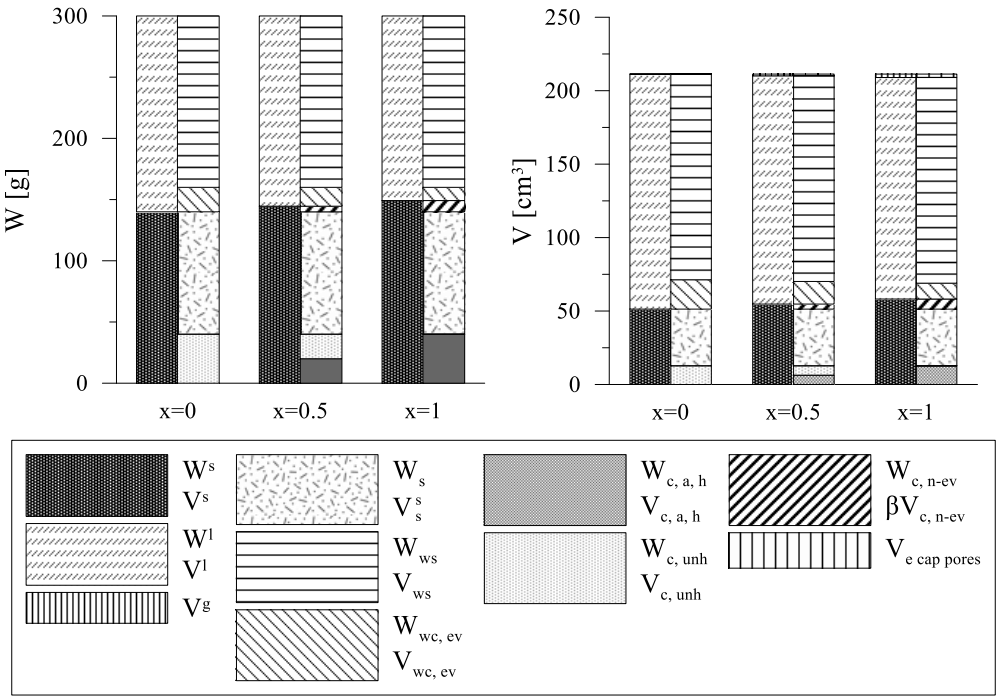

Figure 5-1 Graphical representation of mass and volume balances for W_s=100 g, w_s=1.4, c/s=0.4, w_c/c=0.5, V_f=0.

In Figure 5-2 the evolution of w, e and n, for W_s=100 g, V_f=0, c/s=0.4, w_c/c=0.5 with progress of hydration is presented. Water content decreases with time due to water chemically combined, thus reducing the liquid phase and increasing the solid phase (even if no outward water flow occurs). This also justifies the reduction of void ratio and porosity.

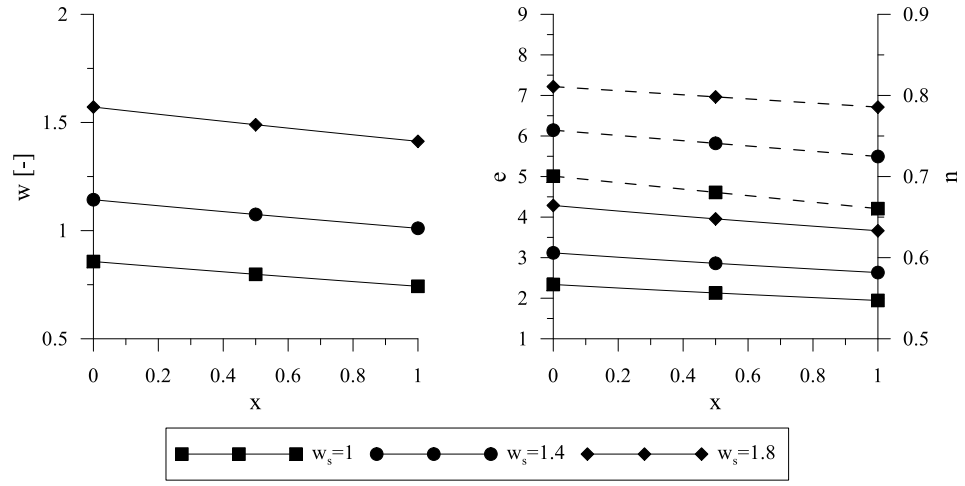

Figure 5-2. Evolution of bulk properties at varying x and w_s with W_s=100 g, V_f=0, c/s=0.4, w_c/c=0.5. On the left, the water content; on the right, the solid lines refer to e whereas the dashed lines refer to n.

Starting from equations above it is also possible to determine the amounts of soil, cement and foam per unit volume by dividing them to the volume of material (5-32):

$$m_s^s = \frac{W_s^s}{W_s^s\left[\frac{1}{\rho_s} + \frac{w_s}{\rho_w} + \left(\frac{c}{s}\right)\left(\frac{1}{\rho_{c,a}} + \frac{w_c/c}{\rho_w}\right)\right] + V_f} = \frac{1}{\left[\frac{1}{\rho_s} + \frac{w_s}{\rho_w} + \left(\frac{c}{s}\right)\left(\frac{1}{\rho_{c,a}} + \frac{w_c/c}{\rho_w}\right)\right] + \frac{V_f}{W_s^s}} \quad (5\text{-}44)$$

$$m_{c,a} = \frac{\frac{c}{s}}{\left[\frac{1}{\rho_s} + \frac{w_s}{\rho_w} + \left(\frac{c}{s}\right)\left(\frac{1}{\rho_{c,a}} + \frac{w_c/c}{\rho_w}\right)\right] + \frac{V_f}{W_s^s}} \quad (5\text{-}45)$$

$$m_{ws} = \frac{w_s}{\left[\frac{1}{\rho_s} + \frac{w_s}{\rho_w} + \left(\frac{c}{s}\right)\left(\frac{1}{\rho_{c,a}} + \frac{w_c/c}{\rho_w}\right)\right] + \frac{V_f}{W_s^s}} \quad (5\text{-}46)$$

$$m_{wc} = \frac{\frac{w_c}{c}\frac{c}{s}}{\left[\frac{1}{\rho_s} + \frac{w_s}{\rho_w} + \left(\frac{c}{s}\right)\left(\frac{1}{\rho_{c,a}} + \frac{w_c/c}{\rho_w}\right)\right] + \frac{V_f}{W_s^s}} \quad (5\text{-}47)$$

$$m_f = \frac{\frac{\gamma_f V_f}{W_s^s}}{\left[\frac{1}{\rho_s} + \frac{w_s}{\rho_w} + \left(\frac{c}{s}\right)\left(\frac{1}{\rho_{c,a}} + \frac{w_c/c}{\rho_w}\right)\right] + \frac{V_f}{W_s^s}} \quad (5\text{-}48)$$

It is worth noting that the sum of unit amounts is equal to the unit weight of material, while the sum of volumetric amounts, which can be derived dividing the gravimetric unit amounts by their specific weight, respectively ρ_s, $\rho_{c,a}$, ρ_w and γ_f) is equal to 1, as also shown by Tsuchida and Egashira (2004):

$$m_s^s + m_{ws} + m_{c,a} + m_{wc} + m_f = \gamma \quad (5\text{-}49)$$

$$\frac{m_s^s}{\rho_s} + \frac{m_{ws}}{\rho_w} + \frac{m_{c,a}}{\rho_{c,a}} + \frac{m_{wc}}{\rho_w} + \frac{m_f}{\gamma_f} = 1 \quad (5\text{-}50)$$

5.2. Mix proportion design

Some parameters were introduced in equations derived in section 5.1. The water content of slurry, w_s, is a state parameter commonly used to define the amount of water in a soil slurry and it's often related to the liquid limit of the soil.

The water to cement ratio by weight, w_c/c, is commonly used to define the amount of water for cement paste; however, this parameter is unnecessary when the cement is added as a powder to the mix ($w_c/c=0$). The amount of cementitious material used to treat the soil can be related to both dry weight of soil, referred to as cement factor, c/s, and to the volume of material produced, referred to as cement content, $m_{c,a}$ (Marzano, 2017). These parameters can be used for mix design, and, based on the approach, it could not be necessary to introduce a parameter for foam (except for foam unit weight γ_f).

The approach proposed by Tsuchida and Egashira (2004) is based on w_s, $m_{c,a}$ and γ. The water to cement ratio w_c/c is equal to zero because of the treatment method chosen by the authors, but the same approach can be easily used once w_c/c is set beforehand. They also suggest determining the optimal w_s based on rheological properties, via a flow test (3.1.5), that should be between 1.5 and 3 times the liquid limit.

Considering equations (5-51) and (5-52), which can be regarded as a system of two equations, there are six variables with four degrees of freedom. Once w_s and w_c/c are set, two other design parameters stay. This is a common approach in literature, thus mix design methods usually differ for the last two design parameters, which are m_{ca} and γ in the case of Tsuchida and Egashira (2004). Increasing m_{ca}, an enhancement in mechanical properties is expected, while the unit cost increases. Tsuchida and Egashira (2004) suggest that m_{ca} must be included between 90 to 300 kg/m^3. On the other hand, γ reflects one of the main effects of foam that is lowering the density and it can be related to design requirements. The other unit amounts (m_s^s, m_{ws}, m_{wc}, m_f) can be easily obtained from (5-51) and (5-52). Other approaches generally require a parameter to establish the amount of foam to be added and different parameters can be used. In some cases, the volume of foam is related to volume of soil slurry (Teerawattanasuk et al., 2015), or to the total volume of soil slurry and foam (Horpibulsuk et al., 2012).

A similar approach was used in this study. Both w_s and w_c/c are set. The second one must ensure a proper viscosity of cement suspension to allow a homogenous mixing with soil slurry and, subsequently, with foam. The last two parameters adopted for mix design are the cement factor, c/s, and n_f, defined as the ratio between the volume of foam and the volume of material produced:

$$n_f = \frac{V_f}{V} = \frac{W_f}{V\gamma_f} = \frac{m_f}{\gamma_f} \quad (5\text{-}51)$$

This parameter can be regarded as a theoretical porosity induced by foam. Conversely to other parameters, n_f is not directly related to the weight of soil. A convenient way to determine the volume of foam to be used to obtain a specific n_f, is to express the volume of foam in relation of the sum of the volumes of the two slurries:

$$e_f' = \frac{V_f}{V_{soil\ slurry} + V_{grout}} = \frac{V_f}{V - V_f} = \frac{n_f}{1 - n_f} \quad (5\text{-}52)$$

If n_f is a theoretical porosity due to foam, e_f' is not a void ratio due to foam because the denominator in (5-52) is not the solid phase of the LWCS. From (5-32), with V_f=0:

$$V(n_f = 0) = V_{soil\ slurry} + V_{grout} = W_s^s \left[\frac{1}{\rho_s} + \frac{w_s}{\rho_w} + \left(\frac{c}{s}\right)\left(\frac{1}{\rho_{c,a}} + \frac{w_c/c}{\rho_w}\right)\right] \quad (5\text{-}53)$$

$$e_f' = \frac{V_f}{W_s^s \left[\frac{1}{\rho_s} + \frac{w_s}{\rho_w} + \left(\frac{c}{s}\right)\left(\frac{1}{\rho_{c,a}} + \frac{w_c/c}{\rho_w}\right)\right]} \quad (5\text{-}54)$$

$$\frac{V_f}{W_s^s} = \frac{W_f}{\gamma_f W_s^s} = e_f' \left[\frac{1}{\rho_s} + \frac{w_s}{\rho_w} + \left(\frac{c}{s}\right)\left(\frac{1}{\rho_{c,a}} + \frac{w_c/c}{\rho_w}\right)\right] \quad (5\text{-}55)$$

By this way it is possible to relate directly n_f (which has a clearer physical meaning than e_f') to the ratio between the volume of foam and the weight of dry soil.

The approach used in this study requires to set w_s, w_c/c, c/s and n_f. Then, given the amount of dry soil to treat, W_s^s, it's trivial to derive the amounts of water for soil slurry, cement and water for grout whereas the volume of foam to add can be easily determined from (5-55). From equations derived in 5.1 it's possible to estimate the physical properties of the material and the unit amounts.

5.2.1.1. Volume of foam correction

Breakage of bubbles can occur due to mechanical mixing of foam with other suspensions (i.e. soil and cement suspensions), thus the actual volume of foam

and the "actual" n_f, defined in the following as n_f^*, can result to be lower than the theoretical values. Given:

- V_{act} actual volume of material produced;
- V_{th} theoretical volume of material produced (5-32);
- ΔV difference between actual volume and theoretical volume of material;
- W mass weight of material produced;
- γ_{act} actual bulk density;
- γ_{th} theoretical bulk density (5-35);
- $\Delta\gamma = \gamma_{act} - \gamma_{th}$;

n_f^* can be determined as:

$$n_f^* = \frac{V_{f,act}}{V_{act}} = \frac{V_{f,th} + \Delta V_f}{V_{th} + \Delta V_f} \tag{5-56}$$

Assuming perfect homogeneity of mixture and that no water evaporates during mixing, then the loss in volume of the material ΔV is equal to the loss in volume of air bubbles, that is the variation of volume of foam, ΔV_f. Hence:

$$\begin{aligned} \Delta V = \Delta V_f = V_{act} - V_{th} &= \frac{W}{\gamma_{act}} - \frac{W}{\gamma_{th}} = W\left(\frac{1}{\gamma_{act}} - \frac{1}{\gamma_{th}}\right) \\ &= \frac{W}{\gamma_{th}}\left(\frac{\gamma_{th} - \gamma_{act}}{\gamma_{act}}\right) = V_{th}\left(\frac{\gamma_{th} - \gamma_{act}}{\gamma_{act}}\right) \end{aligned} \tag{5-57}$$

$$\frac{\Delta V_f}{V_{th}} = \left(\frac{\gamma_{th} - \gamma_{act}}{\gamma_{act}}\right) = -\frac{\Delta\gamma}{\gamma_{act}} \tag{5-58}$$

Dividing both members of (5-56) by V_{th}:

$$n_f^* = \frac{\frac{V_{f,th}}{V_{th}} + \frac{\Delta V_f}{V_{th}}}{\frac{V_{th}}{V_{th}} + \frac{\Delta V_f}{V_{th}}} = \frac{n_f - \frac{\Delta\gamma}{\gamma_{act}}}{1 - \frac{\Delta\gamma}{\gamma_{act}}} = \frac{\gamma_{act} n_f - \Delta\gamma}{\gamma_{act} - \Delta\gamma} = \frac{\gamma_{act} n_f - \Delta\gamma}{\gamma_{th}} \tag{5-59}$$

It is worth noting that n_f^* can be used in place of n_f to derive bulk properties by using equation (5-55); e'^*_f can be calculated by n_f^*, thus $\frac{V_f}{W_s^s}$ can be calculated with the same equation by simply substituting n_f with n_f^*. However, the term $\frac{W_f}{W_s^s}$ does not have to be modified because the weight of foam in the mixture does not change. Only the volume of foam "decreases" due to collapse of bubbles, as if the bulk density of foam, γ_f, changed upon mixing.

5.3. Materials

5.3.1. Soil

In this experimental study two soils were investigated. A wide experimentation was carried out on a commercially produced fine grained soil, the Speswhite kaolin, and a natural fine-grained soil taken around Caposele (Avellino, Italy) termed Caposele soil. Particle size distributions and physical properties are reported in Figure 5-3 and Table 5-2, respectively.

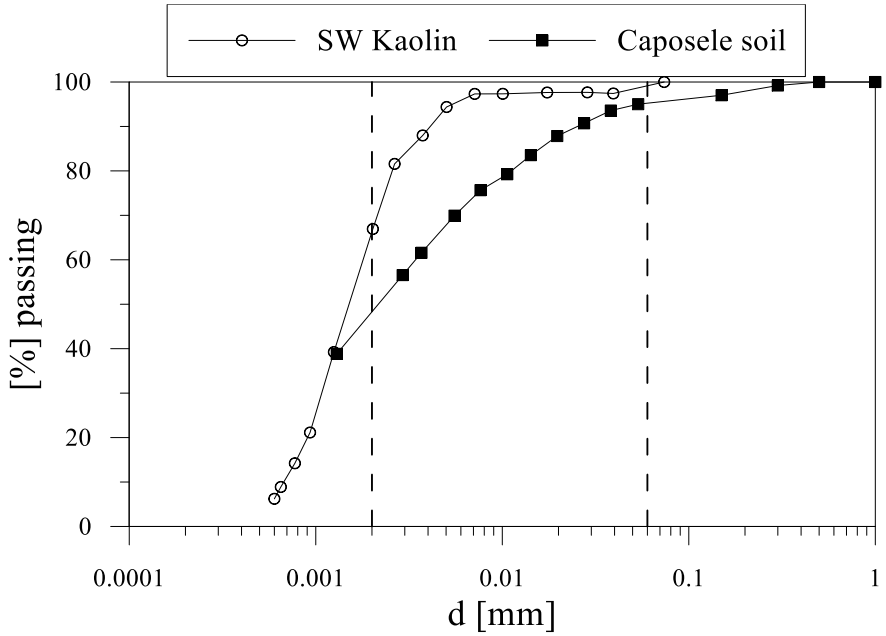

Figure 5-3. Grain size distribution of Speswhite kaolin and Caposele soil.

Table 5-1. Physical properties of Speswhite kaolin and Caposele soil.

	ρ_s [kN/m^3]	w_l [%]	w_p [%]	I_p [%]
SW Kaolin	25.9	70	32	38
Caposele soil	27.5	62	30	32

The Speswhite kaolin is a clayey silt produced from deposits in the southwest of England, mainly composed of kaolinite and muscovite, with presence of quartz, as it results from the XRD analysis (Appendix B) shown in Figure 5-4. The structure and chemical composition of these minerals are discussed in 2.1. The main mineral groups, as reported in Table 5-2, are silica and alumina, which are the main mineral groups of kaolinite and muscovite, with a low percentage of potassium oxide (K_2O), that is present in muscovite structure.

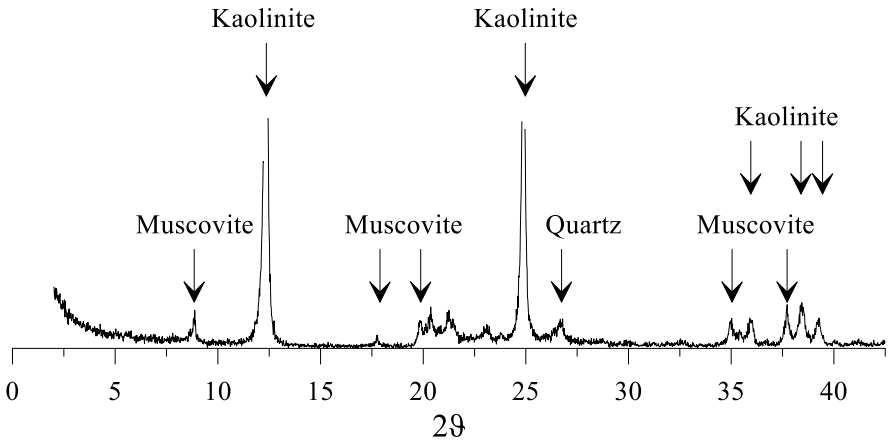

Figure 5-4. Results of X-Ray Diffraction analysis on Speswhite kaolin.

Table 5-2. Composition of Speswhite kaolin.

Group	*Percentage*
SiO_2	53.8
Al_2O3	43.75
K_2O	1.45
Na_2O	0.92
TiO_2	0.05
CaO	0.02

Caposele soil is a clay with silt composed of muscovite, quartz and calcite, as it derived from XRD analysis (Figure 5-5).

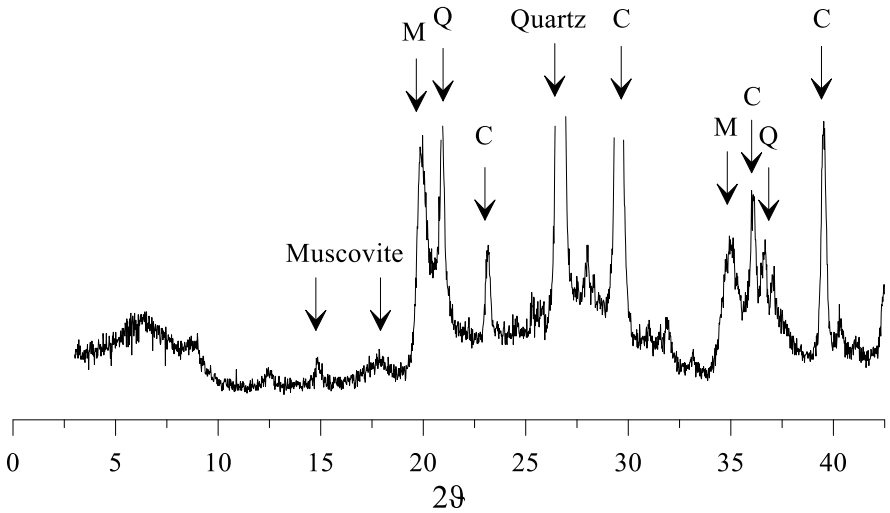

Figure 5-5. Results of X-Ray Diffraction analysis on Caposele soil; C: calcite, M: muscovite, Q: quartz.

5.3.1.1. Soil slurry

SW kaolin and Caposele soil were diluted at a water content of 140 and 120 %, respectively. By this way, water content is approximately equal to $2w_l$ for both and the corresponding liquidity index is 2.84 and 2.81 for kaolin and Caposele, respectively. This value is in the range suggested by different authors ($1.5\text{-}3w_l$). It is worth noting that using equation (2-11), viscosity of suspension is 0.051 Pl for kaolin and 0.053 Pl for Caposele (viscosity of water at 20 °C is 0.001 Pl), that is in the same range of grout viscosity (3.1.5). Fall cone test results at varying water content are shown in Figure 5-6a. Data were fitted via equation (2-10) (coefficients are reported in the figure); the bulk weight decreases at increasing water content, as reported in Figure 5-6b.

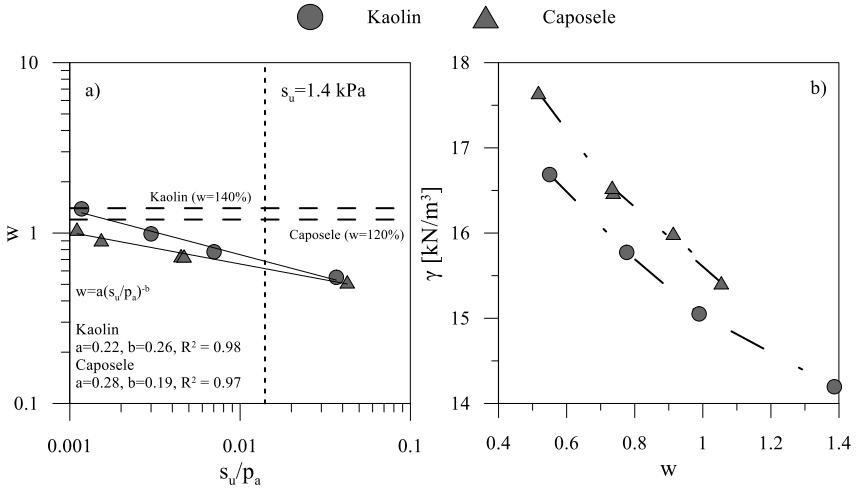

Figure 5-6. a) Fall cone test results. Solid lines refer to fit curves; vertical dotted line refers to s_u at liquid limit, as suggested by Koumoto and Houlsby (2001)*; horizontal dashed lines refer to water content of soil slurry adopted for mixtures. b) Measured unit weight at varying water content.*

5.3.2. Cement

Portland cement was chosen as a binding agent. Specifically, a commercial rapid hardening limestone Portland cement classified as CEM II/A LL 42.5R, was supplied by BUZZI UNICEM, was used for all the tests; the amount of $CaCO_3$ is between 6 to 20 %. Some details about limestone cements have been discussed in 3.1.4. According to commercial datasheet, the unconfined compressive strength after 2 and 28 days is above 25 and 47 MPa (standard requirements are 20 and 42.5 MPa), respectively; initial setting time is above 2 hours (standard requires at least 60 minutes). Sulphates (SO_3) and chlorites (Cl^-) percentages are below 3.5 % and 0.08 % (standard requirements are 4 % and 0.1 %), respectively.

A gravimetric water to cement ratio for grout, w_c/c, equal to 0.5 was used for all the mixtures. The effect of cement factor, c/s, was investigated on treated kaolin with c/s=0.2 and 0.4. Caposele soil was treated with c/s=0.4.

5.3.3. Foam

Foam was generated via an industrial foam generator, the GN-100 AC Bunker. It is composed of two independent devices: a proportional dosing pump to produce the surfactant solution at a specified concentration, and the foam generator, constituted of a pump for surfactant solution and a compressor to inject pressurized air in solution producing foam.

Figure 5-7.Foam generator.

A commercial surfactant, produced by Isoltech Srl, namely ISOCEM S/L, was used. It is liquid, brown with a specific weight of 10.015 g/L and pH equal to 7. It is composed of a mix of anionic and non-ionic surfactants. Surfactant was diluted with tap water at the suggested concentration of 2.5 %. The air pressure was set to 3.2 bar, producing a foam with a bulk density of 75 ± 5 g/L corresponding to a FER approximately equal to 13 ± 1.

The effect of foam was studied on samples made up with two different n_f, i.e. 0.2 and 0.4, and compared to corresponding cemented soil (n_f=0).

5.3.4. Mix proportion

A summary of mixtures tested in this experimental study is reported in Table 5-3. The mixtures are identified by the type of soil (“K” for Speswhite kaolin and “C” for Caposele soil), the cement factor, specified by “csX” (where X is the c/s ratio in percentage) and porosity induced by foam n_f, specified by “nfY” (where

Y is the n_f in percentage); for example, Caposele soil treated with a cement factor equal to 40 % and n_f equal to 20 % is identified by Ccs40nf20.

Table 5-3. Treated soil mixtures.

	w_c/c	w_s [%]	c/s [%]	n_f [%]	
SW Kaolin	0.5	140%	20%	0%	K cs20
				20%	K cs20 nf20
				40%	K cs20 nf40
			40%	0%	K cs40
				20%	K cs40 nf20
				40%	K cs40 nf40
Caposele	0.5	120%	40%	0%	C cs40
				20%	C cs40 nf20
				40%	C cs40 nf40

In Table 5-4 the theoretical amounts per cubic meter have been reported. The symbol m_{surf} refers to the amount of concentrated surfactant additive per cubic meter, while m_f is the amount of foam by weight, that is equal to the amount of diluted surfactant solution at 2.5 %, as specified in 5.3.3. It is worth noting that this amount is always lower than 1 kg per cubic meter. The amounts for Kcs40% nf 0-20-40% are also reported graphically in Figure 5-8a.

Table 5-4. Theoretical amounts of dry soil, water for soil slurry, cement, water for cement, foam, surfactant for unit volume and unit weight.

	m_s [kg]	m_{ws} [kg]	$m_{c,a}$ [kg]	m_{wc} [kg]	m_f [kg]	m_{surf} [kg]	γ [kN/m^3]
K cs20	513	718	103	51	0	0.00	13.8
K cs20 nf20	410	574	82	41	15	0.38	11.2
K cs20 nf40	308	431	62	31	30	0.75	8.6
K cs40	473	663	189	95	0	0.00	14.2
K cs40 nf20	379	530	151	76	15	0.38	11.5
K cs40 nf40	284	398	114	57	30	0.75	8.8
C cs40	529	635	212	106	0	0.00	14.8
C cs40 nf20	423	508	169	85	15	0.38	12.0
C cs40 nf40	317	381	127	63	30	0.75	9.2

In Figure 5-8b the percentages by volumes of each component on total theoretical volume are represented (foam volume percentage is equal to n_f). In this graph, the effect of foam is immediately clear. Increasing the amount of foam, all the other components decrease while foam contribution on total weight is negligible. Because of this, both the amounts of cement and water per cubic meter decrease, and the unit cost decreases as well.

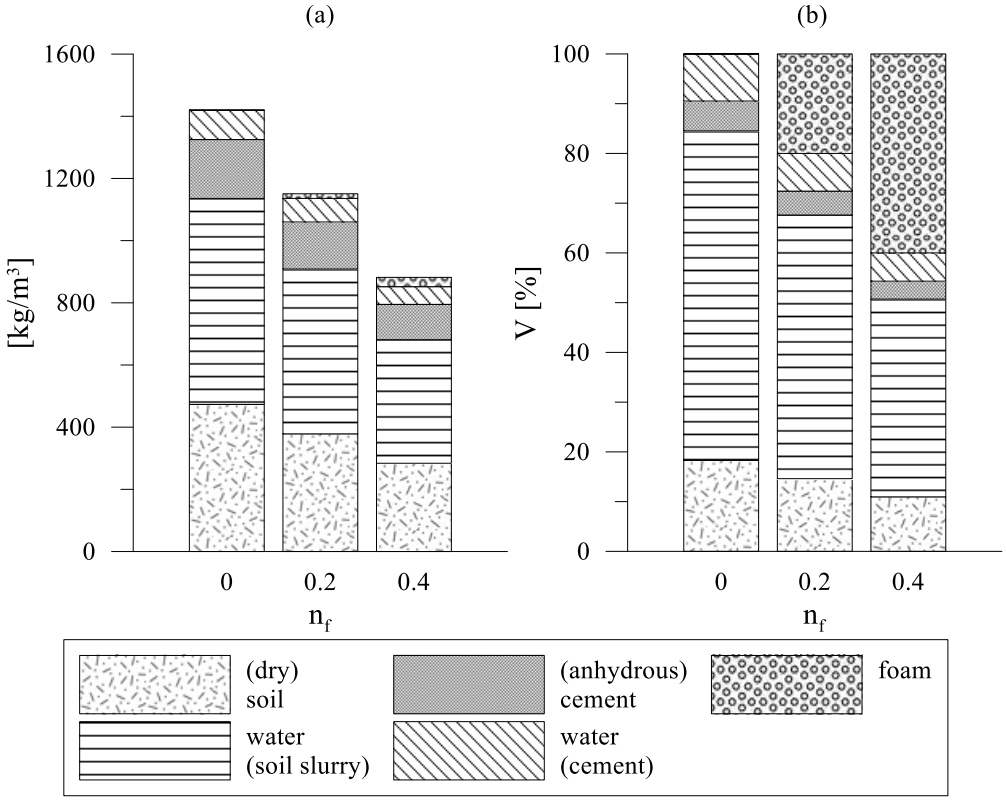

Figure 5-8. Graphical representation of theoretical composition of K cs40% nf 0-20-40%: (a) amounts of each component per cubic meter by weight; (b) percentages by volume.

5.3.5. Specimen preparation

The amount of soil to treat was set beforehand; samples of treated Caposele soil and kaolin were obtained by treating 500 g of dry and 300 g of dry soil, except for some cases. The samples were seal cured to avoid evaporation of the mixture water.

The high workability of the fresh paste allows to prepare the samples pouring the mixture in moulds. A thin layer of silicone grease was put on lateral walls of the mould to minimize the friction when the hardened material had to be extruded. The method adopted in this study has been presented in Introduction, schematically shown in Figure 1-1. The samples for mechanical tests were usually poured in moulds with the geometry required for the specific test, so that disturbance on specimen was minimized. The main disadvantage of this procedure lays on samples shrinkage that may occur during the curing process. In that case, specimen dimensions can slightly decrease, affecting the reliability of the assumption of oedometric condition made in some tests. Due to small dimensions required for microstructural tests, the specimens for these tests were trimmed from bigger samples.

Figure 5-9. Pictures of different stages of specimen preparation. The numbers refer to the stage indicated in this section (5.3.5).

The material was prepared following the lightweight cemented soil method:

1. the amount of dry soil W_s to be treated is mixed with distilled water up to a specific water content, w_s;
2. independently, the amount of cement, $W_{c\ a}$, based on c/s, is mixed with distilled water, W_{wc}, at a specific w_c/c;
3. soil slurry and grout are mixed (if no foam is added, 4 and 5 are skipped)
4. contemporarily, foam is prepared, and density of foam is checked;
5. an amount of foam, W_f, based on n_f and equation (5-55) is added;
6. the mixture is poured in moulds; each sample is weighted and sealed on top with a first layer of cling film to minimize loss in water during preparation of other samples. At the end, samples are sealed with cling film and scotch tape and cured in a humidity-controlled chamber.

5.4. Summary

In this chapter, solid, liquid and gas phases of lightweight cemented soils have been identified. By this way, LWCS bulk properties can be determined starting from initial amounts of soil, cement, water and foam. These properties are time dependent due to progress of hydration; time evolution is taken into account by means of the amount of non-evaporable water which increases with time. The mix design method and parameters adopted in this experimental study have been described. The parameter n_f, defined as the ratio between the volume of foam and theoretical volume of material has been introduced; it can be considered as a theoretical porosity induced by foam which can be different from the actual value because of bubbles breakage upon mechanical mixing. Thus, a method to correct bulk properties after volume of foam reduction has been presented. Finally, materials (i.e. soil, cement, foam), mixtures and experimental procedures used in this study have been described. Mixtures were prepared starting from two different clayey soils, namely Speswhite kaolin and Caposele soil. A commercial limestone Portland cement was used as a cementitious material, whereas foam was produced with an industrial foam generator with a commercial surfactant solution. Samples were prepared following the lightweight cemented soil method, as schematically described in Figure 1-1.

References

Horpibulsuk, S., Suddeepong, A., Chinkulkijniwat, A., Liu, M.D., 2012. Strength

and compressibility of lightweight cemented clays. Appl. Clay Sci. 69, 11–21. https://doi.org/10.1016/j.clay.2012.08.006

Koumoto, T., Houlsby, G.T., 2001. Theory and practice of the fall cone test. Géotechnique 51, 701–712. https://doi.org/10.1680/geot.2001.51.8.701

Marzano, I.P., 2017. Soil Mixing. Tecnologie esecutive, applicazioni, progetto e controlli, Argomenti di ingegneria geotecnica. Hevelius.

Teerawattanasuk, C., Voottipruex, P., Horpibulsuk, S., 2015. Mix design charts for lightweight cellular cemented Bangkok clay. Appl. Clay Sci. 104, 318–323. https://doi.org/10.1016/j.clay.2014.12.012

Tsuchida, T., Egashira, K., 2004. The Lightweight Treated Soil Method: New Geomaterials for Soft Ground Engineering in Coastal Areas. CRC Press - Taylor & Francis Group, London.

6. Mineralogical and microstructural tests

The results of mineralogical and microstructural tests carried out on mixtures presented in 5.3.4 are shown in this chapter. XRD, MIP and TGA were performed at University of Cassino and southern Lazio whereas SEM analyses were carried out at *Institut des Matériaux Jean Rouxel* (IMN) of University of Nantes. A brief description of these methods is given in Appendix B. Tests were carried out on freeze dried samples at different curing times to study the evolution due to progress of hydration; in order to identify the specific sample, the suffix "_td" is adopted, where ("t" is the curing time and "d" refers to "days"). Samples were freeze dried at the specific curing time before performing the tests to stop reactions.

6.1. XRD[2]

X-ray diffraction patterns of non-treated and treated kaolin at increasing curing time are shown in Figure 6-1. Comparing non-treated and cemented kaolin, new reflections are detected in treated samples at very early stages (24 h of curing). These reflections are attributed to formation of portlandite deriving by cement hydration processes, as explained in paragraph 3.1.1. The intensities of these peaks decrease with increasing curing time, suggesting the partial consumption of portlandite over time, consistent with pozzolanic reactions (3.1.1).

This consumption is accompanied by a progressive dissolution of kaolinite, muscovite and calcite. New peaks corresponding to calcium mono-carboaluminate hydrate ($C_4A\bar{C}H_{11}$) are detected after 28 days of curing. Peak intensities of new hydrates increase with curing time.

In Figure 6-2, X Ray diffraction patterns of cement, non-treated kaolin and lightweight cemented samples at increasing curing times are represented. Foam seems not to alter the chemo-mineralogical evolution of the system, both in terms of formed and dissolved phases over time.

[2] X-ray analyses were performed using a Brucker AXS D8 Advance Diffractometer with CuKα (λ = 0.154 nm) radiation and a step size of 0.021°. The diffraction angle, 2θ, is the angle between the diffracted beam and the transmitted beam.

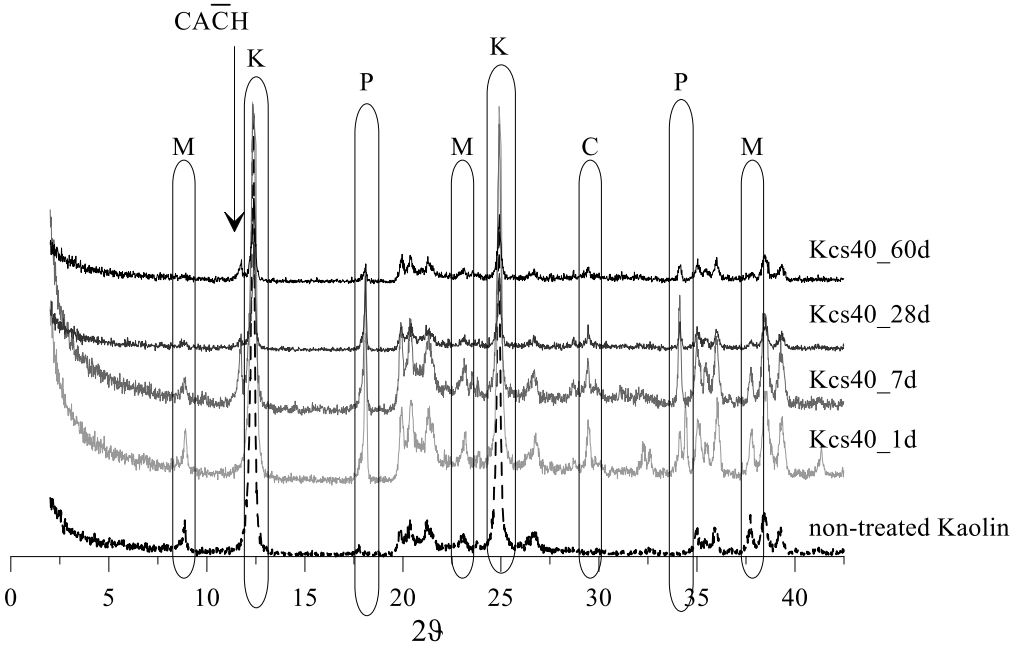

Figure 6-1. X Ray diffraction patterns of non-treated and cemented kaolin (Kcs40) at different curing times. C, K, P, M refer to calcite, kaolinite, portlandite and muscovite, respectively.

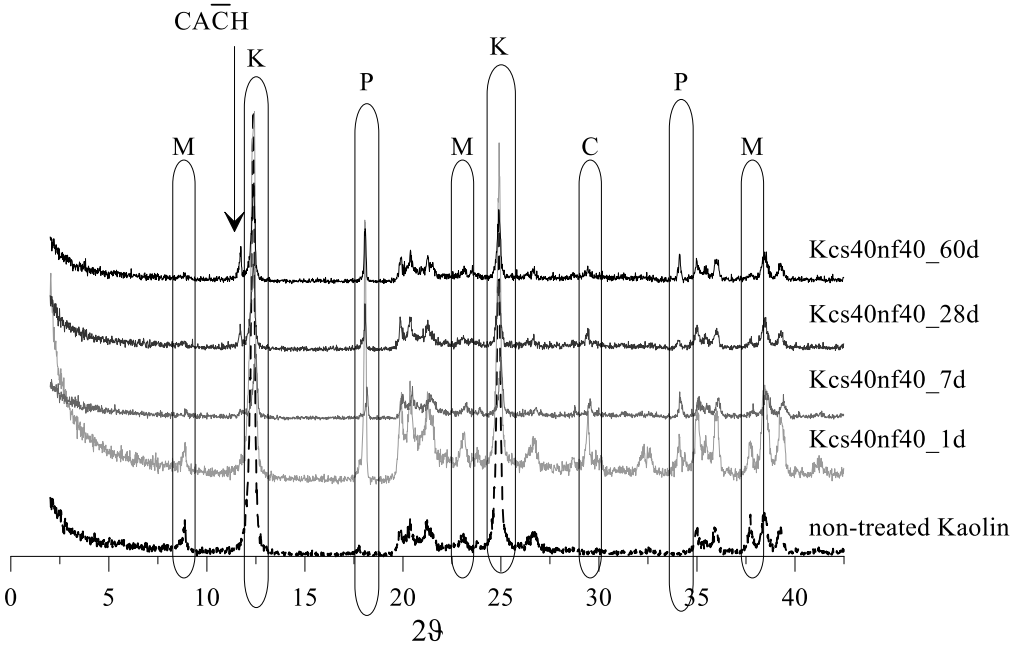

Figure 6-2. X Ray diffraction patterns of non-treated and lightweight cemented kaolin (Kcs40nf40) at different curing times. C, K, P, M refer to calcite, kaolinite, portlandite and muscovite, respectively.

6.2. TGA[3]

The quantitative interpretation of thermogravimetric analyses can be used to study the progress of hydration. Indeed, as shown in paragraph 3.1.1.1, mass loss can be associated to decomposition of specific phases.

In Figure 6-3 TGA and DTG on non-treated kaolin, anhydrous cement and grout ($w_c/c = 0.5$), are presented. Significant weight loss observed on Speswhite kaolin (dotted line), in the range 500 °C - 600 °C is due to dehydroxylation of kaolinite and muscovite. The anhydrous cement (dashed line) is characterized by a significant mass loss between 700 to 900 °C, typical of $CaCO_3$ dissolution. This amount is consistent with the cement adopted (limestone Portland cement) which can be characterized by a percentage by mass of $CaCO_3$ up to 20 % (section 5.3.2). The TGA analysis on grout shows that a significant mass loss occurs below 350 °C related to dehydration of hydrate products. Between 400 and 500 °C, a significant mass loss related to portlandite decomposition is observed, with a peak of mass loss rate at 450 °C. It is noteworthy that ranges of temperature in which kaolinite and portlandite decomposition occurs slightly overlap; the rate of mass loss of Portlandite becomes negligible above 500 °C, whereas a significant rate is observed for Kaolinite right below 500 °C. However, at 500 °C, most of portlandite is decomposed.

In Figure 6-4 a comparison between thermogravimetric analyses performed at different curing times on Kcs40 is represented. The mass loss between 100 and 350 °C (absent in kaolin) is related to cement hydration products, which increase with curing time. Due to partial overlap of kaolinite and portlandite, the peak of portlandite cannot be appreciated. However, at increasing curing time, a slight reduction of portlandite mass loss is detected, which is consistent with XRD results. Similar results are found for Kcs40nf40, as reported in Figure 6-5.

[3] Thermo-gravimetric analyses were performed, with a Netzsch STA 449F3 Jupiter, equipped with a mass spectrometer. Finely ground sample was heated at a rate of 10 °C min^{-1}, under argon atmosphere, from ambient temperature to 1000 °C. The Netzsch Proteus software has been used to process the results, represented as percentage of total weight loss versus temperature (thermogravimetric curve), or rate of loss versus temperature (differential thermogravimetric curve).

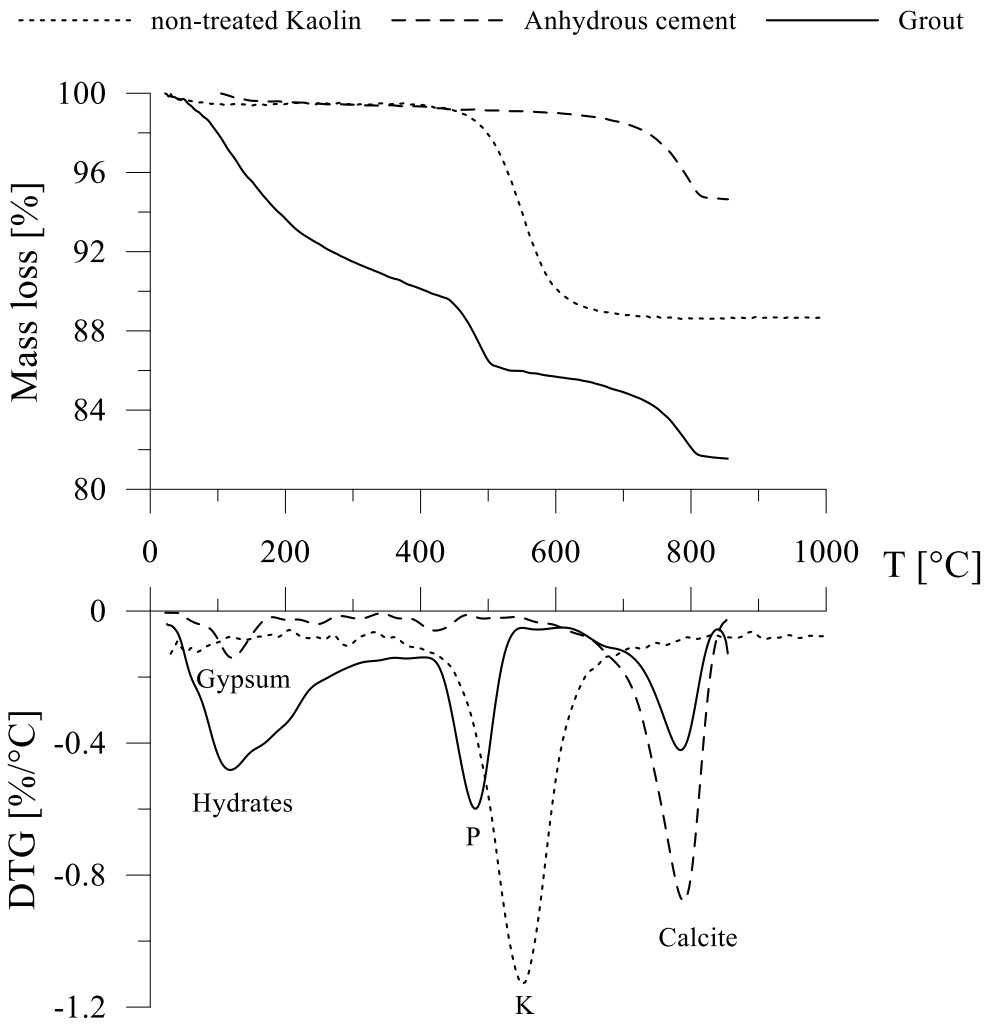

Figure 6-3. Thermogravimetric analyses on anhydrous cement (CEM II/A LL 42.5R), Speswhite kaolin and cement grout (w_e/c=0.5); P and K refer to Portlandite and Kaolinite, respectively.

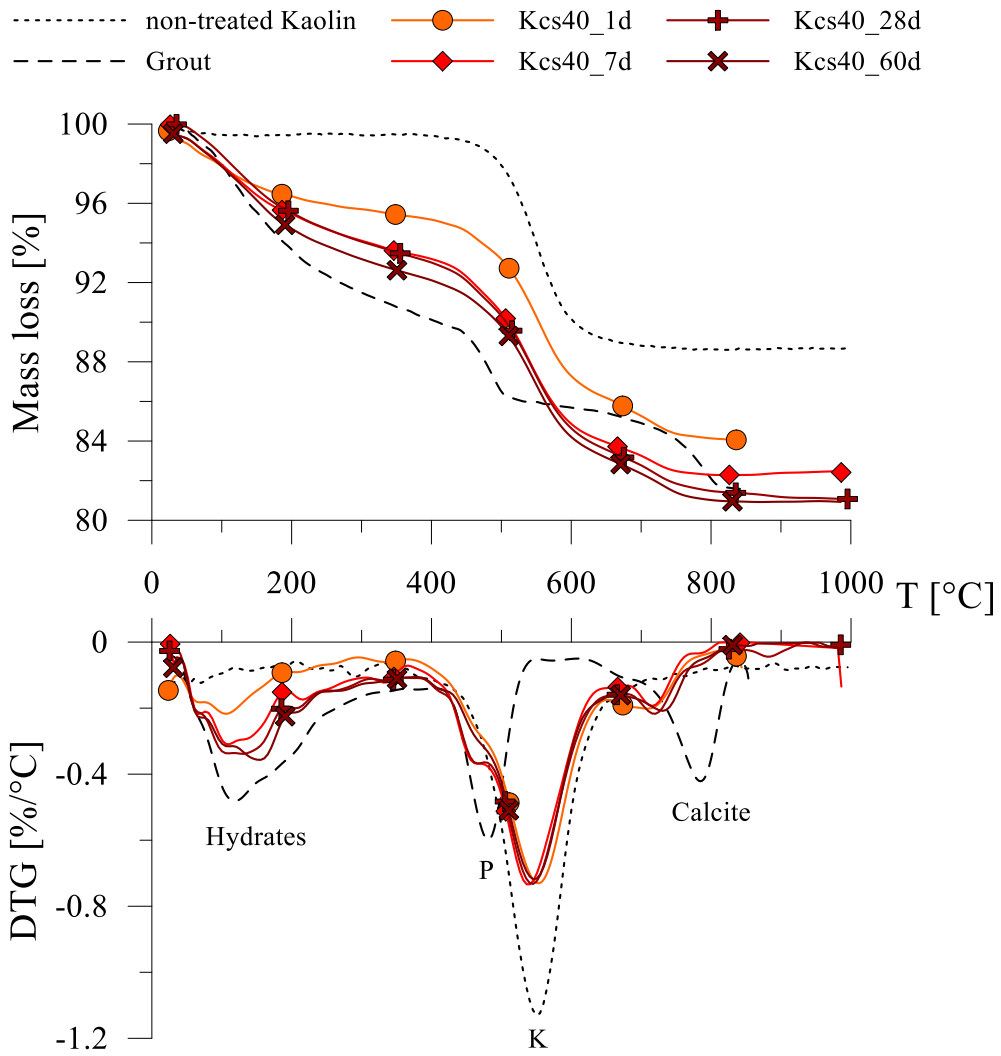

Figure 6-4. Thermogravimetric analyses on Kcs40 at different curing times; Speswhite kaolin (dotted line) and cement grout (dashed line) are also reported; P and K refer to Portlandite and Kaolinite, respectively.

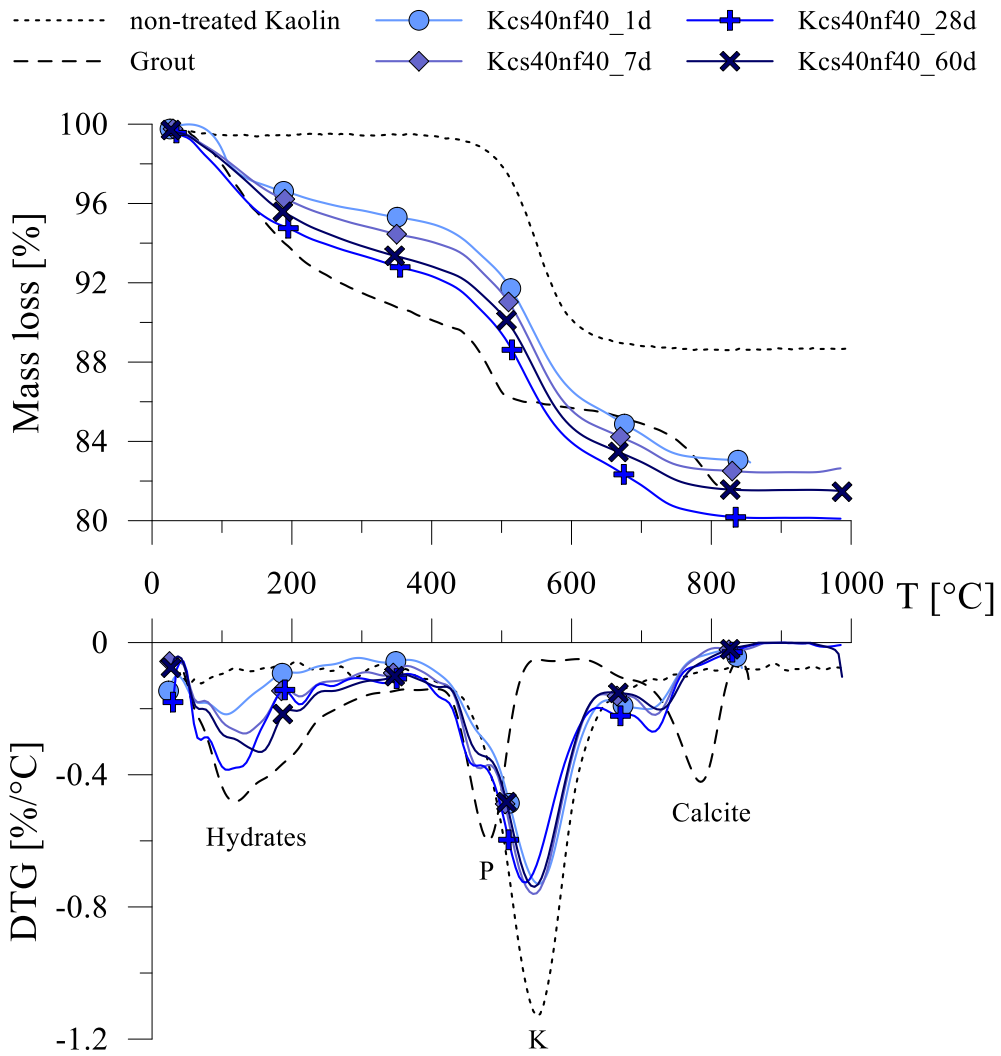

Figure 6-5. Thermogravimetric analyses on Kcs40nf40 at different curing times; Speswhite kaolin (dotted line) and cement grout (dashed line) are also reported; P and K refer to Portlandite and Kaolinite, respectively.

6.2.1. Quantitative analyses of TGA

Quantitative interpretations of TGA are represented in Figure 6-6. Neglecting the influence of kaolinite dehydroxylation, the amount of mass loss between 390 and 500 °C can be related to decomposition of portlandite. A gradual consumption of portlandite is observed after 7 days of curing, consistent with XRD results shown in Figure 6-1 and Figure 6-2.

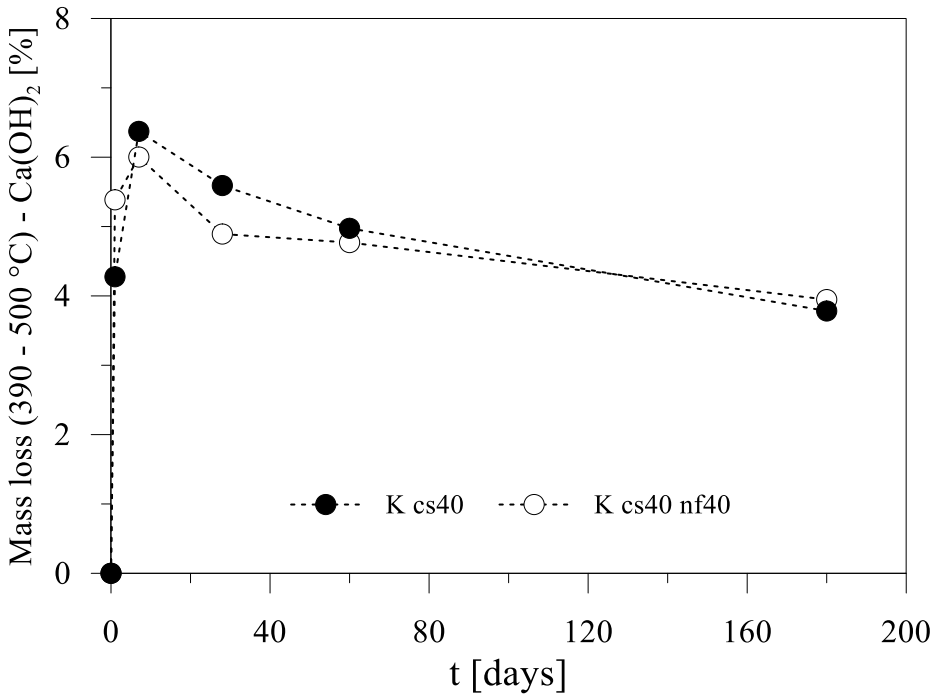

Figure 6-6. Evolution of portlandite with curing time by quantitative interpretation of TGA analyses on Kcs40 and Kcs40nf40.

As stated in 3.1.6 for the cement paste, the amount of non-evaporable water $W_{w\ n\text{-}ev}$ can be derived from the results of a thermogravimetric analysis. In the hypothesis that non-evaporable water is the water combined in gel and, more generally, in products of hydration, mass loss of non-evaporable water occurs between 110 and 350 °C. This amount can be determined as the ratio between the weight loss in the fixed range of temperature and the weight at 110 °C. However, standard procedures consider the weight of solid phase, W^s, as the oven dried weight at 105 °C. Then, assuming a slightly different range of temperature, the mass loss due to hydrates dehydration, i.e. the mass loss of non-evaporable water, is:

$$\frac{W_{w\ n-ev}}{W^s} = w_{n-ev} \cong \frac{Weightlossin(105° - 350°)}{Weight(105°)} \qquad (6\text{-}1)$$

where $w_{n\text{-}ev}$ can be regarded as the water content of non-evaporable water. It is worth noting that this amount of water is not free water but part of the solid phase. Results of tests on treated kaolin with c/s=0.4 are represented in Figure 6-7.

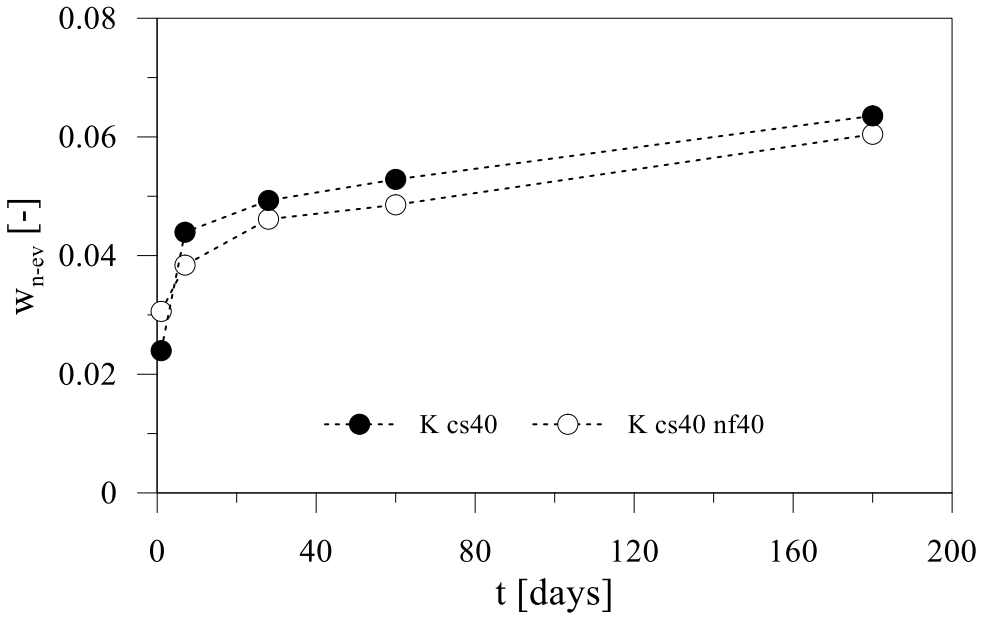

Figure 6-7. Evolution of the amount of non-evaporable water in time of treated kaolin.

Except for t=1 day, the non-evaporable water seems to be slightly higher in the sample without foam. However, there is a very slight difference and the trend is almost the same. The addition of foam seems to not affect significantly the products of hydration, as already observed in XRD.

These data can help to determine physical properties of soil. Indeed, to use equations reported in 5.1, it is necessary to determine the evolution of αx with curing time, that is the ratio between the amount of non-evaporable water and the amount of anhydrous cement (6-1). The non-evaporable water $w_{n\text{-}ev}$ can be expressed as a function of αx and c/s. Equation (6-2) can be verified by multiplying both members of the first expression by the weight of solid soil.

$$\alpha x = \frac{W_{w\ n-ev}}{W_{c,a,h}} \frac{W_{c,a,h}}{W_{c,a}} = \frac{W_{w\ n-ev}}{W_{c,a}} \tag{6-1}$$

$$w_{n-ev} = \frac{\frac{c}{s}\alpha x}{\frac{c}{s}(1+\alpha x)+1} \Rightarrow \alpha x = \frac{w_{n-ev}\left(1+\frac{c}{s}\right)}{(1-w_{n-ev})\frac{c}{s}} \tag{6-2}$$

The product αx was calculated for Kcs40 and Kcs40nf40 at 1, 7, 28, 60 and 180 days of curing. In the hypothesis that the chemo-physical evolution is the same for both lightened and non-lightened materials, all data were used to fit an analytical expression; logarithmic and bi-logarithmic expressions were proposed.

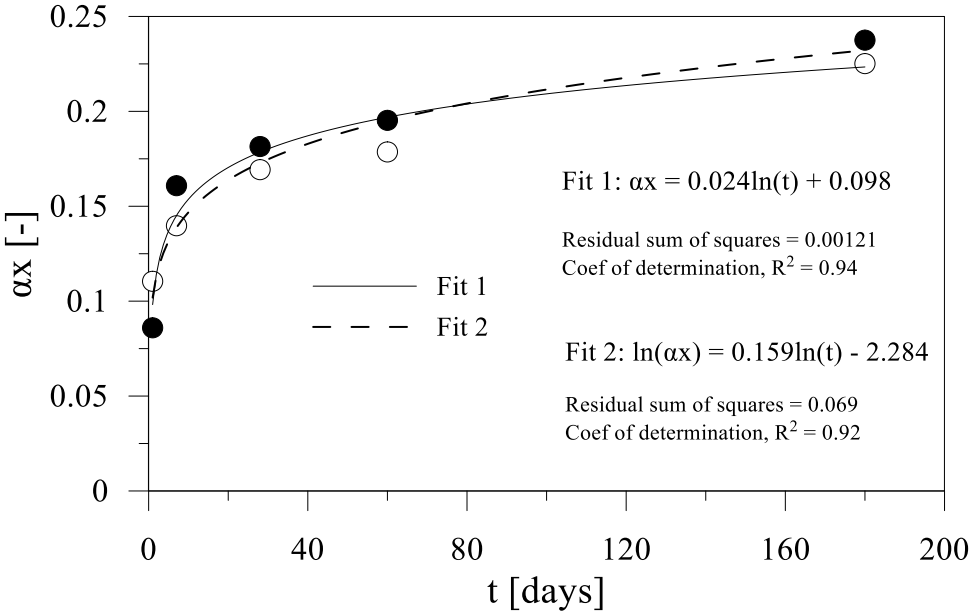

Figure 6-8. Evolution of αx with time and best fit of data.

The logarithmic function seems to fit slightly better the data. Both cannot be applied for t=0, and the logarithmic function gives negative values for time below half an hour; however, no data are available below 1 day of curing.

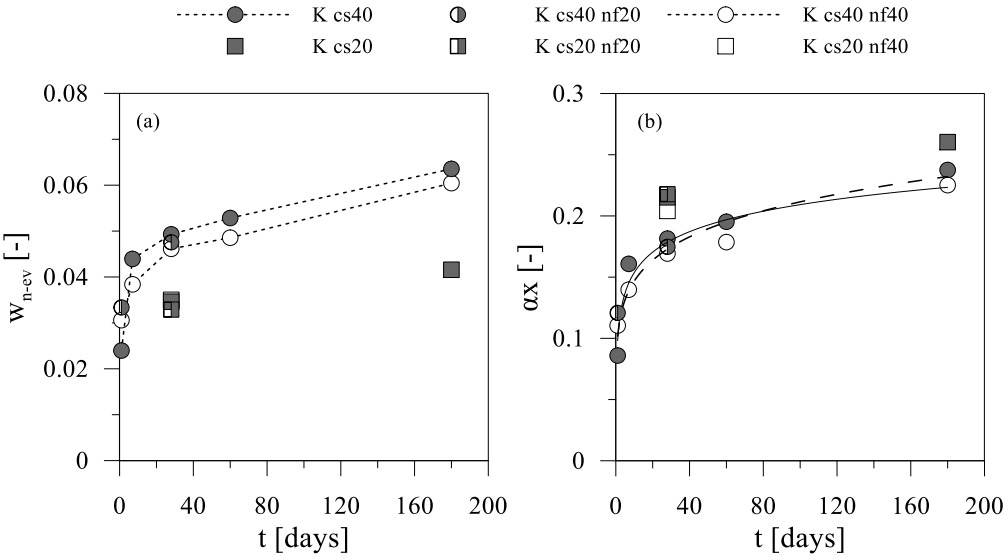

Figure 6-9. Evolution of (a) non-evaporable water and (b) αx with curing time on cemented and lightweight cemented kaolin.

A summary of the results of TGA tests performed on other mixtures is represented in Figure 6-9. Results on Kcs40nf20 samples are in accordance with results on Kcs40 and Kcs40nf40. The amount of non-evaporable water (Figure 6-9a) obtained on Kcs20, Kcs20nf20 and Kcs20nf40 samples is lower than

observed in Kcs40. This is due to the lower amount of cement and it doesn't depend on a slower kinetic. Indeed, looking at Figure 6-9b, the value of αx is also higher than samples treated at a cement factor, c/s, equal to 40%.

6.3. MIP[4]

Microstructural features of cemented and lightweight cemented samples have been investigated by means of Mercury Intrusion Porosimetry (MIP). Pore size distribution curves of cement treated samples at increasing curing times (i.e. 1, 28 and 60 days) are shown in Figure 6-10.

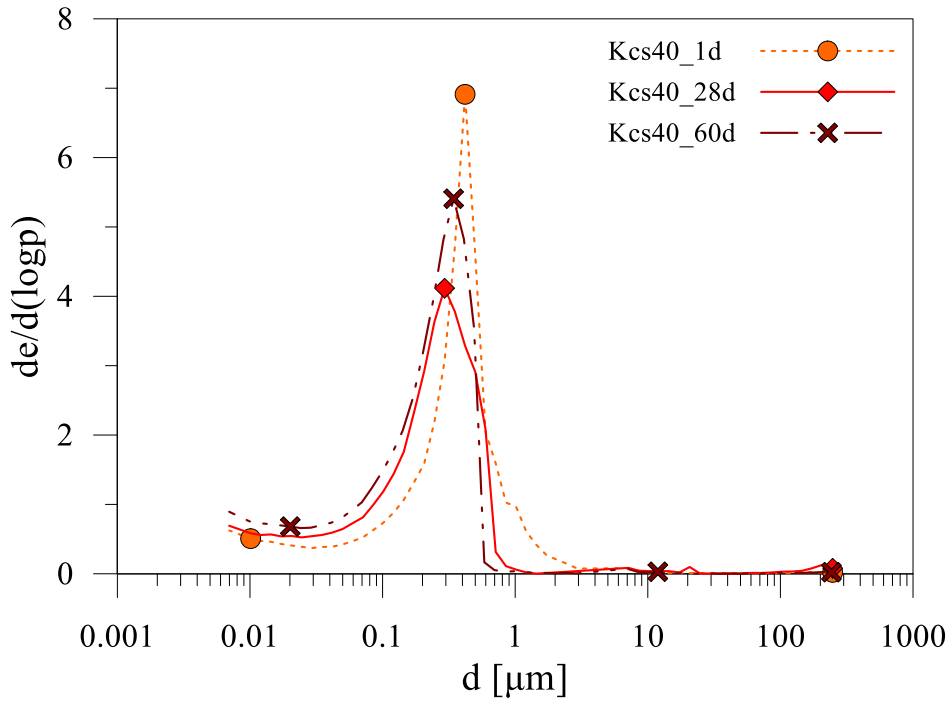

Figure 6-10. MIP on Kcs40 samples at different curing times (1, 28 and 60 days).

Pore size distribution of cement treated samples is characterised by the most frequent class of pores with modal pore diameter ranging between 0.2 µm - 0.4 µm, with slight evolution over time; in the smallest pore range (i.e. entrance pore diameters <0.2 µm), an increase of frequency is observed over curing time. A

[4] MIP tests were by a double chamber Micromeritics Autopore III apparatus. In the filling apparatus (dilatometer) samples were outgassed under vacuum and then filled by mercury allowing increase of absolute pressure up to ambient one. The detected entrance pore diameters range between 134 µm and 7.3 µm (approximately 0.01 MPa - 0.2 MPa for a mercury contact angle of 139°). After depressurisation to ambient pressure, samples were transferred to high-pressure unit, where mercury pressure was increased up to 205 MPa following a previously set intrusion program.

reverse trend is detected for largest pores (i.e. entrance pore diameters > 0.5 µm), with a decrease of frequency of pores as curing time increases, until a complete disappearance of the pore class at 60 days of curing. Pore size distributions of lightweight cemented samples at 1, 28 and 60 days of curing have been compared with those of cement treated samples as shown in Figure 6-11, Figure 6-12 and Figure 6-13.

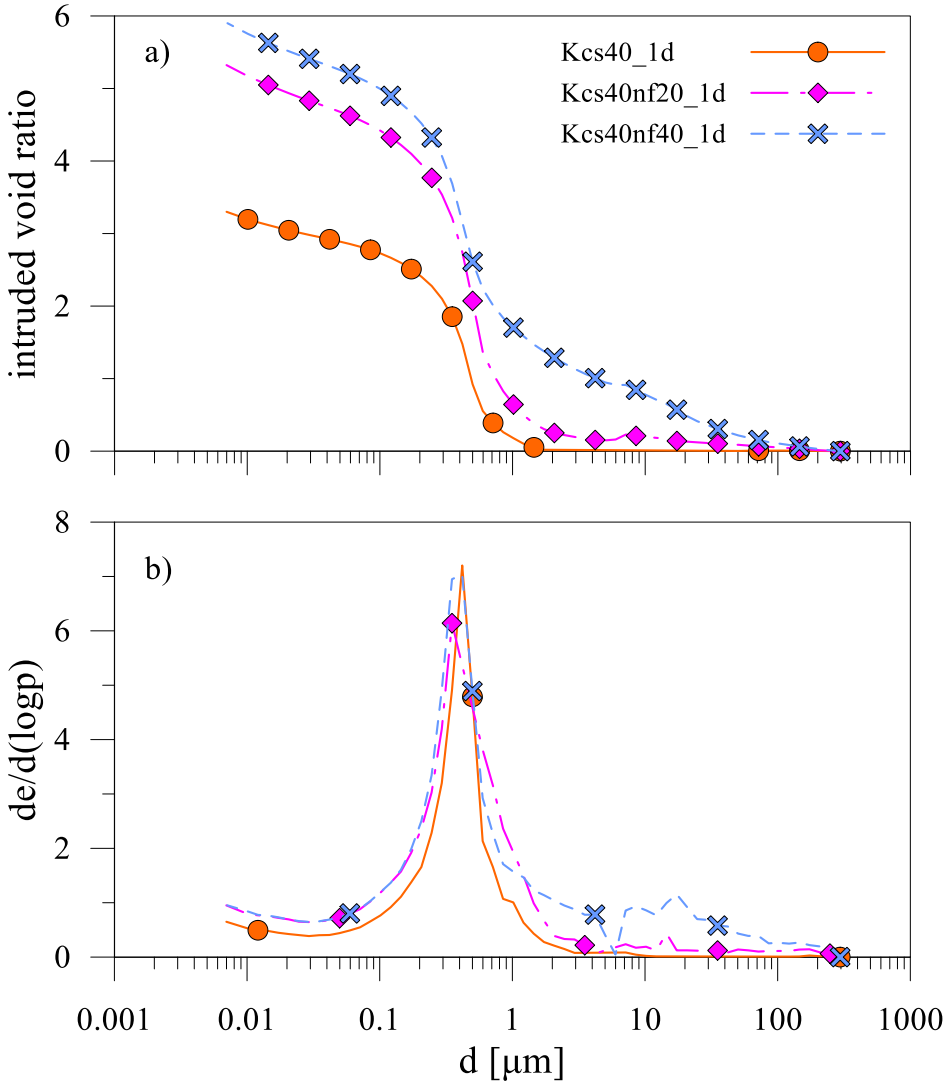

Figure 6-11. (a) Cumulative intruded volumes and (b) pore size distributions of Kcs40 (cemented kaolin), Kcs40nf20 and Kcs40nf40 (lightweight cemented kaolin) after 1 day of curing.

An increase of cumulative intruded mercury volume is observed as air foam content increases, regardless of curing time (Figure 6-11a, Figure 6-12a, Figure 6-13a). Addition of air foam does not modify the modal pore size of cement

treated samples (ranging between 0.2 µm - 0.4 µm). An increase of frequency of pores larger than 0.5 µm is detected for lightweight cemented samples.

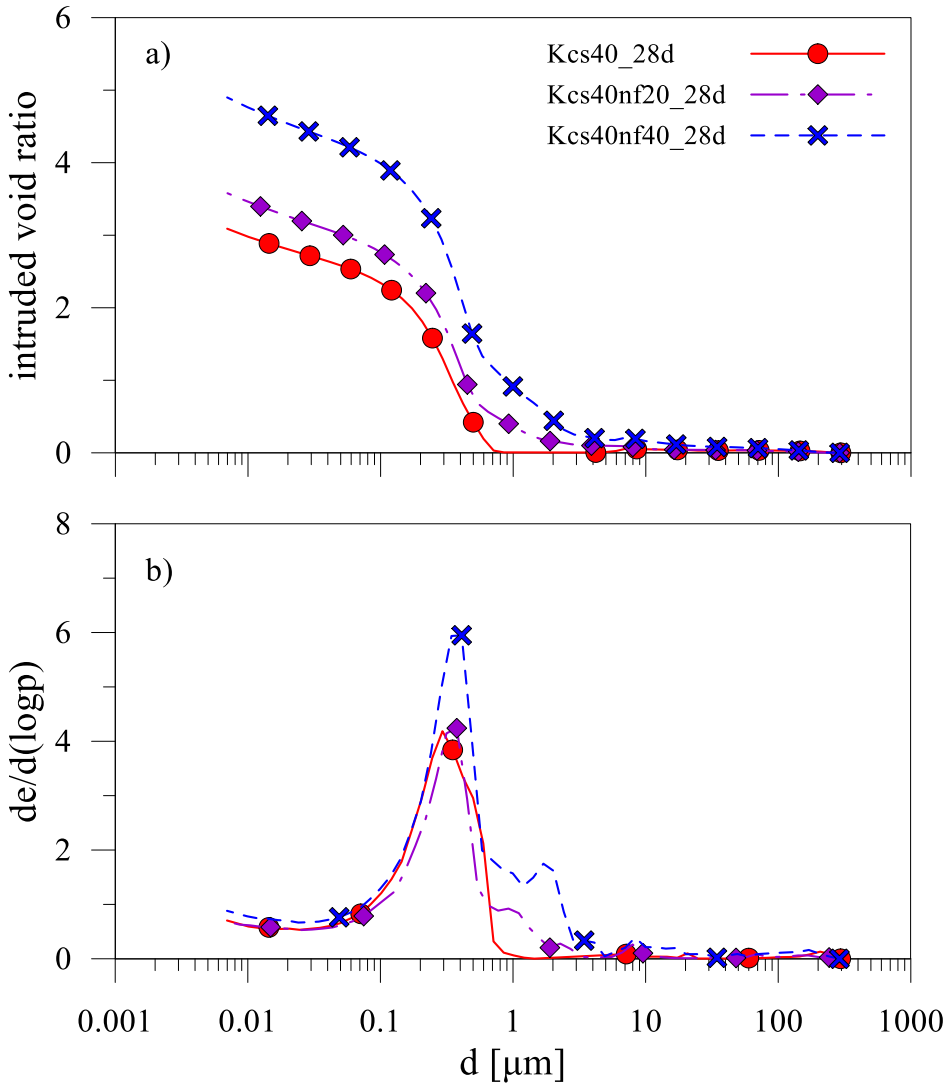

Figure 6-12. (a) Cumulative intruded volumes and (b) pore size distributions of Kcs40 (cemented kaolin), Kcs40nf20 and Kcs40nf40 (lightweight cemented kaolin) after 28 days of curing.

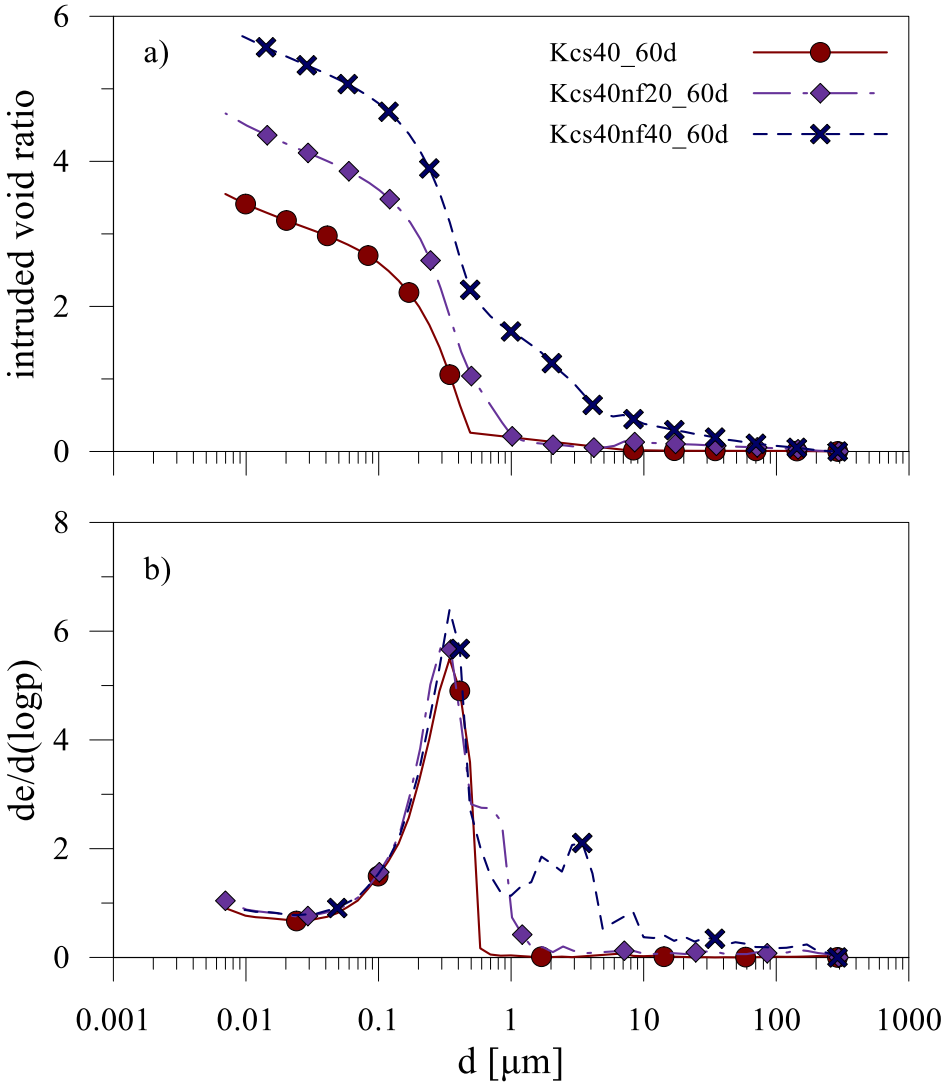

Figure 6-13. (a) Cumulative intruded volumes and (b) pore size distributions of Kcs40 (cemented kaolin), Kcs40nf20 and Kcs40nf40 (lightweight cemented kaolin) after 60 days of curing.

6.4. SEM[5]

SEM observations of non-treated kaolin and cement treated samples (Kcs40) at increasing curing times (i.e. 1 and 60 days of curing) are shown in Figure 6-14.

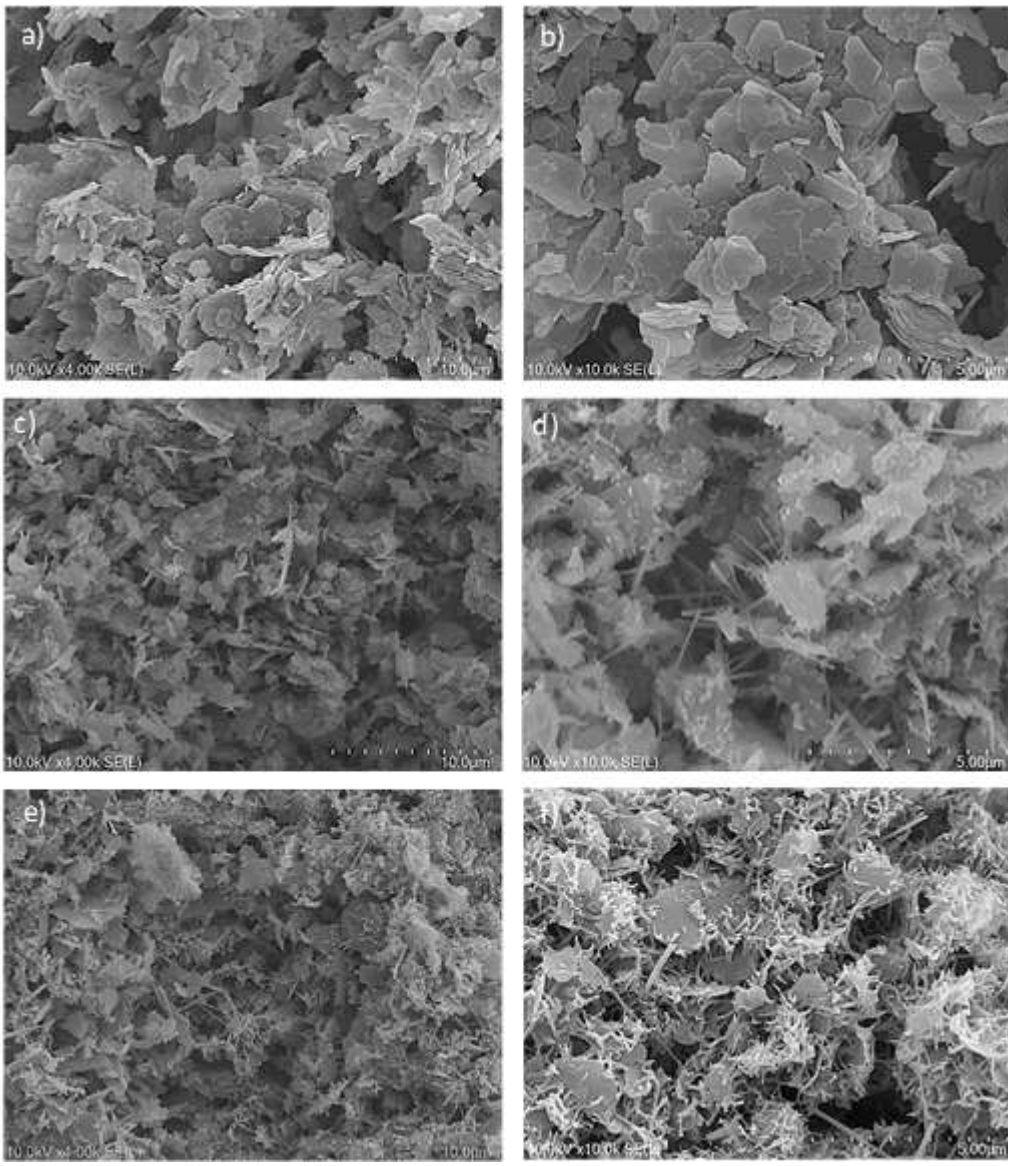

Figure 6-14. SEM observations on non-treated kaolin (a, b) and cement treated sample (Kcs40 - c, d: 24h of curing; e, f: 60 days of curing)

[5] SEM were performed via SU5000 Hitachi Scanning Electron Microscopy at *Institut des Matériaux Jean Rouxel (IMN)* of University of Nantes. A gold coating of the samples has been performed before SEM observations.

The effects of cement addition are clearly observed since the very short term (i.e. 24h of curing), with kaolinite particles embedded into C-S-H gel. At longer curing time (i.e. 60 days) a well-connected matrix of hydrates and particles is detected (Figure 6-14c). SEM micrographs performed at higher magnifications allow an insight into microstructural features of cement treated sample after 60 days of curing (Kcs40), as shown in Figure 6-15, where the presence of C-S-H network and crystals of portlandite, even if partially dissolved and transformed into hydrates, are clearly identified (Figure 6-15a, b, c). New formation of aluminate hydrates is also detected (Figure 6-15d).

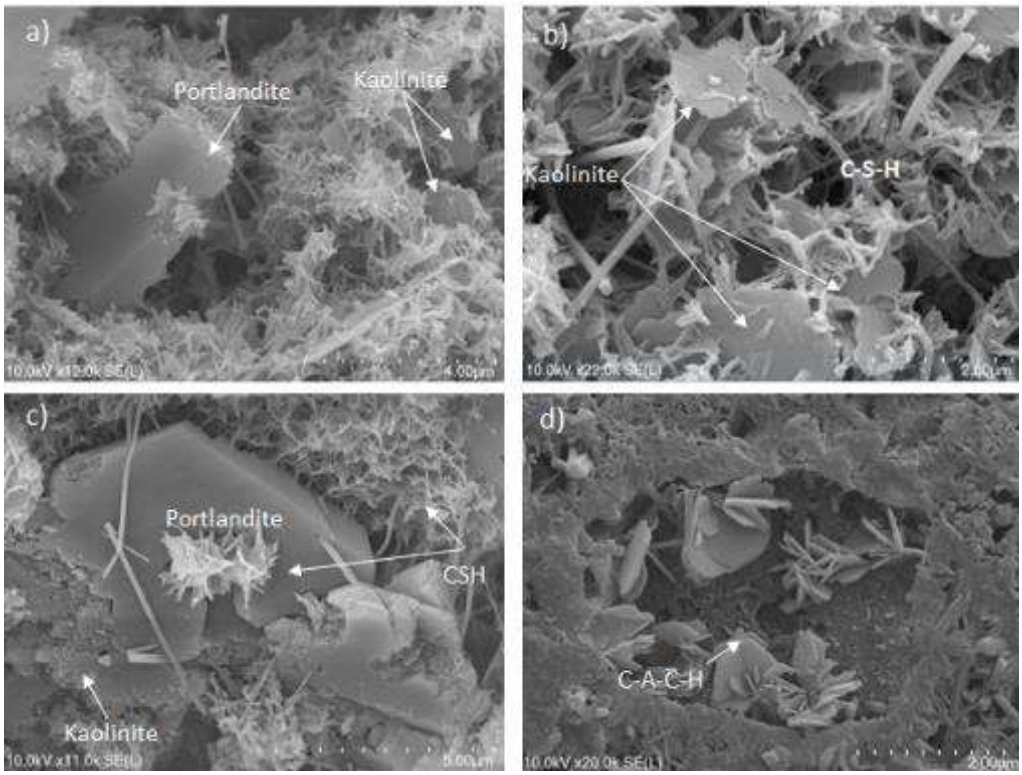

Figure 6-15. SEM observations on Kcs40 (cement treated sample) at 60 days of curing.

SEM observations of cement treated and lightweight cemented samples at 60 days of curing are compared in Figure 6-16. Soil matrix is made of arrangement of kaolinite particles or group of particles, embedded in a network of C-S-H phases. No significant changes of soil matrix for both cement treated and lightweight cemented samples are observed, regardless of air foam content.

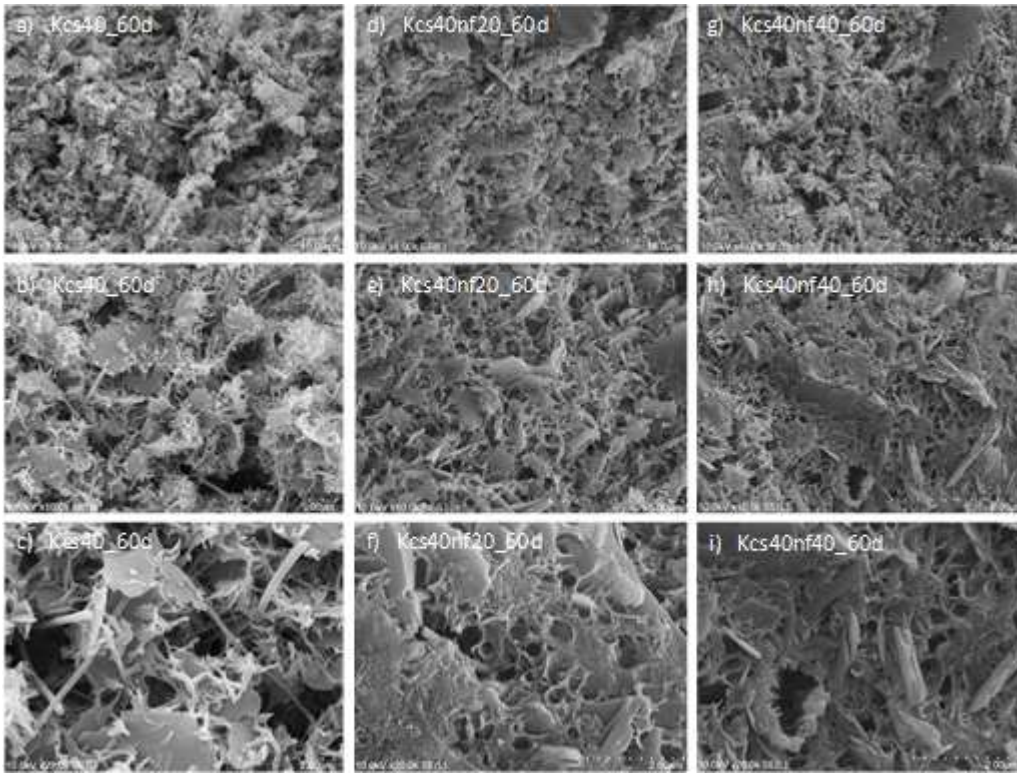

Figure 6-16. SEM observations on Kcs40 (a, b, c), Kcs40nf20 (d, e, f) and Kcs40nf40 (g, h, i) after 60 days of curing.

An insight into the effects of foam on soil-cement-water system with respect to distribution and size of voids is shown in Figure 6-17, Figure 6-18 and Figure 6-19, where SEM observations of lightweight cemented samples, namely Kcs40nf20 and Kcs40nf40 at 60 days of curing are respectively reported. At lower magnification (Figure 6-17), the effect of air foam is clearly evidenced by footprint of air bubbles on the lightweight samples surface as consequence of matrix displacement during mixing, whose extent and frequency increase as air foam content increases.

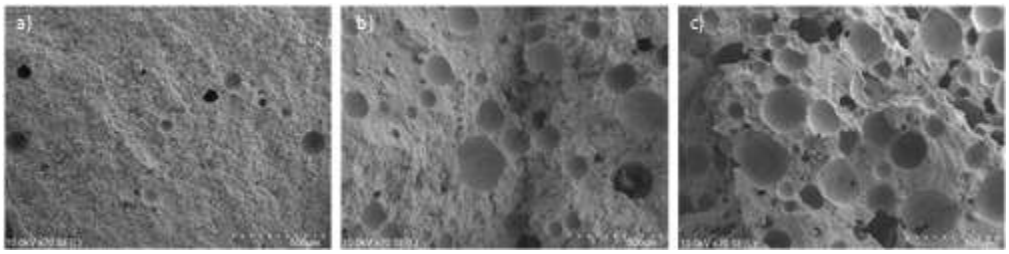

Figure 6-17. SEM observations on Kcs40 (a), Kcs40nf20 (b), Kcs40nf40 (c) after 60 days of curing.

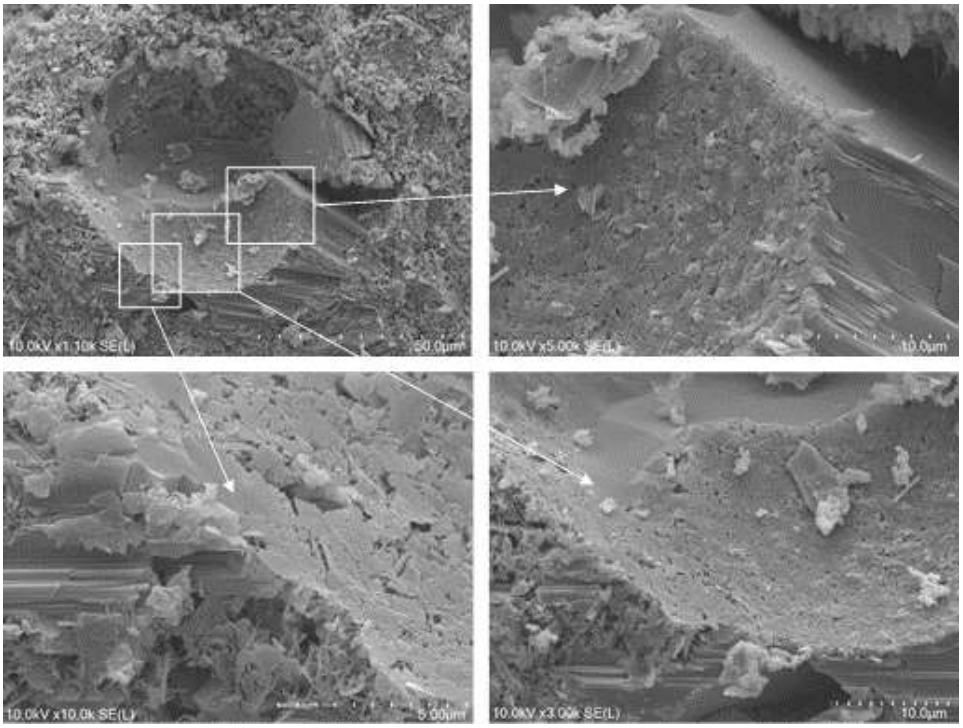

Figure 6-18. SEM observations on Kcs40nf40 (lightweight cemented samples) at 60 days of curing time: details of air bubble footprint surface.

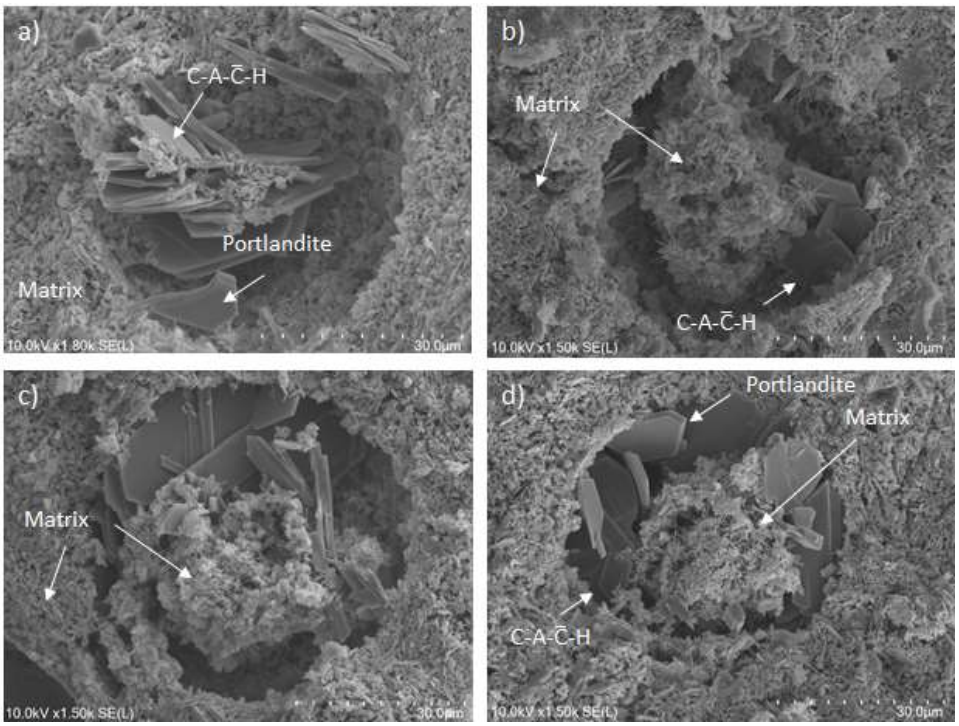

Figure 6-19. SEM observations on Kcs40nf40 (lightweight cemented samples) at 60 days of curing: details of air bubbles filled by portlandite and cement hydrates.

Soil matrix forms the sub-spherical limit surface of air bubbles footprints, as shown in Figure 6-18. Precipitation of portlandite crystals and hydrated phases inside air bubble footprints is frequently observed (Figure 6-19). Cavities of different shape, also smaller than footprints of air bubbles, are often detected in the soil matrix and filled by precipitation of aluminate hydrates and portlandite as in Figure 6-20.

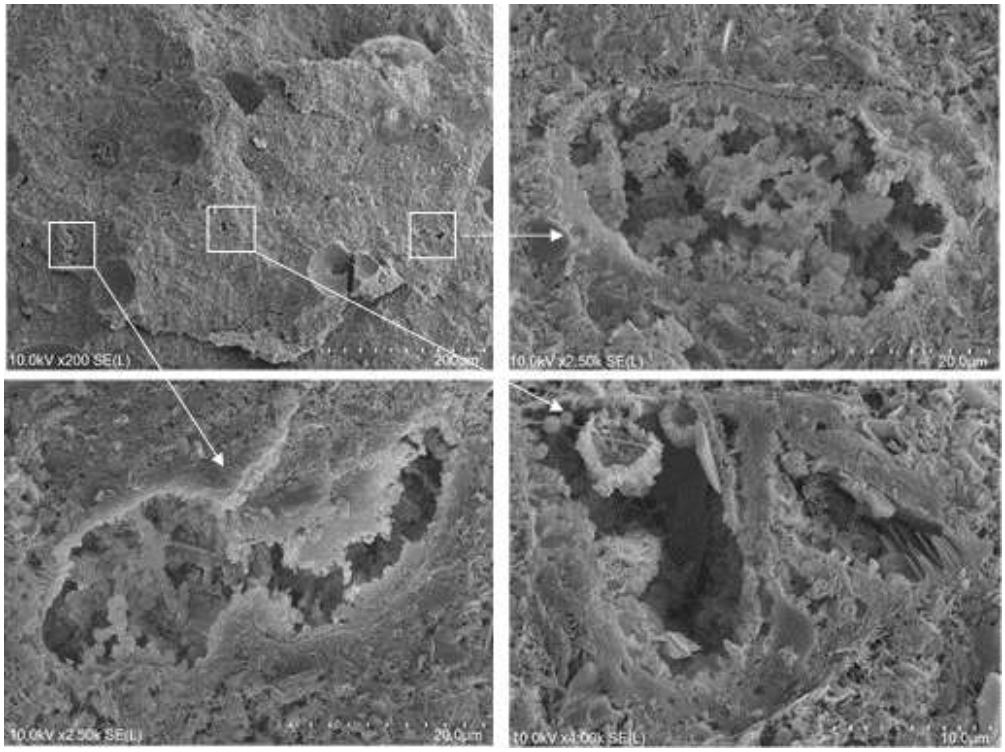

Figure 6-20. SEM observations on Kcs40nf40 (lightweight cemented samples) at 60 days of curing: details of cavities filled by portlandite and cement hydrates.

6.5. Discussion

Chemo-physical evolution of treated samples, regardless of foam addition, is ruled by hydration of cement and pozzolanic reactions. Indeed. addition of foam to soil – cement - water system does not alter chemo-physical evolution of treated samples. Precipitation of portlandite and progressive formation of cementitious gel compounds since the very short term (i.e. 24 hours of curing) have been clearly detected by XRD and TGA analyses. At increasing curing time, a gradual consumption of formed portlandite and progressive dissolution of clay minerals (i.e. kaolinite and muscovite) seems to be consistent with development of pozzolanic reactions. Calcite in anhydrous cement represents a further reacting component during hydration and pozzolanic reactions, as confirmed by formation of carboaluminate phases, i.e. calcium monocarboaluminate (Figure 6-1).

Effects of chemo-physical evolution on microstructural features of cement treated soil have been highlighted by MIP results. Modal pore size seems slightly shifted towards smaller sizes because of formation of a well-connected network of hydrates over time, which increases small pores frequency and contributes to the progressive decrease of pore frequency between 0.6 – 4 μm.

SEM images confirm MIP results interpretation (Figure 6-14), showing kaolinite particles embedded into C-S-H network since early curing times (i.e. 24h). At longer curing time (i.e. 60 days), it is clearly visible that this well-connected network of hydrates fills the space left around kaolinite particles or groups of particles (Figure 6-15).

Bubbles constituting foam, and the surrounding surfactant layers, are able to displace and sustain the soil-cement slurry matrix upon mixing. Addition of foam introduces air in the system included in bubbles of different sizes. Air bubbles remaining stable over cement setting and matrix hardening are responsible of increase of porosity of lightweight cemented samples. Due to matrix (i.e. soil-cement hydrates) hardening, the space left by air in the bubbles is preserved from collapse under matrix overburden. This is consistent with large footprints clearly detected by SEM observations (Figure 6-17). By inspecting the footprints surface, soil matrix is clearly visible with its characteristic pore size distribution, being pores in the small range as well as modal pore size slightly affected by air foam content regardless of curing time.

As shown by MIP analyses, footprints of air bubbles on sample surface are not detected when their size is over the maximum size detectable by MIP (i.e. diameter >300 μm); conversely, bubbles inside the samples (not directly connected with sample surface) can be detected only through the connected smaller pores belonging to soil matrix if accessible from the outer surface of samples. In this case, cumulative curves of intruded mercury show an increase of intrusion corresponding to the modal size of soil matrix, highlighting the volume filling of internal bubbles, and justifying the overall higher porosity of the samples. This mechanism is consistent with MIP results also in terms of pores frequency, which show a similar modal size of the lightweight cemented samples regardless of the foam content, being this distribution characteristic of the matrix. The higher frequency of larger voids (i.e. bubbles, cavities or pores) is ruled by the amount of foam added to the system. The subsequent reduction of larger pores at increasing curing time (i.e. pore entrance diameters between 10 mm and 250 μm), more evident for samples with higher amount of foam (i.e. Kcs40nf40),

depends on the chemo-physical evolution of the soil system, due to the precipitation of hydrates filling the available space in the voids.

7. Physical and mechanical properties of treated samples

Physical characterization and mechanical tests were performed at different curing times to study the effects of chemo-physical evolution of clay-cement-water system on properties of treated soils. A brief description of tests, performed in geotechnical laboratory of University of Naples Federico II, is given in Appendix B.

7.1. Speswhite kaolin

7.1.1. Bulk properties

7.1.1.1. Cemented kaolin

A summary of the mechanical tests performed on cemented kaolin is shown in Table 7-1. As for microscale, tests were carried out at different curing times to study the effect of chemical evolution on mechanical properties; in order to identify the specific sample, the suffix "_td" is adopted, (where "t" is the curing time and "d" stays for "days"). Oedometric tests are identified by suffix "_oed". The other samples refer to direct shear tests; being the majority, for simplicity they are only identified by confining stress at which they are performed, by means of the suffix "_ZkPa" (where Z is the confining stress). For example, cemented kaolin sample with c/s=20% after 7 days of curing tested in direct shear at a confining stress of 100 kPa is "Kcs20_7d_100kPa". The column "t" refers to the curing time at which test was performed, while σ'_v refers to the normal stress applied. Bulk density and dry bulk density are also reported for each sample. The former is the bulk density at t=0, i.e. at time of mixture preparation. The average values for Kcs20 and Kcs40 mixtures are 13.7 and 14.1 kN/m^3, respectively, which are similar to theoretical bulk weight, 13.8 and 14.2 kN/m^3 reported in 5.3.4.

Dry density was determined as the ratio of the oven dry weight of sample after test and volume before test was performed. It refers to a specific time, because dry density grows up slightly along with the progress of hydration, which reduces water content and by consequence the volume of pores.

The specific gravity of cemented kaolin with c/s=40% was determined according to ASTM D854. It was 26 kN/m^3, approximately equal to specific gravity of non-treated soil; this confirms the result of (5-43). Assuming this value as constant in time, void ratio can be determined for each sample[6].

[6] According to theoretical equations, specific gravity of cemented soil slightly decreases with time due to progress of hydration.

Table 7-1. Summary of direct shear tests performed on cemented soil.

		t [days]	σ'_v [kPa]	γ [kN/m^3]	γ_{dry} [kN/m^3]	e
K cs20	*Kcs20_7d_50kPa*	7	50	13.5	6.2	3.2
	Kcs20_7d_100kPa	7	100	13.7	6.1	3.2
	Kcs20_7d_150kPa	7	150	13.6	6.2	3.2
	Kcs20_7d_50kPa	28	50	13.9	6.3	3.1
	Kcs20_7d_100kPa	28	100	13.7	6.2	3.2
	Kcs20_28d_150kPa	28	150	13.7	6.3	3.1
	Kcs20_7d_oed	7	-	13.6	6.4	3.1
	Kcs20_28d_oed	28	-	13.6	6.5	3.0
K cs40	*Kcs40_1d_50kPa*	1	50	14.3	-	-
	Kcs40_1d_100kPa	1	100	14.1	6.8	2.8
	Kcs40_1d_150kPa	1	150	14.0	6.5	3.0
	Kcs40_3d_50kPa	3	50	14.1	-	-
	Kcs40_3d_100kPa	3	100	14.0	6.9	2.8
	Kcs40_3d_150kPa	3	150	14.2	6.1	3.3
	Kcs40_7d_50kPa	7	50	14.3	6.8	2.8
	Kcs40_7d_100kPa	7	100	14.0	6.9	2.8
	Kcs40_7d_150kPa	7	150	13.9	6.4	3.1
	Kcs40_14d_50kPa	14	50	14.2	-	-
	Kcs40_14d_100kPa	14	100	13.9	6.8	2.8
	Kcs40_14d_150kPa	14	150	13.9	6.8	2.8
	Kcs40_28d_50kPa	28	50	14.0	6.8	2.8
	Kcs40_28d_100kPa	28	100	14.3	6.7	2.9
	Kcs40_28d_150kPa	28	150	14.1	6.8	2.8
	Kcs40_60d_50kPa	60	50	14.0	6.9	2.8
	Kcs40_60d_100kPa	60	100	14.1	7.0	2.7
	Kcs40_60d_150kPa	60	150	14.0	7.0	2.7
	Kcs40_90d_50kPa	90	50	14.0	7.0	2.7
	Kcs40_90d_100kPa	90	100	14.1	6.9	2.7
	Kcs40_90d_150kPa	90	150	14.0	6.9	2.8
	Kcs40_7d_oed	7	-	14.1	7.1	2.6
	Kcs40_28d_oed	28	-	14.1	7.0	2.7

In section 5.1 theoretical equations to determine bulk properties starting from mix design parameters were derived (5-41). To apply these equations, it is necessary to know αx(t). Two expressions for this function were proposed in section 6.2.1, derived by interpreting thermogravimetric analyses at different curing times. The following expression will be used:

$$\alpha x = 0.024 \cdot \ln(t) + 0.098 \qquad (7\text{-}1)$$

It is worth noting that according to this equation αx is equal to 0.23 at t=245 days. According to Neville (2011), α is around 0.23 for a fully hydrated paste, and 0.23 would be the maximum value of αx (being x at maximum 1). However, hydration can continue to take place, thus α should be greater than 0.23; this is a

limitation of the equation proposed, which was derived from data up to 180 days. Nonetheless, if the equation is regarded as a simplified model to derive physical properties of cemented soil, it can still be applied.

A comparison between theoretical and measured values of dry unit weight and void ratio is shown in Figure 7-1. It can be observed that data are approximately well fitted. Dry unit weight at 7 days for Kcs20 is slightly overestimated (void ratio is underestimated). Data from Kcs40 are well fitted also at higher curing times (60 and 90 days). Dry unit weight at 28 days is slightly underestimated (void ratio overestimated) for the 3 samples tested in direct shear, while Kcs40_28d_oed is well fitted. In terms of dry unit weight, a significant deviation comes only from Kcs40_1d_150kPa, Kcs40_3d_150kPa and Kcs40_7d_150kPa, in which the error is higher than 5% in terms of dry unit weight and void ratio.

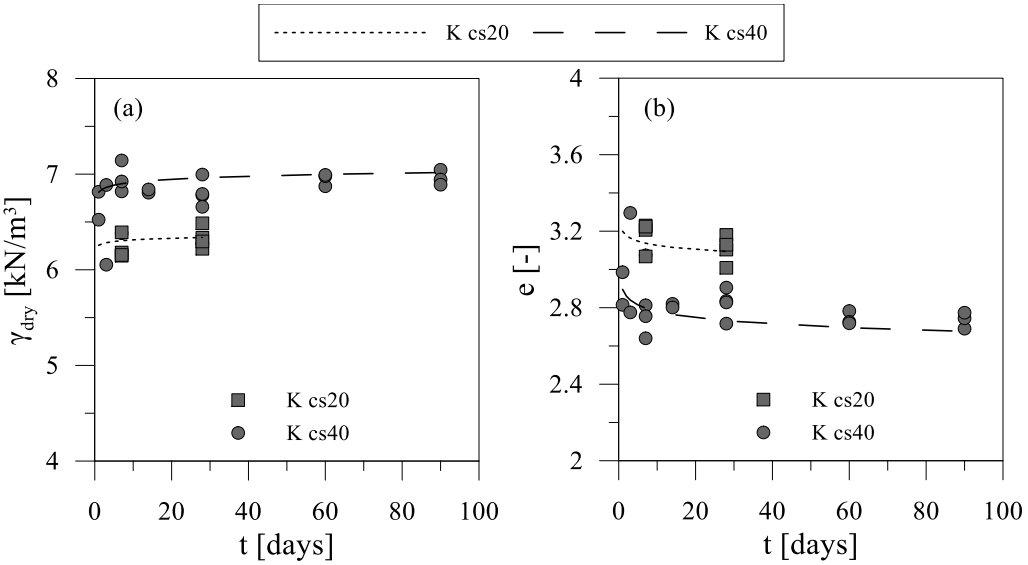

Figure 7-1. Comparison between estimated and measured value of (a) dry unit weight and (b) void ratio at different curing times. Dotted and dashed line refer to theoretical values.

By knowing dry weight and the weight before test, water content can be determined at time t. In the hypothesis of seal curing, total weight should be equal to the initial total weight. However, evaporation can occur if the sample it's not perfectly sealed. In order to compare the measured water content to theoretical value, the water content of the seal cured material at curing time t can be estimated by using initial total weight and the dry weight at time t. The comparison is shown in Figure 7-2a. In this case, the error is more pronounced. As for dry unit weight and void ratio, the larger deviations occur for

Kcs40_3d_100kPa and Kcs40_7d_150kPa in which measured water content is significantly different compared to theoretical value and the error is above 10%.

In Figure 7-2b, data from samples prepared to measure oven dried (OD) water content at varying curing time are compared with theoretical values. Data from freeze dried samples (FD) used for microstructural analyses are also reported. The water content of Kcs40 samples is well fitted, while water content of Kcs20 samples appears to be slightly overestimated.

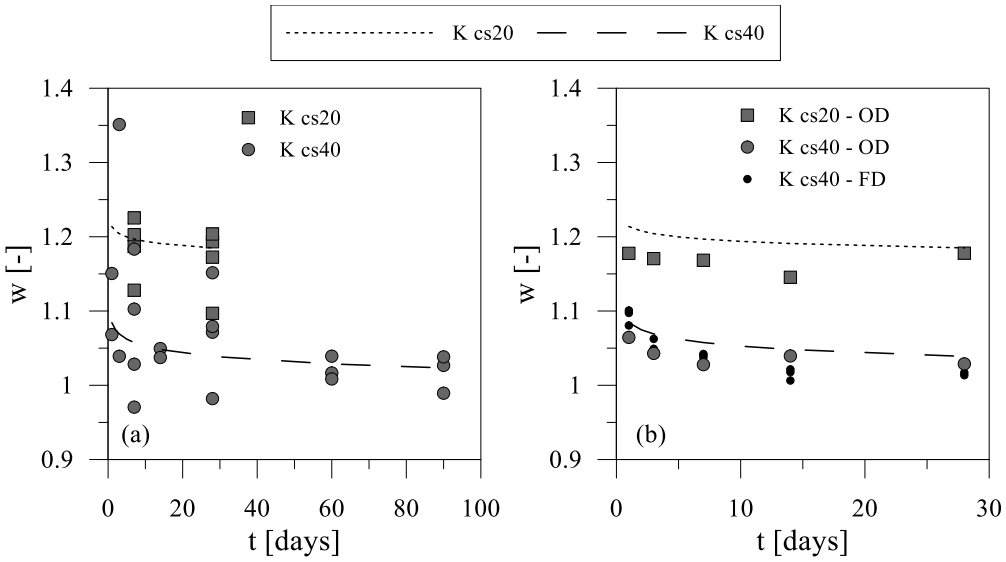

Figure 7-2. Water content of cemented soil at different curing time. (a) Data from samples after direct shear test; (b) data from oven dried and freeze-dried samples.

7.1.1.2. Lightweight cemented kaolin

A summary of the mechanical tests performed on lightweight cemented kaolin is given in Table 7-2.

Table 7-2. Summary of tests on lightweight cemented kaolin.

		t [days]	σ'_v [kPa]	γ [kN/m^3]	γ_{dry} [kN/m^3]	e
K cs20 nf20	*Kcs20_nf20_7d_50kPa*	7	50	12.8	5.7	3.5
	Kcs20_nf20_7d_100kPa	7	100	12.3	5.5	3.8
	Kcs20_nf20_7d_150kPa	7	150	12.9	6.2	3.2
	Kcs20_nf20_28d_50kPa	28	50	13.0	5.8	3.5
	Kcs20_nf20_28d_100kPa	28	100	13.0	5.8	3.5
	Kcs20_nf20_28d_150kPa	28	150	12.5	5.6	3.6
	Kcs20_nf20_7d_oed	7	-	12.5	5.8	3.5
K cs40 nf20	*Kcs40_nf20_7d_50kPa*	7	50	12.6	6.0	3.3
	Kcs40_nf20_7d_100kPa	7	100	12.8	6.1	3.2
	Kcs40_nf20_7d_150kPa	7	150	12.8	6.1	3.3
	Kcs40_nf20_14d_50kPa	14	50	12.5	6.0	3.4
	Kcs40_nf20_14d_100kPa	14	100	12.8	-	-
	Kcs40_nf20_14d_150kPa	14	150	12.9	5.9	3.4
	Kcs40_nf20_28d_50kPa	28	50	12.5	6.1	3.3
	Kcs40_nf20_28d_100kPa	28	100	13.0	6.2	3.2
	Kcs40_nf40_28d_150kPa	28	150	13.0	-	-
K cs20 nf40	*Kcs20_nf20_7d_50kPa*	7	50	10.2	4.7	4.6
	Kcs20_nf20_7d_100kPa	7	100	10.2	4.4	4.9
	Kcs20_nf20_7d_150kPa	7	150	10.4	4.5	4.8
	Kcs20_nf20_28d_50kPa	28	50	10.2	4.5	4.8
	Kcs20_nf20_28d_100kPa	28	100	10.2	4.5	4.8
	Kcs20_nf20_28d_150kPa	28	150	10.4	4.3	5.1
	Kcs20_nf40_14d_oed	14	-	10.2	4.7	4.5
	Kcs20_nf40_28d_oed	28	-	10.2	4.7	4.6
K cs40 nf40	*Kcs40_nf40_1d_50kPa*	1	50	10.3	4.8	4.4
	Kcs40_nf40_1d_100kPa	1	100	10.0	4.6	4.6
	Kcs40_nf40_3d_50kPa	3	50	10.5	4.8	4.5
	Kcs40_nf40_3d_100kPa	3	100	10.6	4.7	4.6
	Kcs40_nf40_3d_150kPa	3	150	10.5	4.7	4.5
	Kcs40_nf40_7d_50kPa	7	50	10.1	4.7	4.5
	Kcs40_nf40_7d_100kPa	7	100	10.7	4.9	4.3
	Kcs40_nf40_7d_150kPa	7	150	10.8	5.3	3.9
	Kcs40_nf40_14d_50kPa	14	50	10.4	4.9	4.3
	Kcs40_nf40_14d_100kPa	14	100	10.0	4.7	4.5
	Kcs40_nf40_28d_50kPa	28	50	10.3	5.0	4.2
	Kcs40_nf40_28d_100kPa	28	100	10.6	5.0	4.2
	Kcs40_nf40_28d_150kPa	28	150	10.0	-	-
	Kcs40_nf40_60d_50kPa	60	50	10.8	5.0	4.2
	Kcs40_nf40_60d_100kPa	60	100	10.8	5.1	4.1
	Kcs40_nf40_90d_50kPa	90	50	10.3	5.1	4.1
	Kcs40_nf40_90d_100kPa	90	100	10.7	4.8	4.4
	Kcs40_nf40_90d_150kPa	90	150	10.9	-	-
	Kcs40_nf40_7d_oed	7	-	10.2	5.0	4.2
	Kcs40_nf40_14d_oed	14	-	10.3	5.1	4.1
	Kcs40_nf40_28d_oed	28	-	10.2	5.0	4.2

The same approach used for cemented kaolin was used to determine γ, γ_{dry}, e and w of lightweight samples. In this case, the measured unit weight is higher than theoretical value (respectively 11.2 and 8.6 kN/m^3 for Kcs20nf20 and Kcs20nf40, and 11.5 and 8.8 kN/m^3 for Kcs40nf20 and Kcs40nf40 - Table 5-3). Indeed, the average values of measured unit weights are 12.8 and 10.3 kN/m^3 for Kcs20nf20 and Kcs20nf40, and 12.8 and 10.5 kN/m^3 for Kcs40nf20 and Kcs40nf40. This difference depends mainly on the breakage of foam bubbles upon mechanical mixing. In this case, theoretical properties derived from equations (5-33) - (5-41) would deviate significantly from data. In order to compare data with theoretical values, the approach presented in 5.2.1.1 was used. It is assumed that the difference between theoretical and measured unit weight is only due to the breakage of foam bubbles; then an "actual" volume of foam is determined and, hence, the "actual" ratio V_f/V, referred to as n_f^*. By this way, theoretical unit weight is matched to the measured unit weight and the actual n_f^* is determined for each sample. The average n_f^* values are 9 % and 28 % for Kcs20nf20 and Kcs20nf40, and 11 % and 29 % for Kcs40nf20 and Kcs40nf40. The theoretical values of bulk properties shown thereafter are determined with the average values of n_f^*.

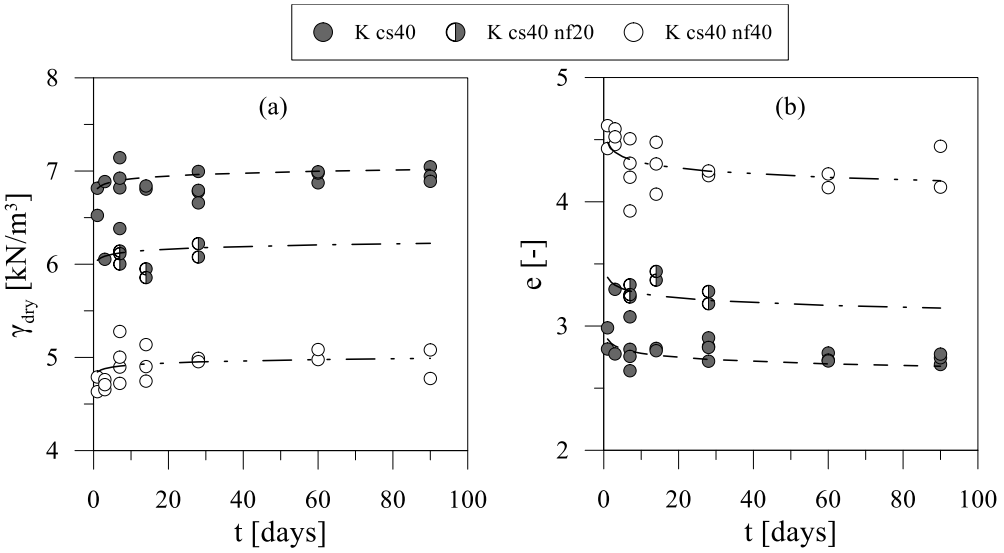

Figure 7-3. Comparison between estimated and measured (a) dry unit weight and (b) void ratio of Kcs40nf 0-20-40 at varying curing time. Dashed lines refer to theoretical values.

The comparison between measured and estimated values (after volume correction) of unit dry weight and void ratio are shown in Figure 7-3a and Figure 7-3b, respectively. Data regarding Kcs40 are also reported. The lightweight

material has a significantly lower (higher) dry unit weight (void ratio), especially comparing Kcs40 and Kcs40nf40. Data are well fitted, except for Kcs40nf40_7d_150kPa and Kcs40nf40_90d_100kPa. The same can be observed in Kcs20 nf 0-20-40, as shown in Figure 7-4; the void ratio is slightly higher than Kcs40 nf 0-20-40 (comparing samples with the same n_f). This is due to the lower amount of cement, which reduces the solid phase.

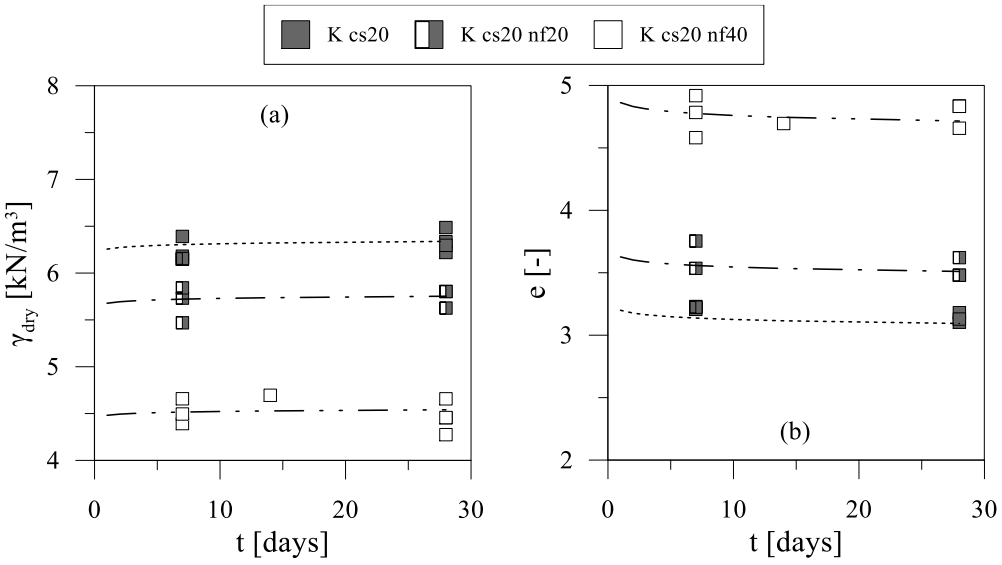

Figure 7-4. Comparison between estimated and measured (a) dry unit weight and (b) void ratio of Kcs20nf 0-20-40 at varying curing time. Dashed lines refer to theoretical values

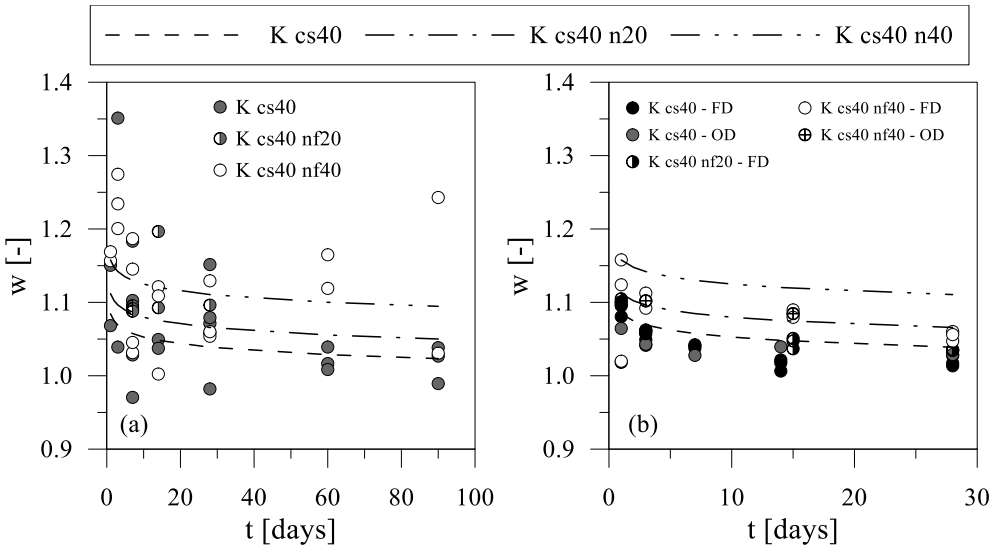

Figure 7-5. Water content time evolution of Kcs40nf0-20-40.

In terms of water content, data from samples of Kcs40 nf0-20-40 subjected to mechanical tests are highly dispersed between 100 and 120 % (Figure 7-5a). However, data from freeze dried samples for microstructural and mineralogical tests, and data from oven dried samples prepared for this purpose are well fitted (Figure 7-5b). The same scatter was observed in Kcs20 nf0-20-40 (Figure 7-6).

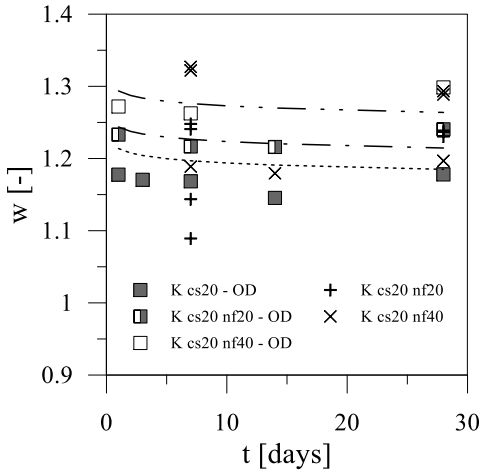

Figure 7-6. Water content time evolution of Kcs20 nf0-20-40 oven dried samples.

Finally, it is worth noting that saturation degree of lightened samples is significantly lower than 1 because of air bubbles, while saturation degree of cemented kaolin is almost 1 (98% on average for both Kcs20 and Kcs40). The average degree of saturation for Kcs20nf 20-40 is 90% and 70%, respectively, while for Kcs40nf 20-40 is 87% and 69%, respectively.

7.1.2. Mechanical tests

7.1.2.1. Direct shear tests[7]

In the following section, direct shear test results on cemented Speswhite kaolin are presented. The effects of cement factor, curing time and confining stress on mechanical behaviour of cemented kaolin will be highlighted.

In Figure 7-7 results of tests performed after 7 days of curing are shown. At increasing cement/soil ratio (c/s), both peak strength and initial stiffness increase. The volumetric behaviour of Kcs40 is dilative for both confining stresses; at a confining stress of 50 kPa, the behaviour is initially contractive, and it becomes dilative only after peak is reached, which is consistent with results of Schnaid et

[7] The adopted shear box apparatus is a standard one. All direct shear tests have been performed at a displacement rate of 0.005 mm/min. Micrometer dial gauges with a resolution of 0.001 and 0.01 mm have been respectively used to measure vertical and horizontal displacements.

al. (2001). For Kcs40 samples, at increasing confining stress, failure occurs at higher deformations, but a brittle behaviour is observed in both cases. Non-linearity of stress-strain curves occur just before peak strength is reached. Conversely, the behaviour of Kcs20 after 7 days of curing is contractive and ductile, similar to non-treated kaolin (dotted and dashed lines in Figure 7-7). Increasing the confining stress, there is no change in initial stiffness whereas an increase in peak strength is observed. It is worth noting that peak strength of all these samples is higher than non-treated kaolin.

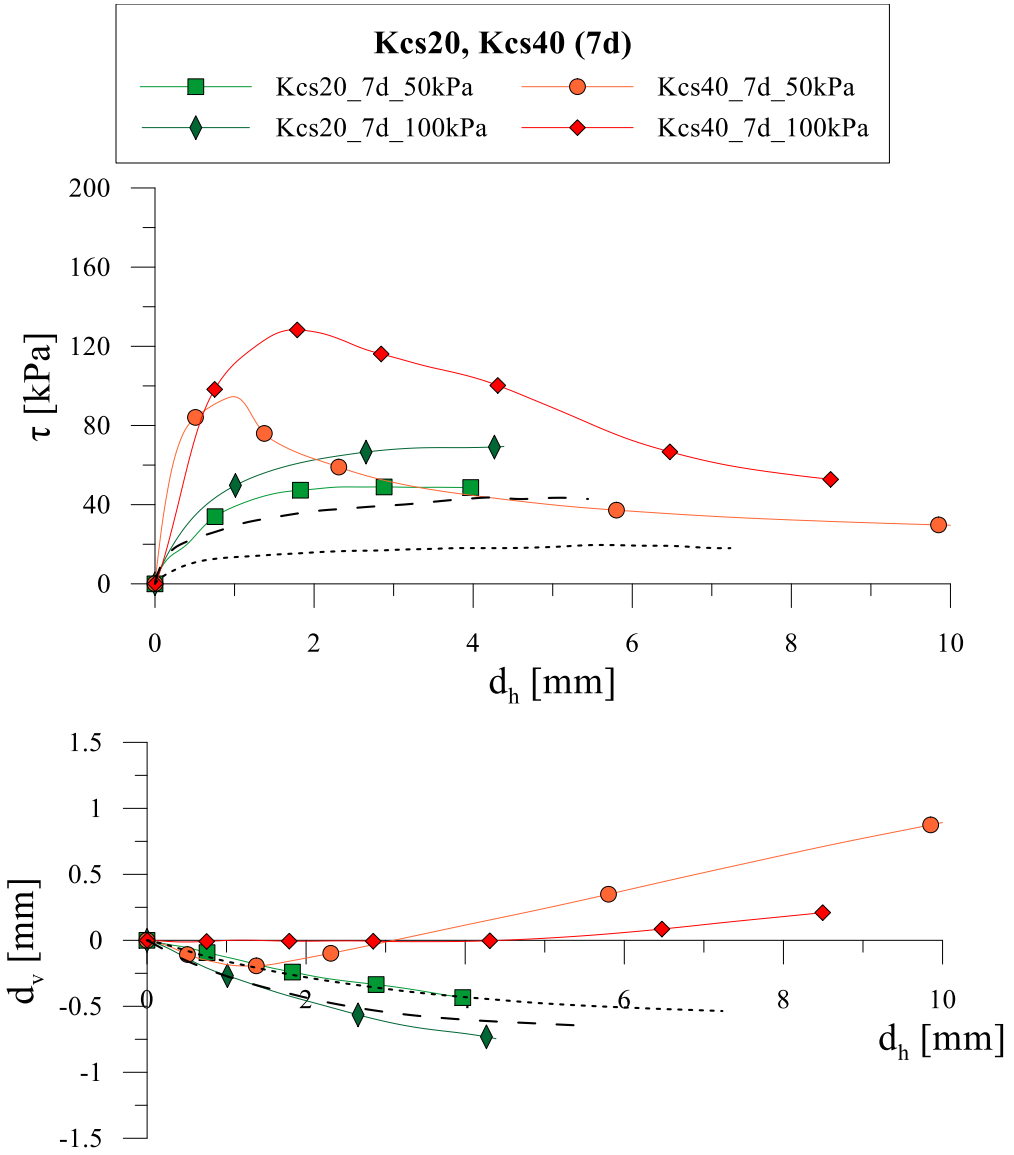

Figure 7-7. Direct shear tests on Kcs20 and Kcs40 at 7 days of curing. Dotted and dashed lines refer to tests at 50 kPa and 100 kPa on non-treated kaolin, respectively.

Similar results are observed on samples tested at 28 days of curing, as shown in Figure 7-8. At increasing cement content, both peak strength and stiffness increase. The behaviour of Kcs40 is brittle and dilative. In this case, a softening stage at high deformations is observed also on Kcs20 samples; a slight dilatancy is observed at a confining stress of 50 kPa, while it is contractive at σ'_v = 100 kPa.

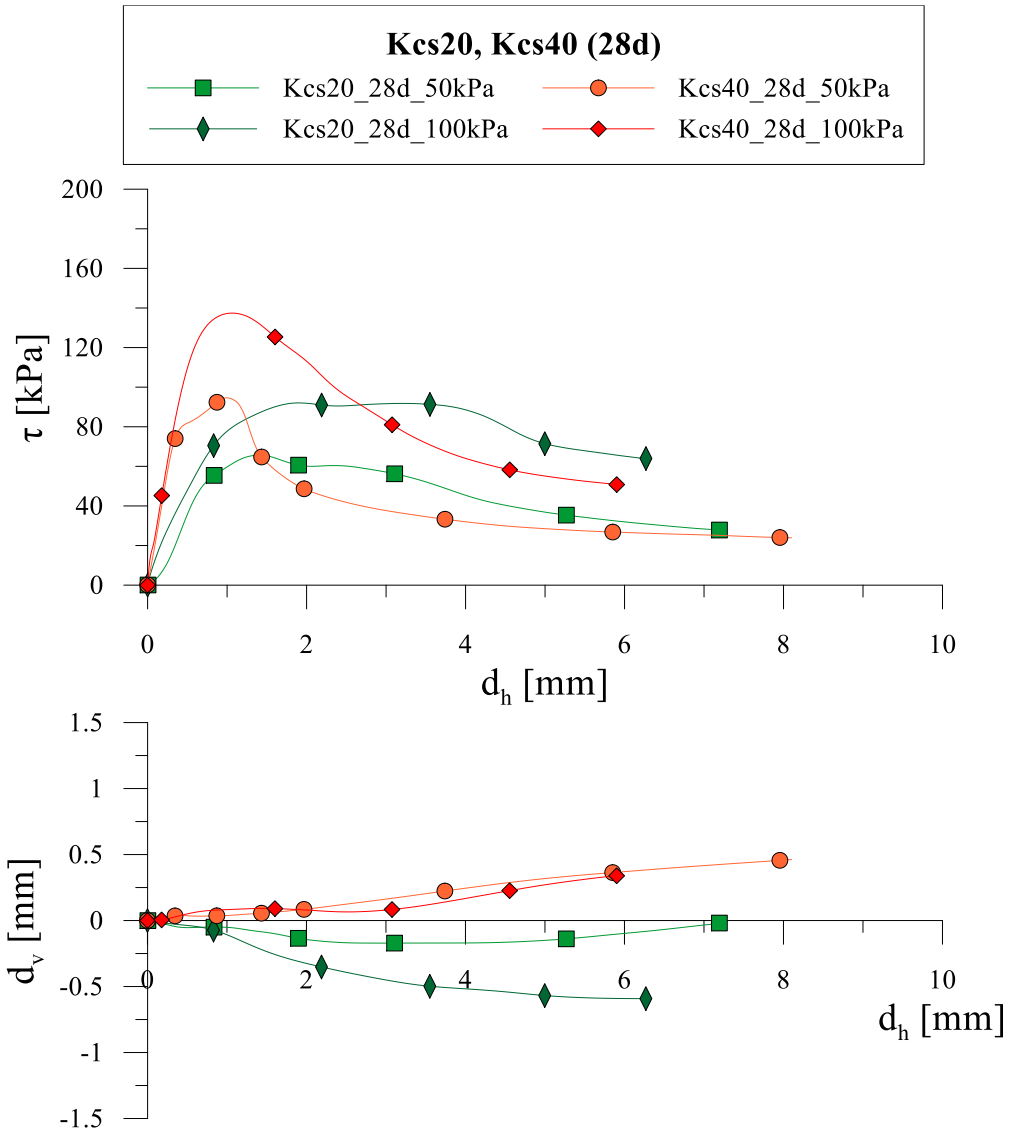

Figure 7-8. Direct shear tests on Kcs20 and Kcs40 after 28 days of curing.

The effect of curing time at different cement contents is evidenced in Figure 7-9. From 7 to 28 days an increase in both peak strength and initial stiffness is observed at both cement factors. A constant value is not achieved in any of the tests, but the curves seem to converge towards the same value, with different rates.

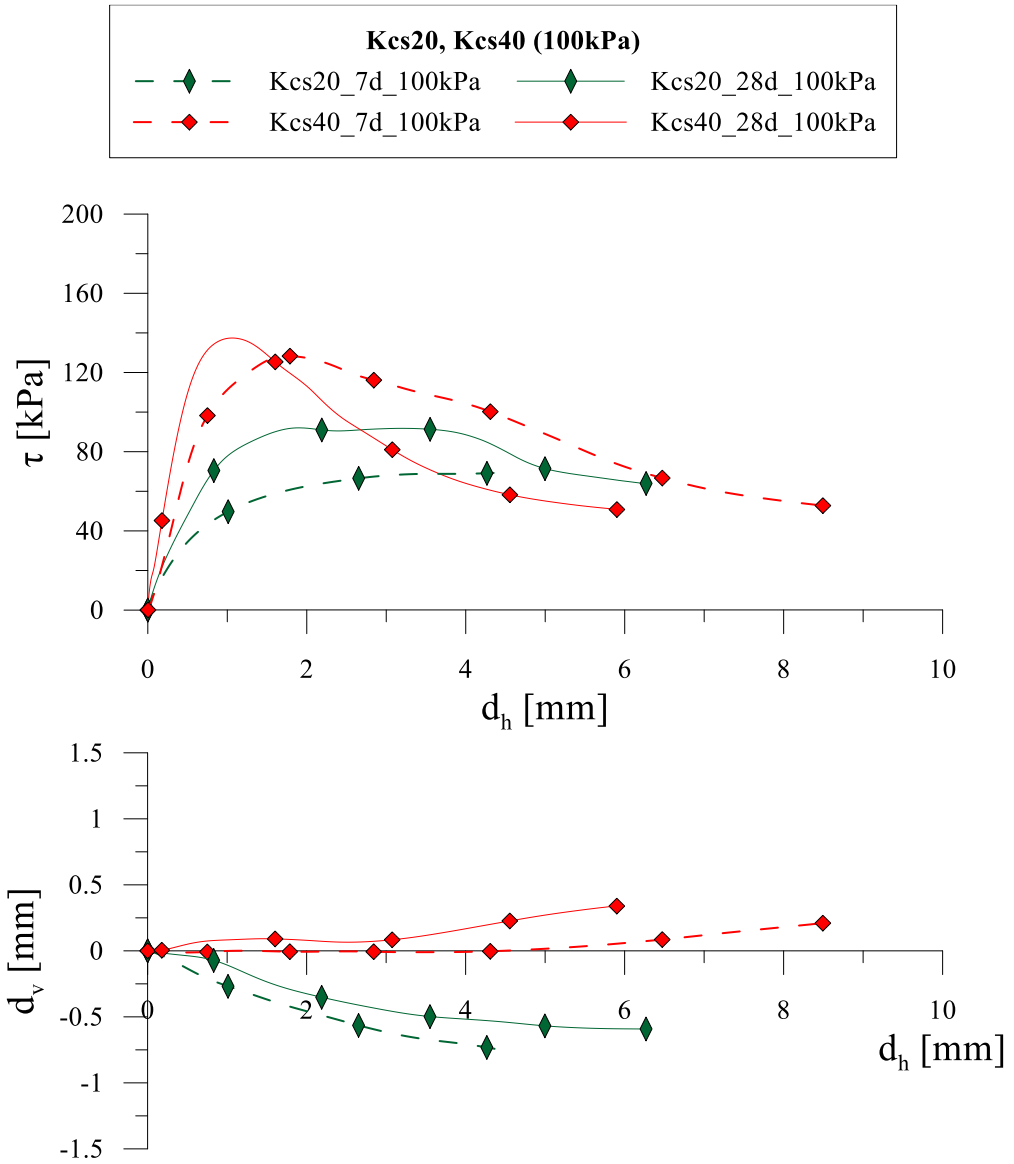

Figure 7-9. Direct shear tests on Kcs20 and Kcs40 at $\sigma_v^{'}$=100 kPa at 7 (dashed lines) and 28 (solid lines) days of curing.

Comparing tests on Kcs40 at 28 days respect to tests at 7 days of curing, a higher brittleness is observed; with reference to Kcs20, softening is observed only at 28 days of curing. However, a lower displacement was achieved at 7 days of curing, thus softening could have occurred also at 7 days if larger deformations were reached. At increasing curing time, the volumetric behaviour becomes more dilative for Kcs40 and less contractive for Kcs20.

In Figure 7-10 results of tests at 1, 3, 7 and 14 days of curing at a confining stress of 50 kPa are shown. The initial stiffness seems to be similar at varying curing time, except for the test at 1 day of curing. At increasing curing time, the

peak strength increases, and it is achieved at lower deformations. However, stress-strain curves seem to converge towards a unique value, regardless the curing time, which results in an augmented brittleness. The volumetric behaviour is dilative at all curing times, but an increase in dilatancy is observed along with the progress of hydration.

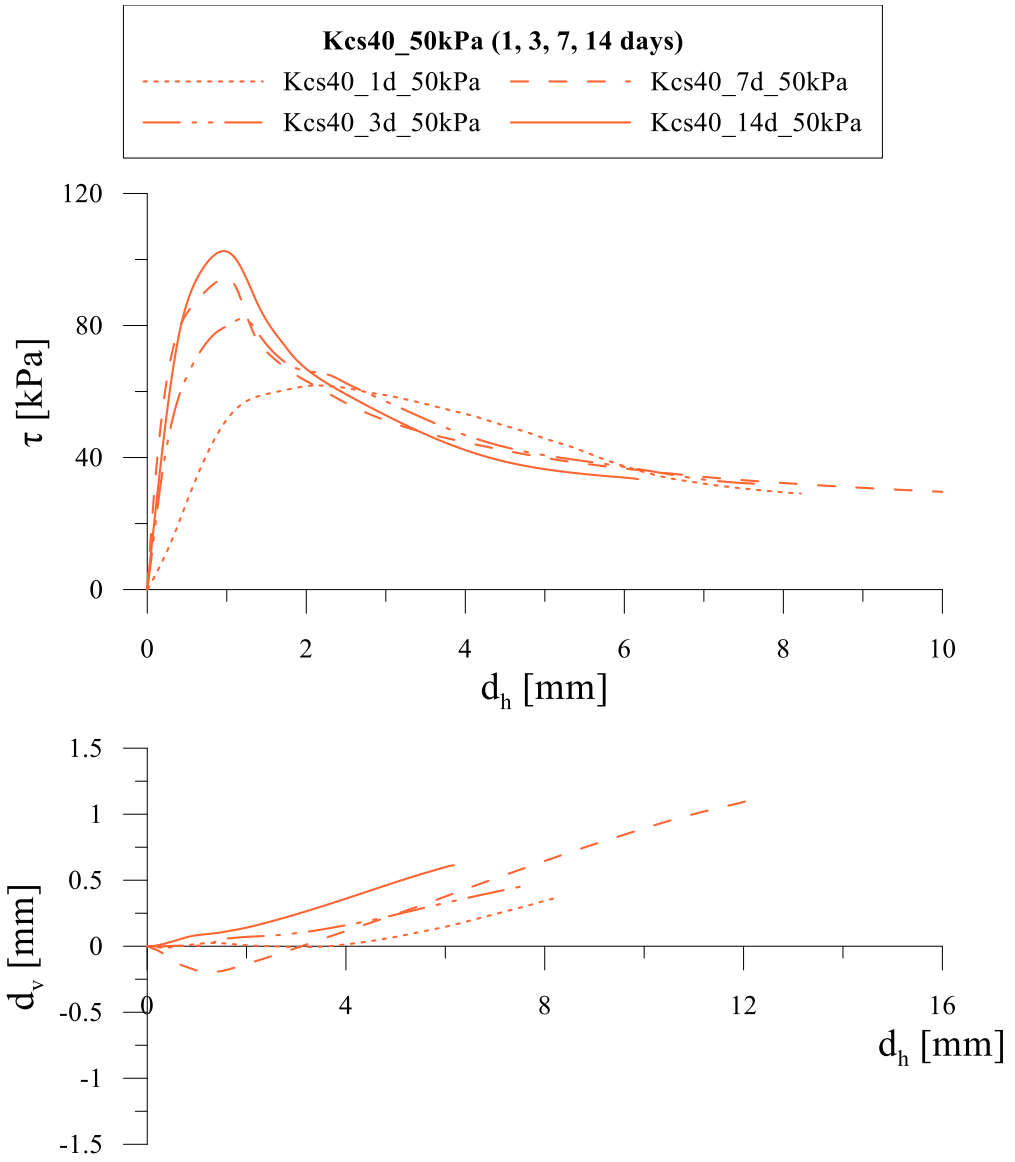

Figure 7-10. Direct shear tests on Kcs40 at $\sigma_v^{'}$=50 kPa at early stages of curing (1, 3, 7, 14 days).

Results of direct shear tests at the same curing times and $\sigma_v^{'}$ = 150 kPa are shown in Figure 7-11. Increasing curing time, an increase in strength is observed, except for t=14 days. However, respect to tests performed at 50 kPa, the increase in strength is less pronounced, with a more ductile behaviour. The volumetric

behaviour is always contractive, and (except for Kcs40_1d_150kPa) it becomes slightly dilative only at large deformations after failure occurs.

Results at $\sigma_v^{'}$ = 150 kPa, at longer curing times (28, 60, 90 days) are plotted in Figure 7-12 along with the result at 7 days of curing. Except for the test at 60 days, an increase in strength is observed at increasing curing time. This suggests that hydration progresses significantly even after 28 days. Again, the volumetric behaviour becomes much more dilative at increasing curing time.

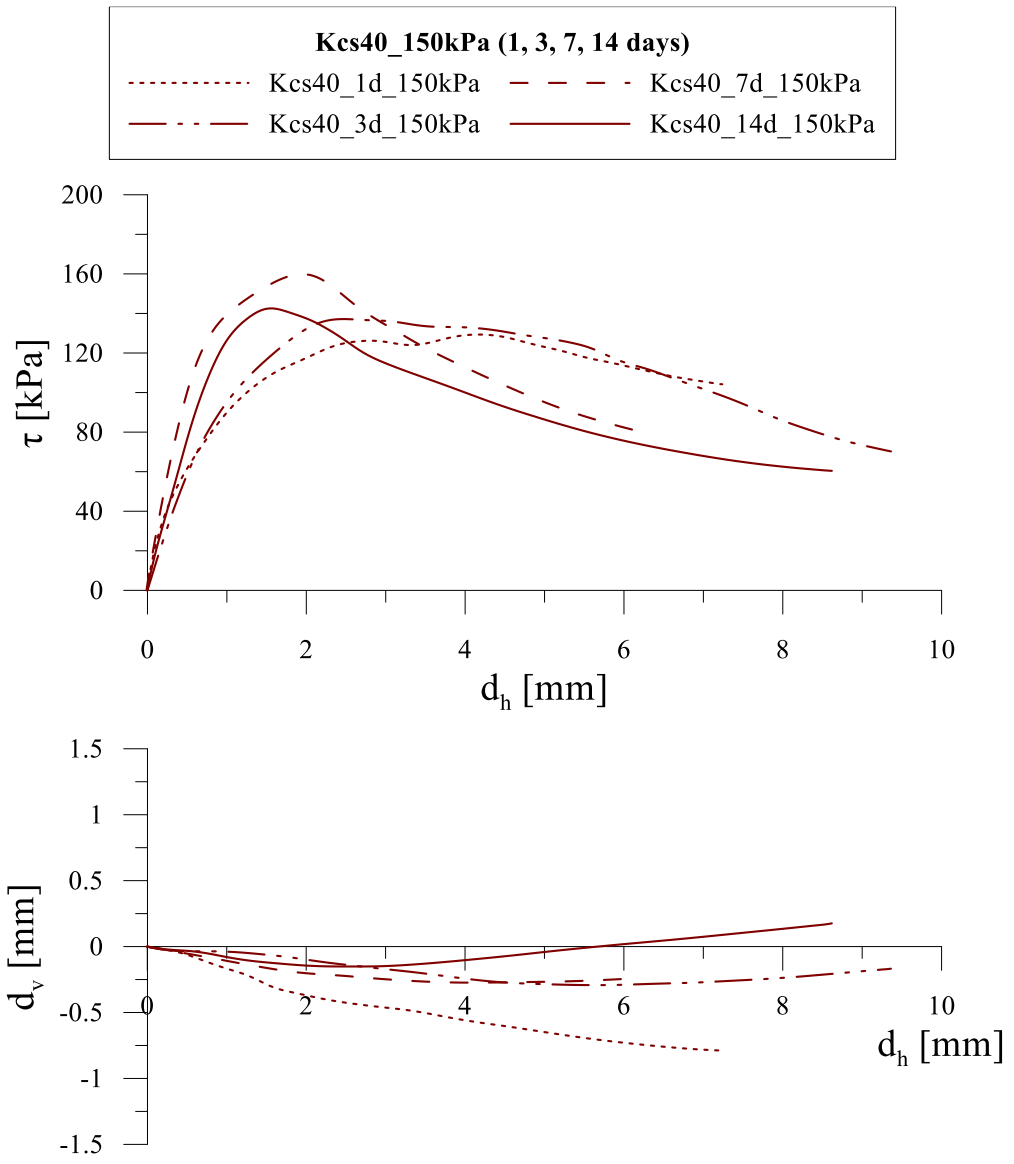

Figure 7-11. Direct shear tests on Kcs40 at $\sigma_v^{'}$=150 kPa at early stages of curing (1, 3, 7, 14 days).

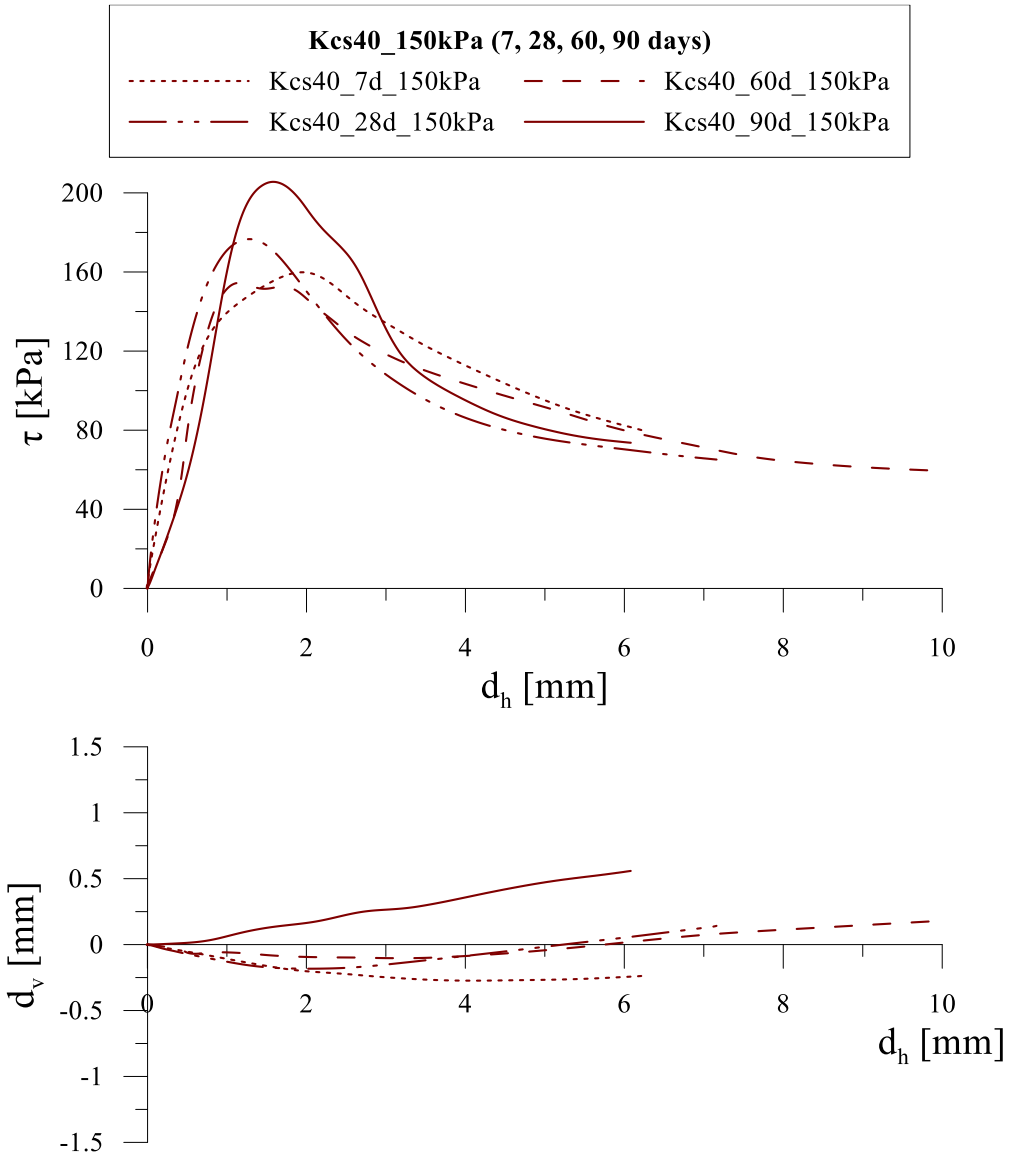

Figure 7-12. Direct shear tests on Kcs40 at σ_v'=150 kPa at different curing times (7, 28, 60, 90 days).

7.1.2.2. Oedometric tests[8]

The results of oedometric tests at different curing times and cement factors are represented in Figure 7-13 in the plane ε_v-logσ_v'. Below yielding stress, strains are very low with a slight increase in stiffness with cement factor. The yielding stress increases significantly with cement content, as observed by other authors

[8] The apparatus used in laboratory is a standard device with controlled incremental load. Specimen diameter is 55 mm with a height of 20 mm. Vertical displacements are measured via a Linear Variable Differential Transducer (LVDT). The load increment is applied when the 100% of primary consolidation is supposed to be reached.

(S. Horpibulsuk et al., 2004; Sasanian, 2011). At larger stresses, large deformations occur. The curves at different curing time and same cement factor are quite similar. It's worth noting that, in Kcs40, the yielding stress is significantly above the maximum vertical stress adopted in direct shear tests (150 kPa). Conversely, in Kcs20, non-negligible strains are observed at 150 kPa, which means that compared to Kcs40, direct shear tests are performed at an initial stress state closer to yielding surface.

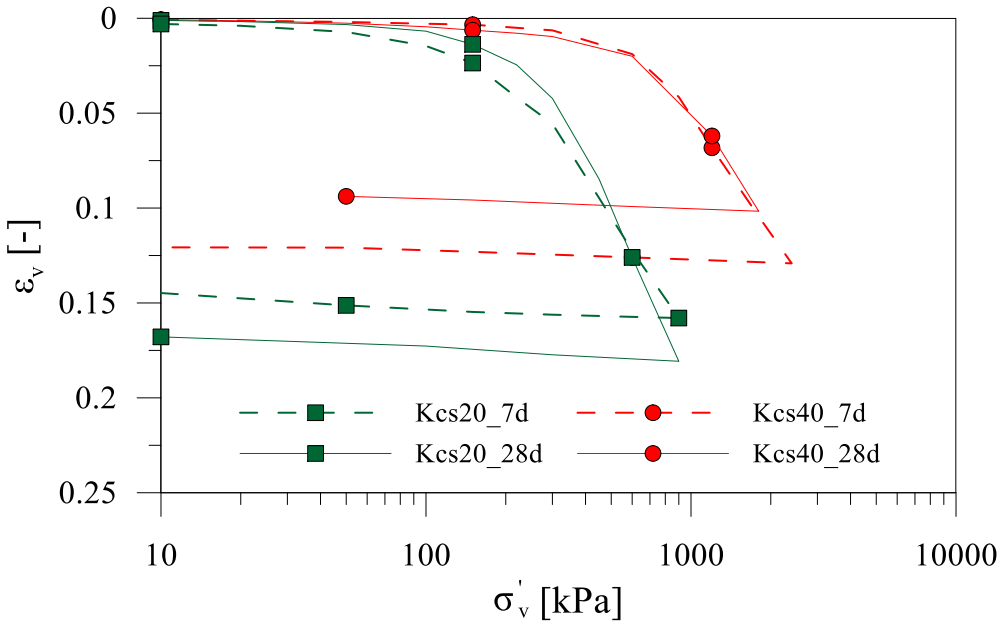

Figure 7-13. Oedometric tests on Kcs20 and Kcs40 at 7 and 28 days of curing (ε-log σ'_v).

In Figure 7-14 the results are plotted in the plane e-log(σ'_v). The two samples are characterized by different physical states in the stress field investigated. The initial void ratio of Kcs20 is slightly higher than Kcs40, but after yielding stress, situation is reversed due to the higher yielding stress of the latter. The comparison between the cemented kaolin sample and the non-treated one is represented in Figure 7-15. The initial void ratio, at very low confining stress, is much higher in cemented sample. The physical states observed up to 2 MPa are impossible for non-treated soil. In the range of stress applied it's not possible to determine if cemented sample, after yielding, tends towards the intrinsic compression line of non-treated one.

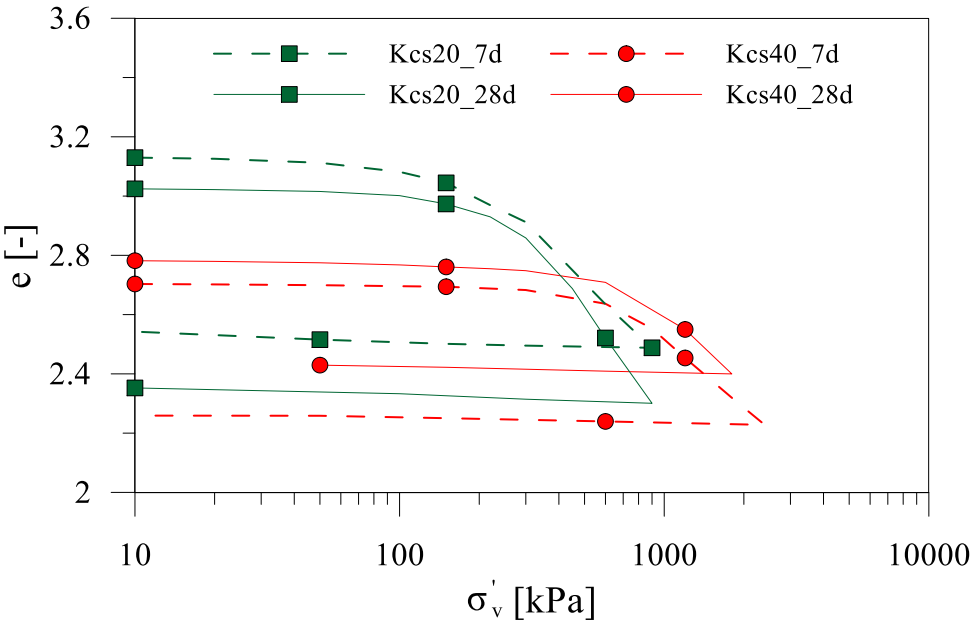

Figure 7-14. Oedometric tests on Kcs20 and Kcs40 at 7 and 28 days of curing (e-log σ'_v).

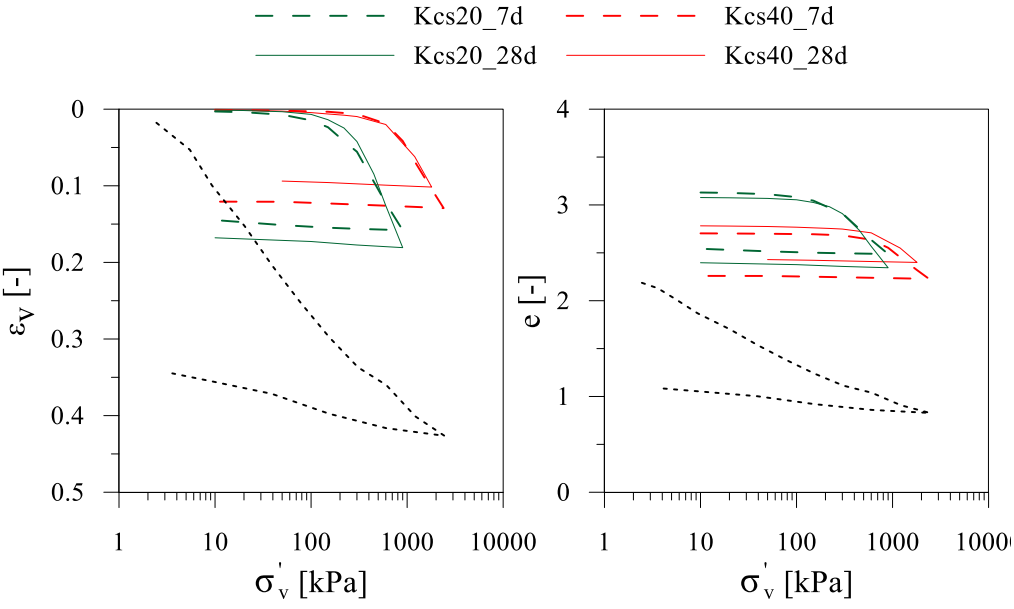

Figure 7-15. Comparison between oedometric tests on cemented and non-treated kaolin (dotted line).

7.1.2.3. Lightweight cemented kaolin

The effect of foam addition on cemented soil was studied for both cement factors at different curing times. In Figure 7-16 and Figure 7-17 results of tests at 28 days of curing at different vertical stress on Kcs20nf40 and Kcs40nf40, respectively, are shown. In both cases, the peak strength increases at increasing confining stress, while volumetric behaviour is contractive and ductile in all the

tests, except for a slight softening at large displacement in Kcs40nf40_28d_50kPa. The volumetric behaviour of the three samples of Kcs20nf40 is almost the same characterized by large vertical displacements, whereas the behaviour of Kcs40nf40 becomes gradually more contractive as the vertical stress increases.

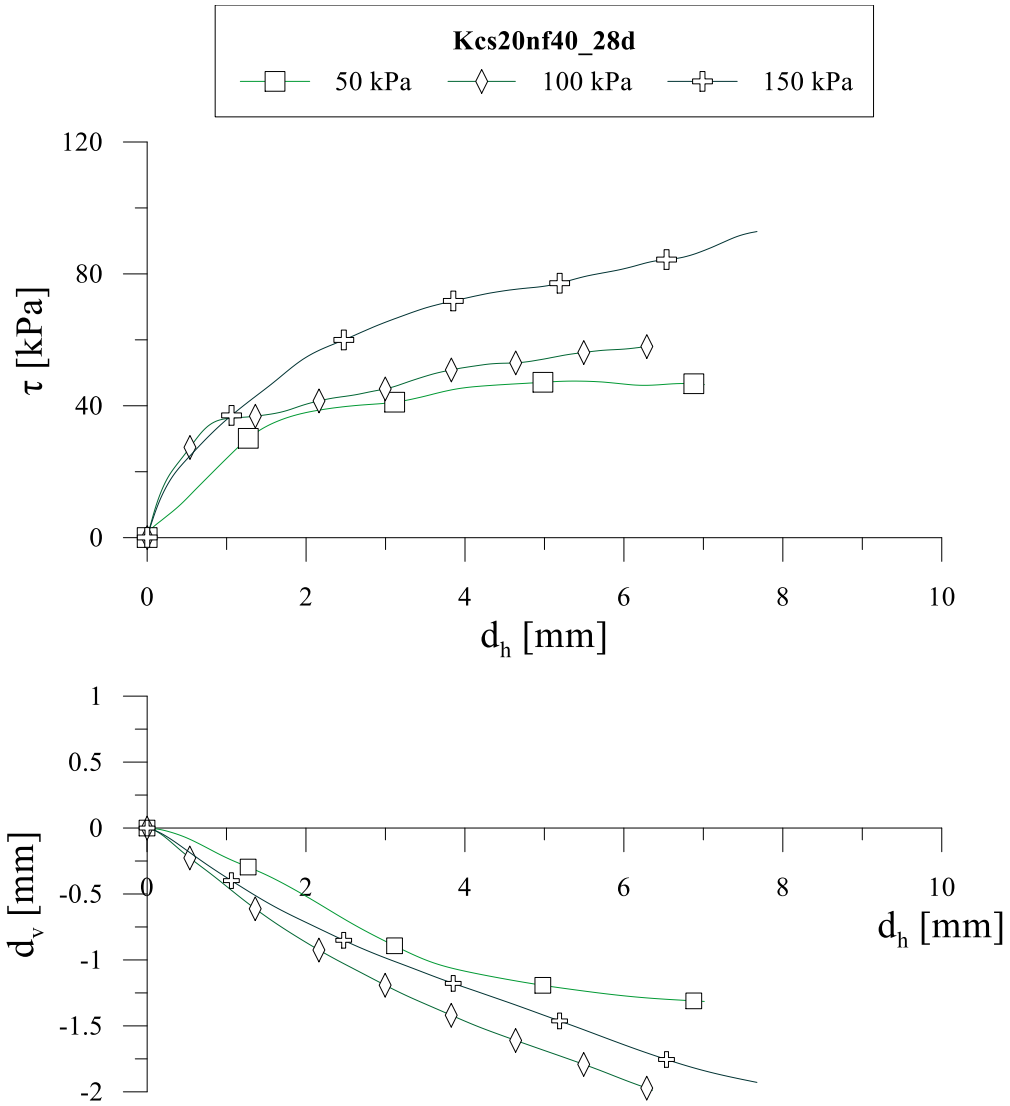

Figure 7-16. Direct shear tests on Kcs20nf40 after 28 days of curing at different vertical stress.

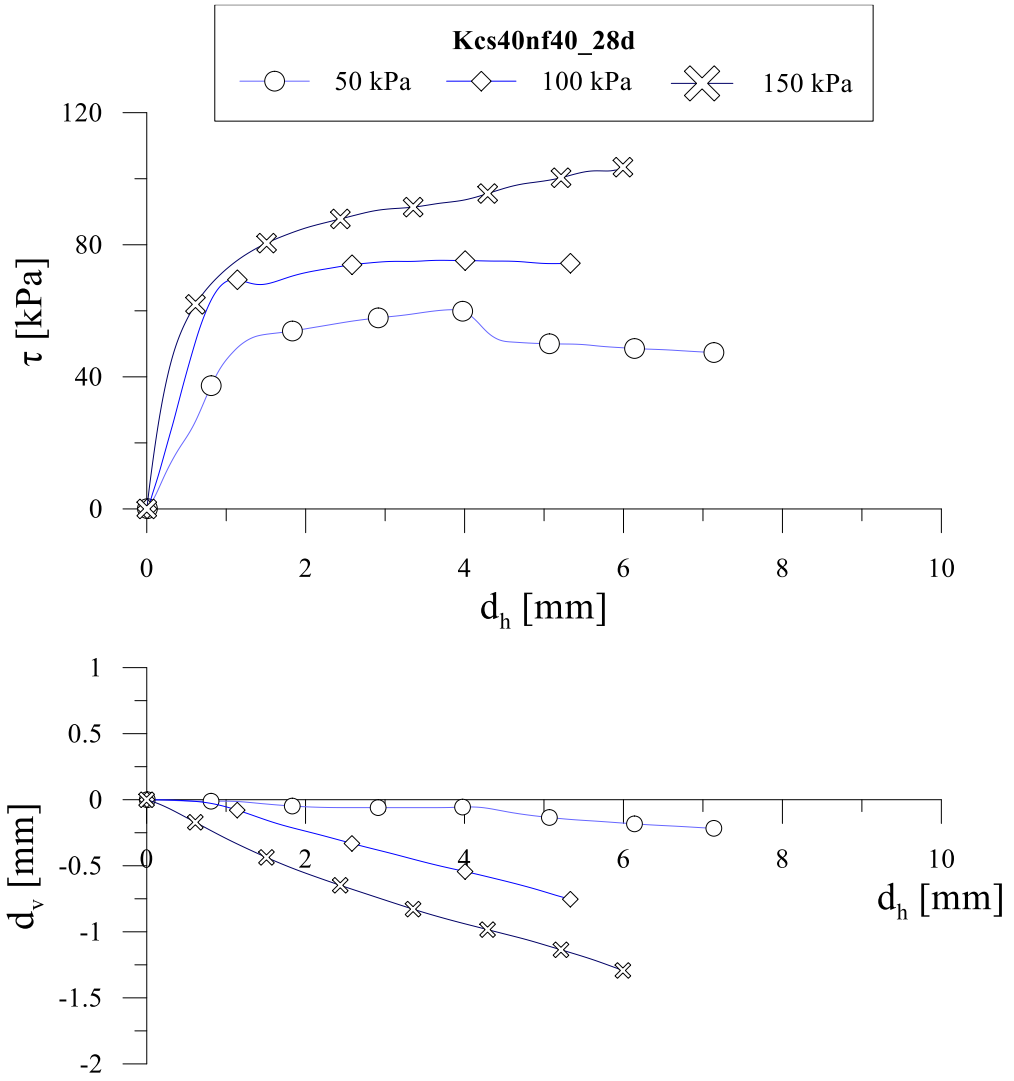

Figure 7-17. Direct shear tests on Kcs40nf40 after 28 days of curing at different vertical stress.

In Figure 7-18 the results of direct shear tests on Kcs40, Kcs40nf20 and Kcs40nf40 at a vertical stress of 50 kPa and after 7 days of curing are represented. Increasing the amount of foam, the initial stiffness slightly decreases, while a significant reduction of peak strength is observed, that it is still higher than non-treated sample even for Kcs40nf40. The volumetric behaviour, that is slightly dilative in Kcs40 sample, becomes contractive with the addition of foam; Kcs40nf20 sample is already characterized by a contractive behaviour even if a slight softening is still observed. Increasing the amount of foam, the behaviour becomes gradually more ductile and contractive, so that vertical displacements larger than non-treated soil are observed on Kcs40nf40 sample.

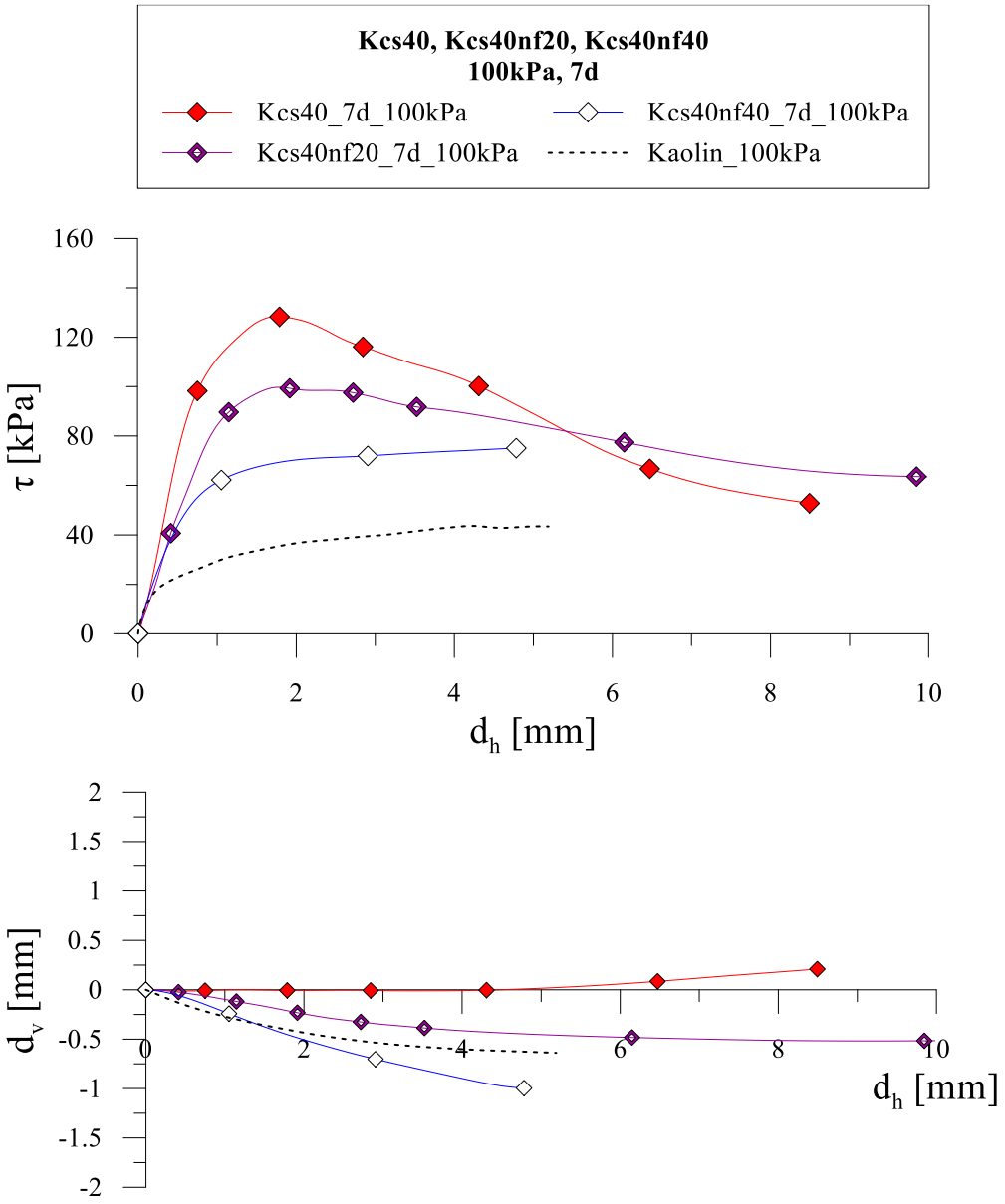

Figure 7-18. Direct shear tests on Kcs40, Kcs40nf20 and Kcs40nf40 at σ_v'=100 kPa after 7 days of curing.

Similar results are found on Kcs20, Kcs20nf20 and Kcs20nf40 samples. Increasing the amount of foam, compared to Kcs40, the reduction of peak strength is less evident; the peak strength of Kcs20 and Kcs20nf20 is almost the same. A lower peak strength is observed in Kcs20nf40, but still higher than non-treated kaolin. The volumetric behaviour is always contractive, with larger settlements observed at increasing amount of foam, higher than non-treated kaolin in all the cases.

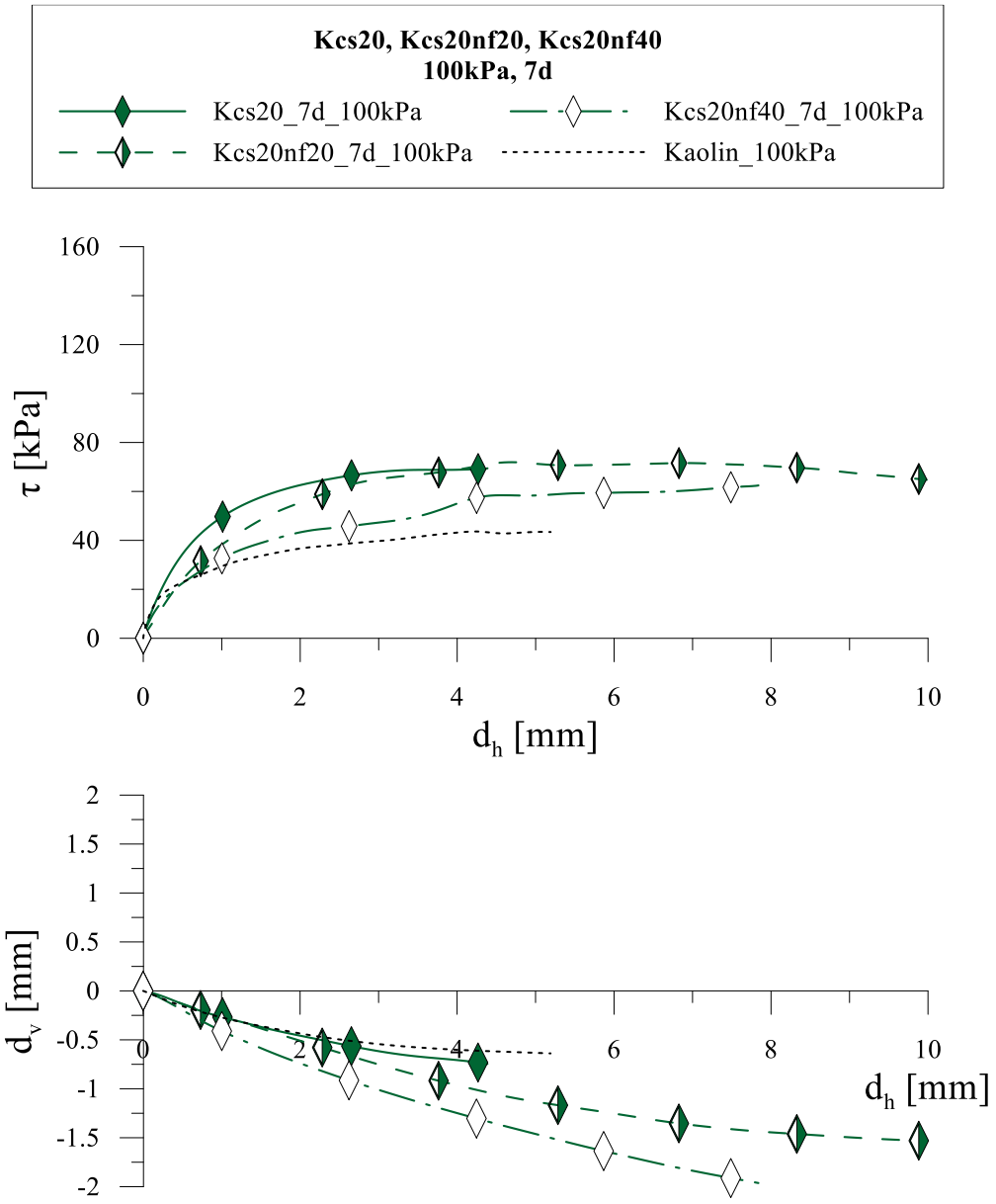

Figure 7-19. Direct shear tests on Kcs20, Kcs20nf20 and Kcs20nf40 at σ_v'=100 kPa after 7 days of curing.

The results of direct shear tests performed after 28 days of curing at a vertical stress of 100 kPa are shown in Figure 7-20 and Figure 7-21. As for samples tested after 7 days of curing, at increasing amount of foam (starting from Kcs40, Figure 7-20) peak strength and stiffness decrease, while the behaviour becomes more ductile and contractive.

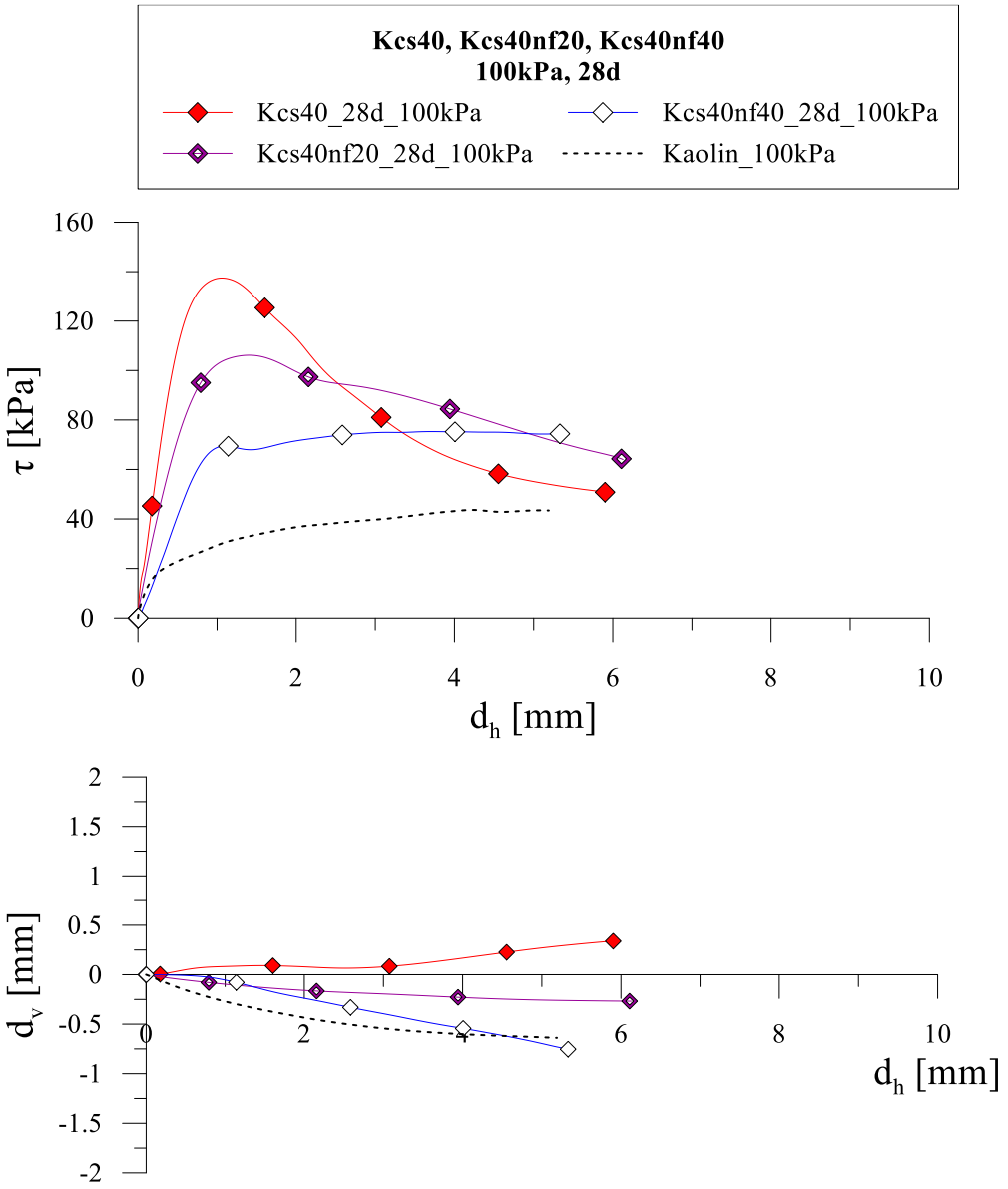

Figure 7-20. Direct shear tests on Kcs40, Kcs40nf20 and Kcs40nf40 at σ'_v=100 kPa after 28 days of curing.

The decrease in strength of lightened samples with c/s=20% at increasing amount of foam, compared to tests at 7 days (Figure 7-19), is more pronounced after 28 days of curing (Figure 7-21); indeed, in this case, a significant reduction of peak strength is observed between Kcs20 and Kcs20nf20. The behaviour of Kcs20nf40, in terms of stress-strain curve, is quite similar to non-treated sample, although it is characterized by larger vertical displacements. Moreover, the strength of Kcs20nf40 doesn't achieve a constant value but it is still increasing at the maximum displacement reached in test.

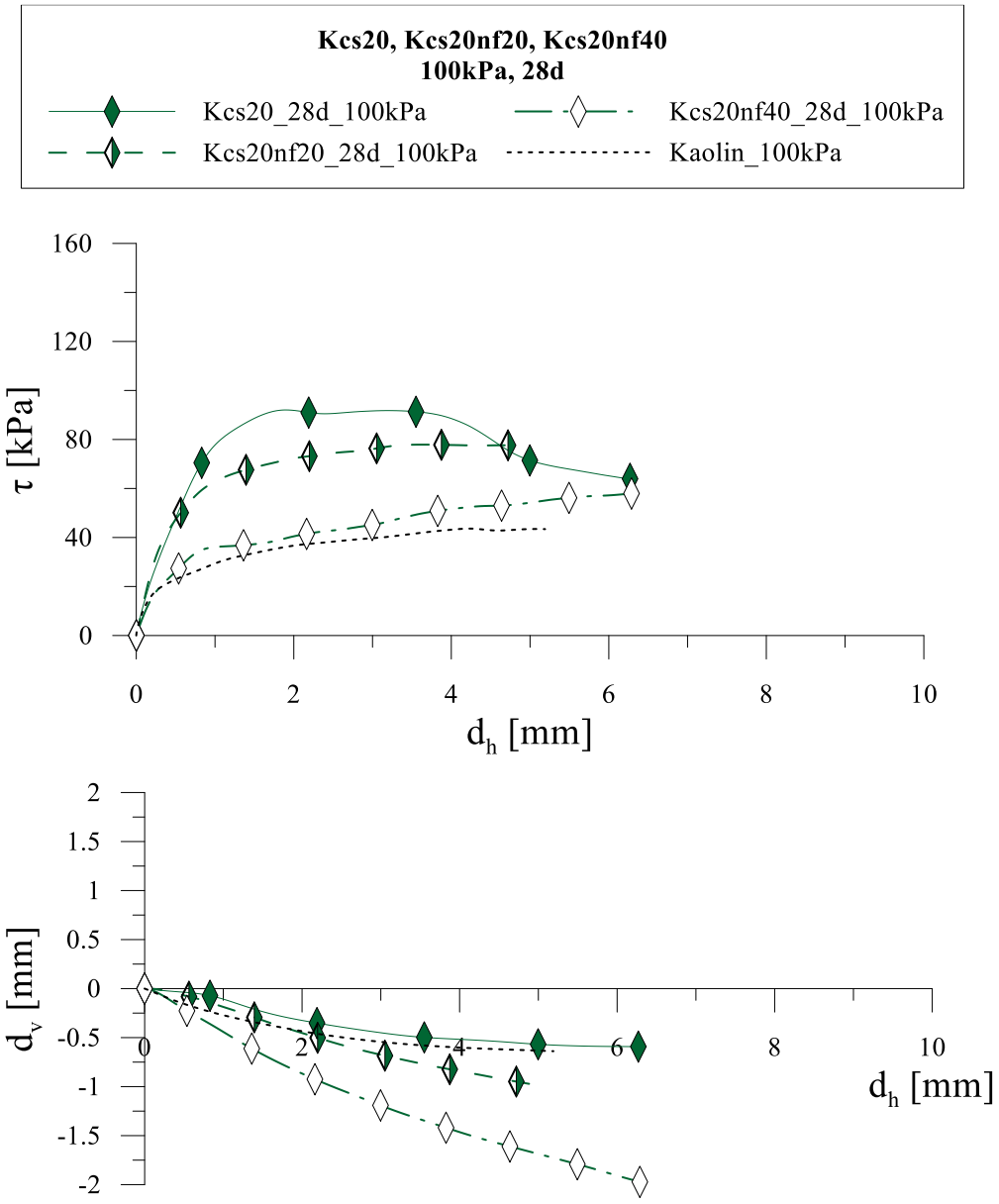

Figure 7-21. Direct shear tests on Kcs20, Kcs20nf20 and Kcs20nf40 at σ_v'=100 kPa after 7 days of curing.

In Figure 7-22 results of direct shear tests after 28 days of curing at a vertical stress of 50 kPa on Kcs20, Kcs20nf20, Kcs40 and Kcs40nf40 are represented. A higher peak strength and initial stiffness of Kcs40nf40 respect to Kcs20nf40 is observed. The two lightweight cemented samples (Kcs20nf40 and Kcs40nf40) seem to converge towards the same value of stress, higher than non-lightened material (Kcs20 and Kcs40) thus showing a more ductile behaviour. It is also clear that the behaviour becomes more contractive and ductile adding foam

and/or reducing the amount of cement. Furthermore, the volumetric behaviour of Kcs20 and Kcs40nf40 is quite similar.

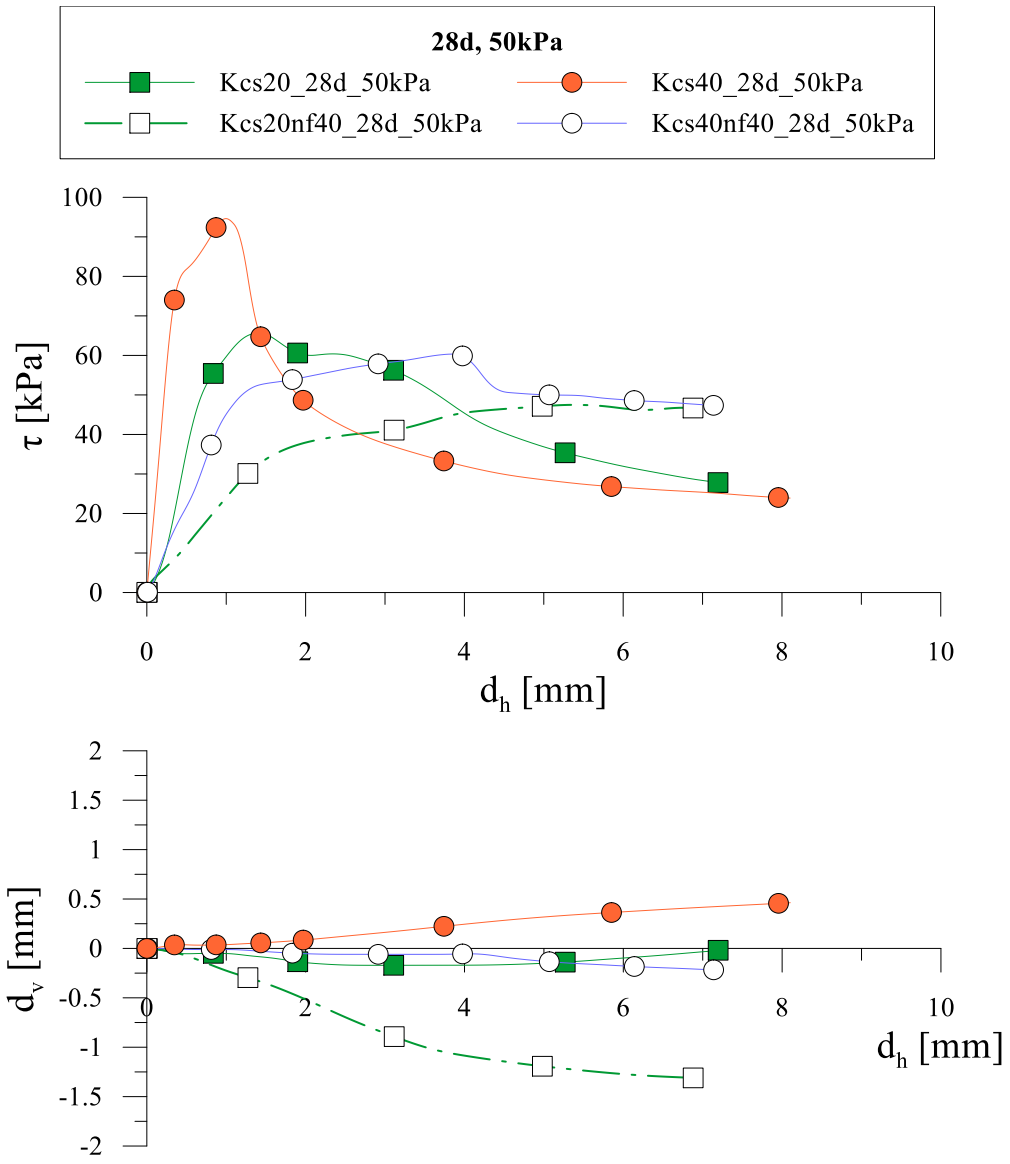

Figure 7-22. Direct shear tests at σ_v'=50 kPa after 28 days of curing on Kcs20, Kcs40, Kcs20nf20 and Kcs40nf40.

The same is observed at a vertical stress of 150 kPa. The lightened samples (Kcs20nf40 and Kcs40nf40) show a more ductile and contractive behaviour. Again, the behaviour of Kcs20 and Kcs40nf40 is quite similar.

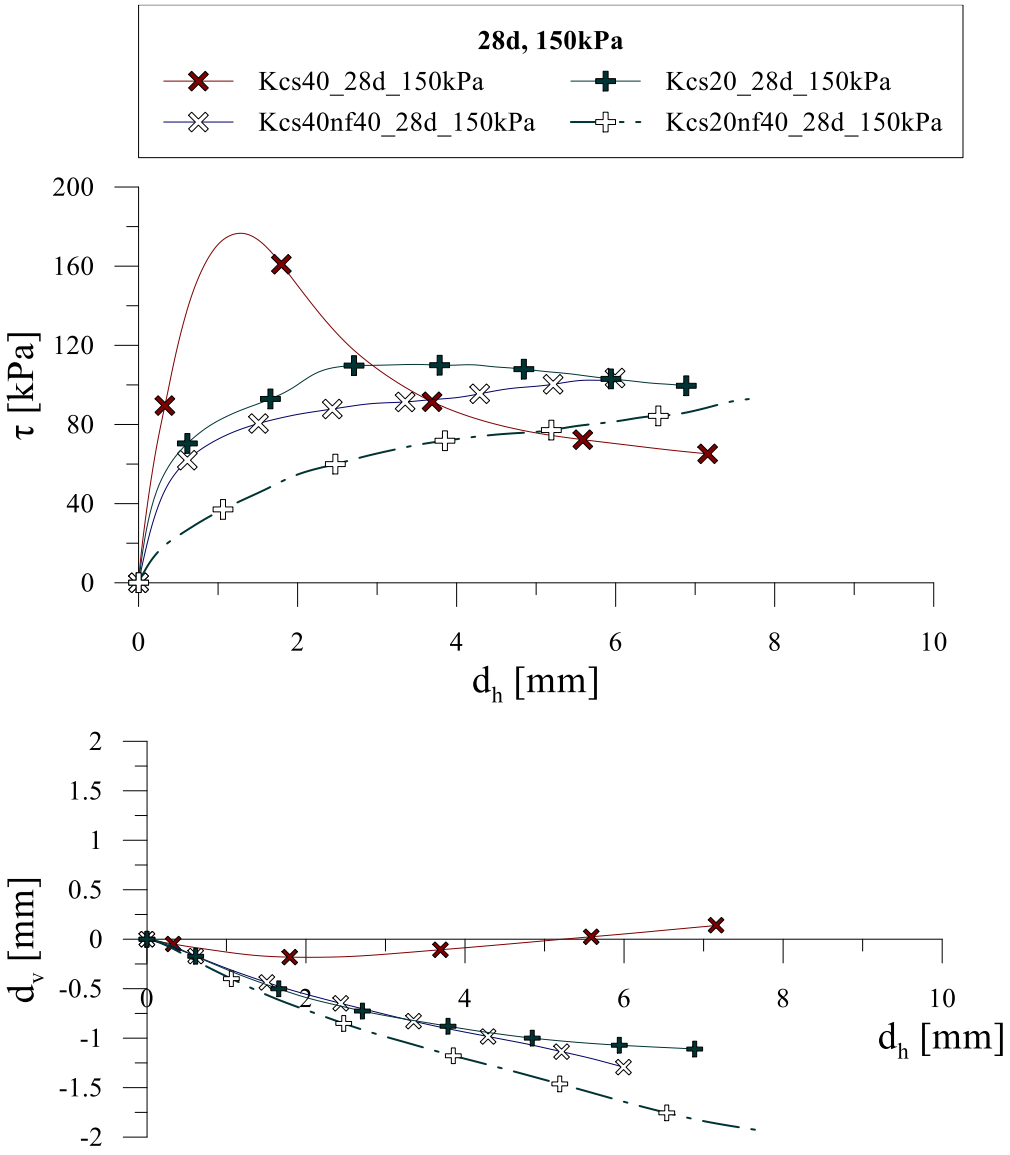

Figure 7-23. Direct shear tests at σ_v'=150 kPa after 28 days of curing on Kcs20, Kcs40, Kcs20nf20 and Kcs40nf40.

The effect of curing time on strength evolution of Kcs40nf40 is evidenced thereafter. In Figure 7-24, direct shear tests after 1, 3, 7 and 14 days of curing at a vertical stress of 50 kPa are shown. The same initial stiffness is observed, and the curves appear to converge towards a unique ultimate value with a ductile behaviour, except for Kcs40nf40_14d_50kPa that shows a very slight softening with a peak strength a little higher than the one observed at 7 days. From 1 to 3 days, non-linearity of stress-strain curves occur at larger displacements. The volumetric behaviour is contractive in all the tests, with decreasing vertical displacements from 1 to 7 days.

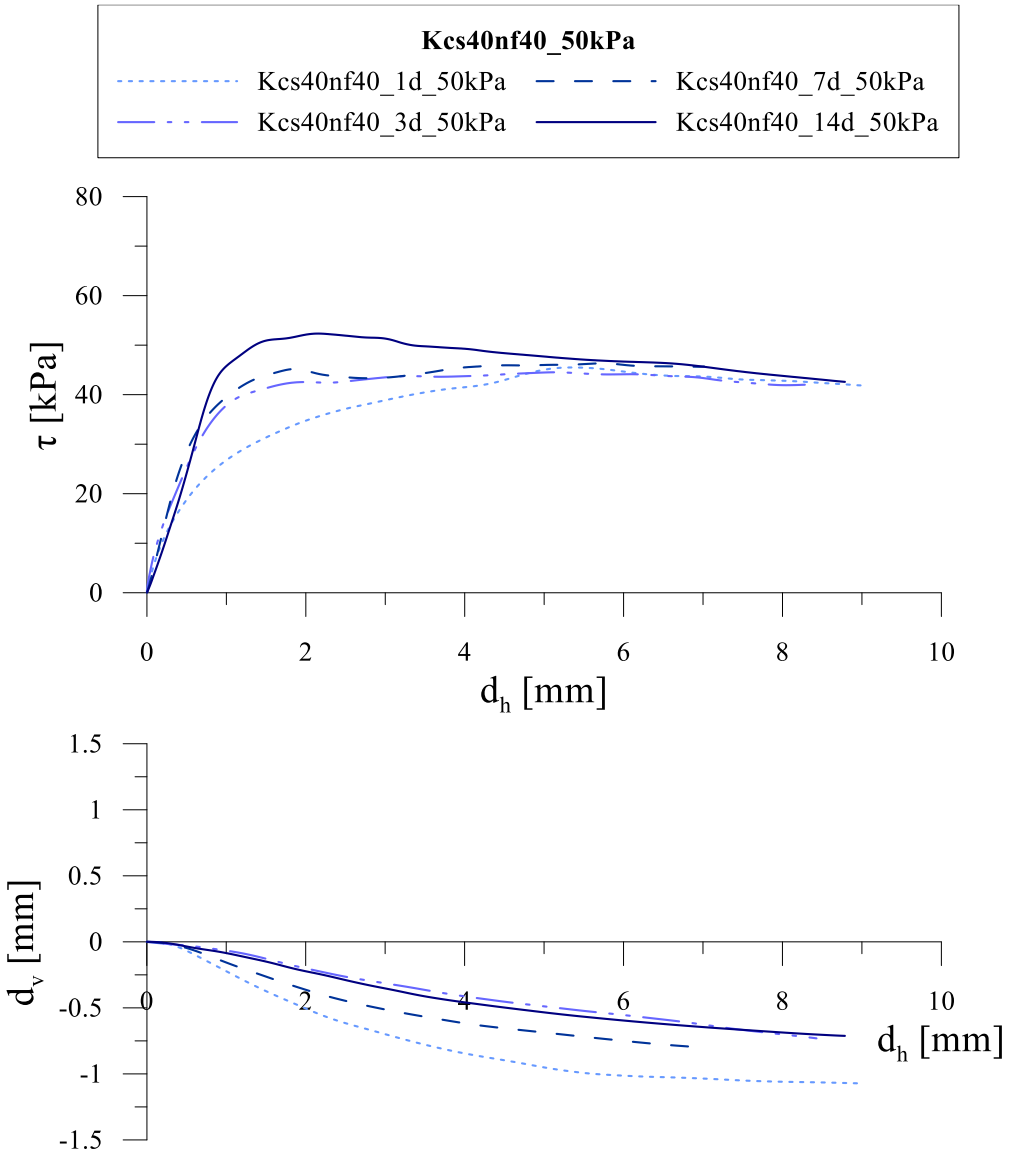

Figure 7-24. Direct shear tests on Kcs40nf40 at $\sigma_v^{'}$=50 kPa at early stages of curing (1, 3, 7, 14 days).

At a vertical stress of 100 kPa (Figure 7-25) the behaviour is always ductile (also at 14 days no softening is observed). The final strength, in this case, is slightly lower after 1 and 3 days of curing. No difference is observed in terms of volumetric behaviour.

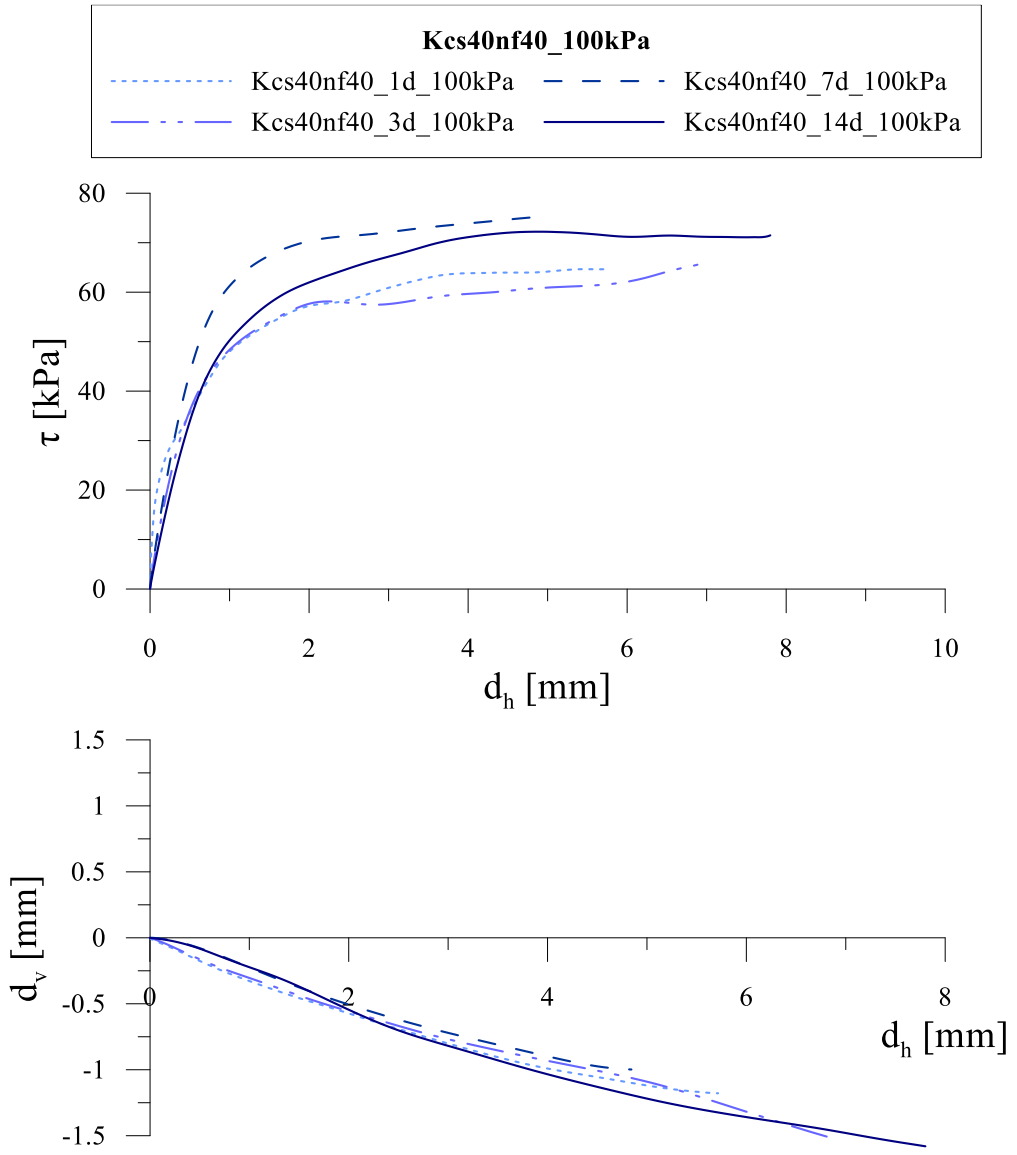

Figure 7-25. Direct shear tests on Kcs40nf40 at σ_v'=100 kPa at early stages of curing (1, 3, 7, 14 days).

A comparison of tests performed at 7, 28, 60 and 90 days of curing on Kcs40nf40 is presented in Figure 7-26 and Figure 7-27. At a vertical stress of 50 kPa (Figure 7-26), the behaviour is still ductile even at high curing times, with a slight softening observed only at large displacements. However, at increasing curing time, a significant change in volumetric behaviour is observed, that is contractive at 7 days of curing and dilative at 90 days. Curves tend towards the same value measured at early stages of curing.

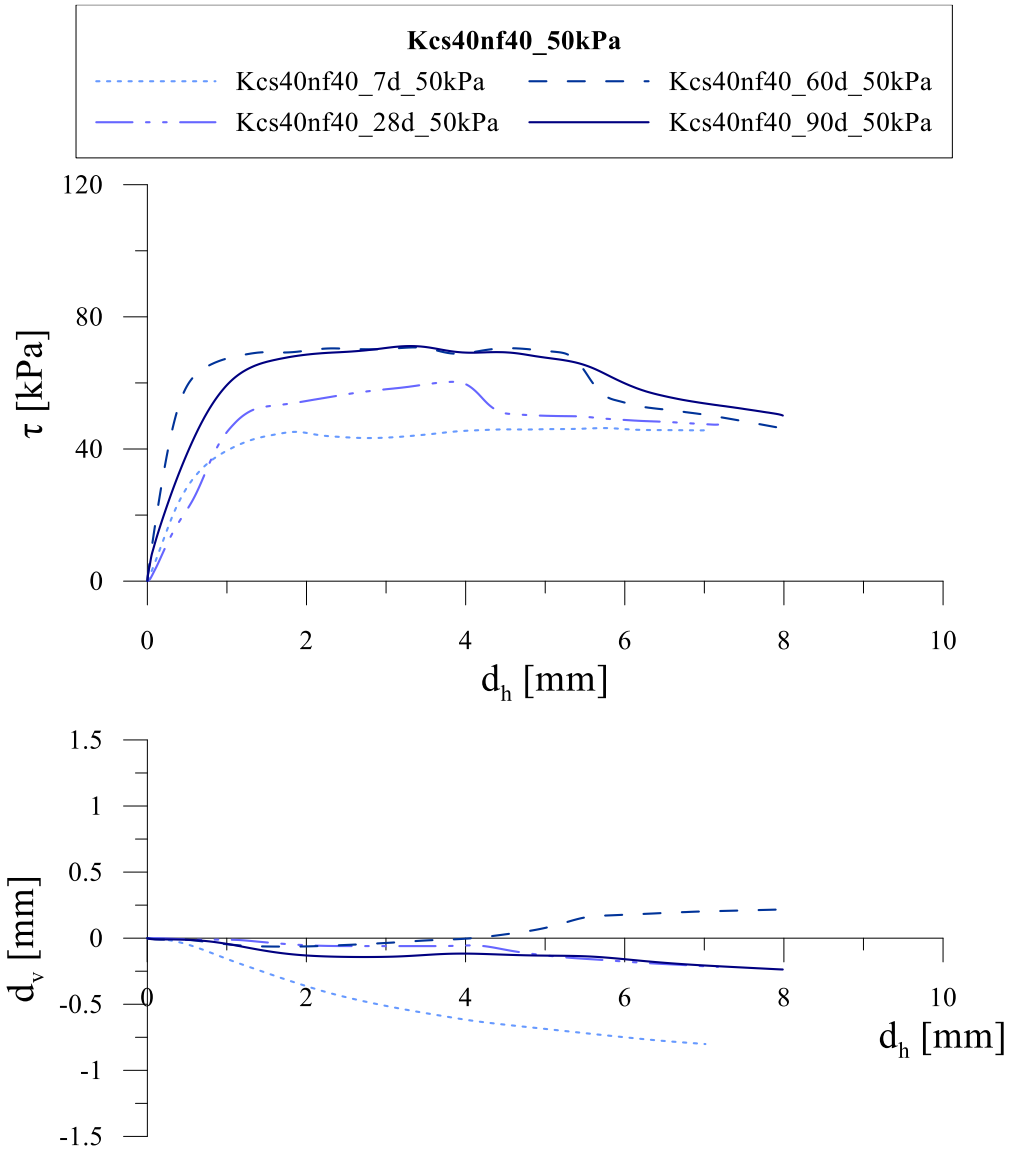

Figure 7-26. Direct shear tests on Kcs40nf40 at σ_v'=50 kPa at different curing times (7, 28, 60, 90 days).

Similar results were found at 100 kPa (Figure 7-27). The curves tend towards the same value, while peak strength slightly increase from 28 to 90 days, so that a small softening can be observed at 90 days of curing. The behaviour is contractive, conversely to tests at the same curing time and lower vertical stress. Except for the test at 90 days, at increasing curing time the volumetric behaviour becomes more dilative.

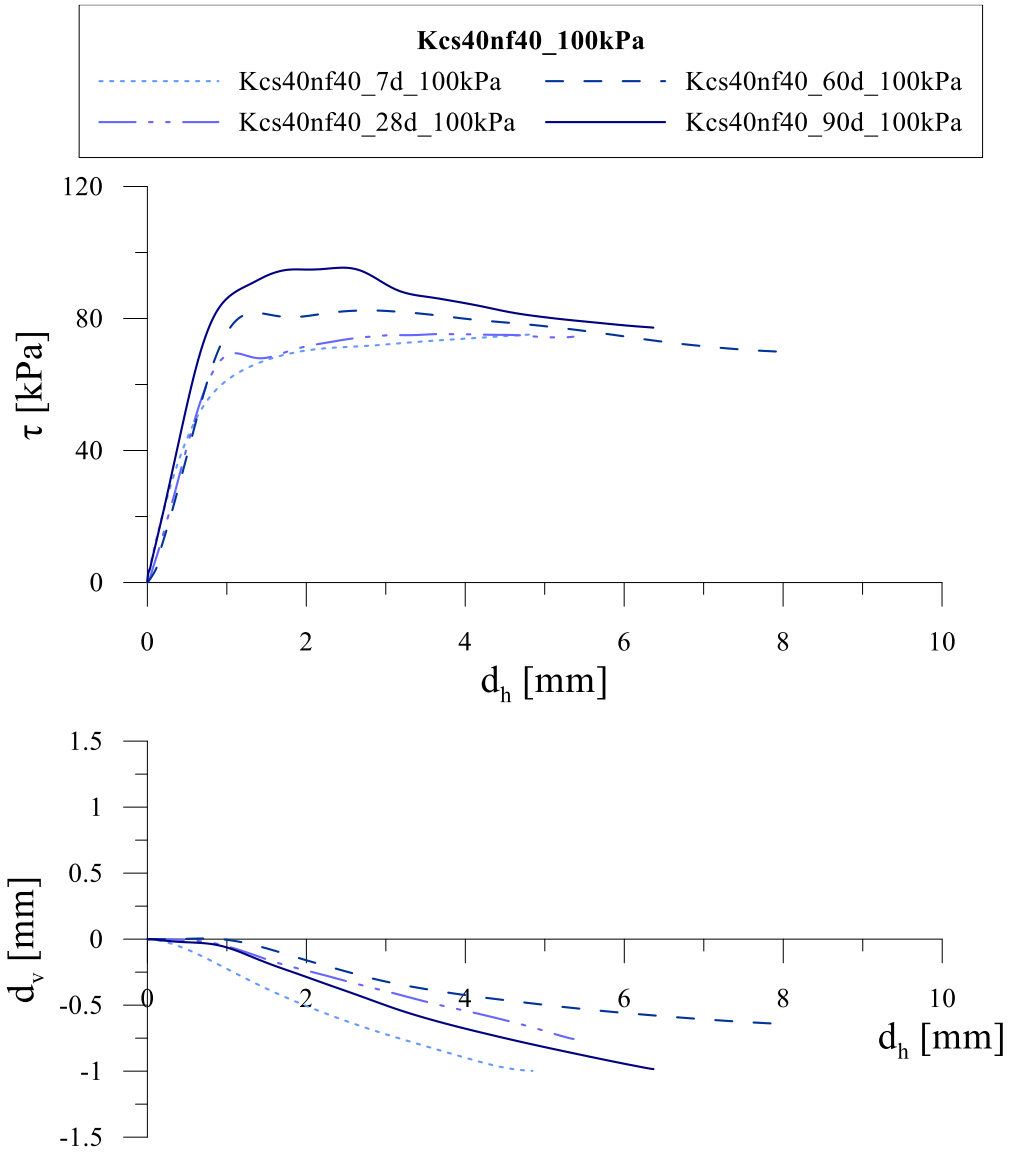

Figure 7-27. Direct shear tests on Kcs40nf40 at σ_v' =100 kPa at different curing times (7, 28, 60, 90 days).

7.1.2.4. Oedometric tests

Oedometric tests results on lightweight samples are shown in the following. In Figure 7-28 a comparison between tests on Kcs40 and Kcs40nf40 at two different curing times is shown. In the plane ε-logσ_v' the reduction of yield stress due to addition of foam (respect to Kcs40) can be clearly observed. At 7 days of curing, the yield stress is approximately equal to 150 kPa, but non-negligible strains are observed also at lower stresses (50 and 100 kPa). At 28 days, the Kcs40nf40 sample shows significant deformations above 220 kPa, with very large strains above 300 kPa.

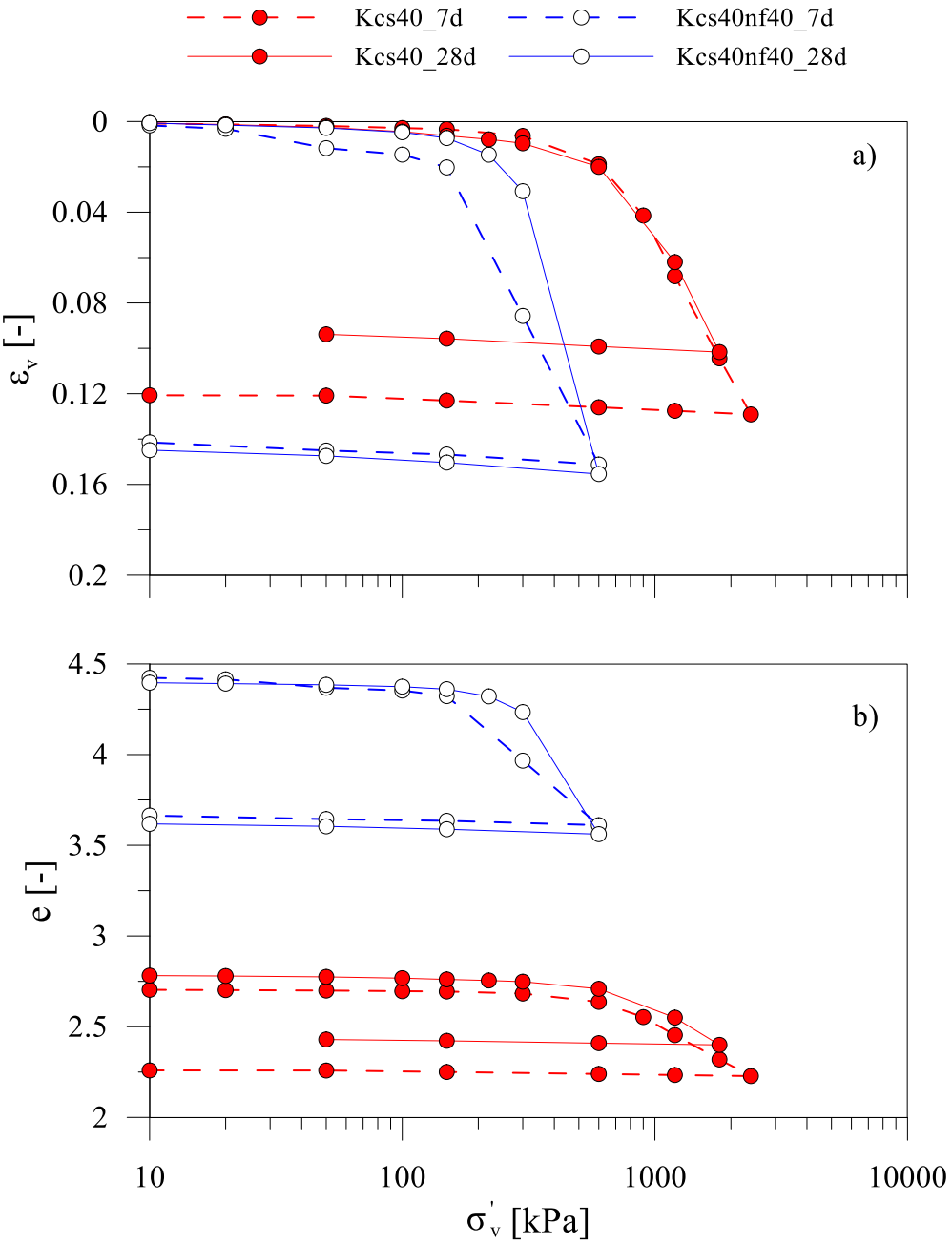

Figure 7-28. Comparison between oedometric tests on Kcs40 and Kcs40nf40 after 7 and 28 days of curing.

This significant reduction of yield stress can be explained by the increase of porosity, especially in terms of void ratio. Indeed, the initial void ratio of lightweight samples is significantly larger than non-lightened ones. In Figure 7-14 results of oedometric tests on Kcs20, Kcs40, Kcs20nf20 and Kcs40nf40 at 28 days are presented. The same reduction in yield stress, respect to Kcs20, is

observed on Kcs20nf40 sample, in which non-negligible strains occur above 50 kPa and very large strains occur above 150 kPa.

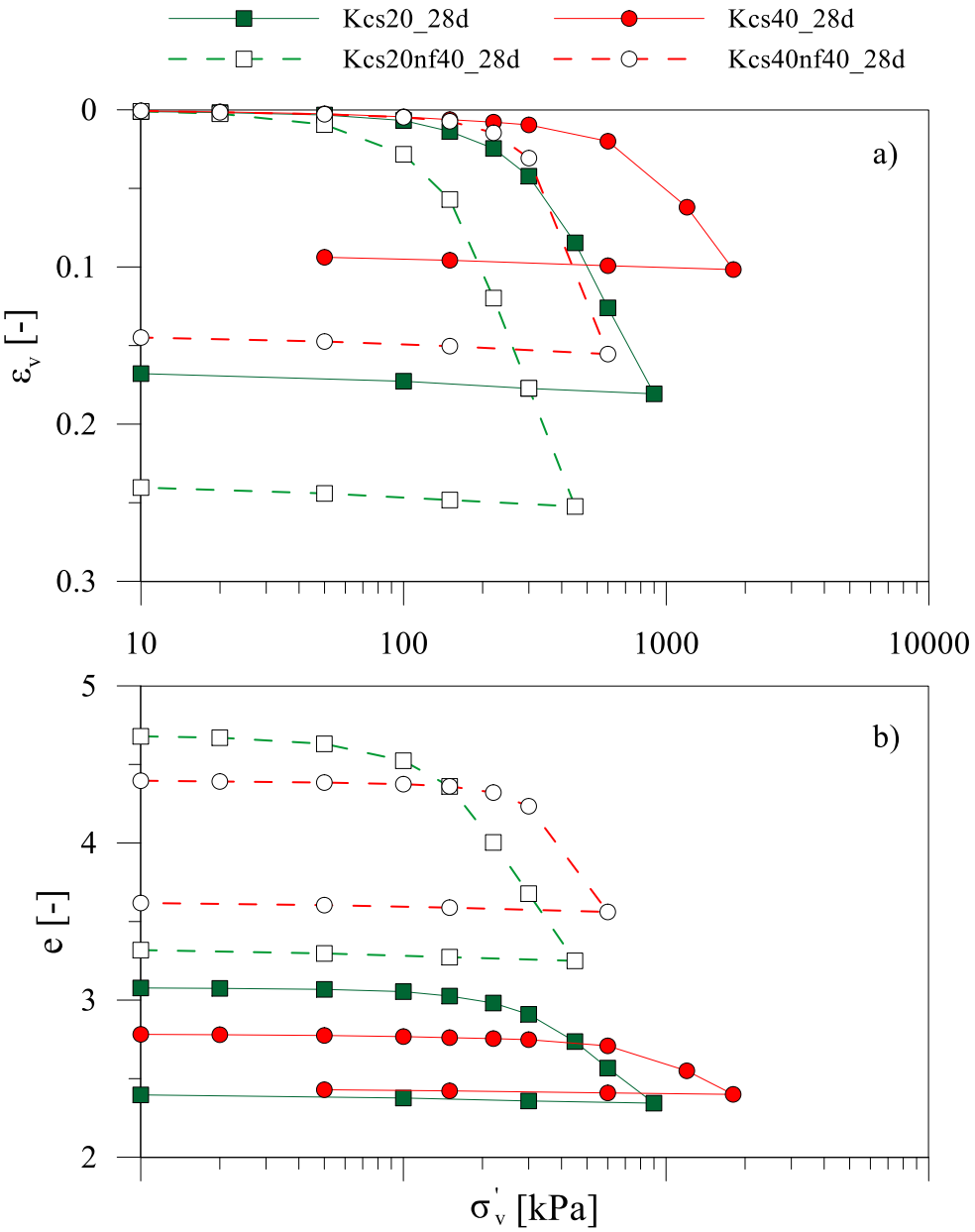

Figure 7-29. Comparison between oedometric tests on Kcs20, Kcs20nf40, Kcs40 and Kcs40nf40 after 28 days of curing.

The behaviour of Kcs20 and Kcs20nf40 is quite similar in terms of strains (the same similarity was found in direct shear tests, Figure 7-22 and Figure 7-23); however, the physical states are different. The initial void ratio of Kcs40nf40 is approximately 1.5 times the initial void ratio of Kcs20.

It is also worth noting that yield stress of Kcs40nf40 is higher than Kcs20nf40, while void ratio of the former is only slightly lower than the latter. In Figure 7-30 a comparison with compression curves of non-treated kaolin (dotted lines) is shown. The void ratio of lightweight samples is highly above non-treated soil so that they are almost incomparable in the plane e-log$\sigma_v^{'}$.

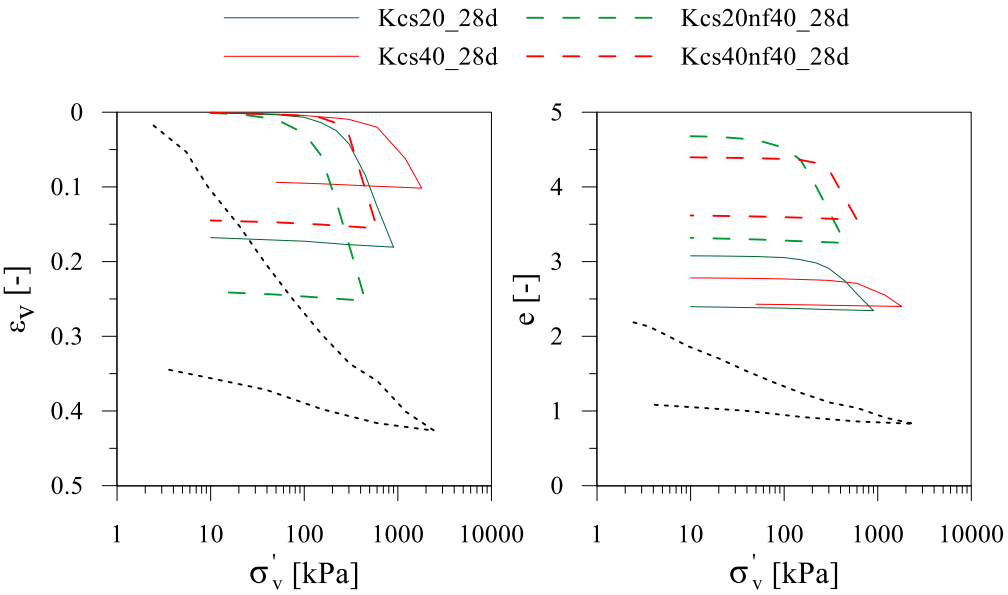

Figure 7-30. Comparison between oedometric tests on cemented and non-treated kaolin (dotted line).

7.2. Influence of degree of cementation

Relationships based on index properties and mix design parameters to predict the strength of cemented and lightweight cemented soil, usually in terms of unconfined compressive strength (UCS), have been proposed by different authors, as discussed in section 4.4. These equations show a strong dependency on cement content and water content (or porosity). The purpose of these equations is usually to have, at least, a reduction of number of tests required to design the material, or even an estimation of the expected strength when the mixtures are designed. An attempt to describe the evolution of mechanical strength due to investigated variables (cement factor, curing time, foam) is shown thereafter.

7.2.1. Cemented soil

To take account of cementation, the void ratio of bonds, e_b, a state parameter introduced by Pinyol et al. (2007) in a constitutive model (described in section 4.3), was chosen. It is defined as the ratio of bonds volume (assumed non-porous) to the solid volume of clay matrix and it is used to take account of the volume of

bonds in a soft clayey rock. If the volume of bonds is equal to the volume of hydrated cement, then this parameter can be expressed as:

$$e_b = \frac{V_{bonds}}{V_s^s} = \frac{V_{c,h}}{V_s^s} = \frac{\frac{xW_{c,a}}{\rho_{ca}} + \frac{\alpha x \beta W_{c,a}}{\rho_w}}{\frac{W_s^s}{\rho_s}} = \frac{\frac{c}{s}\left(\frac{xW_s^s}{\rho_{ca}} + \frac{\alpha x \beta W_s^s}{\rho_w}\right)}{\frac{W_s^s}{\rho_s}} = \rho_s \frac{c}{s}\left(\frac{x}{\rho_{ca}} + \frac{\alpha x \beta}{\rho_w}\right) \quad (7\text{-}2)$$

All the symbols have been already introduced. The fraction x of cement that is hydrated can be derived by dividing the equation (7-1) by α (the ratio by weight of the water held in hydrated cement and the anhydrous hydrated cement (3-23), equal to 0.23 in a well hydrated paste. It's worth noting that e_b is independent of the amount of foam. It increases with cement factor, c/s, and curing time, thus representing the degree of cementation.

Assuming the Mohr-Coulomb criterion and that cohesion depends on the volume of bonds expressed via e_b, then:

$$\tau_{lim} = c + \sigma_v' \tan(\varphi_0) = f(e_b) + \sigma_v' \tan(\varphi) \quad (7\text{-}3)$$

where τ_{lim}, c and φ are shear strength, cohesion and friction angle, respectively. To understand the effect of e_b on peak strength, the results of all the tests on cemented kaolin were plotted in the plane τ_{lim}-σ_v'tan(φ)-e_b, as shown inFigure 7-31. By this way, the effect of confining stress was subtracted so that the evolution of cohesion with e_b could be observed. At first, the friction angle of non-treated soil, equal to 22°, was considered. It's worth noting that tests at different curing time and cement factor are considered together. A linear function between cohesion and e_b (passing through origin, so that no cohesion exists without bonds) was assumed. Hence:

$$\tau_{lim} = c_b e_b + \sigma_v' \tan(\varphi) \quad (7\text{-}4)$$

where c_b is a parameter that takes account of the effect of bonds on cohesion and φ is the friction angle.

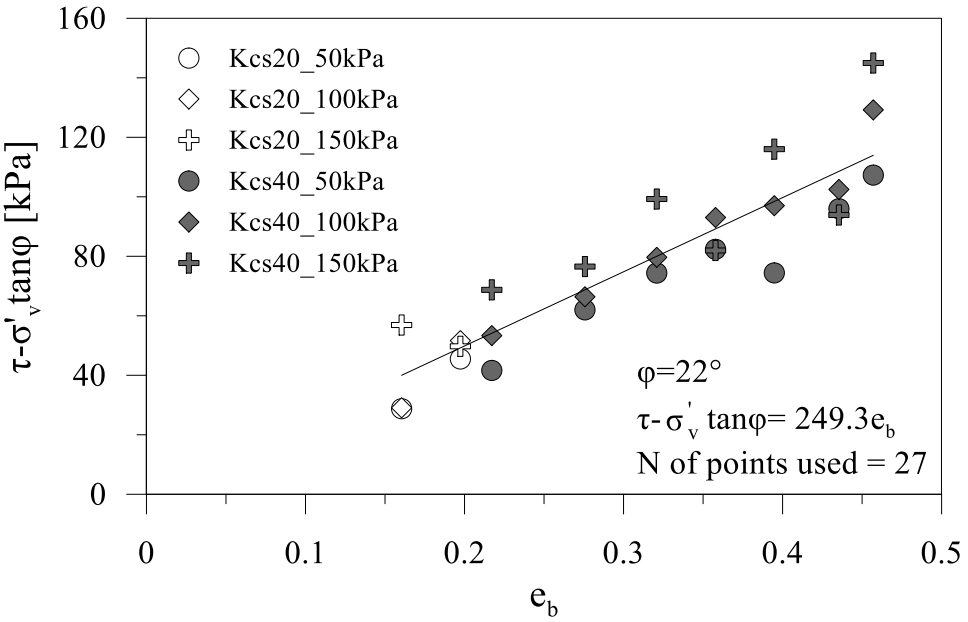

Figure 7-31. Effect of void ratio of bonds on peak strength of cemented kaolin, assuming φ=22° (non-treated kaolin).

The friction angle of a cemented soil is not necessarily equal to the friction angle of non-treated soil; thus, it can be assumed as a fitting parameter. The best fit of the two parameters (c_b, φ) was carried out minimizing the residual sum of squares on all data on cemented kaolin (Kcs20, Kcs40), obtaining φ=27.6° and c_b=215 kPa. The results are shown in Figure 7-33.

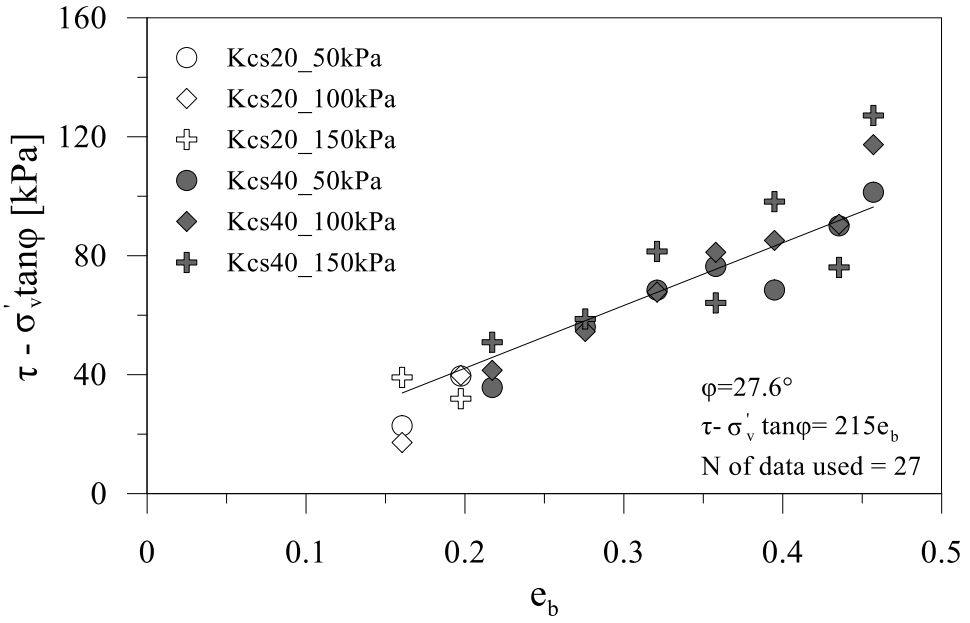

Figure 7-32. Effect of void ratio of bonds on peak strength of cemented kaolin.

In Figure 7-33, direct shear test results are reported in the plane τ/σ_v'-d_h. It is expected that, at large displacements, cohesion goes to zero due to debonding and curves converge towards a critical value, so that τ/σ_v' is equal to tanφ. It appears that 27.6° seems to be consistent with the angle of friction at ultimate strength.

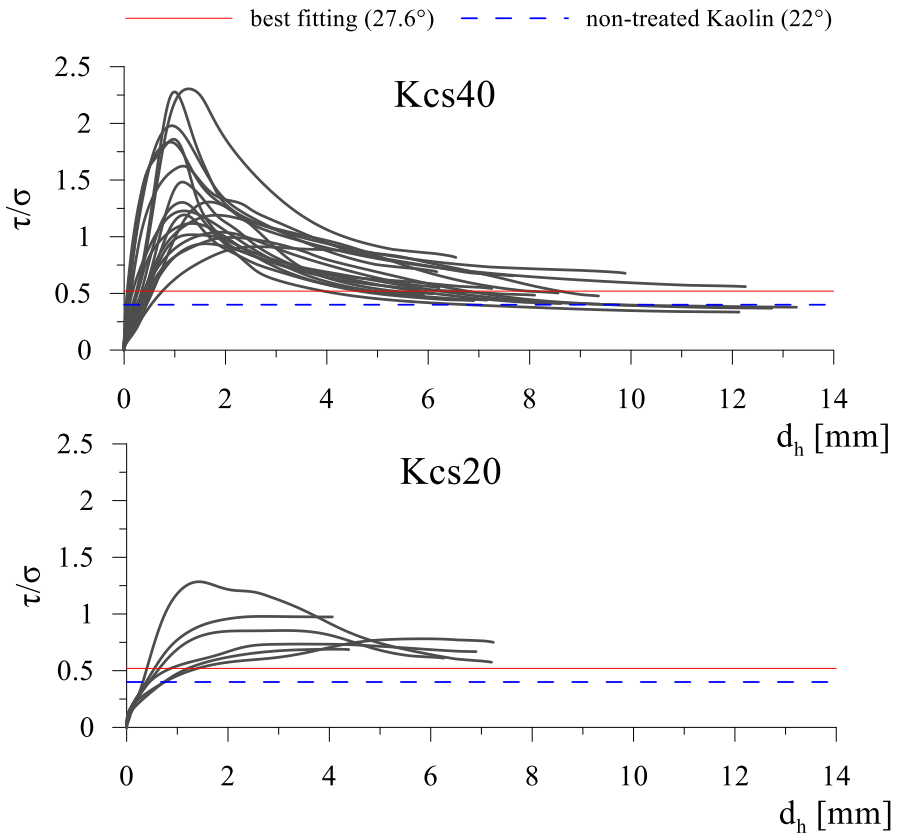

Figure 7-33. Direct shear test results on cemented kaolin in τ/σ-d_h plane.

A limit of this approach is that the influence of porosity is not considered; many authors have shown the negative effect of porosity on the strength (usually the UCS) of a cemented soil. The porosity of the cemented soil, when soil water content is above liquid limit (so that it can be treated as a slurry without air entrapped), depends significantly on the initial water content of slurry itself. Thus, the effect of water content (and porosity) cannot be appreciated in these tests, because the water content of soil slurry is constant and there is only a slight change in porosity with cement factor and curing time. However, especially for a lightweight cemented clay, the purpose of the high soil slurry water content is the reduction of viscosity. It has been observed that the lower the water content, the higher the strength (except for very low water contents); thus, the water content can be set beforehand based on literature suggestions or via rheological

tests (Tsuchida and Egashira, 2004). If water content is set, as it is in this case, the change in porosity is not so emphasized, thus it can be neglected.

Another assumption is that cohesion depends only on volume of bonds, which is dependent on both cement factor and curing time. The peak strength at higher curing times and lower cement factor can be equal or higher than the strength of cemented soil at lower curing time but higher cement factor. In other words, it is assumed that the mechanical behaviour does not depend on the amount of cement, but only on the volume of hydrated cement, i.e. the degree of cementation. Because of this, results of both Kcs20 and Kcs40 have been interpreted together.

7.2.2. Lightweight cemented soil

The same approach was used to study the effect of foam on shear strength. The effect of foam on friction angle was neglected, thus φ was assumed equal to non-lightened soil one (27.6°). The peak strength of Kcs20nf20 and Kcs40nf20 samples (Figure 7-34) and Kcs40nf40 and Kcs40nf40 samples (Figure 7-35). was plotted in the plane $(\tau_{lim} - \sigma'_v \tan\varphi)$-$e_b$ and c_b was determined.

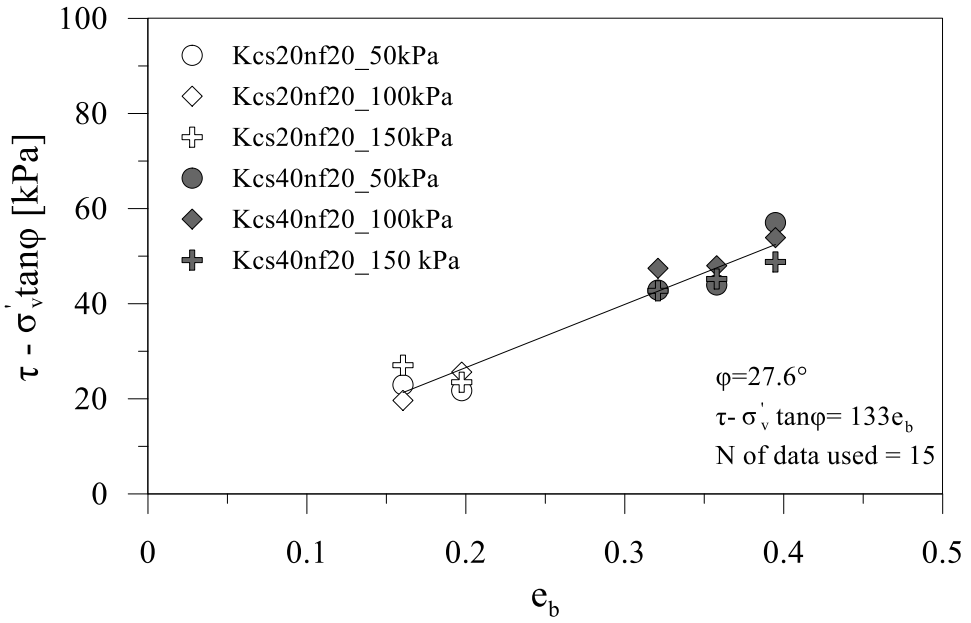

Figure 7-34. Effect of e_b on lightweight cemented kaolin with n_f=20%.

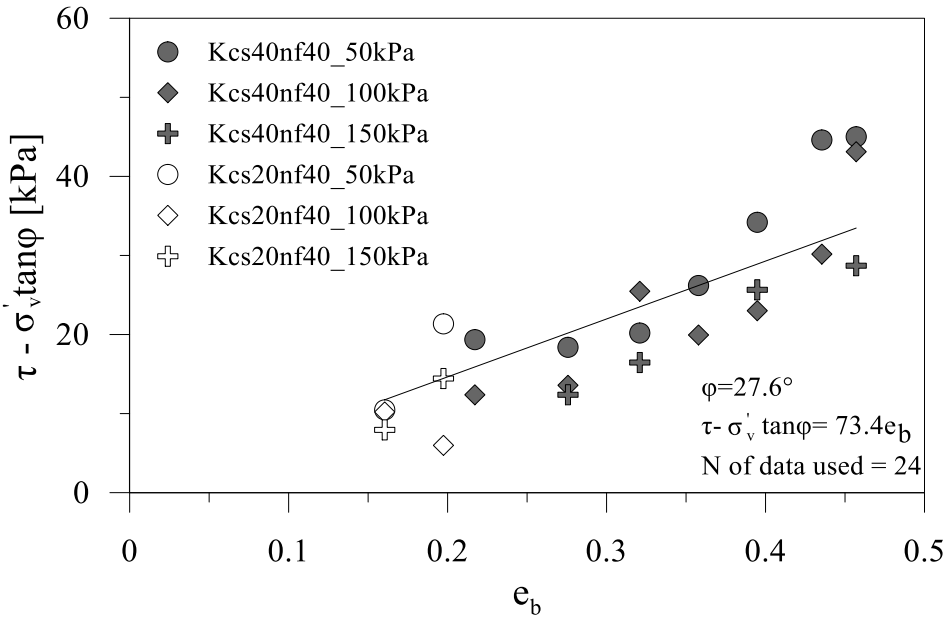

Figure 7-35. Effect of e_b on lightweight cemented kaolin with n_f=40%.

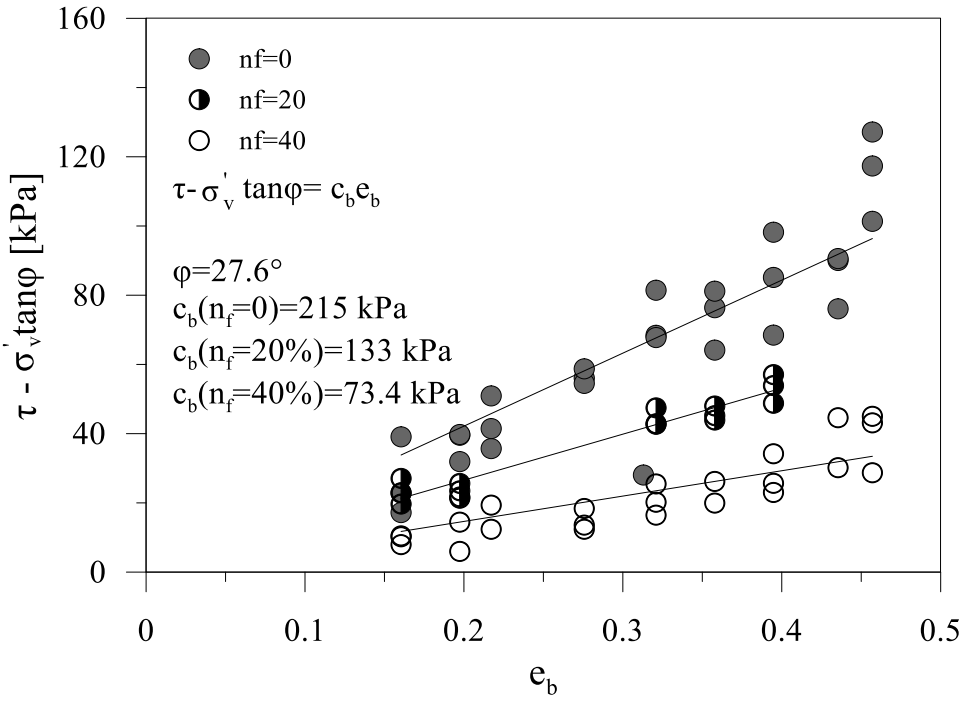

Figure 7-36. Effect of e_b on cemented kaolin and lightweight cemented kaolin at varying n_f.

The best fits of cemented and lightweight cemented kaolin are plotted in Figure 7-36. The coefficient c_b of lightweight cemented samples is equal to 133 and 73.4 kPa for n_f equal to 20 % and 40 %, respectively. As expected, the coefficient c_b decreases with n_f, thus a lower peak strength is observed at the same e_b at increasing amount of foam.

To take account of the effect of foam on cohesion, studies on cellular material were considered (Gibson, L. J., Ashby, M. F. and Triantafillou, 1989; Triantafillou and Gibson, 1990). In these studies, assuming a microstructure composed of cells (i.e. cellular structure), the authors derive a theoretical failure surface for brittle foams ("foam" is intended in the broader sense of cellular material) subjected to multiaxial loading; they adopt the relative density, defined as the ratio of bulk density of the lightweight material to the density of cell material, as a parameter to describe the effect of the increased porosity. The failure surface is derived for very low values of relative density (below 0.3), which can occur, for example, in foam concrete with n_f higher than 60%. However, in a lightweight cemented soil, due to the highly porous cell strut material, the amount of foam cannot be so high. Thus, the relative density is much higher than 0.3 and the resulting material could not have a well-defined cellular structure Due to this, the same failure surface cannot be used; nonetheless the same parameter was adopted, by using the relative dry bulk density (which is independent of water content), $\frac{\gamma_{dry}(n_f)}{\gamma_{dry}(n_f=0)}$, to describe the effect of foam. According to (5-38) and (5-54):

$$\frac{\gamma_{dry}(n_f)}{\gamma_{dry}(n_f=0)} = \frac{\left[\frac{1}{\rho_s}+\frac{w_s}{\rho_w}+\left(\frac{c}{s}\right)\left(\frac{1}{\rho_{c,a}}+\frac{w_c/c}{\rho_w}\right)\right]}{\left[\frac{1}{\rho_s}+\frac{w_s}{\rho_w}+\left(\frac{c}{s}\right)\left(\frac{1}{\rho_{c,a}}+\frac{w_c/c}{\rho_w}\right)\right]+\frac{V_f}{W_s}} = \frac{1}{1+e_f'} = 1-n_f \qquad (7\text{-}5)$$

This ratio doesn't depend on curing time, but it depends only on the volume of foam and, by consequence, on n_f. Due to breakage of bubbles, it has been shown that the "actual" volume of foam is lower than theoretical one, and it can be different for each sample. However, it would be much more convenient to have a unique value to characterize the mixtures. Due to this, the average values of n_f^* (9 % and 11 % for Kcs20nf20 and Kcs40nf20, and 28 % and 29 % for Kcs40nf40 and Kcs40nf40) were considered. The ratio of dry bulk weights was calculated, giving respectively 0.91 and 0.89 for Kcs20nf20 and Kcs40nf20, and 0.72 and 0.71 for Kcs20nf40 and Kcs40nf40. It seems reasonable to use the average values, 0.90 for nf20 and 0.71 for nf40. In Figure 7-37 the ratio $c_b(n_f)/c_{b0}(n_f=0)$ (where c_{b0} is the coefficient c_b of non-lightened mixture) is plotted against relative dry density.

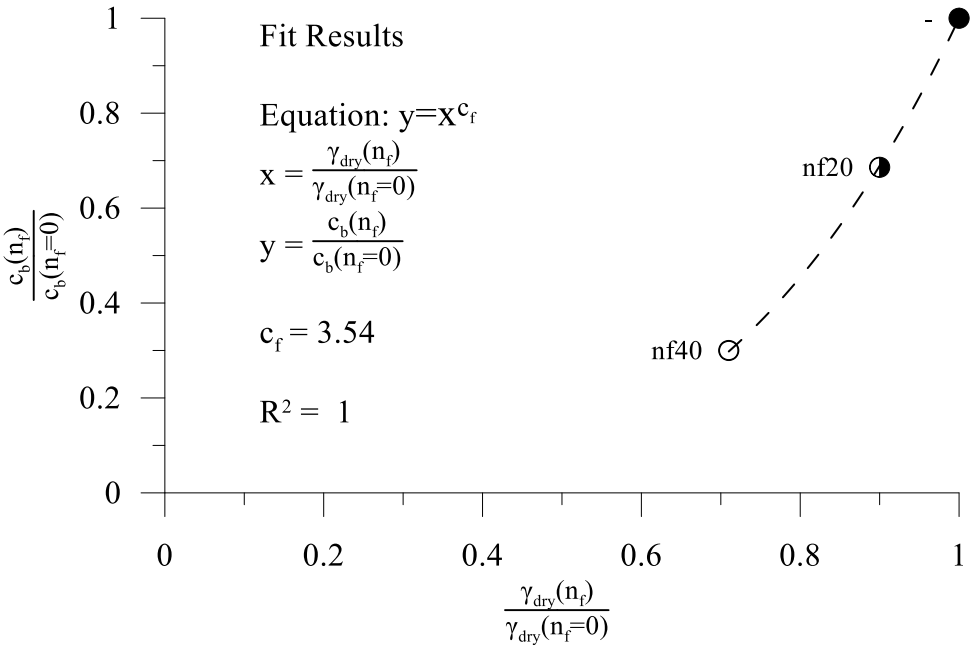

Figure 7-37. Ratio of bond coefficient c_b/c_{b0} against relative density. The dashed line is the fitting curve.

Data were fitted with the following power law (7-6):

$$\frac{c_b}{c_{b0}} = \left(\frac{\gamma_{dry}}{\gamma_{dry,0}}\right)^{c_f} \tag{7-6}$$

where c_f is a fitting parameter, equal to 3.54 in this case. Hence, the failure surface becomes:

$$\begin{aligned}\tau_{lim} &= c_{b0}\left(\frac{\gamma_{dry}}{\gamma_{dry,0}}\right)^{c_f} e_b + \sigma_v' \tan(\varphi) \\ &= c_{b0}\left(1-n_f\right)^{c_f} e_b + \sigma_v' \tan(\varphi)\end{aligned} \tag{7-7}$$

The first term of equation (7-7) states that cohesion decreases with an exponential law at increasing porosity induced by foam and, by consequence, at increasing overall porosity. A similar expression was adopted by Kearsley and Wainwright (2002) for foamed concrete, starting from the Balshin equation for concrete (Balshin, 1949):

$$UCS = UCS_0(1-n)^c \tag{7-8}$$

where n is the porosity, UCS is the unconfined compressive strength, UCS_0 is the unconfined compressive strength at zero porosity and c is a constant (akin to c_f). By fitting results of unconfined compressive tests on foamed concrete

(after 1 year of curing) with varying porosity (from 0.3 to 0.7), they found c=3.6, similar to the value of c_f determined for lightweight cemented kaolin.

In the following, a comparison between measured and calculated time dependent peak strength is shown, with parameters: φ = 27.6°, c_{b0} = 215 kPa, c_f = 3.54. In Figure 7-38, the surfaces at constant $\sigma_v^{'}$ are plotted in the space e_b-$\frac{\gamma_{dry}}{\gamma_{dry,\ 0}}$- τ, while in Figure 7-39 the surfaces at constant $\frac{\gamma_{dry}}{\gamma_{dry,\ 0}}$ are presented. This parameter can be a little tricky: increasing the amount of foam, $\frac{\gamma_{dry}}{\gamma_{dry,0}}$ decreases; increasing $\frac{\gamma_{dry}}{\gamma_{dry,0}}$, the amount of foam is reduced.

In Figure 7-38, it is clear that decreasing the $\frac{\gamma_{dry}}{\gamma_{dry,0}}$ ratio, the effect of e_b decreases as well and cohesion increases slowly in time even if the progress of hydration is the same.

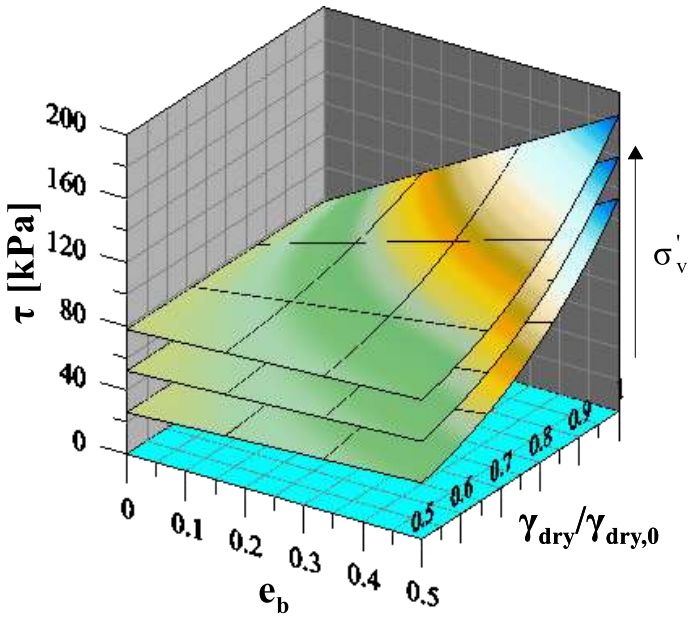

Figure 7-38. Representation of failure surfaces at constant $\sigma_v^{'}$ (50 – 100 – 150 kPa) given by (7-7) for φ = 27.6°, c_{b0} = 215 kPa, c_f = 3.54.

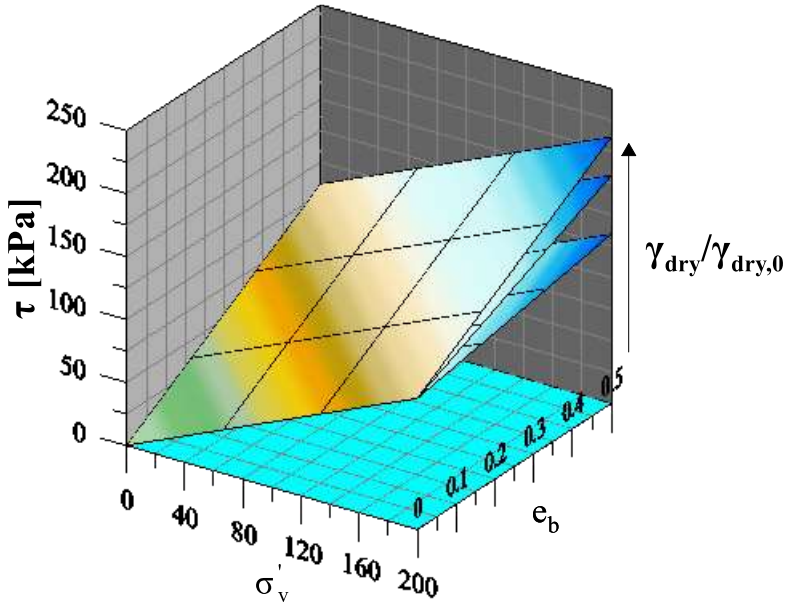

Figure 7-39. Representation of failure surfaces at constant $\frac{\gamma_{dry}}{\gamma_{dry,0}}$ (0.71 – 0.9 – 1) given by (7-7) for φ = 27.6°, c_{b0} = 215 kPa, c_f = 3.54.

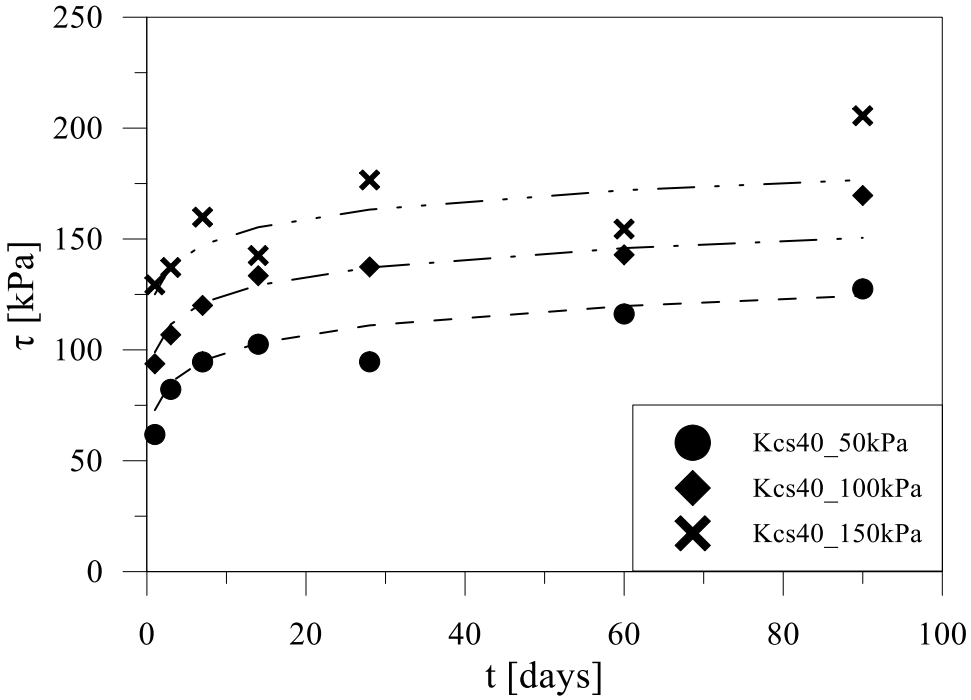

Figure 7-40. Comparison between measured and estimated τ_{lim} in time (Kcs40).

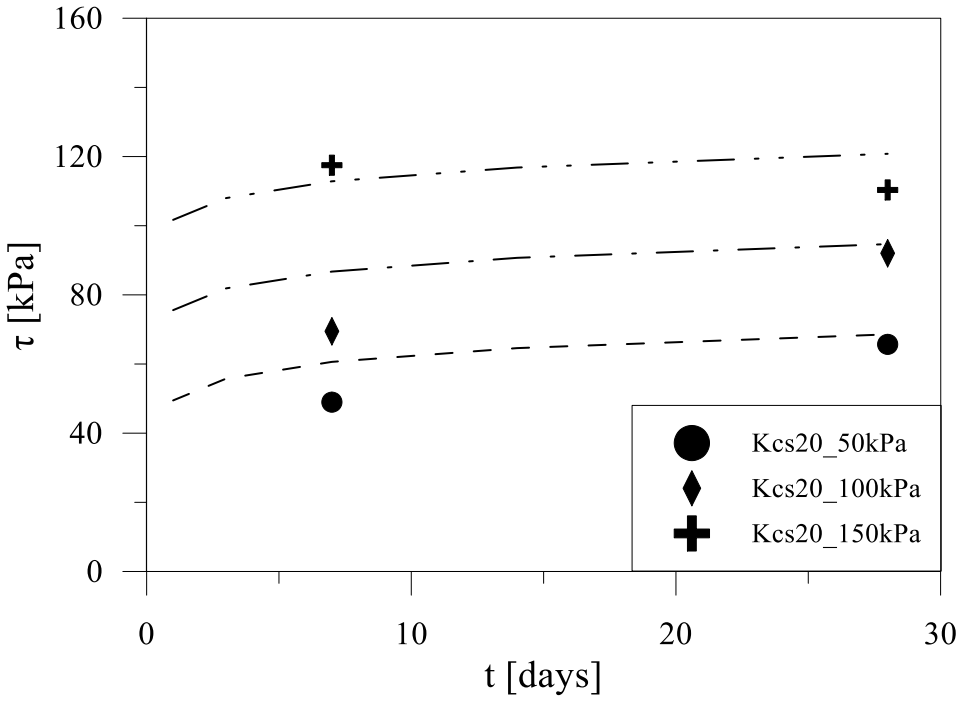

Figure 7-41. Comparison between measured and estimated τ_{lim} in time (Kcs20).

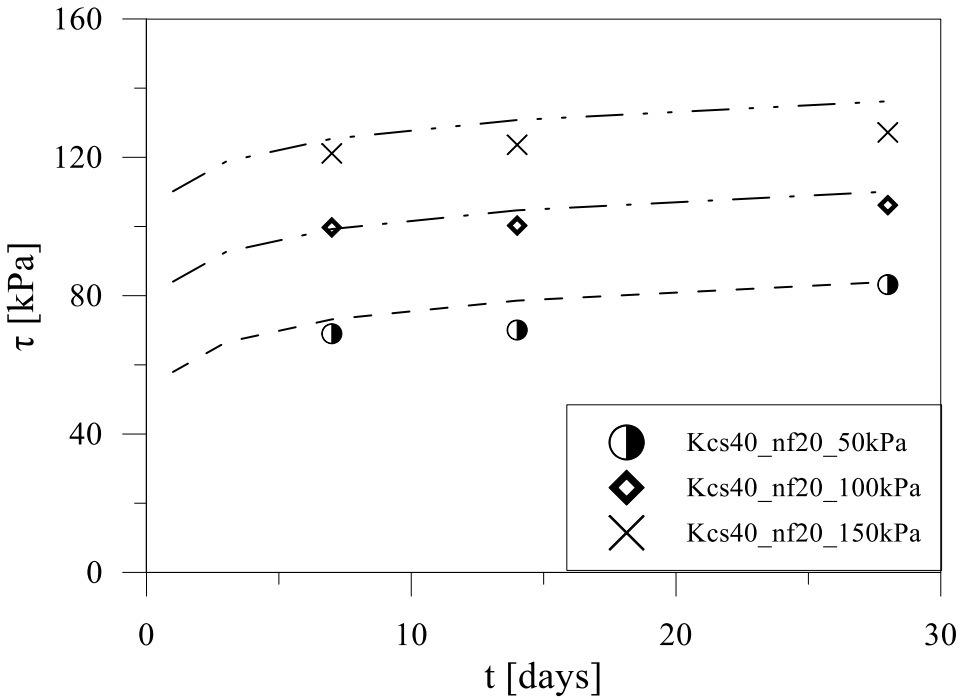

Figure 7-42. Comparison between measured and estimated τ_{lim} in time (Kcs40nf20).

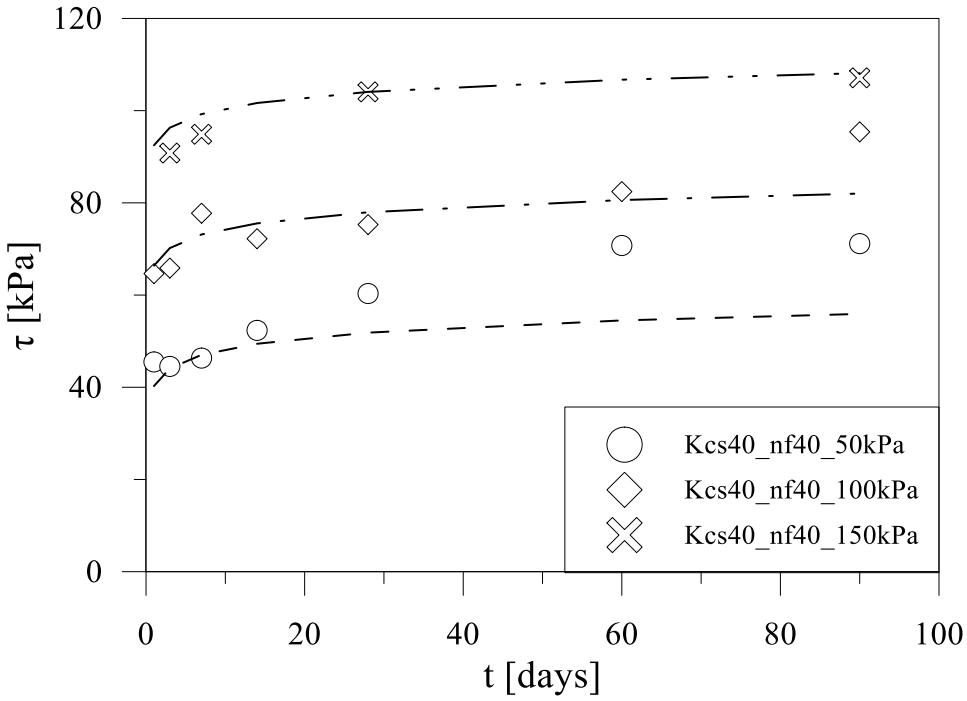

Figure 7-43. Comparison between measured and estimated τ_{lim} in time (Kc40nf40).

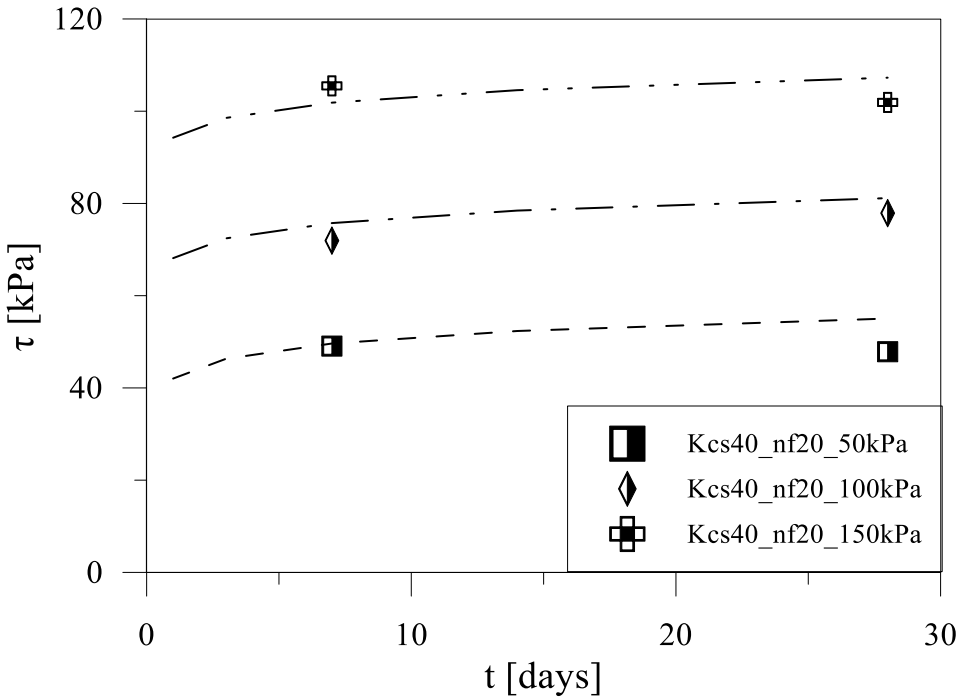

Figure 7-44. Comparison between measured and estimated τ_{lim} in time (Kcs20nf20).

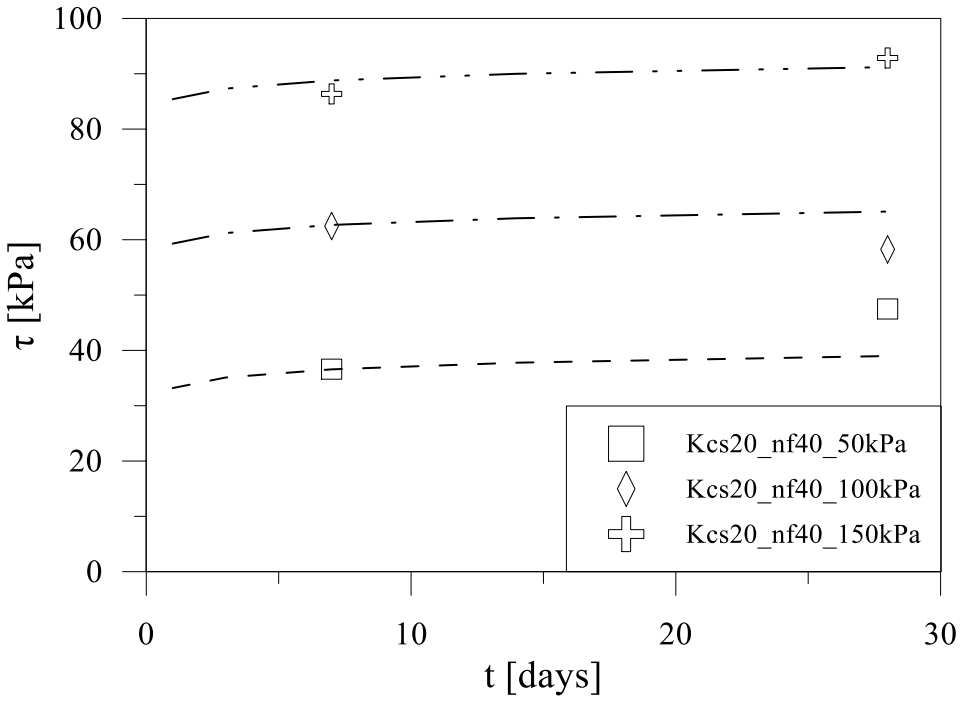

Figure 7-45. Comparison between measured and estimated τ_{im} in time (Kcs20nf40).

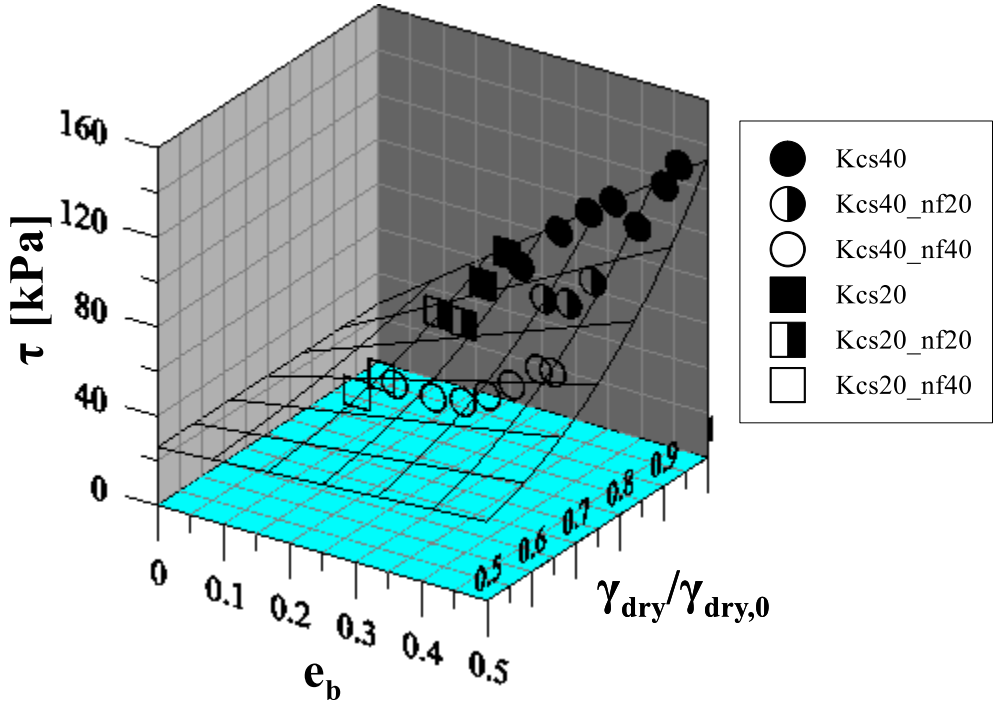

Figure 7-46. Comparison between measured and estimated τ_{im} in time, σ_v'=50 kPa.

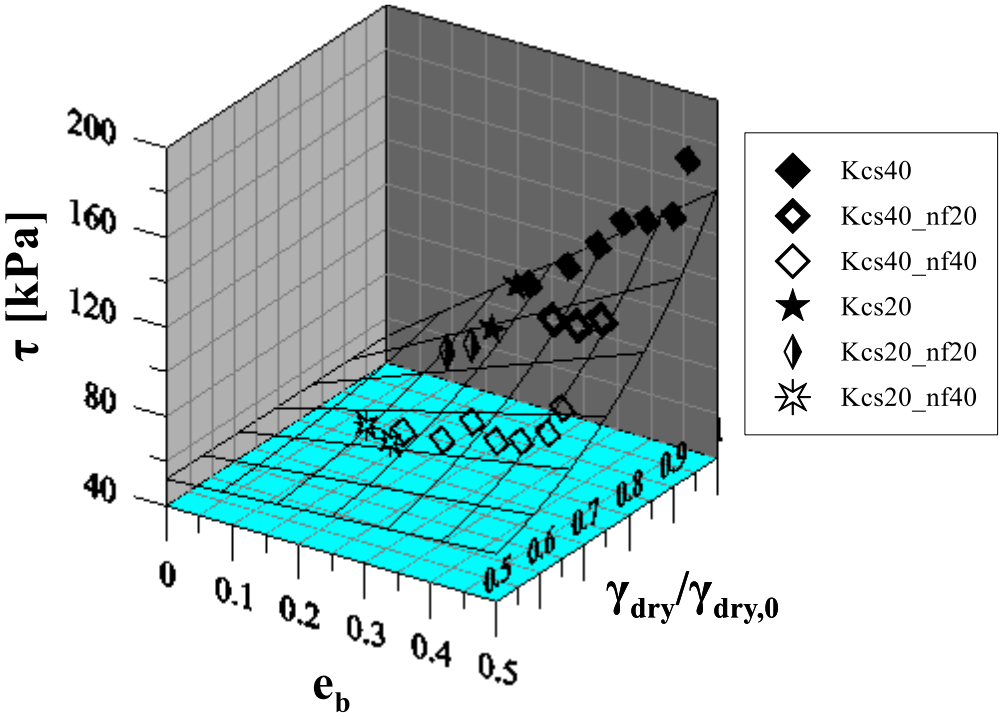

Figure 7-47. Comparison between measured and estimated τ_{lim} in time, σ_v'=100 kPa

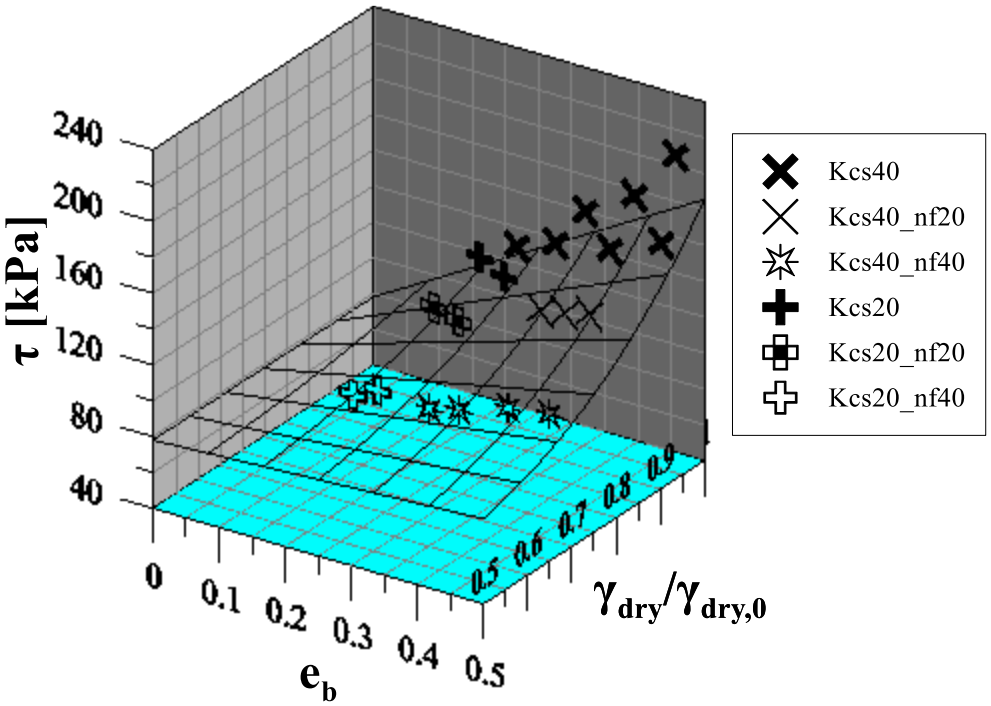

Figure 7-48. Comparison between measured and estimated τ_{lim} in time, σ_v'=150 kPa

Triantafillou and Gibson (1990) also suggest that an influence of relative density on the effect of isotropic stress on failure surface exists, and a proportionality with the square root of relative density is identified. However, as already pointed out, this is derived for brittle foams with relative density lower than 0.3, thus the exponent could be different in the case discussed here and it would be another parameter to fit. Then, more tests at different amount of foams would be required to have a solid fitting of parameters. However, the aim of such an approach is to reduce the number of tests required to have a good prediction of strength and, in the range of investigated amounts of foam, it seems consistent to neglect this effect. Indeed, the main problem of the lightweight cemented soil is related to the high number of factors that affect its mechanical properties, which can be identified in c/s, w_s and n_f (or equivalent parameters). Furthermore, the effect of confining stress must be considered, and tests must be done at the same curing time to be compared. They are usually referred to 28 days, which can be a significant amount of time when mix design parameters can be still modified. The proposed approach, despite its limits, allows to consider in a consistent way both curing time and cement factor, so that tests at different times and cement content can be considered together whereas strength at higher curing times can be estimated from tests at early curing, so that corrections to mix design can be applied in a few days.

7.2.2.1. Simplified method to estimate αx(t)

In order to use all the equations proposed it is necessary to know the function αx(t). In this study, it was derived from the interpretation of TGA at different curing times, but this is not feasible in each design. In the following, a simplified method is proposed. The linear relationship between volume of bonds and cohesion was assumed to describe the effect of cementation on failure surface:

$$c = c_b e_b \rightarrow \frac{c}{c_{max}} = \frac{e_b}{e_{bmax}} = \frac{\left(\frac{\rho_w}{\rho_{ca}} x + \alpha x \beta\right)}{\left(\frac{\rho_w}{\rho_{ca}} + (\alpha x)_{max} \beta\right)} \propto \frac{\alpha x}{(\alpha x)_{max}} \cong x \qquad (7\text{-}9)$$

If a proportionality exists between cohesion of a cemented soil and the amount of non-evaporable water, then the same proportionality can be assumed between the UCS of cement paste and αx. Hence:

$$\frac{UCS(t)}{UCS_{max}} \approx x \qquad (7\text{-}10)$$

This equation states that if x=0 (no cement is hydrated) then UCS=0, while maximum unconfined compressive strength occurs when all the cement is

hydrated; the linear dependency of UCS on x is also assumed. Assuming this proportionality, by knowing the evolution in time of UCS of cement paste, it is easy to determine the function x(t). However, hydration progresses almost indefinitely in time so that it is difficult to define a maximum strength to which relate the total hydration. Furthermore, the linear dependency of UCS from x can be a bit of a stretch. Nonetheless, the function αx(t) is needed to estimate the strength of a cemented soil in a limited period, such as 3 or 6 months; furthermore, the linear proportionality between strength and αx has already been proven for cohesion. Thus, in these hypotheses, by knowing the UCS of the cement paste from commercial datasheet at different times, one can derive the function αx(t) from (7-10). For the cement used in this study, the unconfined compressive strength after 2 and 28 days is above 25 and 47 MPa, respectively. Assuming a logarithmic function for UCS in time, as it is suggested in literature (Çolak, 2006; Elaty, 2014), the UCS trend in time can be derived:

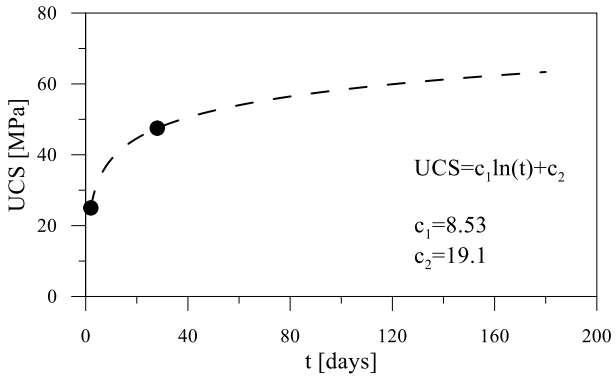

Figure 7-49. Theoretical evolution of UCS in time for CEM II/A 42.5R. Circles refer to minimum strength at 2 and 28 days according to commercial datasheet.

According to standard BS 12 1996, the compressive strength of CEM 42.5R at 28 days must be between 42.5 and 62.5 MPa. In the hypothesis that 62.5 MPa is the maximum compressive strength of the cement paste, the ratio UCS/UCS_{max} can be calculated. If this ratio is equal to x, the trend of x in time is a logarithmic function obtained by dividing the equation shown in Figure 7-49 by 62.5 MPa. As already pointed out, this is not necessarily true, but the purpose is to define a reasonable function to describe the evolution of αx in a simplified way. Hence, assuming α=0.23, the function αx(t) is determined.

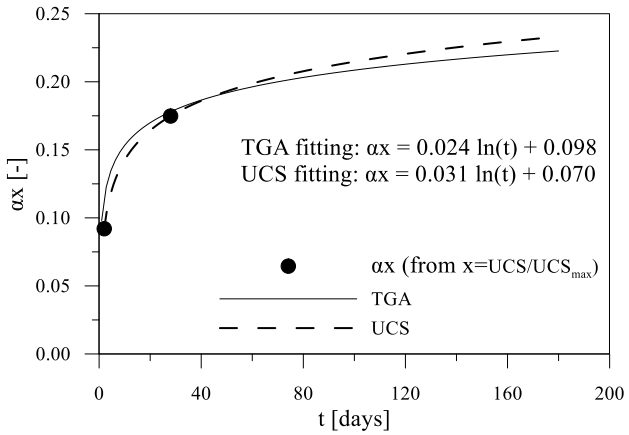

Figure 7-50. Comparison between αx evolution in time derived by TGA analyses and by evolution of UCS in time, assuming 62.5 MPa as maximum strength.

The two functions are quite similar. This is a very simple approach, but it could be used as a simplified method to describe progress of hydration. This approach will be used in the following section for Caposele soil.

7.3. Caposele soil

The lightweight cemented soil method has been used on a natural soil in order to understand if it is possible to generalize the results obtained on Speswhite kaolin. As already shown in 5.3.4, similar mixtures were prepared. The cement factor is kept constant (c/s = 0.4) and the same n_f were adopted, thus the theoretical amounts of foam per unit volume of lightened mixtures are the same of kaolin. A slightly lower water content of soil slurry, equal to 2 times the liquid limit of Caposele soil (≅62 %), was adopted (120 %). The water to cement ratio of grout (w_c/c) is 0.5.

7.3.1. Bulk Properties

In Table 7-3 the physical properties of cement and lightweight cemented samples are presented. The column "t" refers to the curing time at which test is performed, σ'_v refers to the vertical stress applied in direct shear test, γ is the bulk weight, γ_{dry} is the dry bulk weight, derived from dry weight after test, as done for kaolin (7.1.1.1).

Table 7-3. Physical properties of cemented and lightweight cemented Caposele soil.

		t [days]	σ'_v [kPa]	γ [kN/m^3]	γ_{dry} [kN/m^3]	e
C cs40	*Ccs40_7d_50kPa*	7	50	14.5	7.6	2.6
	Ccs40_7d_150kPa	7	150	14.6	7.6	2.6
	Ccs40_28d_50kPa	28	50	14.6	7.5	2.7
	Ccs40_28d_150kPa	28	150	14.8	7.6	2.6
	Ccs40_7d_oed	7	-	14.9	7.6	2.6
	Ccs40_28d_oed	28	-	14.3	7.6	2.6
C cs40 nf20	*Ccs40nf20_7d_50kPa*	7	50	12.2	6.0	3.6
	Ccs40nf20_7d_150kPa	7	150	12.2	6.2	3.4
	Ccs40nf20_28d_100kPa	28	50	12.0	6.2	3.4
	Ccs40nf20_28d_150kPa	28	150	12.0	6.1	3.5
	Ccs40nf20_28d_oed	28	-	12.4	6.5	3.2
C cs40 nf40	*Ccs40nf40_7d_50kPa*	7	50	10.5	5.3	4.2
	Ccs40nf40_7d_150kPa	7	150	10.6	5.1	4.4
	Ccs40nf40_28d_100kPa	28	50	9.2	4.5	5.1
	Ccs40nf40_28d_150kPa	28	150	10.5	5.2	4.3
	Ccs40nf40_7d_oed	7	-	10.0	10.0	4.7
	Ccs40nf40_28d_oed	28	-	9.7	9.7	4.6

A comparison between estimated and measured properties is presented. The theoretical bulk weights, as shown in 5.3.4, are respectively 14.8, 12 and 9.2 kN/m^3. As for cemented kaolin, the bulk weight of non-lightened samples is almost the same of theoretical value. A higher difference is observed for Ccs40nf40, except for some samples. Unlike lightweight cemented kaolin, measured bulk weights of Ccs40nf20 samples are quite similar to theoretical value. As already pointed out, the higher measured bulk weight compared to theoretical value depends on breakage of foam bubbles during mixing. By applying the correction proposed (5.2.1.1), the "actual" n_f can be derived for each sample; the average values for Ccs40nf20 and Cs40nf40 are 0.19 and 0.33, respectively. Assuming these values, the bulk properties were determined. In this case TGA are not available thus αx evolution cannot be estimated directly as for kaolin. The curve derived from proportionality with UCS thresholds, as shown in 7.2.2.1, was used (7-11):

$$\alpha x = 0.031 \ln(t) + 0.07 \qquad (7\text{-}11)$$

A comparison between theoretical and measured bulk properties is shown in Figure 7-51. Data are well fitted by theoretical values, except for Ccs40nf40 at 28 days of curing, characterized by a higher scatter.

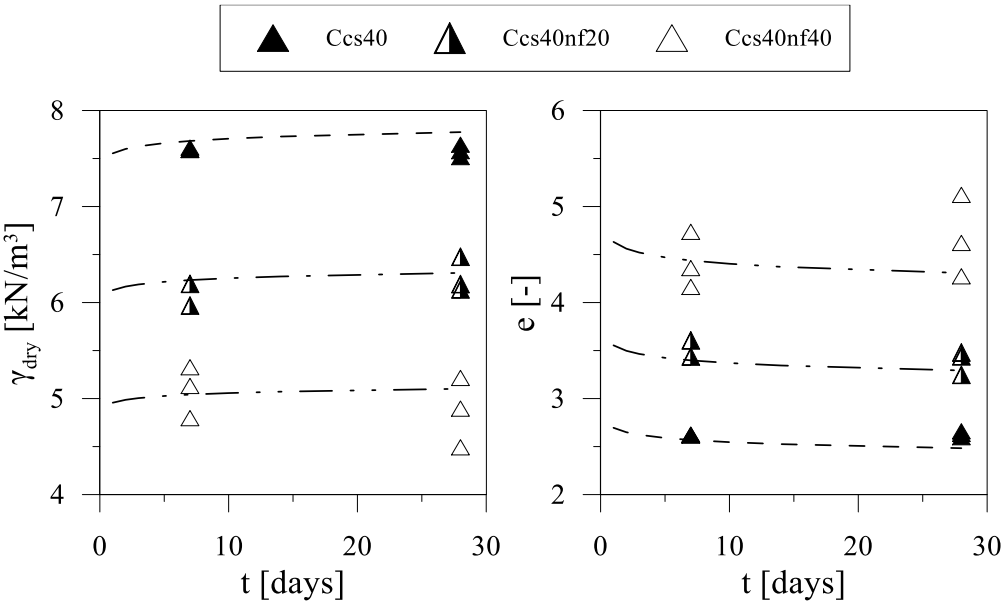

Figure 7-51. Comparison between theoretical and measured dry bulk weight and void ratio of cemented and lightweight cemented Caposele soil.

In Figure 7-52 the comparison between estimated and measured water content is shown. As for kaolin, a larger error is observed on water content, underestimated (especially for Ccs40nf40), respect to dry bulk weight and void ratio.

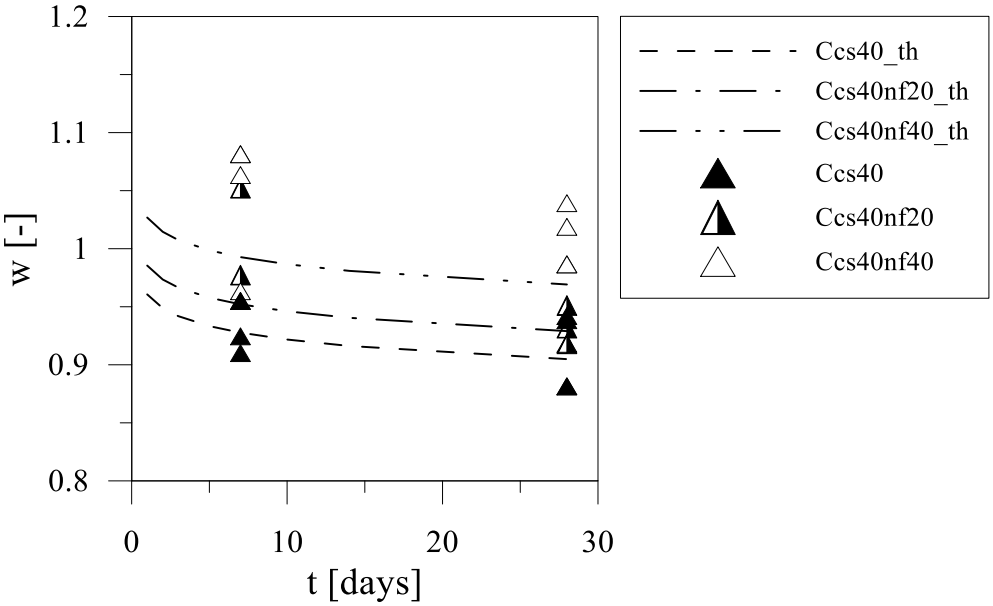

Figure 7-52. Comparison between theoretical and measured water content of cemented and lightweight cemented Caposele soil.

7.3.2. Mechanical tests

7.3.2.1. Direct shear tests

Direct shear tests performed on Caposele soil are presented in this section. In Figure 7-53, results on Ccs40 samples are shown. At increasing vertical stress, an increase in peak strength is observed at both curing times, while behaviour goes from brittle to ductile. The volumetric behaviour is contractive at 150 kPa and dilative at 50 kPa. However, at increasing curing time, the behaviour becomes less contractive (more dilative) at 150 kPa (50 kPa). It is worth noting that peak of dilatancy at 50 kPa is observed after the deformation at which peak strength is gained.

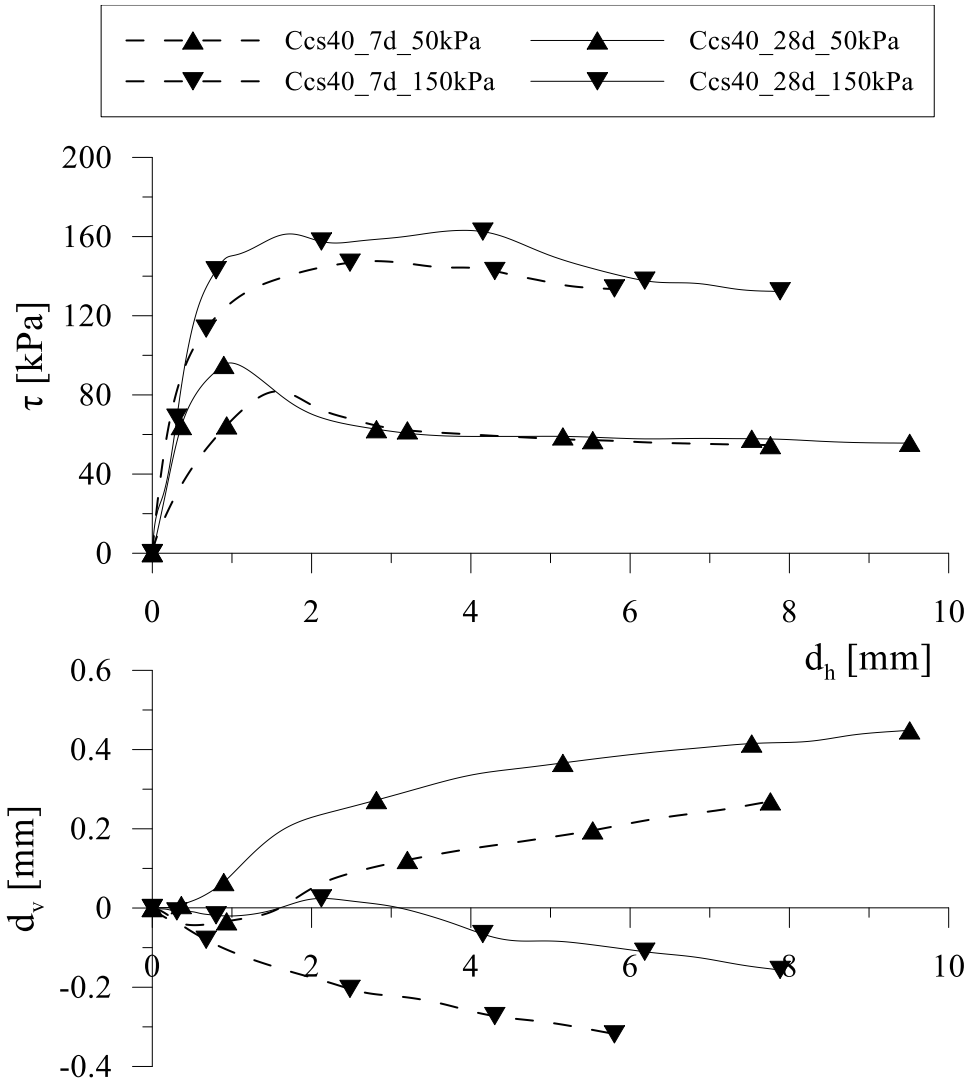

Figure 7-53. Direct shear tests on Ccs40 at σ_v' equal to 50 and 150 kPa, at 7 (dashed lines) and 28 (solid lines) days of curing.

In Figure 7-54 direct shear tests on Ccs40nf20 are presented. At 7 days (dashed lines) the behaviour is ductile and contractive at both vertical stresses, with a more contractive behaviour at a vertical stress equal to 150kPa. After 28 days of curing, the behaviour becomes brittle and slightly dilative at 50 kPa, while it is still ductile and contractive at 150 kPa.

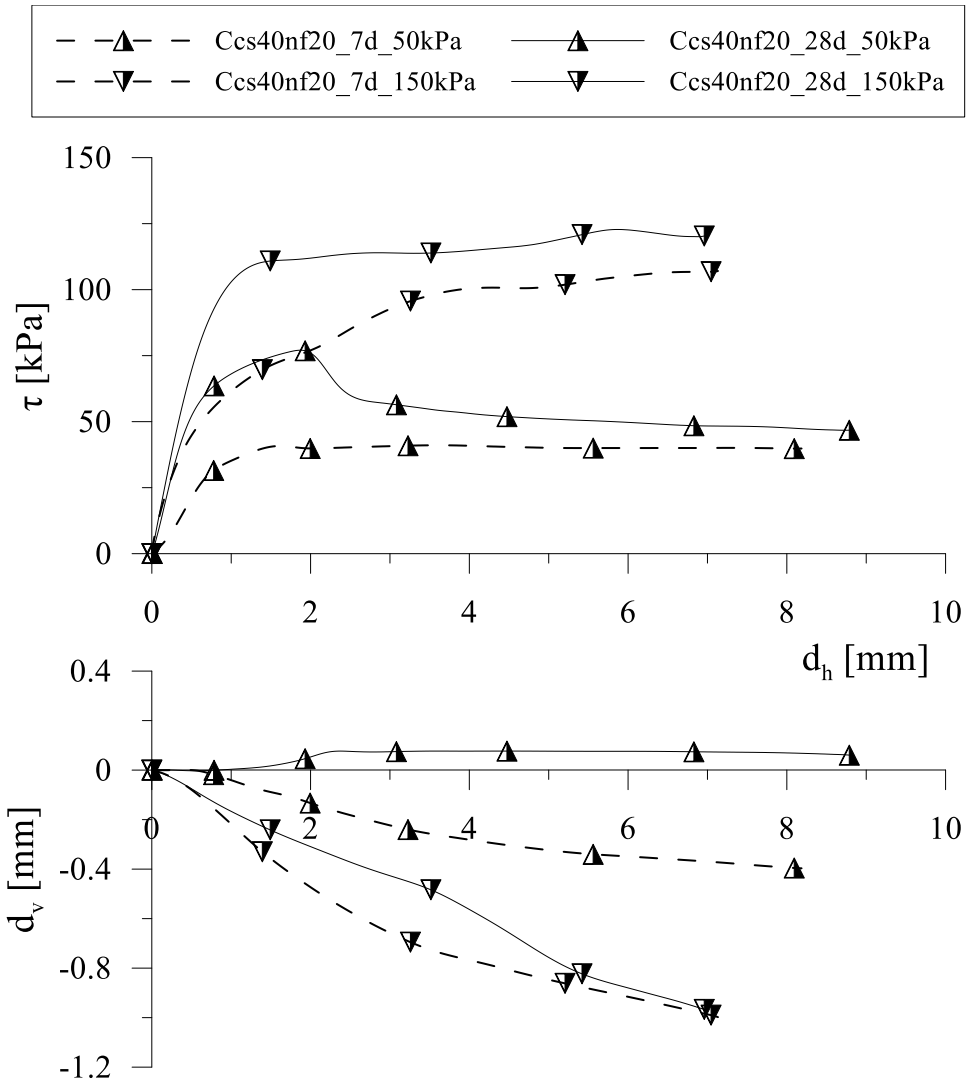

Figure 7-54. Direct shear tests on Ccs40nf20 at σ_v' equal to 50 and 150 kPa, at 7 (dashed lines) and 28 (solid lines) days of curing.

The effect of a further increase of the amount of foam is reported in Figure 7-55. In this case, regardless of confining stress and curing time, the volumetric behaviour is always contractive, and curves are quite similar. The stress-strain curves at 7 and 28 days at a confining stress of 150 kPa are almost coincident;

the behaviour is ductile and (except for Ccs40nf40_28d_50kPa) characterized by a plastic hardening.

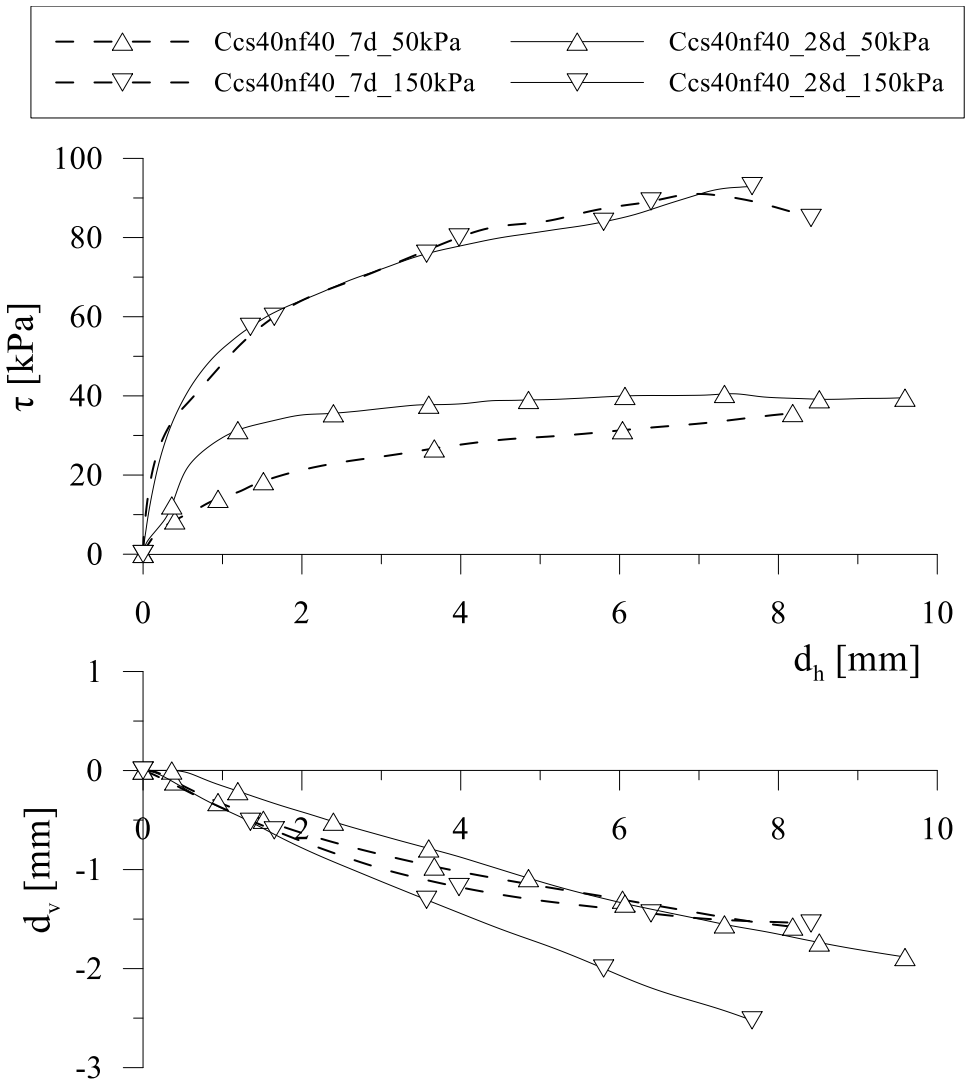

Figure 7-55. Direct shear tests on Ccs40nf40 at σ'_v equal to 50 and 150 kPa, at 7 (dashed lines) and 28 (solid lines) days of curing.

In Figure 7-56 the effect of foam addition on cemented Caposele soil after 7 days of curing is presented; tests performed on non-treated soil are also reported (dotted lines). On the left, results at σ'_v = 50 kPa are shown. The addition of foam causes a reduction of peak strength and the behaviour becomes ductile and contractive. However, curves seem to converge towards the same value, with hardening observed in Ccs40nf40, that shows higher vertical displacements and a similar stress-strain curve compared to non-treated sample. At 150 kPa, the volumetric behaviour of non-lightened sample is already contractive, enhanced

by the addition of foam. The slight softening observed in Ccs40 is not observed on lightened sample.

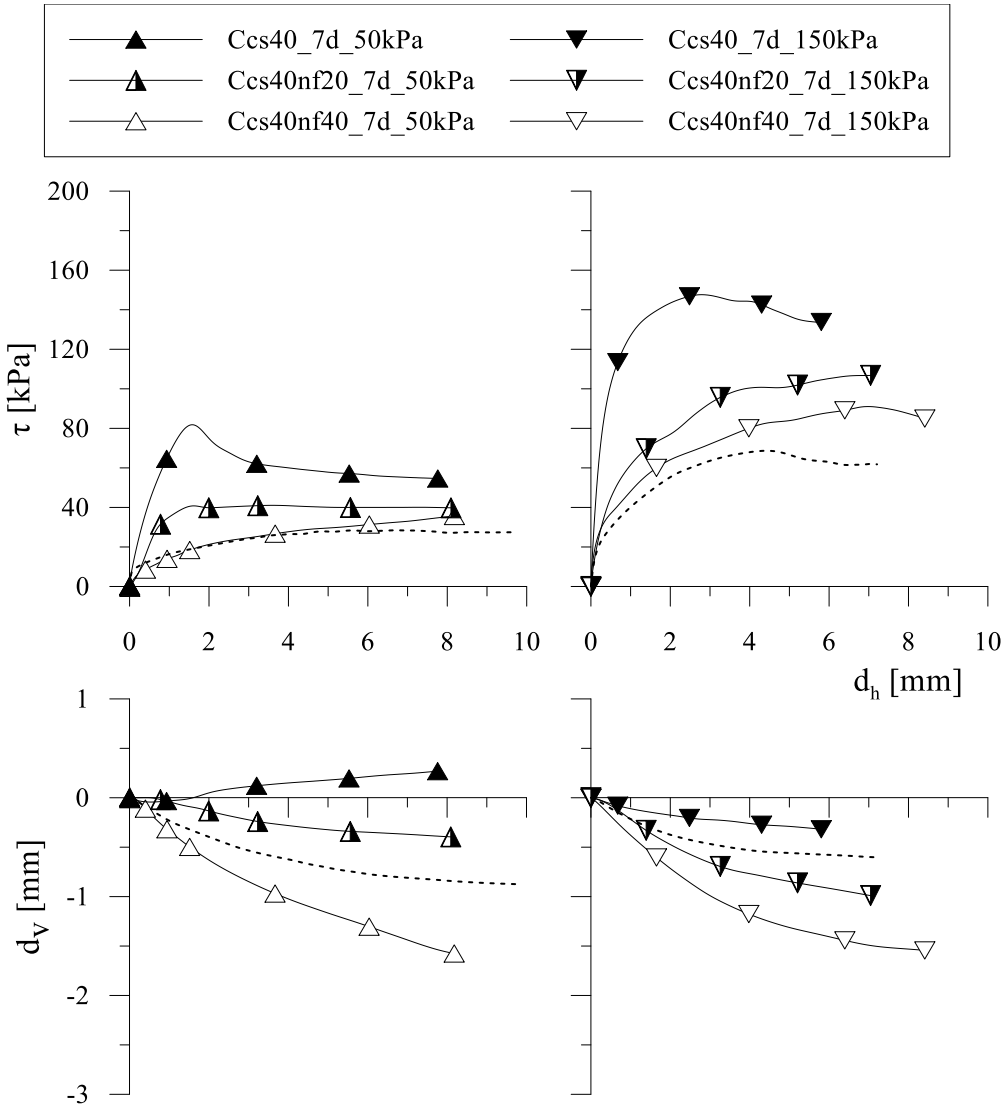

Figure 7-56. Direct shear tests on cemented and lightweight cemented Caposele soil at 7 days of curing and two vertical stresses (50 and 150 kPa). Dotted lines refer to non-treated Caposele soil.

Figure 7-57 shows the same results at 28 days. At a vertical stress of 150 kPa, results are similar to the ones observed at 7 days of curing. At a vertical stress of 50 kPa, instead, the reduction in peak strength is clearer, with the gradual transition from a brittle and dilative to ductile and contractive behaviour at increasing amount of foam.

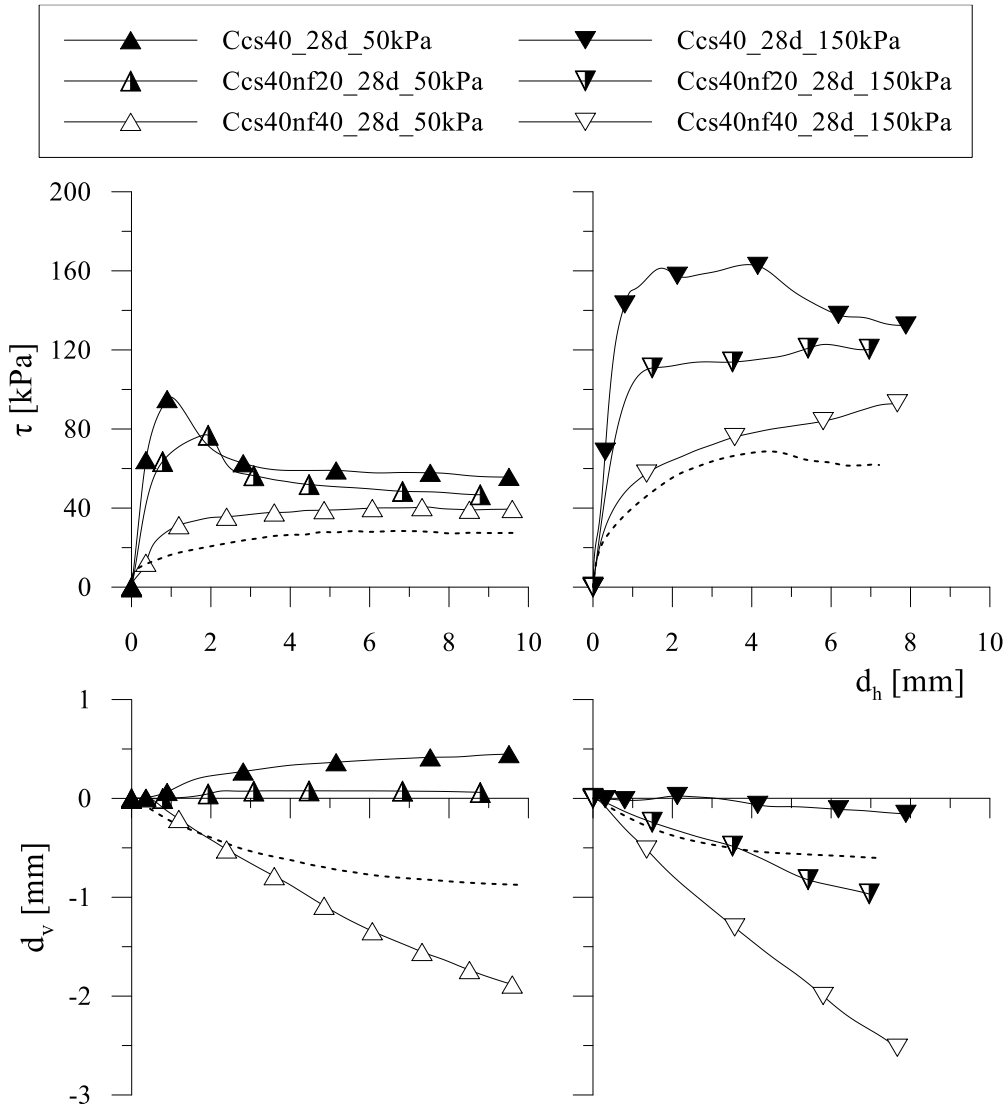

Figure 7-57. Direct shear tests on cemented and lightweight cemented Caposele soil at 28 days of curing and two vertical stresses (50 and 150 kPa). Dotted lines refer to non-treated Caposele soil.

7.3.2.2. Unconfined compressive tests

In Figure 7-58, results of unconfined compressive tests are shown. Solid and dashed lines refer to 28 and 7 days of curing, respectively. The addition of foam determines a progressive reduction of UCS. However, at increasing curing time (from 7 to 28 days), a significant increase in strength can be observed for both Ccs40 and Ccs40nf40.

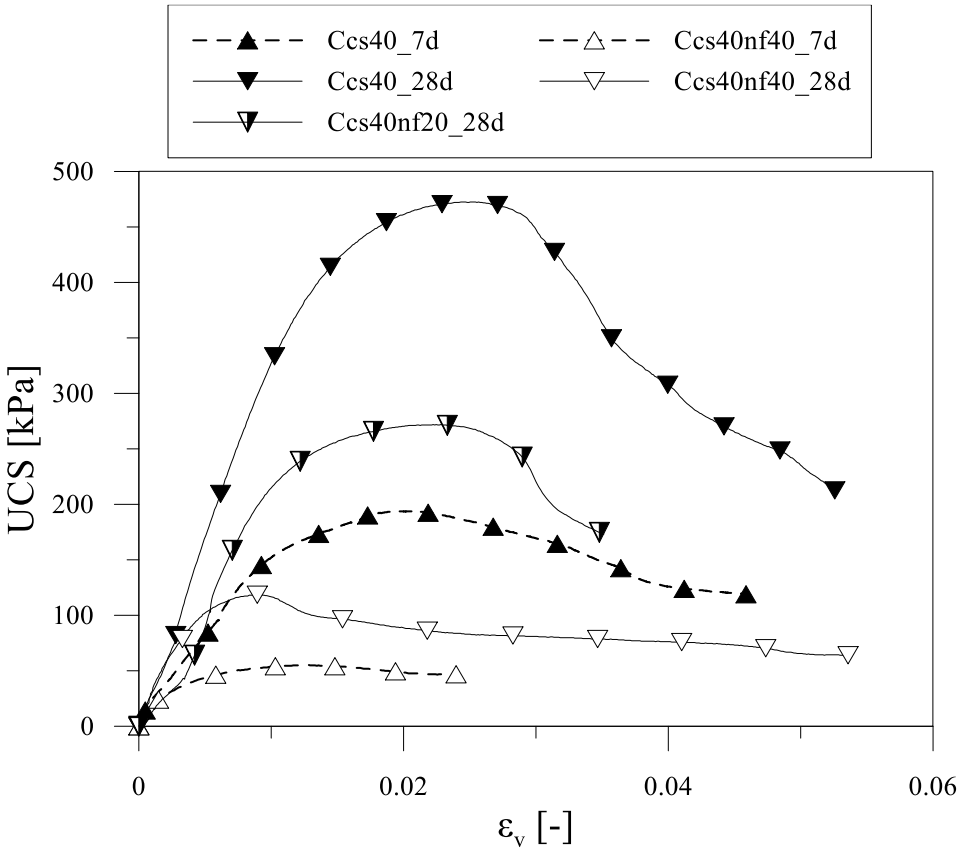

Figure 7-58. Unconfined compressive tests on cemented and lighweight cemented Caposele soil at different curing times.

7.3.2.3. Oedometric tests

In Figure 7-59, oedometric test results at different amounts of foam at 28 days of curing are shown; results are plotted in both ε-log$\sigma_v^{'}$ and e-log$\sigma_v^{'}$. In the former, the significant reduction of yielding stress with increasing amount of foam can be appreciated. Indeed, the Ccs40nf40 is characterized by large deformations (around 10 %) at a vertical load equal to 150 kPa. The same vertical strain occurs between 450 and 600 kPa in Ccs40nf20 and between 900 and 1200 kPa in non-lightened sample. The reconstituted Caposele soil sample has a completely different behaviour. However, the initial physical states of non-treated, cemented and lightweight cemented Caposele soil samples are different. As it can be seen in the plane e-log$\sigma_v^{'}$, the initial void ratio of lightweight material is significantly higher than cemented soil one, and they are both characterized by physical states that are impossible for non-treated soil.

It is possible to observe that cemented and lightweight cemented samples tend towards the same compression line at high stresses. However, the achieved

void ratios are still higher than non-treated sample, thus it's not possible to observe a possible trend towards the same compression line.

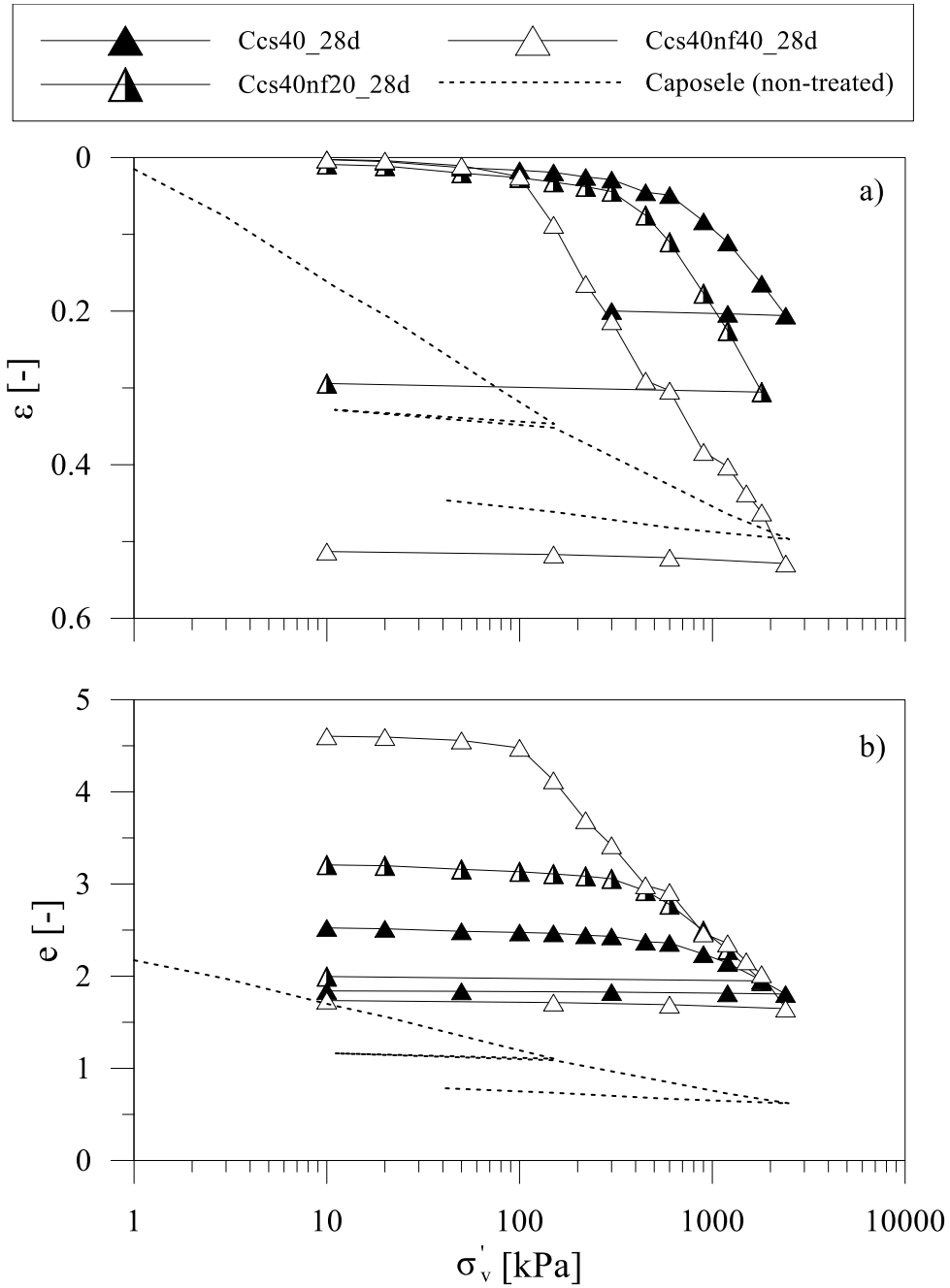

Figure 7-59. Oedometric tests on cemented and lightweight cemented Caposele soil at different amounts of foam after 28 days of curing in ε-logσ_v' and e- logσ_v' planes.

In Figure 7-60 a comparison between Ccs40 and Ccs40nf40 at different curing times is shown.

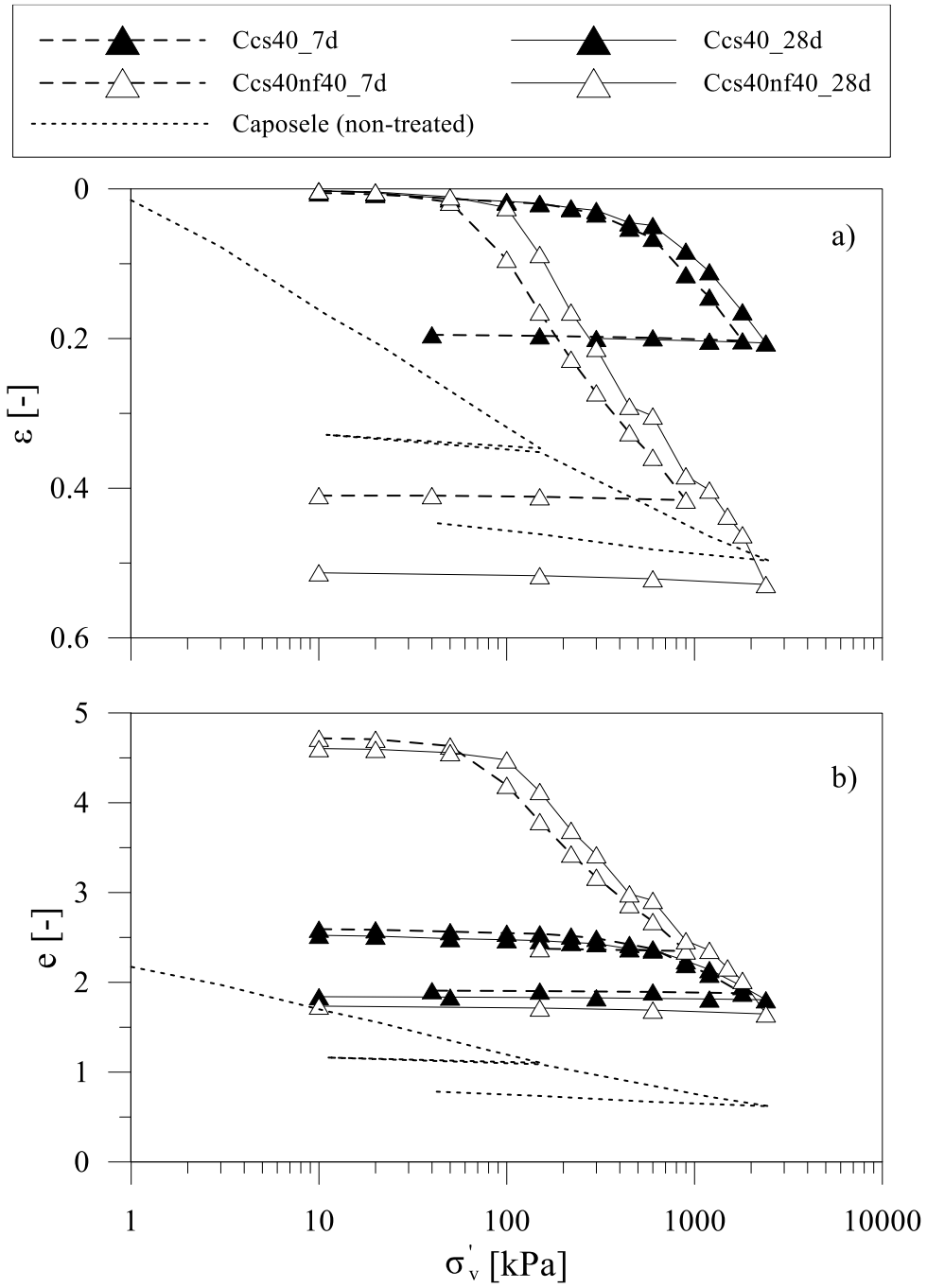

Figure 7-60. Comparison between oedometric tests on Ccs40 and Ccs40nf40 at 7 and 28 days of curing.

In both cases, especially on lightened mixture, an increase in yield stress at increasing curing time is observed. Indeed, significant strains (10%) are observed already at 100 kPa for Ccs40nf40 at 7 days, while the same strains are observed only above 150 kPa after 28 days of curing. Comparing the same mixture at

increasing curing time, it can be observed that the initial void ratio slightly decreases, but curves seem to converge towards the same compression line.

7.3.3. Caposele-kaolin comparison

A comparison between the two investigated soils is presented. It's worth noting that even if both soils are treated with the same cement factors and amounts of foam, the void ratio of the samples can be slightly different. Indeed, the water content of soil slurry is slightly lower in Caposele soil mixtures.

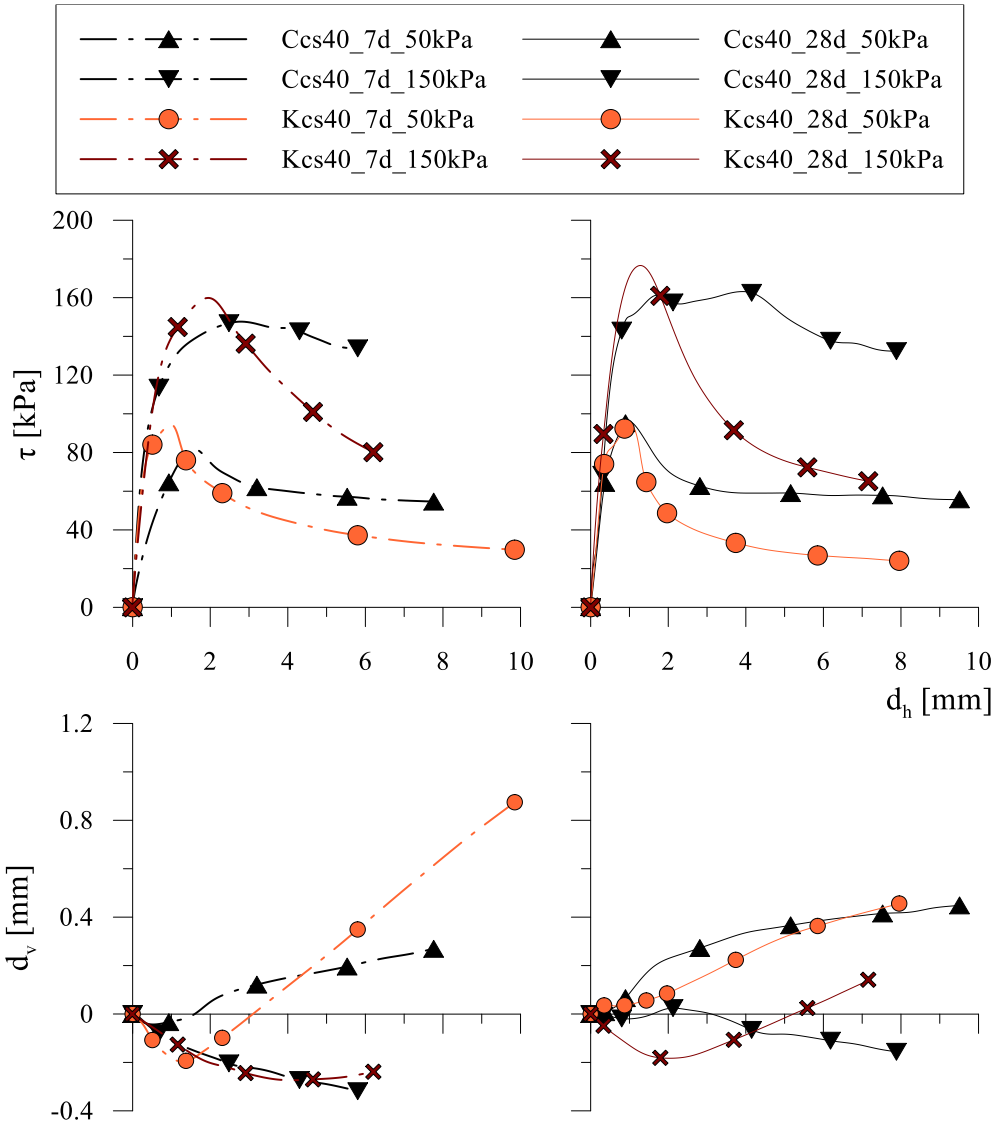

Figure 7-61. Direct shear tests. Comparison between cemented kaolin and cemented Caposele soil, at different curing times and confining stresses.

In Figure 7-61, direct shear tests performed at a vertical stress of 50 and 150 kPa at 7 and 28 days of curing on Kcs40 and Ccs40 are reported. At 7 days of curing and a vertical stress of 50 kPa, strength and stiffness of cemented Caposele soil samples are smaller than kaolin, but characterized by a similar behaviour, which is brittle and dilative (after peak strength) for both. At 150 kPa and 7 days of curing, the peak strength of Caposele soil is slightly lower than kaolin, with a more ductile behaviour but the same volumetric response.

At 28 days of curing, the initial stiffness is the same for both treated soils. At a vertical stress of 50 kPa, the peak strength of cemented kaolin and Caposele soil is the same. At 150 kPa, peak strength of Caposele soil sample is slightly lower than cemented kaolin sample; it is also characterized by a ductile behaviour, conversely to the brittle behaviour observed on cemented kaolin sample. In all the tests, the strength at large deformation is higher in cemented Caposele soil respect to cemented kaolin.

In Figure 7-62, the same comparison is proposed between Kcs40nf20 and Ccs40nf20. At 7 days of curing, both initial stiffness and peak strength are lower in Caposele soil. At a vertical stress of 50 kPa, the behaviour of Ccs40nf20 is ductile, while lightweight cemented kaolin shows a brittle behaviour; also, volumetric behaviour is significantly different, being contractive for lightweight cemented Caposele soil and dilative for lightweight cemented kaolin. At 150 kPa, the behaviour is ductile and contractive for both soils, with a slightly higher peak strength of treated kaolin sample. At 28 days of curing, the comparison between the two cemented soils show a quite similar behaviour, both in terms of stress and deformation. Peak strength of lightweight Caposele soil is almost the same as lightweight cemented kaolin at both vertical stresses; curves are very similar, except for a more ductile behaviour of Ccs40nf20 compared to Kcs40nf20.

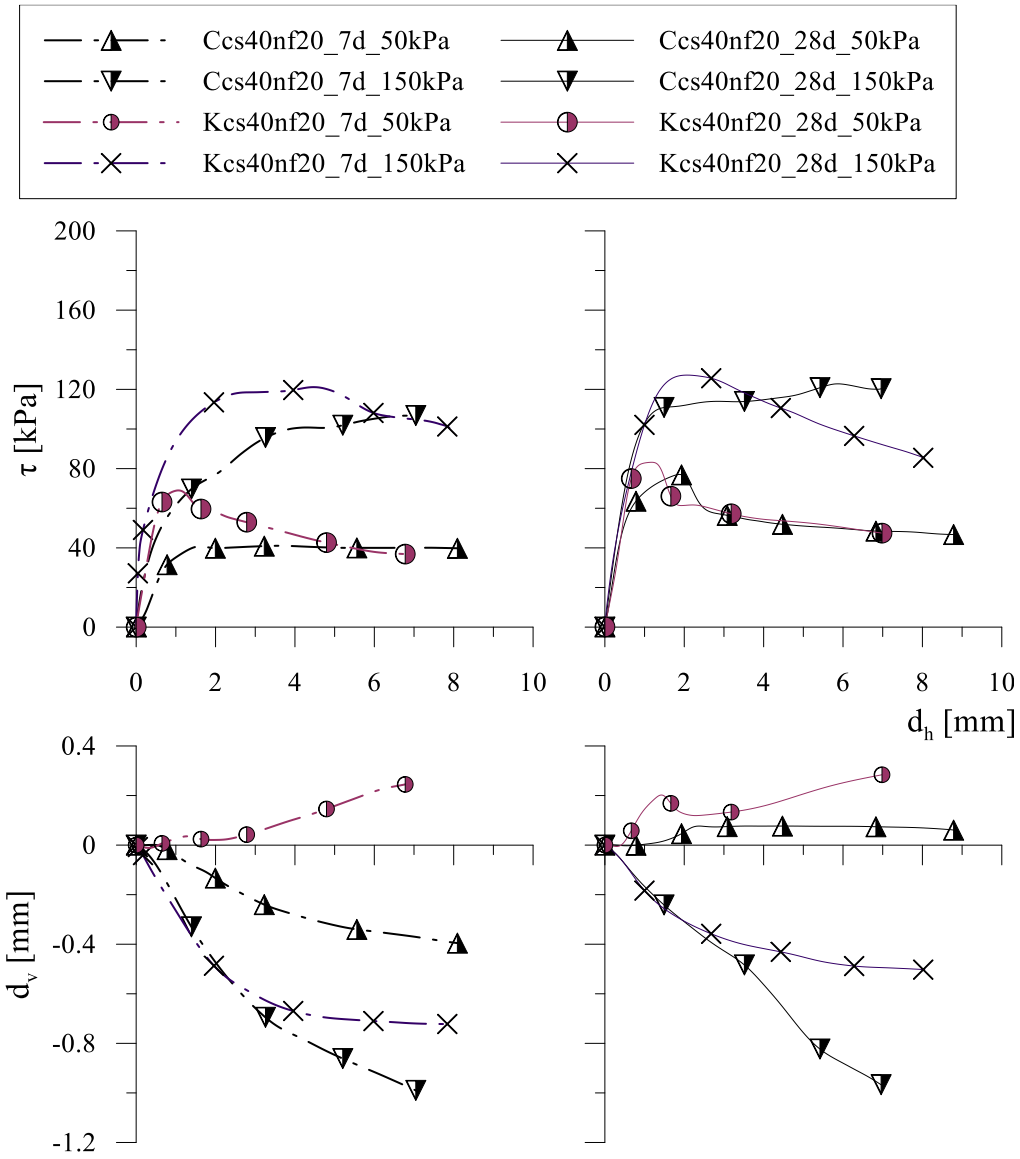

Figure 7-62. Direct shear tests. Comparison between Kcs40nf20 and Ccs40nf20, at different curing times and vertical stresses.

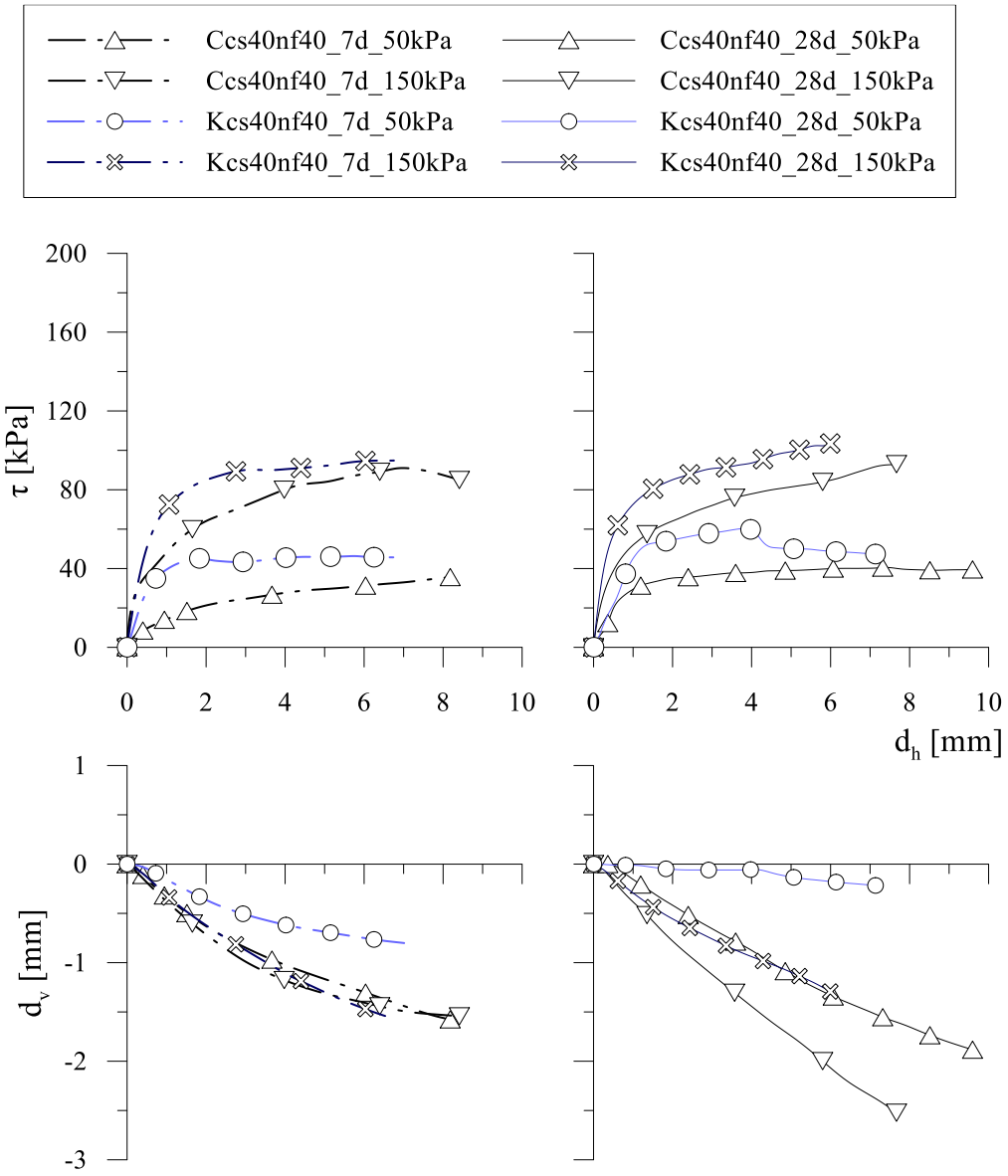

Figure 7-63. Direct shear tests. Comparison between cemented kaolin and cemented Caposele soil, at different curing times and vertical stresses.

The comparison of lightened samples at the maximum amount of foam investigated is shown in Figure 7-63. At 7 days of curing, the volumetric behaviour is contractive in all the tests and, except for Kcs40nf40_50kPa that is slightly less contractive, curves are almost coincident. In terms of stress, treated Caposele soil show a lower initial stiffness. At 150 kPa, the same peak strength is reached, but at significantly higher deformations, due to the hardening behaviour of Ccs40nf40; a similar trend is observed at 50 kPa.

After 28 days of curing and a vertical stress equal to 50 kPa, the initial stiffness of the two treated soils is the same, but a higher peak strength is observed on treated kaolin sample. Kcs40nf40_28d_50kPa shows very low vertical deformations, while Ccs40nf40_50kPa shows a contractive behaviour. In terms of peak strength, lightweight cemented kaolin at 50 kPa shows a higher peak strength than lightweight cemented Caposele soil. At 150 kPa, both treated soils show a contractive and hardening behaviour (with a slightly higher strength observed in lightweight cemented kaolin).

In Figure 7-64 and Figure 7-65, a comparison between oedometric tests performed on Ccs40, Ccs40nf40, Kcs40 and Kcs40nf40 after 7 and 28 days of curing, respectively, is presented.

At 7 days of curing, the initial stiffness of treated samples is quite similar, except for Kcs40_7d which exhibits slightly lower strains in the elastic domain. The yield stress of cemented Caposele soil is significantly lower than cemented kaolin. A vertical strain of about 10 % is achieved only at 1200 kPa in Kcs40_7d, while the same strain is observed between 600 and 900 kPa in Ccs40. The same difference is observed between Kcs40nf40 and Ccs40nf40; in the former, significant strains are observed only above 150 kPa, conversely to the second one in which a strain of about 10 % is observed at 100 kPa.

Void ratio of cemented kaolin is slightly higher than treated Caposele soil, due to the higher water content of soil slurry. However, this condition is reversed comparing the lightweight samples. Even if n_f is the same, void ratio depends also on the breakage of foam bubbles upon mixing which is lower in Caposele soil, thus justifying the higher void ratio of the latter.

After 28 days of curing (Figure 7-65), similar results are found. An increase in yield stress with curing time is observed for each mixture; yield stress of cemented and lightweight cemented kaolin samples is higher than Caposele soil one (by comparing tests at the same n_f).

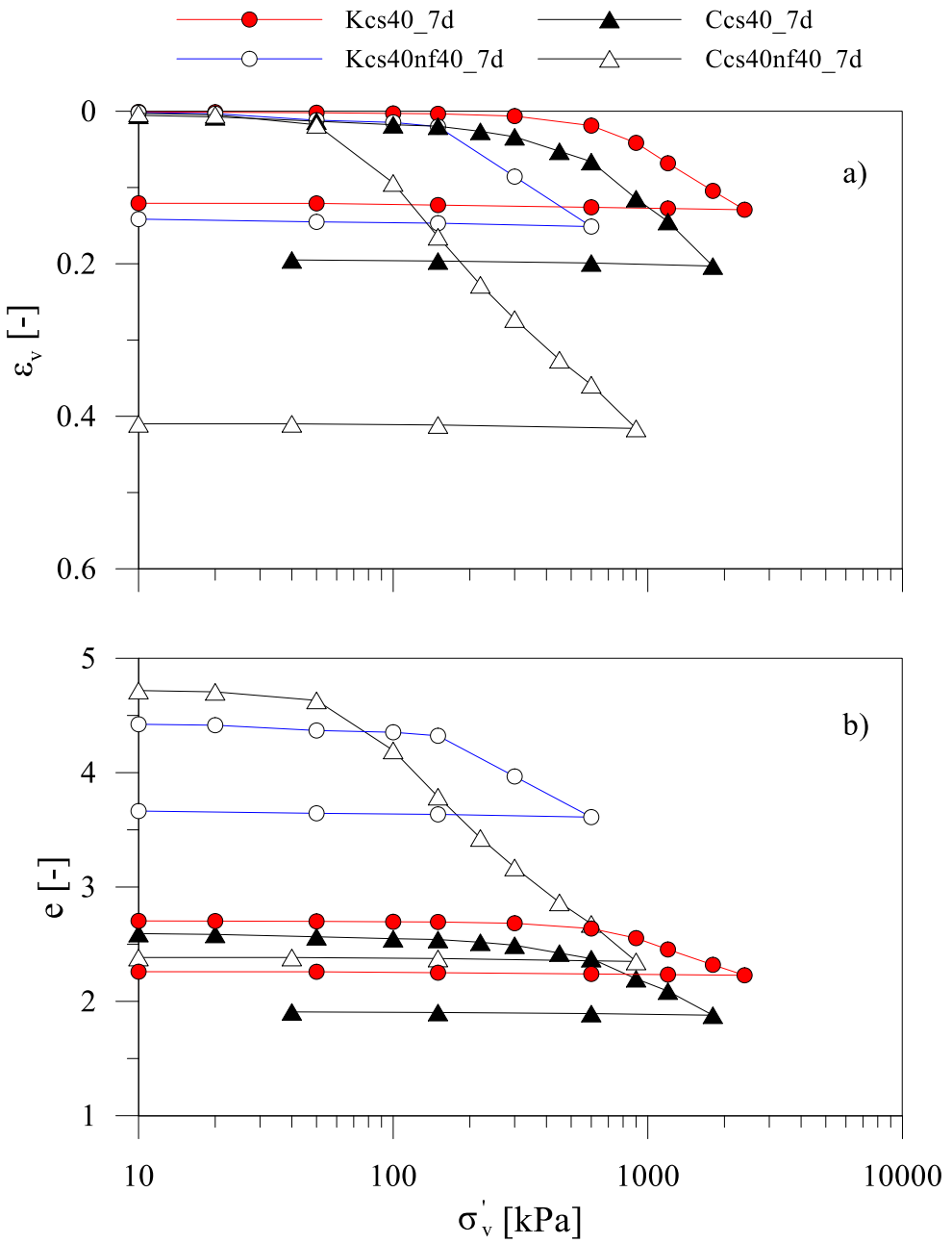

Figure 7-64. Oedometric tests on cemented and lightweight cemented kaolin and Caposele soil after 7 days of curing.

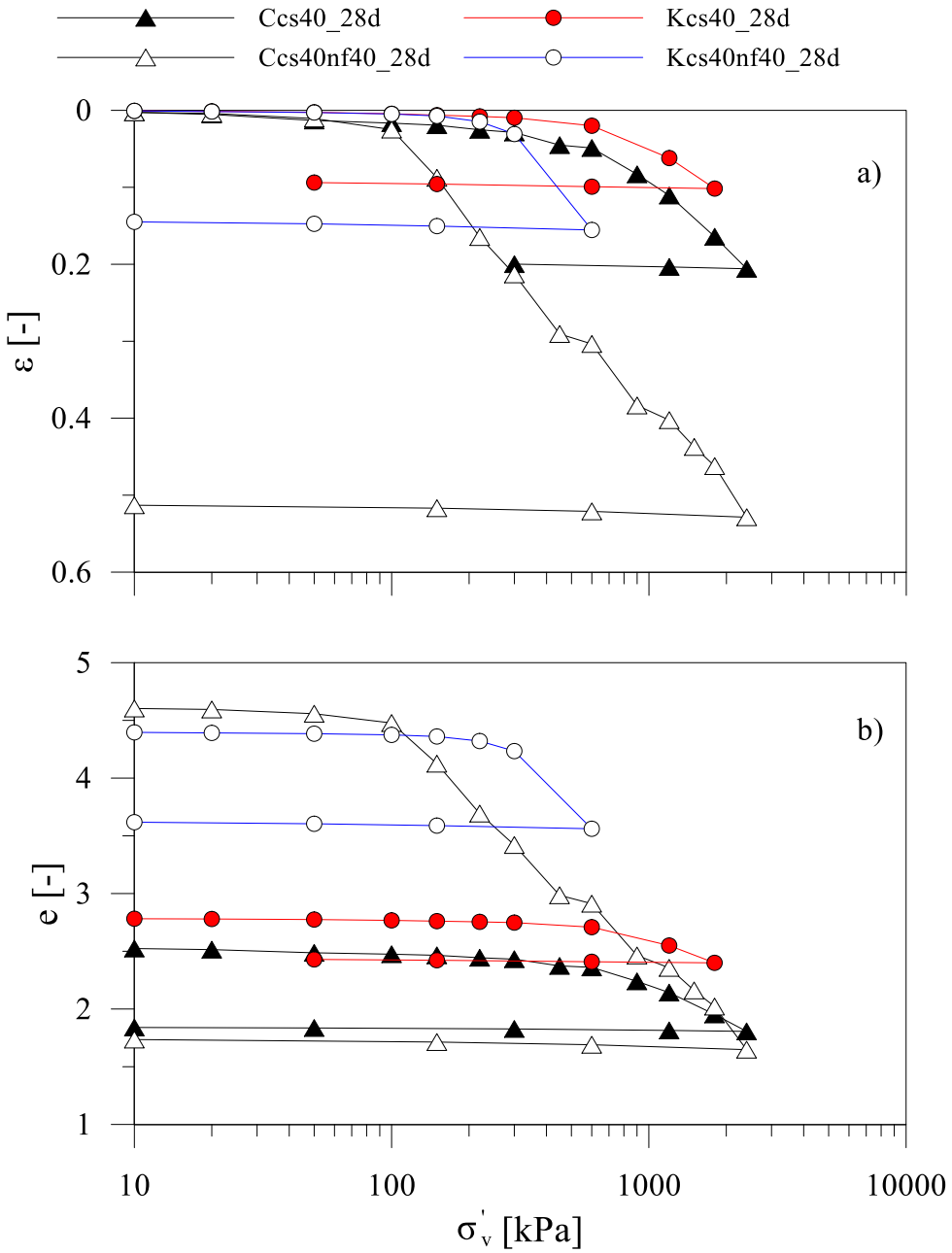

Figure 7-65. Oedometric tests on cemented and lightweight cemented kaolin and Caposele soil after 28 days of curing.

7.3.4. Failure surface

The framework derived for lightweight cemented kaolin, in which cohesion of Mohr-Coulomb failure surface (7-7) is identified by two variables (e_b and $\frac{\gamma_{dry}}{\gamma_{dry,0}}$) and two constants ($c_{b0}$ and c_f), was applied on lightweight cemented Caposele soil. In this case, φ, c_{b0} and c_f were fitted by minimizing the residual

sum of squares of all data available from direct shear tests on cemented and lightweight cemented Caposele soil.

The obtained friction angle is φ=29.4°, slightly higher than treated kaolin, whereas constants for cementation and foam are c_{b0}=185 kPa, and c_f=4. The lower c_{b0} of Caposele soil respect to kaolin (215 kPa) is consistent with the slightly lower strength observed on samples at the same curing time. Conversely, c_f is slightly higher (3.54 for kaolin), so that foam seems to have a slightly larger negative effect on peak strength. However, as it can be seen in Figure 7-66, this difference is almost negligible.

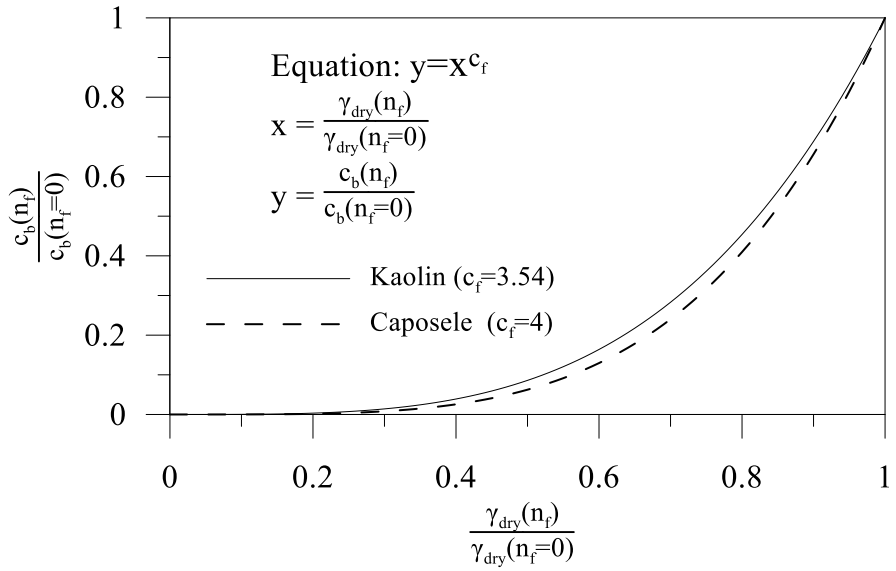

Figure 7-66. Effect of foam on c_b: comparison between kaolin (solid line) and Caposele (dashed line).

The resulting failure surfaces for treated Caposele soil at different amounts of foam are plotted in the space e_b- σ_v' -τ in Figure 7-67.

The comparison between measured and estimated value of peak strength in time is represented in Figure 7-68. The peak strength of Ccs40 and Ccs40nf40 at both normal stresses is well fitted, as Ccs40nf20 at 150 kPa. A larger error is only observed Ccs40nf20 samples at 50 kPa.

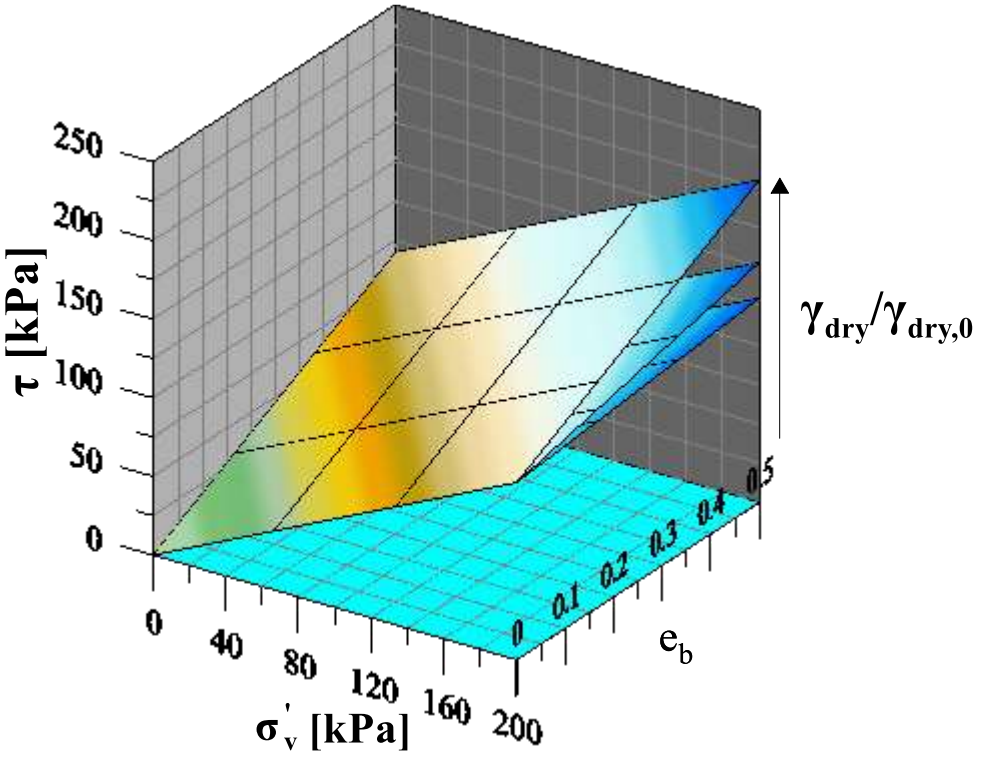

Figure 7-67. Failure surface planes at constant $\frac{\gamma_{dry}}{\gamma_{dry,0}}$, with c_f=4, c_{b0}=185 and φ=29.4. Increasing $\frac{\gamma_{dry}}{\gamma_{dry,0}}$, the amount of foam decreases.

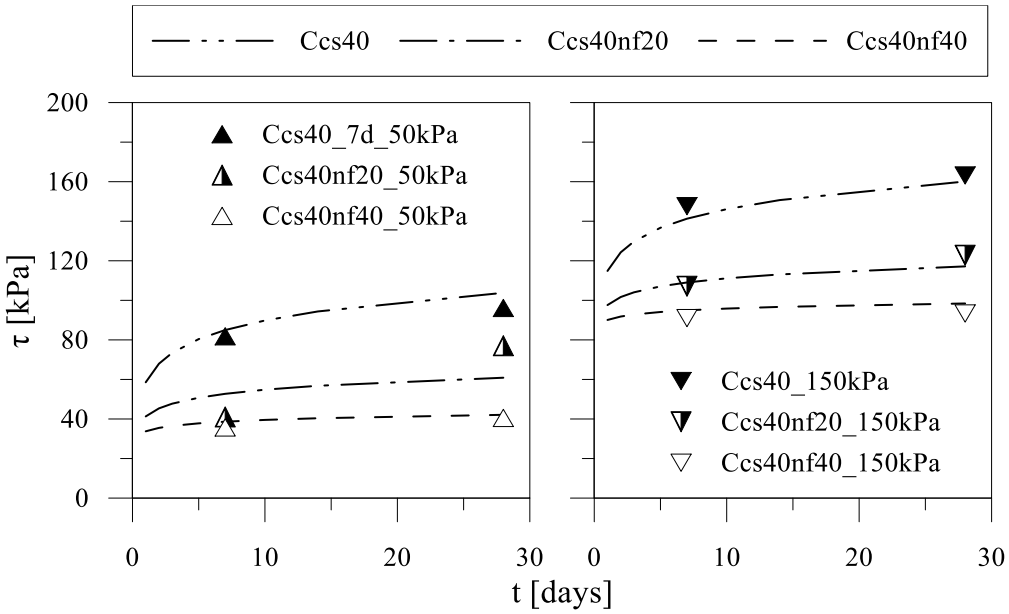

Figure 7-68. Comparison between measured and estimated τ_{lim} in time of cemented and lighweight cemented Caposele soil at two confining stresses.

In Figure 7-69 and Figure 7-70 data are reported in the e_b-$\frac{\gamma_{dry}}{\gamma_{dry,0}}$-τ space; surfaces at constant $\sigma_v^{'}$ are also reported.

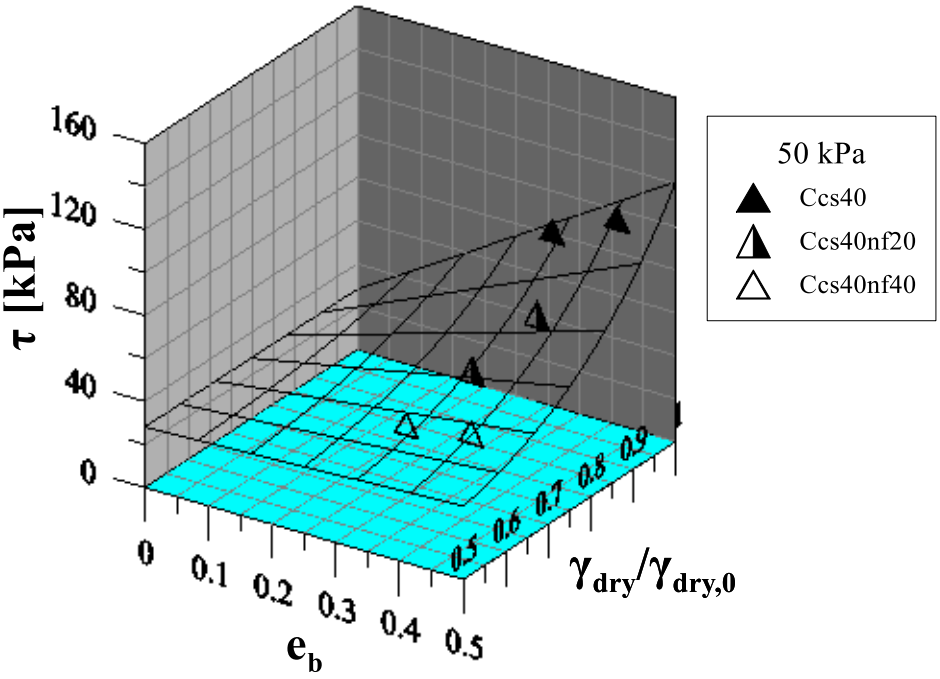

Figure 7-69. Comparison between measured and estimated τ_{lim} in time, $\sigma_v^{'}$=50 kPa.

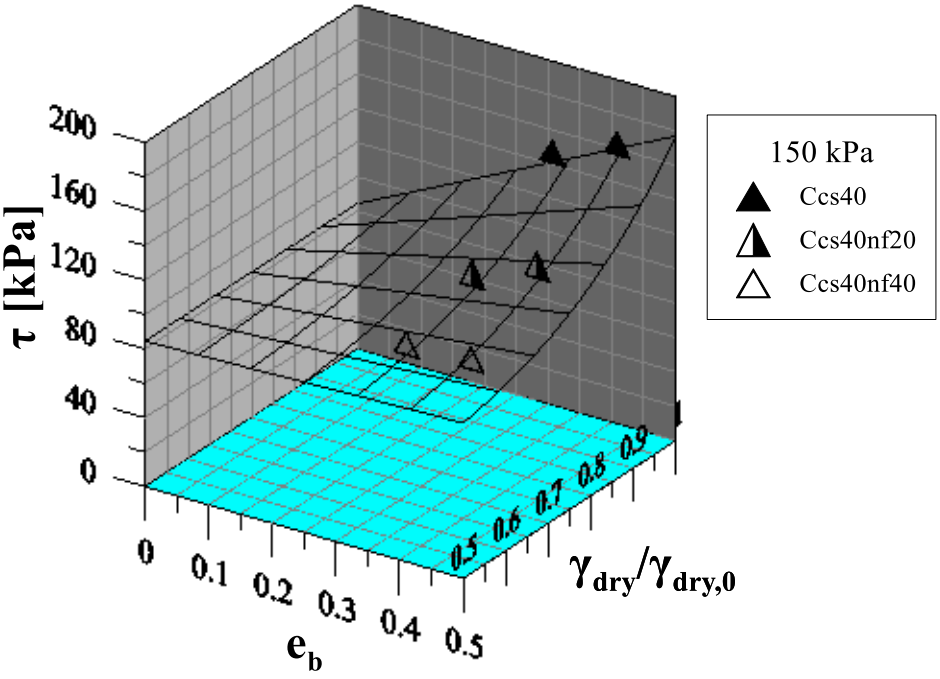

Figure 7-70. Comparison between measured and estimated τ_{lim} in time, $\sigma_v^{'}$=150 kPa.

7.4. Discussion

The bulk properties of treated soils were compared to theoretical values derived by equations proposed in section 5.1. To calculate physical properties time evolution, the amount of non-evaporable water, represented by the function $\alpha x(t)$, is required. This function was derived by quantitative interpretation of TGA analyses for treated kaolin (7-1), while it was estimated by UCS of cement paste for Caposele soil (Figure 7-50).

The measured bulk densities of non-lightened cemented samples (Kcs20, Kcs40, Ccs40), are similar to theoretical values. A good agreement was found also for dry bulk density and void ratio with curing time, whereas a larger scatter was observed for water content on cemented kaolin samples after direct shear tests (Figure 7-2a). However, a good agreement was observed on water content of cemented kaolin oven dried samples prepared for the specific purpose (Figure 7-2b) and on cemented Caposele soil samples after direct shear tests (Figure 7-52).

The measured bulk density of lightened materials (Kcs20nf20, Kcs20nf40, Kcs40nf20, Kcs40nf40, Ccs40nf20, Ccs40nf40) was higher than theoretical values, except for Ccs40nf20. This significant difference is due to breakage of bubbles upon mechanical mixing with soil-cement slurry. Despite of foam collapse, a significant increase in void ratio is observed, accompanied by a reduction of dry bulk weight (Figure 7-1, Figure 7-51). This increase in void ratio has also been highlighted by MIP in the previous section (Figure 6-11, Figure 6-12, Figure 6-13).

A method to derive the "actual" volume of foam (and the related parameter, n_f), suggested in 5.2.1.1, was applied; the actual values, identified by an asterisk (V_f^*, n_f^*), are obtained by matching theoretical and measured bulk densities. The average values of n_f^* are reported in Table 7-4, in which also average values of bulk density, actual cement content and relative dry density, $\frac{\gamma_{dry}(n_f)}{\gamma_{dry}(n_f=0)} = \frac{\gamma_{dry}}{\gamma_{dry,\,0}}$, defined as the ratio of dry bulk density of lightened cemented soil to dry bulk density of non-lightened cemented soil (at the same cement factor), are reported. The last one is a measure of the actual weight reduction due to addition of foam, and it is independent on curing time. It is worth noting that reduction of n_f determines an increase of cement content, $m_{c,\,a}$, while cement factor, c/s, is not affected at all. This means that the required amount of cement per unit volume increases respect to theoretical value, as soil and water contents.

Table 7-4. Physical properties and parameters of lightweight cemented soils after volume of foam correction.

	n_f20				n_f40			
	n_f*	$m_{c,a}$ [kg]	γ [kN/m^3]	$\gamma_{dry}/\gamma_{dry,0}$	n_f*	$m_{c,a}$ [kg]	γ [kN/m^3]	$\gamma_{dry}/\gamma_{dry,0}$
Kcs20	9%	93	12.8	0.91	28%	74	10.3	0.72
Kcs40	11%	168	12.8	0.89	29%	134	10.4	0.71
Ccs40	19%	171	12.1	0.81	33%	142	10.3	0.67

The average values of n_f^* reported in Table 7-4 were used to derive bulk dry density and void ratio with curing time and a good agreement was found (Figure 7-3, Figure 7-4, Figure 7-51). A larger scatter was found for water content, especially in lightweight cemented kaolin (Figure 7-5, Figure 7-6), while water content seems to be underestimated in lightweight cemented Caposele soil (Figure 7-52).

Compressibility was studied via oedometric tests at different curing times. The effect of cementation was investigated on kaolin, treated at two cement factors (c/s), 20 and 40 %. By comparing results at the same curing time, a significant increase in yield stress was observed (Figure 7-13), with a slight increase in initial stiffness. At increasing curing time (from 7 to 28 days), a slight increase in yield stress is observed; this is likely depending on the amount of bonds developed due to products of hydration, with a subsequent increase of degree of cementation. Physical states reached by cemented soils are impossible for non-treated soil (Figure 7-15, Figure 7-59b). Due to high initial void ratio of cemented soil, although significant vertical strains were achieved during the tests (up to 20 %), it wasn't possible to observe a convergence of cemented soil compression curves towards intrinsic compression lines of non-treated soil.

By comparing results at the same curing time and cement factor, it can be seen that the addition of foam determines a significant reduction of yield stress in both treated kaolin (Figure 7-28a, Figure 7-29a) and treated Caposele soil (Figure 7-59a, Figure 7-60a). However, physical states of lightweight cemented soil samples are quite different, with significantly larger initial void ratio (Figure 7-29b, Figure 7-59b, Figure 7-60b, Figure 7-65b). The lower yield stress can be likely explained by the increased void ratio due to foam addition, because no effect of foam on hydration processes was observed in XRD (6.1) and TGA (6.2) analyses. In the case of treated Caposele soil, due to high vertical strains achieved, it was possible to observe the convergence of lightweight cemented soil and non-lightened cemented soil compression lines (Figure 7-60b).

The shear strength of cemented and lightweight cemented soils was investigated by means of direct shear tests. Due to limitations related to the test, discussed inAppendix B, only qualitative info can be derived. However, it was possible to identify the effects of different parameters. Generally, increasing the vertical stress, a less brittle and dilative behaviour and a higher maximum strength is observed in all the samples.

Increasing the cement factor, at the same curing time and vertical stress, an expected increase of peak shear strength, with a more brittle and dilative (or less contractive) behaviour is observed (Figure 7-7, Figure 7-8, Figure 7-9). Similar effects are observed at increasing curing time, that was intensively studied (especially on Kcs40 and Kcs40nf40 mixtures). With reference to cemented kaolin (Kcs40), an increase in curing time (at the same confining stress) causes an increase in peak strength and a more brittle and dilative behaviour (or less ductile and contractive, depending on vertical stress, Figure 7-10, Figure 7-12) typically related to an increase of the degree of cementation (4.2). Indeed, the formation of hydrates with curing time leads to a higher volume of bonds, as already pointed out. The increase in peak strength is less evident at early stages of curing (up to 7 days) and higher vertical stress (Figure 7-11). This can be due to the proximity of initial stress state to yielding surface, leading to a higher debonding before peak strength is reached. Indeed, the same increase in peak strenght observed at 50 kPa at low curing times is also observed at 150 kPa at higher curing times (28, 60, 90 days).

The addition of foam causes a reduction in peak strength and a more ductile and contractive behaviour as observed for both treated kaolin and Caposele soil. In the case of treated kaolin at a cement factor of 0.4 (Kcs40, Kcs40nf20 and Kcs40nf40), this gradual transition can be observed at 50 and 100 kPa (Figure 7-18, Figure 7-20). Similar results are found at 28 days of curing and a vertical stress of 50 kPa on Caposele soil (Figure 7-57). In some cases, the behaviour of non-lightened samples (at the same curing time, cement factor and confining stress), is already ductile and contractive. This is the case of high vertical stresses and low curing times and/or low cement factor (in other terms, at high confining stresses and low degrees of cementation). In these cases, at increasing amount of foam, a more contractive behaviour with larger vertical displacements is observed, whereas non-linearity of stress-strain curves occurs at smaller displacements with a lower initial stiffness (Figure 7-23, Figure 7-56, Figure 7-57). In some cases (at the highest foam contents and vertical stresses investigated), a hardening behaviour is observed (Figure 7-21, Figure 7-53). This

behaviour is consistent with the significant reduction of yield stress observed in oedometric tests at increasing foam content. Indeed, in some cases, the yield stress in oedometric compression is lower or very close to vertical stress applied in direct shear tests (Figure 7-13, Figure 7-60a) so that debonding due to vertical stress can occur before shear stress is applied; then, due to the high porosity which characterize the material, highly contractive behaviour (also larger than non-treated soil, Figure 7-19) is observed.

The effect of curing time on lightened mixtures has been intensively investigated on Kcs40nf40. In this case, at early stages of curing, a slight increase in peak strength is observed only at a confining stress of 50 kPa (Figure 7-24), while the same volumetric behaviour, as well as for stress-strain curve, is observed at a confining stress of 100 kPa (Figure 7-25). At higher curing times (Figure 7-26, Figure 7-27) the effect of cementation observed on non-lightened samples can be observed, especially on volumetric behaviour.

It is worth noting that reduction in mechanical performances (in terms of peak strength and yield stress) observed at increasing foam content, depends only on the different physical state of lightweight cemented soil, characterized by a significantly higher void ratio, whereas no difference in terms of kinetic and products of hydration exists, as shown in section 6.

The comparison between kaolin and Caposele soil was also presented; a lower peak strength of treated Caposele soil was observed in direct shear tests for both cemented and lightweight cemented samples (Figure 7-61, Figure 7-62, Figure 7-63), as well as a lower yield stress (Figure 7-64, Figure 7-65). However, the same behaviours observed on treated kaolin were also observed on treated Caposele soil, as already discussed.

Finally, the failure surface of a lightweight cemented soil was related to two variables, namely the void ratio of bonds, e_b, and relative dry density, $\frac{\gamma_{dry}(n_f)}{\gamma_{dry}(n_f=0)}$. The former was introduced by Pinyol et al. (2007) as a parameter to take account of bonds in argillaceous rocks; it is defined as the ratio of volume of bonds and volume of solid soil. The relative density is suggested by Triantafillou and Gibson (1990) as a parameter to identify the failure surfaces of brittle foams subjected to multiaxial loading. As it has been observed, similar effects are observed at both increasing curing time and cement factor. Indeed, they both affect the degree of cementation, which affects the mechanical behaviour of a cemented soil. Thus, a unique parameter to identify the degree of cementation

(which takes account for both curing time and cement factor) was adopted. The volume of bonds was substituted by the volume of hydrated cement; e_b is independent of foam content and it is dependent on curing time, via $\alpha x(t)$, and cement factor. It has been calculated from equations derived in 5.1.

The Mohr-Coulomb criterion was assumed. The hypothesis of a linear dependency of cohesion on e_b, via the coefficient c_{b0}, seemed to be consistent, based on direct shear test results on all the cemented kaolin samples (regardless of vertical stress, curing time and cement factor). The friction angle, φ, was assumed as independent of degree of cementation, and it was considered as a parameter to best fit data (as c_{b0}). However, the calculated friction angle (27.6°) proved to be consistent with a possible residual friction angle of cemented kaolin (Figure 7-32). In the hypothesis that foam doesn't affect friction angle, the coefficient c_b was then derived for nf20 and nf40 and a reduction of this coefficient (due to lower strength of lightweight samples) was observed (Figure 7-34, Figure 7-35). The percentage reduction respect to c_{b0}, i.e. c_b of non-lightened material, was related to relative dry density (Figure 7-37) and an exponential law with a third constant, namely c_f, was derived. By this way, an expression of failure surface depending on the amount of foam and degree of cementation was determined (7-12). Then, the same approach was applied on Caposele soil in which the three parameters (φ, c_b and c_f) were best fitted by minimizing the residual sum of squares on all the samples. Parameters derived for failure surface (7-12) are reported for both soils in Table 7-5.

$$\tau_{lim} = c_{b0}\left(1 - n_f\right)^{c_f} e_b + \sigma_v' \tan(\varphi) \qquad (7\text{-}12)$$

Table 7-5. Parameters for failure surface derived for kaolin and Caposele soil

	φ	c_{b0} [kPa]	c_f [-]
Kaolin	27.6°	215	3.5
Caposele	29.4°	185	4.0

The effect of foam and cement factor on friction angle was neglected; these hypotheses can be consistent for low amounts of foam and limited ranges of cement factor. The effect of water content of soil slurry, which affects the void ratio of treated soil, is not considered. However, the proposed framework allows to consider in a consistent way both curing time and cement factor, so that tests at different *t* and *c/s* can be considered together. The main issues are summarized below:

- theoretical bulk density is almost equal to measured values for cemented soil, while it can be significantly higher in lightweight cemented soil due to breakage of bubbles upon mixing;
- despite foam collapse, the dry bulk density has been reduced up to 71% in lightweight cemented kaolin and 67% in lightweight cemented Caposele soil;
- a good agreement of estimated dry bulk density and void ratio with measured values was found, while water content is affected by a larger scatter;
- the yield stress in k_0 compression increases significantly with cement factor and slightly increases with curing time, while initial stiffness is slightly affected;
- an increase in peak strength, with a more brittle and dilative behaviour, is observed at increasing curing time and cement factor in non-lightened cemented soil samples;
- the addition of foam causes a significant reduction in yield stress in k_0 compression; however, the initial void ratio is significantly higher due to addition of foam;
- a reduction of peak strength is generally observed at increasing amount of foam, with a transition to a more ductile and contractive behaviour;
- the reduction of peak strength and yield stress likely depends on the increased porosity; indeed, hydration processes are not affected by the amount of foam (chapter 6);
- a unique variable, e_b, was identified to describe the degree of cementation, by taking account of both curing time and cement factor;
- a failure surface, depending on vertical stress, degree of cementation and amount of foam and three constants (φ, c_{b0} and c_f) was identified; the relative dry density was used as a variable to describe the effect of foam on cohesion.

References

ASTM, 2000. D854 - Standard Test Methods for Specific Gravity of Soil Solids by Water Pycnometer, Astm D854. https://doi.org/10.1520/D0854-10.2

Balshin, M.Y., 1949. Relation of mechanical properties of powder metals and their porosity and the ultimate properties of porous metal-ceramic materials, in: Dokl Akad Nauk SSSR. pp. 831–834.

Çolak, A., 2006. A new model for the estimation of compressive strength of Portland cement concrete. Cem. Concr. Res. 36, 1409–1413. https://doi.org/10.1016/j.cemconres.2006.03.002

Elaty, M. abd allah A., 2014. Compressive strength prediction of Portland cement concrete with age using a new model. HBRC J. 10, 145–155. https://doi.org/10.1016/j.hbrcj.2013.09.005

Gibson, L. J., Ashby, M. F. and Triantafillou, T.C., 1989. Failure surfaces for cellular materials under multixial loads - I. Modelling. Int. J. Mech. Sci. 31, 635–663.

Horpibulsuk, S., Bergado, D.T., Lorenzo, G.A., 2004. Compressibility of cement-admixed clays at high water content. Géotechnique 54, 151–154. https://doi.org/10.1680/geot.2004.54.2.151

Kearsley, E., Wainwright, P.J., 2002. The effect of porosity on the strength of foamed concrete, Cement and Concrete Research. https://doi.org/10.1016/S0008-8846(01)00665-2

Neville, A.M., 2011. Properties of concrete, 5th ed. Pearson Education Limited.

Pinyol, N., Vaunat, J., Alonso, E.E., 2007. A constitutive model for soft clayey rocks that includes weathering effects. Géotechnique 57, 137–151. https://doi.org/10.1680/geot.2007.57.2.137

Sasanian, S., 2011. The Behaviour of Cement Stabilized Clay At High Water Contents. Theses.

Schnaid, F., Prietto, P.D.M., Consoli, N.C., 2001. Characterization of Cemented Sand in Triaxial Compression. J. Geotech. Geoenvironmental Eng. 0241, 857–868. https://doi.org/10.1061/(ASCE)1090-0241(2001)127:10(857)

Triantafillou, T.C., Gibson, L.J., 1990. Multiaxial Failure Criteria for Cellular Materials. MRS Proc. 207, 479–496. https://doi.org/10.1557/PROC-207-9

Tsuchida, T., Egashira, K., 2004. The Lightweight Treated Soil Method: New Geomaterials for Soft Ground Engineering in Coastal Areas. CRC Press - Taylor & Francis Group, London.

8. Summary and conclusions

The effects of cement and foam addition on soil properties were investigated. The experimental study was carried out on a commercial fine grained soil, the Speswhite kaolin, and a natural soil, namely Caposele soil. The former is an artificial clay, characterized by well-known chemo-physical properties; therefore, it was considered in order to simplify the interpretation of the experimental results and hence the understanding of the evolution of a complex system as the soil-water-cement-foam mixture. The Caposele soil was chosen to compare results on a natural soil, that could be typically encountered in engineering practice, with similar plasticity and grain size distribution. A summary of mixtures tested in this experimental study is reported in Table 8-1.

Table 8-1. Treated soil mixtures.

	w_c/c	w_s [%]	c/s [%]	n_f [%]	
SW kaolin	0.5	140%	20%	0%	**K cs20**
				20%	**K cs20 nf20**
				40%	**K cs20 nf40**
			40%	0%	**K cs40**
				20%	**K cs40 nf20**
				40%	**K cs40 nf40**
Caposele	0.5	120%	40%	0%	**C cs40**
				20%	**C cs40 nf20**
				40%	**C cs40 nf40**

Chemo-physical and microstructural evolution of Speswhite kaolin mixtures were studied by means of X Ray Diffraction (XRD), Thermogravimetric Analysis (TGA), Scanning Electron Microscopy (SEM) and Mercury Intrusion Porosimetry (MIP).

XRD and TGA show that chemo-physical evolution of treated samples is ruled by hydration of cement and pozzolanic reactions whereas foam addition does not alter chemo-physical evolution of treated samples. Thermogravimetric analyses were used to quantitively study the progress of hydration via non-evaporable water, $W_{n\text{-}ev}$, identified as the water combined in products of hydration; the ratio between non-evaporable water and the amount of anhydrous cement, αx, can be used to describe the progress of hydration of samples treated at different cement factors (Figure 8-1).

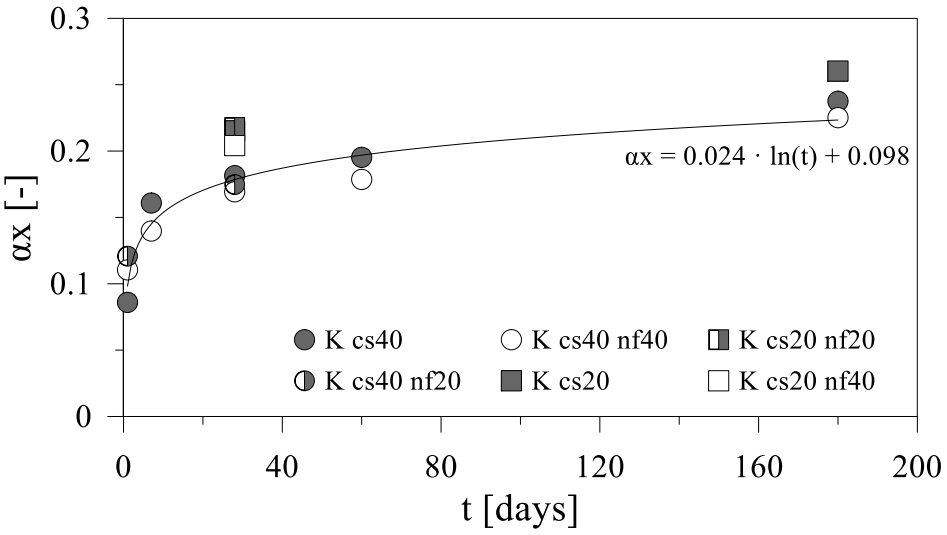

Figure 8-1. αx time evolution of Speswhite kaolin mixtures.

Bubbles of different sizes constituting foam are able to displace and sustain the soil-cement slurry matrix upon mixing, thus introducing air in the system which remains stable over cement setting and matrix hardening. Indeed, an increase of pores frequency larger than 1 μm is detected in MIP for lightweight cemented samples; furthermore, the addition of air foam does not modify the modal pore size of cement treated samples (ranging between 0.2 μm - 0.4 μm).

SEM images confirm MIP results interpretation showing kaolinite particles embedded into C-S-H network since early curing times (i.e. 24h); the effect of air foam is clearly evidenced by footprint of air bubbles such as cavities of different shape detected on the lightweight samples surface as a consequence of matrix displacement during mixing, whose extent and frequency increase as air foam content increases; these cavities can be filled by precipitation of aluminate hydrates and portlandite with progress of hydration.

At volume scale the effects of cement and foam addition were investigated in terms of bulk properties and mechanical behaviour on both kaolin and Caposele soil.

A theoretical formulation to estimate physical properties time evolution of lightweight cemented soils starting from design parameters has been derived based on the hypotheses that shrinkage does not occur and samples are seal cured. The solid phase increases because of water combined in products of hydration due to cement hydration reactions, thus dry weight increases and void ratio decreases. It was highlighted that a significant breakage of foam bubbles upon mixing can occur; thus, a correction to calculate the “actual” volume of foam

based on bulk weight increase was proposed. The "actual" porosity induced by foam was determined for each sample and the average values of each mixture were considered to calculate theoretical properties. In Table 8-2, the main characteristics of the mixtures are reported.

Table 8-2. Mixtures characteristics after volume of foam correction (void ratio, e, refers to 28 days of curing).

	n_f^*	m_s [kg]	$m_{c,a}$ [kg]	m_f [kg]	γ [kN/m^3]	e [-]
K cs20	-	513	103	-	13.8	3.1
K cs20 nf20	9%	467	93	17	12.8	3.5
K cs20 nf40	28%	369	74	36	10.3	4.7
K cs40	-	473	189	-	14.2	2.7
K cs40 nf20	11%	421	168	17	12.8	3.2
K cs40 nf40	29%	336	134	36	10.4	4.3
C cs40	-	529	212	-	14.8	2.5
C cs40 nf20	19%	428	171	15	12.1	3.3
C cs40 nf40	33%	354	142	34	10.3	4.2

Results were compared to measured bulk properties determined via standard procedures. A good agreement with dry bulk density and void ratio was found, while a larger scatter was observed for water content. Despite bubbles breakage, the addition of foam (in the range investigated in this study) leads to a reduction of bulk weight and dry bulk weight up to 70% of non-lightened mixtures, with a significant reduction of the amount of cement required for unit volume of material (Figure 8-2).

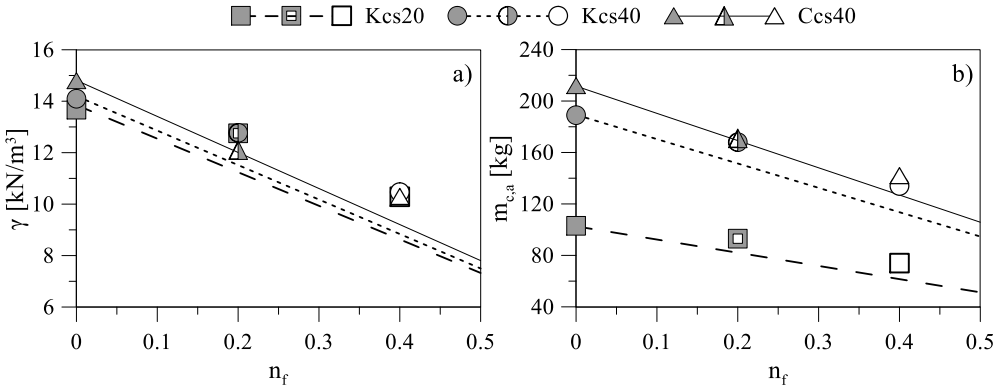

Figure 8-2. Properties of mixtures (lines refer to theoretical values): a) bulk weight (symbols refer to measured values); b) amount of cement per unit volume (symbols refer to corrected values 5.2.1.1).

Macroscopic behaviour of cemented and lightweight cemented soils was investigated by means of direct shear tests and oedometric tests. Test results evidence an evolution of mechanical behaviour of cement treated samples over time due to the progress of hydration reactions. An increase of cement factor and/or curing time leads to an increase of yield stress in k_0 compression and an increase in peak strength with a more brittle and dilative behaviour in shearing paths. As expected, an increase in vertical stress in direct shear tests leads to an increase in peak strength, with a reduction of brittleness and dilatancy (comparing samples at same curing time and cement factor, Figure 8-3a).

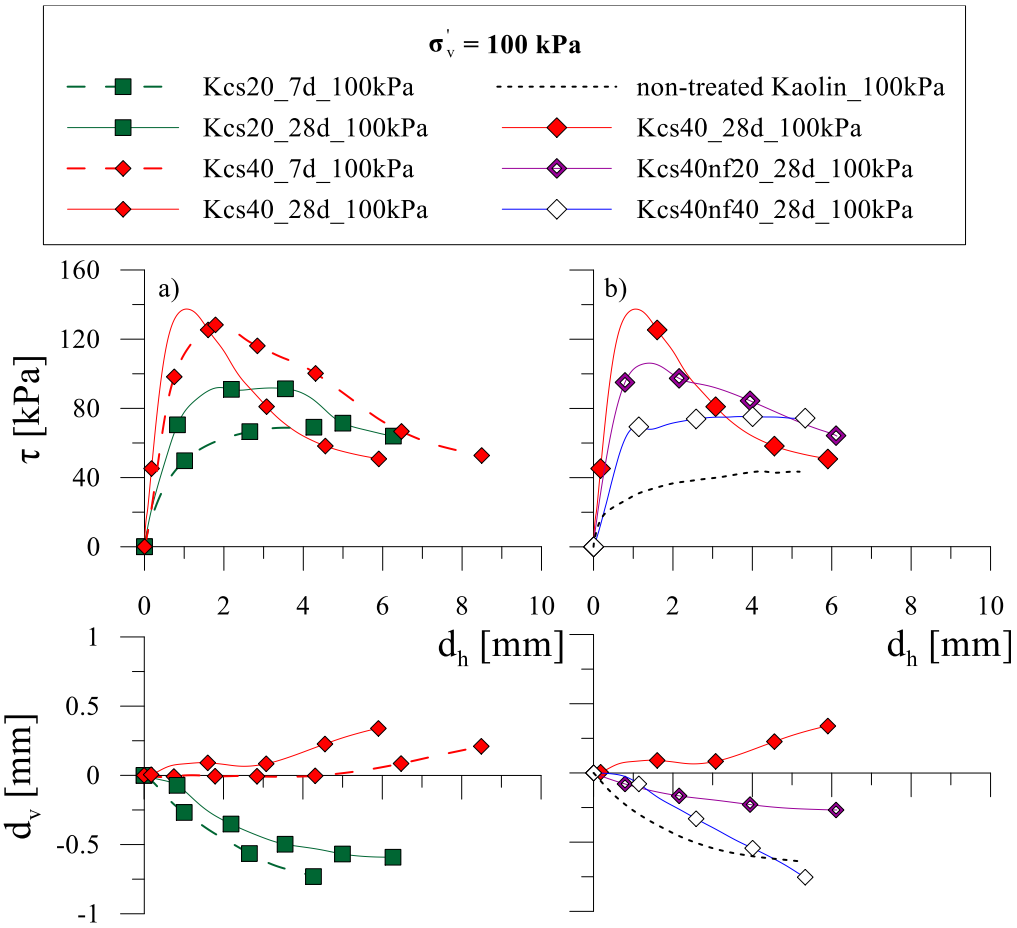

Figure 8-3. Direct shear test results on different mixtures and curing times.

The addition of foam causes a significant reduction in yield stress in k_0 compression. A reduction of peak shear strength in direct shear tests is observed at increasing amounts of foam, with a transition to a more ductile and contractive behaviour (Figure 8-3). The effect of foam on mechanical performances can be explained by the significant increase in void ratio, since hydration reactions

induced by cement are not altered by foam addition as evidenced by microscale analyses.

At increasing curing time, a gradual increase of peak strength was observed also on lightened samples, as shown in Figure 8-4, along with a transition to a less ductile and contractive behaviour. These phenomena are less evident than observed on non-lightened samples, but this can be due to the lower yield stress in k_0 compression which leads to an initial stress state (in direct shear tests) closer to yield surface, thus the effect of cementation cannot be appreciated in the same way. Similar results were found for both Speswhite kaolin and Caposele soil. Hence it seems reasonable that the effects of the proposed technique on the mechanical behaviour experimentally observed in the case of a commercial kaolin and of the natural Caposele soil can develop even in the case of other natural soils.

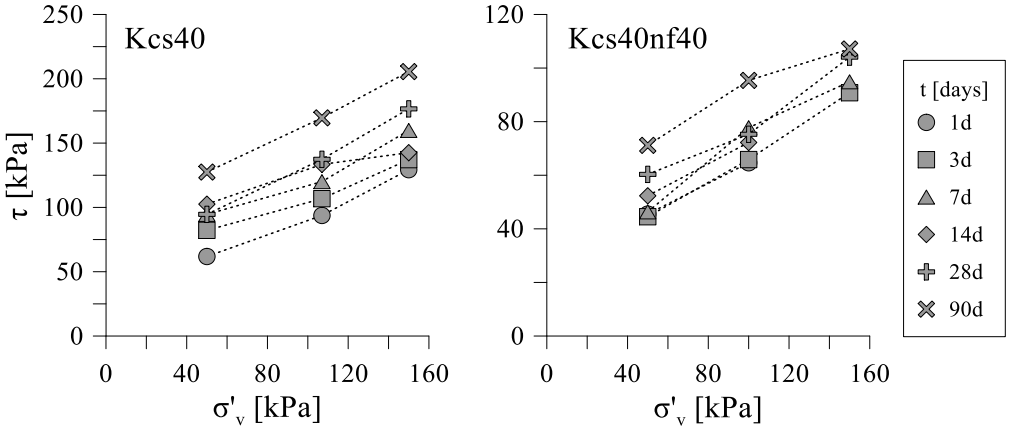

Figure 8-4. Direct shear test results: maximum shear strength at varying curing time of Kcs40 and Kcs40nf40 in τ-σ'_v plane.

The Mohr Coulomb criterion was adopted to describe the failure surface of cemented and lightweight cemented soils. The effect of foam and curing time on friction angle was neglected, and a unique value for all the mixtures of each soil was determined. The void ratio of bonds, e_b, defined as the ratio of volume of hydrated cement (i.e. volume of bonds) and volume of solid soil, was identified as a parameter to describe the increase in strength due to the degree of cementation. A linear relation passing through origin was assumed between cohesion and void ratio of bonds ($c = c_b e_b$), as shown in Figure 8-5a.

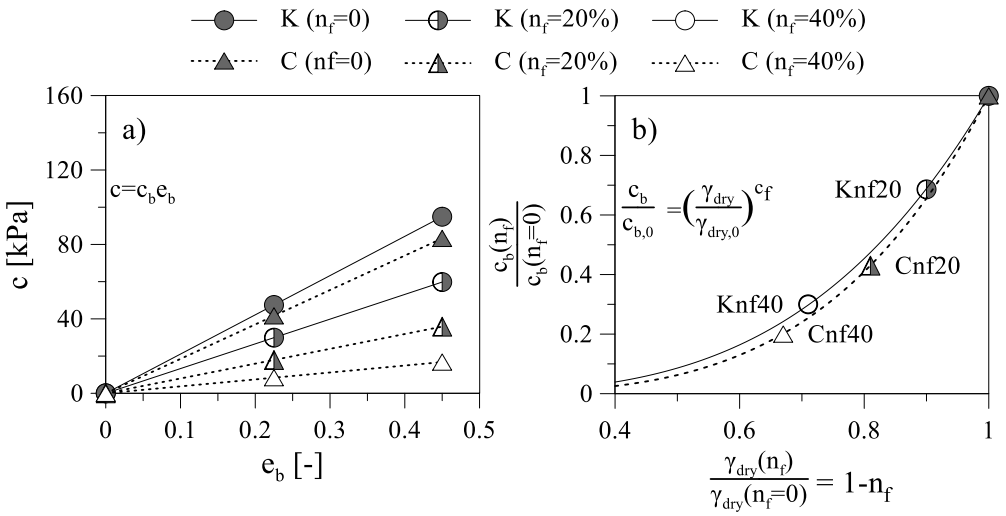

Figure 8-5. a) increase of cohesion with e_b; b) relative reduction of c_b with relative density.

The decrease of strength at increasing amount of foam has been considered correlating the reduction of c_b to the relative dry density (independent of cement factor and curing time) representing the effect of foam (Figure 8-5b). A unique failure surface which takes account of cement factor, curing time and amount of foam, depending on three constants (φ, c_{b0} and c_f), was determined (8-1). The constants determined for each soil are reported in Table 8-3.

$$\tau_{lim} = c_{b0}\left(1 - n_f\right)^{c_f} e_b + \sigma'_v \tan(\varphi) \qquad (8\text{-}1)$$

Table 8-3. Parameters for failure surface derived for kaolin and Caposele soil

	φ	c_{b0} [kPa]	c_f [-]
Kaolin	27.6°	215	3.5
Caposele	29.4°	185	4.0

8.1. Further developments

The experimental study was focused on chemo-mechanical evolution of lightweight cemented soils. It has been proved that results on a commercial fine-grained soil can be extended to a natural excavated soil, which is the aim of the treatment method. However, the two soils investigated, even if characterized by different mineralogical composition, had similar grain size distribution and plasticity. Thus, further studies might be focused on treatment of soils characterized by higher plasticity; in this case, more difficulties can arise. The higher demand in water content to obtain a slurry with a proper viscosity could lead to a significantly higher porosity, thus reducing mechanical performances. Indeed, many authors have shown that at increasing water content of soil slurry, a significant reduction of mechanical performances is observed. Thus, the main

objective would be the reduction of water demand without affecting viscosity, in order to have a deflocculated suspension with high concentrations. Additives required for this purpose, such as salts, could affect chemo-physical evolution, and a further study would be required.

The mechanical tests allowed to investigate qualitatively the effects of the addition of foam on mechanical behaviour evolution. In the future, more accurate mechanical investigations will be performed for numerical modelling of the observed behaviours. Tests performed in the range of curing time investigated, up to 3 months, showed a significant increase in peak strength with time. However, in this study, samples were seal cured before testing whereas site conditions could be different. Depending on the case, the material could be subjected to wetting-drying cycles, freeze-thaw cycles and seepage of deleterious chemicals that could affect long-time mechanical performances; thus, studies on durability of lightweight cemented soils should be carried out. These matters are also related to hydraulic properties that should be investigated due to the significant importance in geotechnical applications.

Appendix A

Clay minerals

Basic units

Most of clay minerals are composed of two basic structural units. One is built of silica tetrahedron with a silicon atom equidistant from four oxygens at the centre of the tetrahedron with formula SiO_4^{-4} (Figure A-1). The tetrahedron groups are arranged to form a sheet, a phyllosilicate, with the bases in the same plane and tips pointing in the same direction, repeated indefinitely with composition $Si_4O_6(OH)_4$ (Grim, 1968). In Figure A-3 the tetrahedral sheet is represented. In Figure A-3b, the dashed line represents the repeated unit $[Si_4O_{10}]^{-4}$.

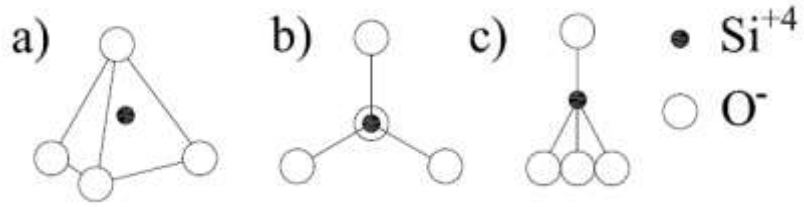

Figure A-1. Silica tetrahedron group. (a) and (b) structure representation; (c) bidimensional representation.

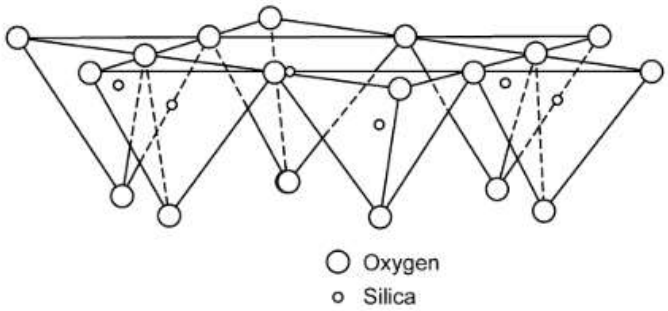

Figure A-2. Diagrammatic sketch of the tetrahedral sheet (Murray, 2006).

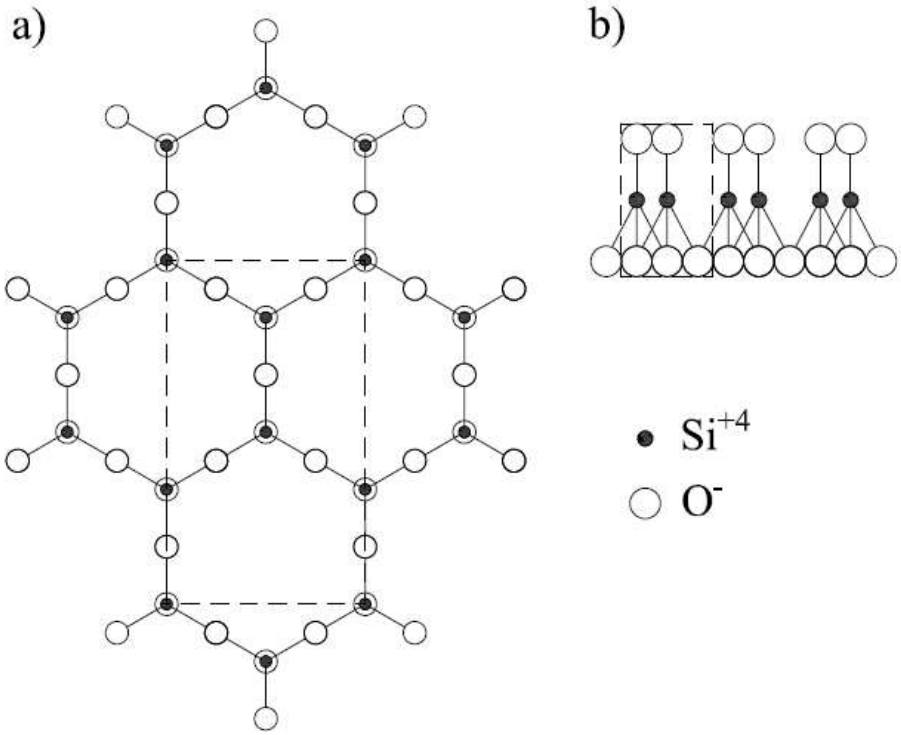

Figure A-3. Diagrammatic sketch of tetrahedral sheet. (a) planar sketch; (b) bidimensional representation.

The second basic unit is composed of octahedral sheets, comprised of closely packed oxygens and hydroxyls in which aluminum and magnesium atoms are arranged in octahedral coordination (Murray, 2006).

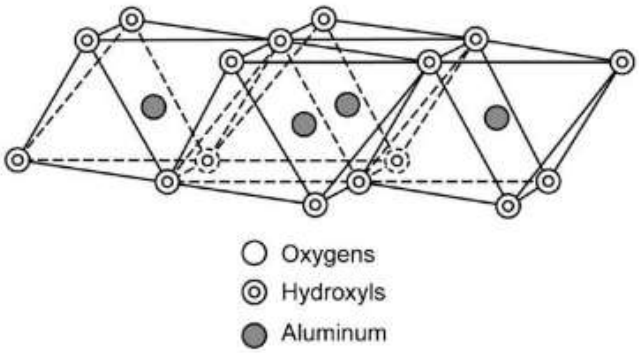

Figure A-4. Diagrammatic sketch of the octahedral sheet (Murray, 2006).

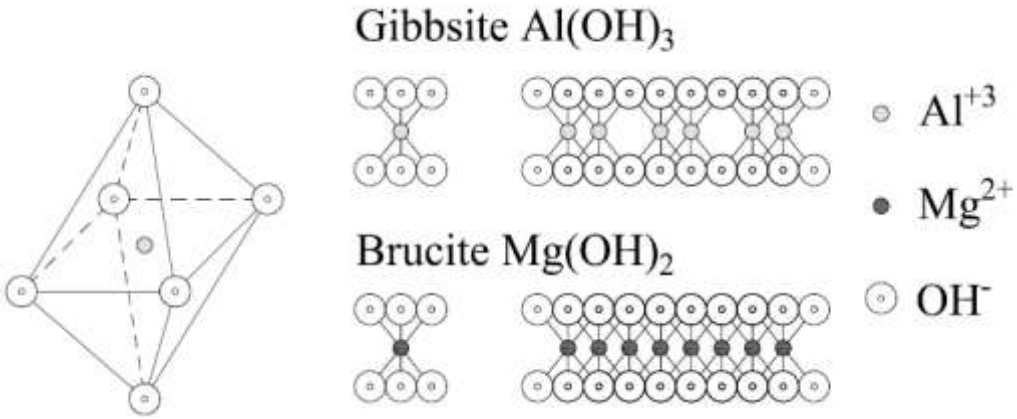

Figure A-5. Octahedron unit and bidimensional representation of Gibbsite and Brucite.

In the first case, namely gibbsite structure, the aluminum with a positive valence of three is present; only two-thirds of possible positions are filled, and the sheet has formula $Al_2(OH)_6$. When magnesium (with a positive charge of two) is present, the structure is called brucite. In order to balance the structure, all the positions have to be filled and the formula is $Mg_3(OH)_6$. Both minerals can indefinitely develop on horizontal plane while (being the oxygen valences saturated), only hydrogen bonds can allow a growth in normal direction. Starting from these basic units, clay minerals, such as kaolinite, can be identified.

Mineral groups

Kaolinite-serpentine group

The structure of kaolinite is composed of a single phyllosilicate and a single alumina octahedral sheet so that a composite octahedral-tetrahedral layer is formed (T-O mineral) (Grim, 1968). One layer of gibbsite and the plane containing the tips of the tetrahedral sheet unite in a common layer, as shown in Figure A-6. In this layer, two thirds of the atoms are shared. In Figure A-6, two formulas to represent kaolinite are shown. The first one is the chemical formula, while the second one, the mineralogical one, allows to identify the composition of the mineral. The mineral is defined as a *dioctahedral* phyllosilicate because only two thirds of possible position are occupied by aluminum.

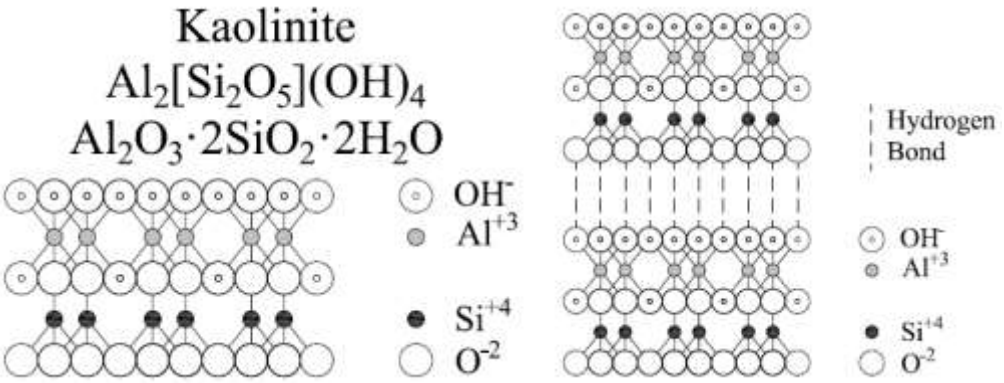

Figure A-6. Representation of kaolinite structure.

The group can repeat indefinitely in the horizontal plane, while (due to charge saturation), it cannot grow in normal direction, except for hydrogen bonds which can be formed thanks to OH^- layer (Figure A-6). Kaolinite appears as well-formed six-sided flakes with maximum dimension of flake surface from 0.3 μm up to 4 μm, elongated in one direction from 0.05 to 2 μm (Grim, 1968).

Molecules of water (zeolitic water) can be placed between the planes forming hydrogen bonds. In this case, the mineral is called *Halloysite*, with formula $Al_4[Si_4O_{10}](OH)_8 \cdot 4H_2O$. As reported by Joussein et al. (2005), the dominant halloysite particles, conversely to kaolinite, appear as tubular particles with lengths from 0.02 to >30 μm and widths from 0.05 μm to 0.2 μm, at least.

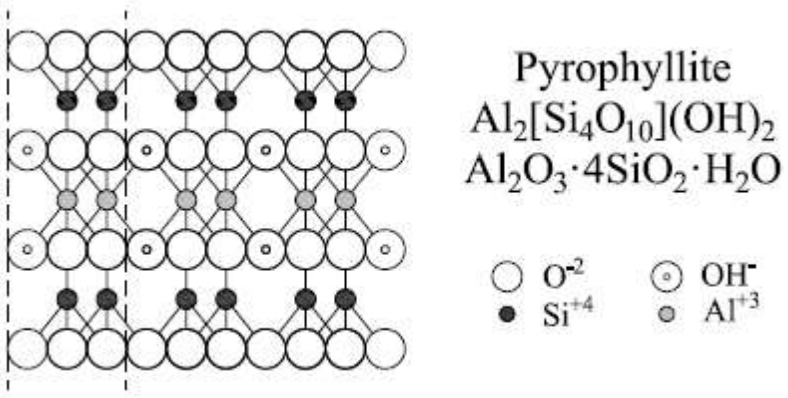

Figure A-7. Pyrophyllite bidimensional representation and formula.

Another structure that comes from gibbsite is the *Pyrophyllite*, represented in Figure A-7. Both layers of gibbsite are in common with the phyllosilicate sheet, with a T-O-T structure. As the previous ones, pyrophyllite can repeat indefinitely in the horizontal plane. Conversely to them, development in normal

direction cannot occur because of charge saturation, neither with hydrogen bonds. They can only connect by means of interlayer water with weak bonds.

Starting from brucite, *serpentine* and *talc* are akin to kaolinite and pyrophyllite, respectively a T-O and a T-O-T mineral (Figure A-8). Due to magnesium valence, all the positions are filled, so they can be defined as trioctahedral minerals.

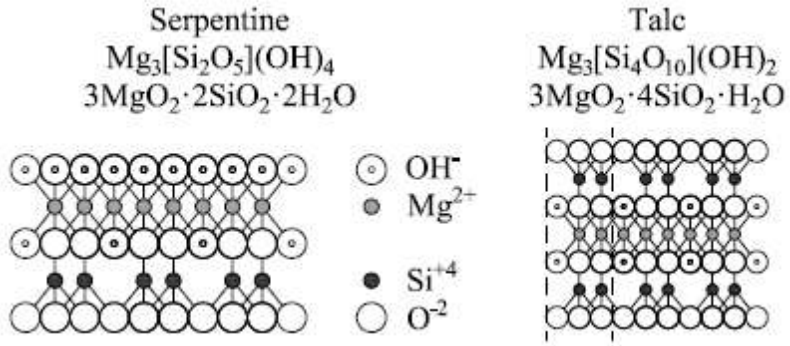

Figure A-8. Serpentine and talc bidimensional representations and formula.

Illite minerals

In some cases, substitution of silica atoms in tetrahedral sheets can occur. These minerals are called micas. When a substitution occurs, it can cause a charge deficiency in T-O-T groups, that has to be balanced by other ions as sodium and potassium.

An example of dioctahedral mica is the *Muscovite* (white mica), obtained by substitution of Si^{+4} with Al^{+3} in pyrophyllite (about one-fourth substitution) which causes a net negative charge balanced by K^+ ions. The structural formula is $(OH)_4K_2(Si_6Al_2)Al_4O_{20}$. Ionic bonds between TOT sheets are stronger than hydrogen bonds, preventing water from occupying interlayer position (Murray, 2006).

Illite is another clay mineral mica, also referred to as hydrous mica. As muscovite, it is characterized by Al^{+3} substitution in tetrahedral sheets, but it differs from that because about one-sixth of Si^{+4} are substituted and there are less K^+ ions (Mitchell and Soga, 2005; Murray, 2006). Illite particles are mainly irregular aggregates of poorly defined flakes with diameter that usually goes from 0.1 to 0.3 μm.

An example of trioctahedral mica is the *biotite* or black mica, obtained from talc, due to Si^{+4} substitution with Al^{+3} in tetrahedral sheets and Mg^{+3} substitution

with Fe^{2+} in octahedral sheets. As muscovite, K^{+} ions balance the charge deficiency and their properties are similar. Another clay mineral is *vermiculite*, composed of biotite sheets interlayed by double molecular layers of water. Even if charge deficiency due to Si^{+4} substitution can be partially balanced by other substitutions in mica lattice, a net-charge always stays. This is balanced by cations, usually Ca^{+2} and Mg^{+2}, between biotite like layers and they are largely exchangeable (Grim, 1968).

Smectite (montmorillonite) minerals

Another group of minerals is named *smectite* minerals. They are composed of a central alumina octahedral sheet between two silica tetrahedral sheet, as pyrophyllite, with water placed between units. Smectites always have substitution. In the tetrahedral sheet, substitution of Si^{+4} with Al^{+3} is up to 15% and, in the octahedral sheet, substitution of magnesium and iron for aluminum occurs, varying from few to complete. Moreover, the lattice is always unbalanced by substitutions that can only be partially compensated by the ones in other layers. This results in a net charge on the lattice that is balanced by exchangeable cations, as calcium and sodium, adsorbed between unit layers and around edges. Indeed, this is one of important differences between illites and smectites. In the former, the charge deficiency is mainly in tetrahedral sheet, with potassium mainly balancing it thus structural unit layers are relatively fixed in position. In smectites, the charge deficiency is in the octahedral sheet, polar molecules can enter between units with ease and cations are easily exchangeable.

When a limited substitution of Al^{+3} occurs, the smectite is called *beidellite* and it is a dioctahedral smectite. By contrast, when a total two on three substitutions of $2Al^{+3}$ with $3Mg^{+2}$ occur, all the positions are occupied and the trioctahedral smectite is called *saponite*. *Nontronite* and *sauconite* come from replacement of Al^{+3} respectively with iron and zinc.

A very common dioctahedral smectite mineral is the *montmorillonite*, that comes from one on one substitution of Al^{+3} with Mg^{+2}. When calcium is the cation balancing the charge in the adsorbed water, it is called calcium montmorillonite and there are two water layers between units. Conversely, in sodium montmorillonite there is one layer of water and sodium is the main adsorbed cation.

Montmorillonite is flake shaped, so thin that particles are like films, with long axis that goes up to 1 or 2 μm and thickness from 1 nm up to 1/100 of width (Mitchell and Soga, 2005). Montmorillonite and, more generally, all smectites

have a very large specific surface. When there is a large amount of iron and/or magnesium substitution, particles have elongated shape like a needle.

Other clay minerals

Another group of clay minerals, distinguished by a TOT+O configuration, is the chlorite group. Chlorites are composed of a mica-like layer, unbalanced by a substitution of Al^{+3} for Si^{+4} (for example, starting from pyrophyllite) in the central octahedral layer, and a brucite-like layer, which balances the excess charge thanks to a substitution of Al^{+3} for Mg^{+3}, (Grim, 1968). They appear as microscopic grains of platy morphology and poorly defined crystal edges (Mitchell and Soga, 2005).

Amorphous clay minerals are called *allophanes*. These minerals are substantially amorphous to x-ray diffraction, due to a very low order of structural units like silicon in tetrahedral coordination, metallic ions in octahedral coordination with occasional other units. Their composition and shape can vary substantially, and it is difficult to prove unequivocally their presence. However, according to Grim (1968), their importance is marginal on soil physical properties.

Some clay minerals don't have a planar configuration but a chain-like structure, as *palygorskite* and *sepiolite*. The diameter is about 5 – 10 nm and lengths up to 5 μm. However, they are not frequently encountered (Mitchell and Soga, 2005).

Mixed-layer clay minerals are also possible when there is interstratification of two or more clay minerals. The interstratification can be regular, so that a regular repetition of different layers occurs, or it can be irregular with a random interstratification. However, due to the inherent variability, it's not possible to give specific names and they are named after mixtures of layer involved such as the most common montmorillonite–illite, chlorite–vermiculite and chlorite–montmorillonite (Grim, 1968; Mitchell and Soga, 2005).

Non-clay minerals

In clayey soils, minerals which can be abundant but not regarded as clay minerals are often encountered. The main one is certainly *quartz* (SiO_2), which is composed of silica tetrahedra but, conversely to silica sheets, all four of the oxygens are shared with other tetrahedra and grouped forming spirals in a three-dimensional framework (Mitchell and Soga, 2005). Other non-clay minerals

which can be encountered are the carbonates, especially in the form of *calcite* ($CaCO_3$) and *dolomite* $CaMg(CO_3)_2$, and *gypsum* ($CaSO_4 \cdot 2H_2O$).

References

Grim, R.E., 1968. Clay mineralogy, International series in the earth and planetary sciences. McGraw-Hill.

Joussein, E., Petit, S., Churchman, J., Theng, B., Righi, D., Delvaux, B., 2005. Halloysite clay minerals – a review. Clay Miner. https://doi.org/10.1180/0009855054040180

Mitchell, J.K., Soga, K., 2005. Fundamentals of soil behavior. John Wiley & Sons.

Murray, H.H., 2006. Structure and Composition of the Clay Minerals and their Physical and Chemical Properties. Dev. Clay Sci. 2, 7–31. https://doi.org/10.1016/S1572-4352(06)02002-2

Appendix B

Microstructural tests

X Ray Diffraction (XRD)

X-ray diffraction is based on the property of crystals to diffract x-rays in a way that is dependent on their structure, thus revealing the structure itself. This property was discovered in 1912. X-rays are electromagnetic radiations, such as visible light, but characterised by a much shorter wavelength, expressed in Angstrom, A = 10^{-8} cm, approximately in the range 0.5 – 2.5 A (visible light wavelength is in the order of 6000 A). They can be scattered by atoms (scattering centres) which have a spacing of the same order of magnitude of x-ray wavelength, such as crystals; moreover, atoms in crystals are periodically distributed on the lattice. Because of this, scattered rays' waves have specific phases and destructive interference between them occur in most directions of scattering except for a few directions where the diffracted beams are formed thanks to a constructive interference between scattered rays. Given θ the angle formed by the incident beam and the specific crystal plane known as Bragg angle, the angle between the diffracted beam and the transmitted beam is always 2θ; it is known as *diffraction angle* and it is the one usually measured experimentally. It is related to the incident beam (generally monochromatic) wavelength, λ, and the distance between two parallel planes containing scattering centres, d, by the Bragg law (where n is a positive integer).

$$\frac{n\lambda}{2d} = sin\theta \qquad (B\text{-}1)$$

Diffraction directions depend only on shape and size of the unit cell, thus, by measuring intensity of diffracted beam and the diffraction angle, info about the structure of mineral can be gained (Cullity, 1978).

X-ray analyses were performed at University of Cassino and southern Lazio using a Brucker AXS D8 Advance Diffractometer and an x-ray tube with CuKα (λ = 0.154 nm) radiation and a step size of 0.021°.

Thermogravimetric Analysis (TGA)

The thermogravimetric analysis (TGA) is a thermo-analytical technique in which changes in weight are measured as a function of increasing temperature, so the basic instrumental requirements are a precision balance and a furnace programmed for a linear rise of temperature in time (Coats and Redfern, 1963). Results can be represented as weight (or percentage of total weight) versus

temperature, known as thermogravimetric curve, or rate of loss versus temperature (DTG), known as differential thermogravimetric curve. This analysis can provide information about physical and chemical phenomena. For example, it can be used to study the progress of hydration in cementitious materials as shown in 3.1.1.1.

Thermo-gravimetric analyses were performed at University of Cassino and southern Lazio, with a Netzsch STA 449F3 Jupiter, equipped with a mass spectrometer. Finely ground sample was heated at a rate of 10 °C min^{-1}, under argon atmosphere, from ambient temperature to 1000 °C. The Netzsch Proteus software has been used to process the results.

Scanning Electron Microscopy (SEM)

The Scanning Electron Microscopy is a type of electron microscopy. The image of the structure in electron microscopy is obtained via magnetic lens by focusing an electron stream on the sample. The high image resolution and magnification, which can go up to 1000000x, are due to the short wavelength of electrons According to quantum mechanics, an electron which moves at high speed behaves as an electromagnetic wave with a wavelength inversely proportional to its speed, up to 0.003 nm, if accelerated. In addition to scanning, it can be also performed in transmission. (Callister, 1991).

In Scanning Electron Microscopy, the surface of the sample is "scanned" with an electron beam; the reflected electron stream due to the interaction with atoms on the surface are detected by specific detectors to produce an image. This analysis is more suitable to imaging rather than analysis, due to the large depth of field which allows an immediate interpretation by the observer (Reed, 2005).

SEM were performed via SU5000 Hitachi Scanning Electron Microscopy at *Institut des Matériaux Jean Rouxel (IMN)* of University of Nantes. A gold coating of the samples has been performed before SEM observations.

Mercury Intrusion Porosimetry (MIP)

Mercury Intrusion Porosimetry (MIP) is a technique that allows to study the pore size distribution in a sample, but also other information can be acquired. It is based on the principle that a non-wetting liquid requires to be forced to entry in a pore or a capillary. If the pore is cylindrical and the opening is circular in cross-section, the relation between pressure, P, applied to fluid and diameter D is described by Washburn equation, as

$$D = -\frac{4\gamma \cos(\theta)}{P} \qquad \text{(B-2)}$$

where γ is the surface tension of the liquid, θ is the contact angle on solid-liquid interface. Mercury is almost exclusively adopted due to its non-wetting behaviour with most of solid materials (Webb, 2001). As reported by Diamond (1970), surface tension of mercury at 25 °C can be assumed equal to 0.484 N/m, while different contact angles have been observed for clay minerals, but the usual values are 130 or 140 degrees. The value of 130 degree can also be adopted for concrete (Ma, 2014).

The test is usually performed applying a series of small pressure step increments in which pressure and volume are measured after equilibrium is achieved. Pores must be empty of water and any other fluid when analysis begins. Then, applying Washburn's equation (B-2) it is possible to determine the pore size associated to volume intruded. By this way, a cumulative curve is obtained. The volume intruded for each pressure step, i.e., for each pore size class, is the difference between the respective cumulative intrusion volumes. By this way, a volume intruded can be associated to each pore size class. To normalize data, intrusion volume is expressed in terms of fraction of total volume intruded (Webb, 2001). The same procedure can be applied in extrusion, with decreasing pressure steps.

It is worth noting that completely isolated pores which are inaccessible from the outside and pores that would require a pressure higher than instrument capacity cannot be measured. Larger pores (pore cavities), accessible only by smaller pores (pore throats), cannot be intruded until the pressure goes up to the value associated to the smaller diameter. By this way, the volume intruded in both pores (smaller and larger) is associated to the smaller class of pores leading to a bias called "ink bottle" effect (Abell et al., 1999). This phenomenon causes the hysteresis of intrusion-extrusion curve. Indeed, when pressure is reduced, in a throat-cavity connection the throat is emptied at the same pressure at which it has been filled, but cavity remains filled because the pressure is still high enough to make the cavity filled. The cavity can be emptied at the lower pressure associated with its radius or not emptied at all if pore diameters of the paths leading to surface are of inappropriate size (Webb, 2001). In this last case, total volume extruded is lower than volume intruded.

MIP tests were performed at University of Cassino and southern Lazio by a double chamber Micromeritics Autopore III apparatus. In the filling apparatus

(dilatometer) samples were outgassed under vacuum and then filled by mercury allowing increase of absolute pressure up to ambient one. Using the same unit the intrusion pressure was than raised up to approximately 200 kPa by means of compressed air. The detected entrance pore diameters range between 134 μm and 7.3 μm (approximately 0.01 MPa - 0.2 MPa for a mercury contact angle of 139°). After depressurization to ambient pressure, samples were transferred to high-pressure unit, where mercury pressure was increased up to 205 MPa following a previously set intrusion program. Corrections to pore-size distribution due to compressibility of intrusion system were applied performing a blank test.

Mechanical tests

Oedometer test

Oedometer test is a standard test that reproduces in laboratory one dimensional consolidation conditions. The specimen is cylindrical, and the horizontal confinement is obtained via a confining ring. According to standards (ASTM, 1990), diameter and height of sample must be respectively equal or higher than 50 mm and 12 mm while their ratio should be at least 2.5 to minimize the effect of friction between the sample and the confining ring; this one must be stiff enough to ensure that the change in diameter won't exceed 0.03% of the diameter under maximum load (ASTM, 1990). On the bottom and upper surfaces, the sample is confined between two porous stone, with a steel head on the upper porous stone to apply the load. The ring can be either fixed on the base or floating (supported by friction on periphery of specimen) (ASTM, 1990). The sample with confining ring and porous stone is put in a box filled with water.

The apparatus used in laboratory is a standard device with controlled incremental load. Specimen diameter is 55 mm with a height of 20 mm, whose ratio is higher than 2.5 as the standard requires. Vertical displacements are measured via a Linear Variable Differential Transducer (LVDT). The load increment is applied when the 100% of primary consolidation is supposed to be reached (ASTM, 1990). Indeed, as reported by Lancellotta (2012), the amount of deformation that has to be taken into account is the one related to primary consolidation while secondary consolidation is related to creep. In Figure B-1 an example time-deformation curve is represented. The end of primary consolidation is conventionally assumed at the intersection between the tangent to the steepest part of the deformation-log time curve and the straight line through the points representing the final reading, as suggested by Casagrande (1936) and reported by ASTM standard (ASTM, 1990). The standard also suggests another

procedure based on deformation-square root of time curve. The results are usually represented in e-log$\sigma_v^{'}$ or ε-log$\sigma_v^{'}$ planes, where "e" is the void ratio and "ε" is the vertical strain:

$$e = \frac{V_p}{V_s} = H_0 - \frac{\Delta H}{H_s};\ \varepsilon = \frac{\Delta H}{H_0}; \qquad (B\text{-}3)$$

Where V_s is the volume of the solid phase, V_p is the volume of pores, H_0 is the initial height of the sample and H_s is the height of the solid phase.

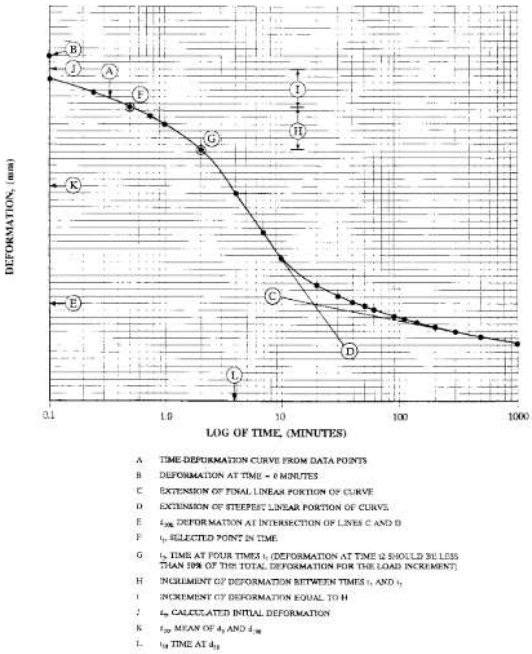

Figure B-1. Time-deformation curve in semi-log space (ASTM, 1990)

Direct shear test

The direct shear apparatus is a standard device used to determine strength parameters soils. The specimen is a rectangular parallelepiped, with a base A that is usually 60x60 mm and 20-25 mm height. The specimen, confined below and above between two porous rough square plates, is put in the shear box, that is stiff enough to ensure oedometric condition under vertical loads (Figure B-2). The box is composed of two steel frames that can slide one on another. The test is composed of two phases. At first, a vertical load N is applied on the head of the sample via the piston in oedometric condition. By this way, a vertical stress $\sigma_v^{'}$ equal to N/A is applied and vertical displacement are measured in time. At the end of primary consolidation, a controlled displacement rate is applied to the bottom frame of the box, which slides below the upper part that is restrained via

a dynamometer that measures the shear load T. During this phase both vertical and horizontal displacements are measured.

Due to test conditions, the shear plane is imposed to be the horizontal plane between the two shear box halves, which means that the shear stress acting on the plane, τ, is equal to T/A. Even if the area of the shear surface decreases during the test, causing an uncertainty regarding the value of shear and normal stress, it shouldn't affect their ratio (ASTM, 2003).

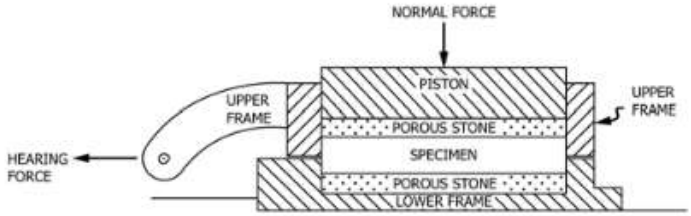

Figure B-2. Shear box apparatus (ASTM, 2003)

Due to the impossibility to control the drainage conditions, only drained tests are reliable. Stress-strain curves have only qualitative meaning due to the non-uniformity of strain in sample and progressive failure. It's also not possible to define the stress state in the sample because only the normal and shear stresses on horizontal plane are known. Moreover, it's not certain if the shear stress is equal to the shear strength on the plane (B-4a) or the maximum shear stress in the sample (B-4b) (Lancellotta 2012).

$$\text{(a) } \tau = \tau_{ff}\text{; (b) } \tau = t = \frac{1}{2}(\sigma_1 - \sigma_3)_{max}; \qquad \textit{(B-4)}$$

In order to determine the strength parameters, three tests are required at different normal loads. Then, the resultant σ_v and τ are conventionally reported in the plane τ-σ' to determine c' and φ'.

The adopted shear box apparatus is a standard one, the shear force being developed by an electric motor driving, providing a variable speed control ranging from $5 \cdot 10^{-4}$ to 2 mm/min. All direct shear tests have been performed at a displacement rate of 0.005 mm/min. Micrometer dial gauges with a resolution of 0.001 and 0.01 mm have been respectively used to measure vertical and horizontal displacements.

References

Abell, A.B., Willis, K.L., Lange, D.A., 1999. Mercury Intrusion Porosimetry and Image Analysis on Cement-Based Materials. J. Colloid Interface Sci. 44, 39–44.

ASTM, 2003. Standard Test Method for Direct Shear Test of Soils Under Consolidated Drained, Test. https://doi.org/10.1520/D3080

ASTM, 1990. Standard test method for one-dimensional consolidation properties of soils, ASTM D 2435-65T. https://doi.org/10.1520/D2435-96

Callister, W.D., 1991. Materials science and engineering: An introduction (2nd edition). Mater. Des. https://doi.org/10.1016/0261-3069(91)90101-9

Casagrande, A., 1936. The Determination of the Pre-Consolidation Load and Its Practical Significance, in: Proceedings of the 1st International Conference on Soil Mechanics. Harvard, pagg. 60–64.

Coats, A.W., Redfern, J.P., 1963. Thermogravimetric analysis. A review. Analyst. https://doi.org/10.1039/AN9638800906

Cullity, B.D., 1978. Elements of X-ray diffraction, 2nd edition. Addison-Wesley Publ. Co. Read. MA. https://doi.org/10.1119/1.1934486

Diamond, S., 1970. Pore Size Distributions in Clays. Clays Clay Miner. 18, 7–23. https://doi.org/10.1346/CCMN.1970.0180103

Lancellotta, R., 2012. Geotecnica, 4th ed.

Ma, H., 2014. Mercury intrusion porosimetry in concrete technology: Tips in measurement, pore structure parameter acquisition and application. J. Porous Mater. 21, 207–215. https://doi.org/10.1007/s10934-013-9765-4

Reed, S.J.B., 2005. Electron Microprobe Analysis and Scanning Electron Microscopy in Geology. Cambridge University Press, Cambridge. https://doi.org/10.1017/CBO9780511610561

Webb, P.A., 2001. An Introduction To The Physical Characterization of Materials by Mercury Intrusion Porosimetry with Emphasis On Reduction And Presentation of Experimental Data. Micrometrics Instrum. Corp. 23. https://doi.org/10.1177/004057368303900411

Appendix C

Mechanical tests results

Cemented Speswhite kaolin

Table C-0-1. Properties of cemented kaolin samples;

		t [days]	γ [kN/m^3]	γ_{dry} [kN/m^3]	e	σ'_v [kPa]	τ_{max} [kPa]
K cs20	*Kcs20_7d_50kPa*	7	13.5	6.2	3.2	50	49
	Kcs20_7d_100kPa	7	13.7	6.1	3.2	100	69
	Kcs20_7d_150kPa	7	13.6	6.2	3.2	150	118
	Kcs20_7d_50kPa	28	13.9	6.3	3.1	50	66
	Kcs20_7d_100kPa	28	13.7	6.2	3.2	100	92
	Kcs20_28d_150kPa	28	13.7	6.3	3.1	150	110
	Kcs20_7d_oed	7	13.6	6.4	3.1	-	-
	Kcs20_28d_oed	28	13.6	6.5	3.0	-	-
K cs40	*Kcs40_1d_50kPa*	1	14.3	-	-	50	62
	Kcs40_1d_100kPa	1	14.1	6.8	2.8	100	94
	Kcs40_1d_150kPa	1	14.0	6.5	3.0	150	129
	Kcs40_3d_50kPa	3	14.1	-	-	50	82
	Kcs40_3d_100kPa	3	14.0	6.9	2.8	100	107
	Kcs40_3d_150kPa	3	14.2	6.1	3.3	150	137
	Kcs40_7d_50kPa	7	14.3	6.8	2.8	50	95
	Kcs40_7d_100kPa	7	14.0	6.9	2.8	100	120
	Kcs40_7d_150kPa	7	13.9	6.4	3.1	150	160
	Kcs40_14d_50kPa	14	14.2	-	-	50	103
	Kcs40_14d_100kPa	14	13.9	6.8	2.8	100	133
	Kcs40_14d_150kPa	14	13.9	6.8	2.8	150	143
	Kcs40_28d_50kPa	28	14.0	6.8	2.8	50	95
	Kcs40_28d_100kPa	28	14.3	6.7	2.9	100	137
	Kcs40_28d_150kPa	28	14.1	6.8	2.8	150	177
	Kcs40_60d_50kPa	60	14.0	6.9	2.8	50	116
	Kcs40_60d_100kPa	60	14.1	7.0	2.7	100	143
	Kcs40_60d_150kPa	60	14.0	7.0	2.7	150	154
	Kcs40_90d_50kPa	90	14.0	7.0	2.7	50	127
	Kcs40_90d_100kPa	90	14.1	6.9	2.7	100	170
	Kcs40_90d_150kPa	90	14.0	6.9	2.8	150	206
	Kcs40_7d_oed	7	14.1	7.1	2.6	-	-
	Kcs40_28d_oed	28	14.1	7.0	2.7	-	-

Kcs40

Direct shear tests

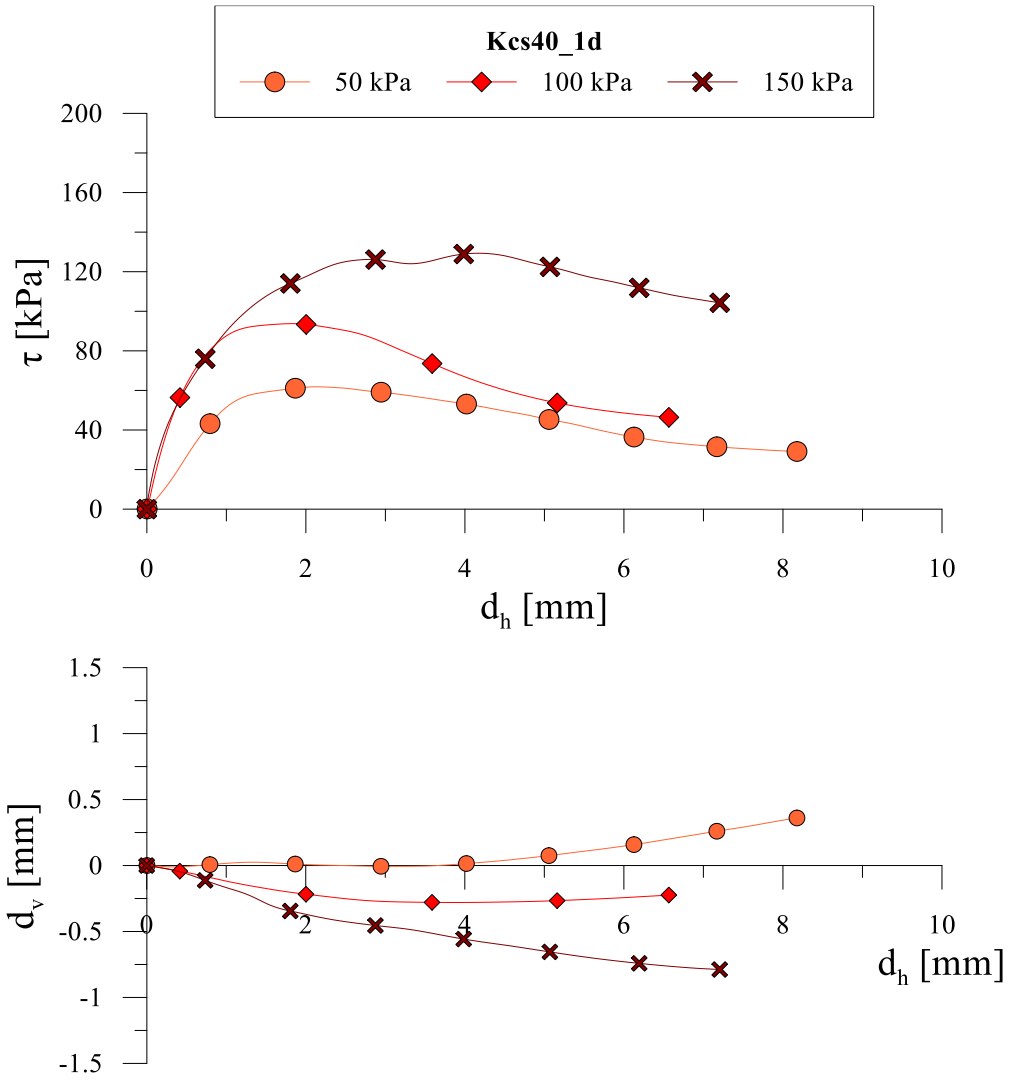

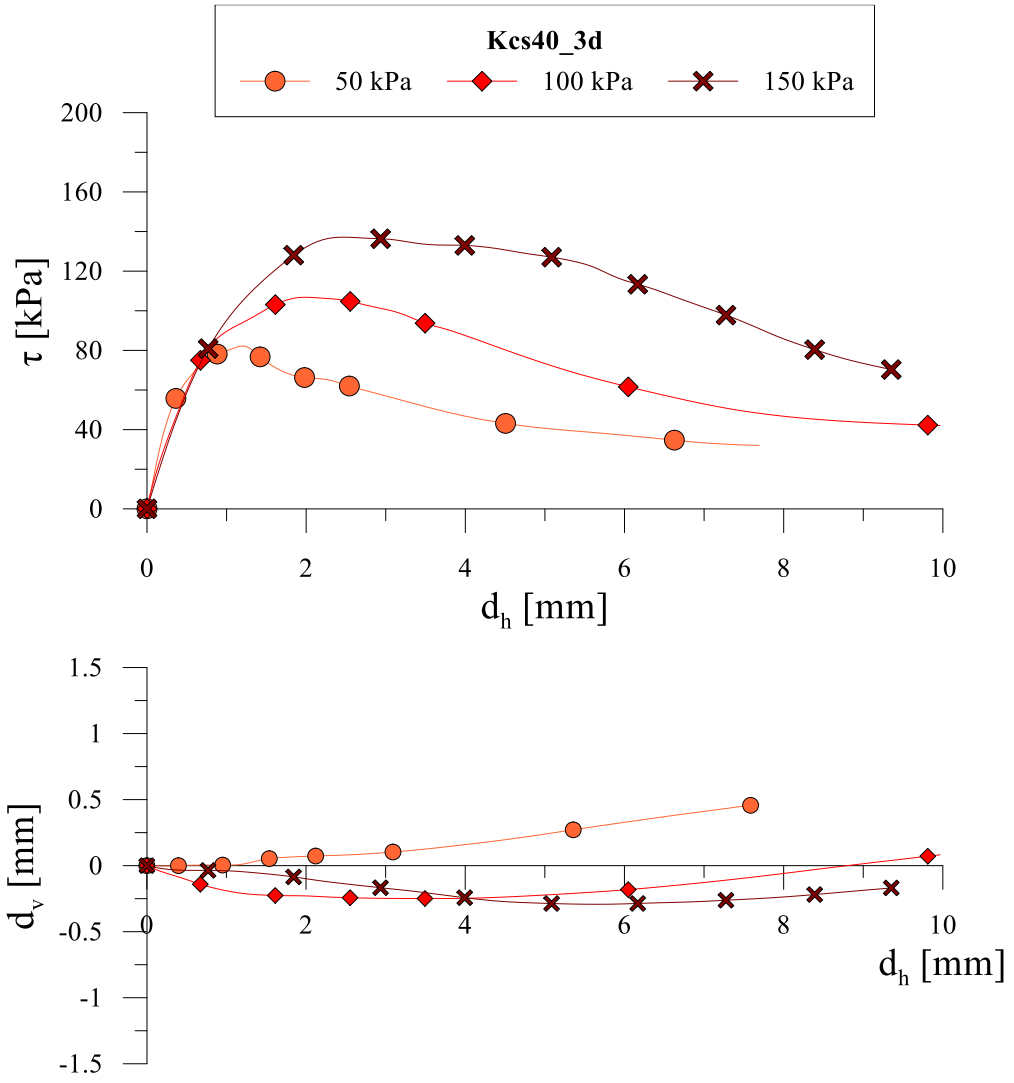
Kcs40_3d
50 kPa
100 kPa
150 kPa
τ [kPa]
200
160
120
80
40
0
0
2
4
6
8
10
d_h [mm]
d_v [mm]
1.5
1
0.5
0
-0.5
-1
-1.5
0
2
4
6
8
10
d_h [mm]

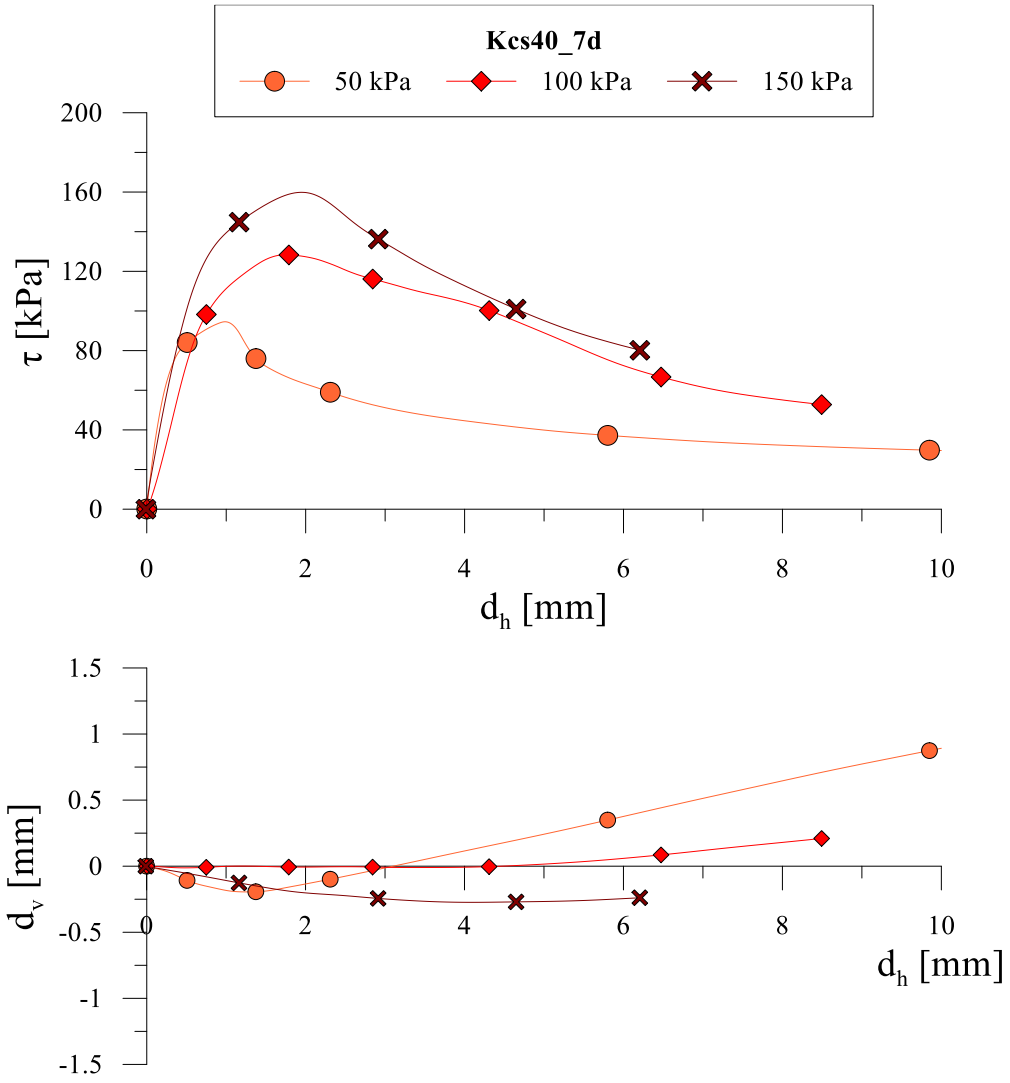
Kcs40_7d
50 kPa
100 kPa
150 kPa
τ [kPa]
200
160
120
80
40
0
0
2
4
6
8
10
d_h [mm]
d_v [mm]
1.5
1
0.5
0
-0.5
-1
-1.5
0
2
4
6
8
10
d_h [mm]

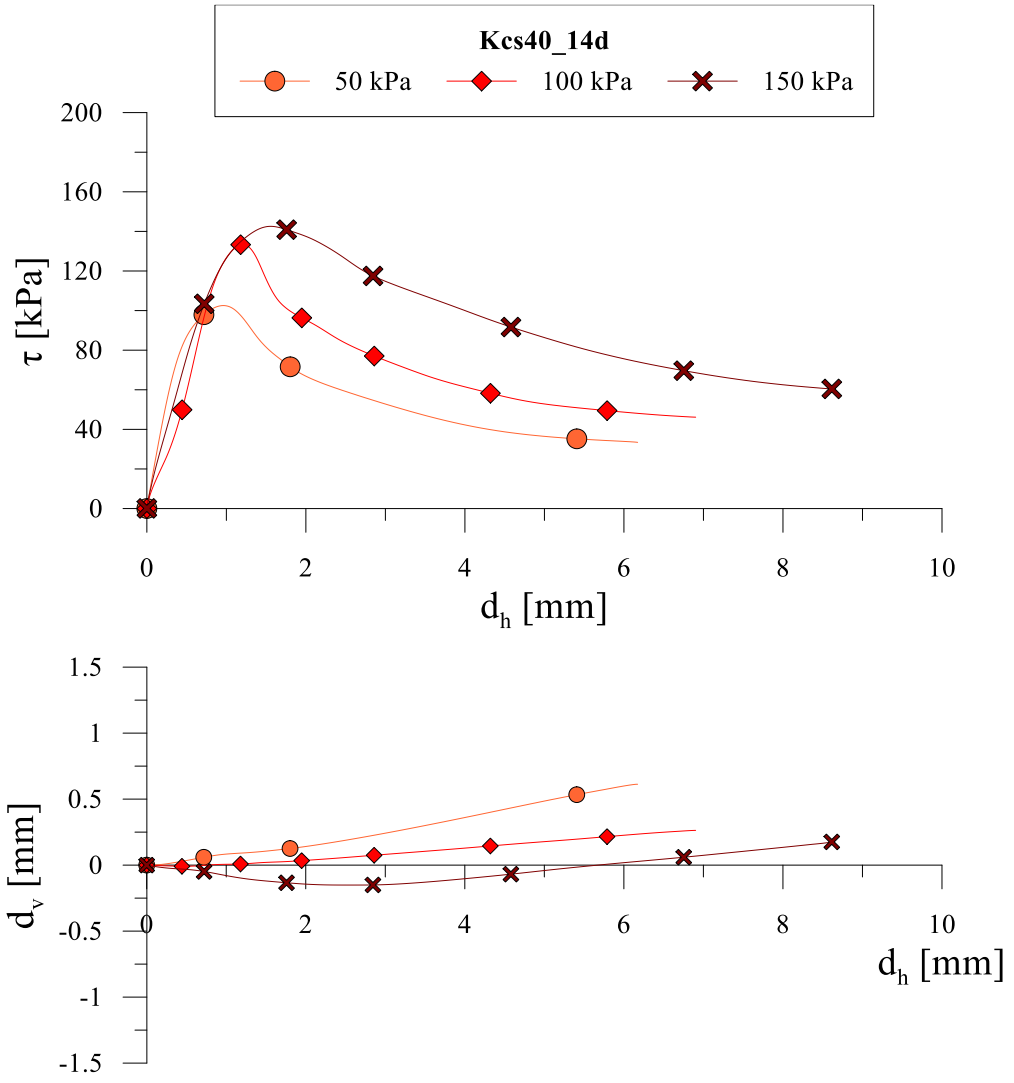
Kcs40_14d
50 kPa
100 kPa
150 kPa
τ [kPa]
200
160
120
80
40
0
0
2
4
6
8
10
d_h [mm]
d_v [mm]
1.5
1
0.5
0
-0.5
-1
-1.5
0
2
4
6
8
10
d_h [mm]

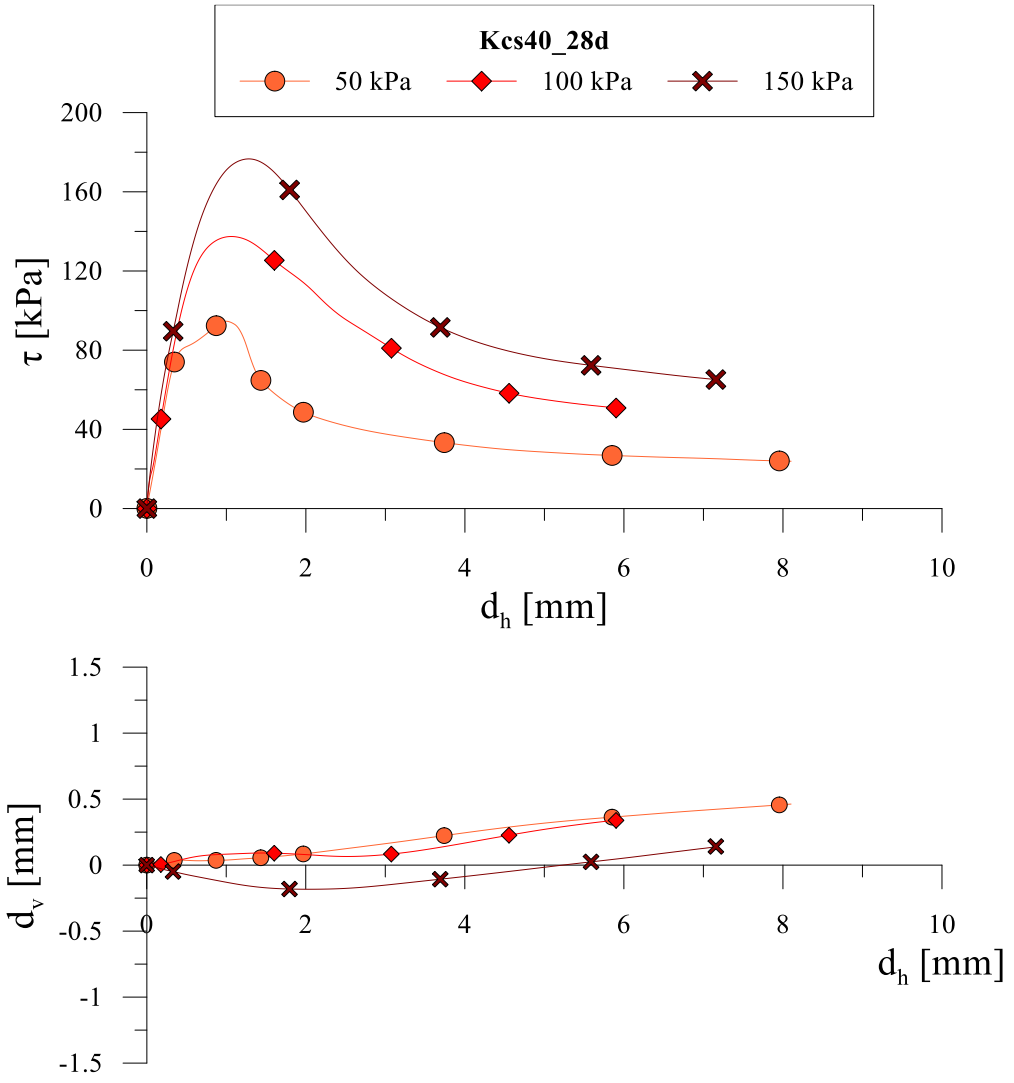
Kcs40_28d
50 kPa
100 kPa
150 kPa
τ [kPa]
200
160
120
80
40
0
0
2
4
6
8
10
d_h [mm]
d_v [mm]
1.5
1
0.5
0
-0.5
-1
-1.5
0
2
4
6
8
10
d_h [mm]

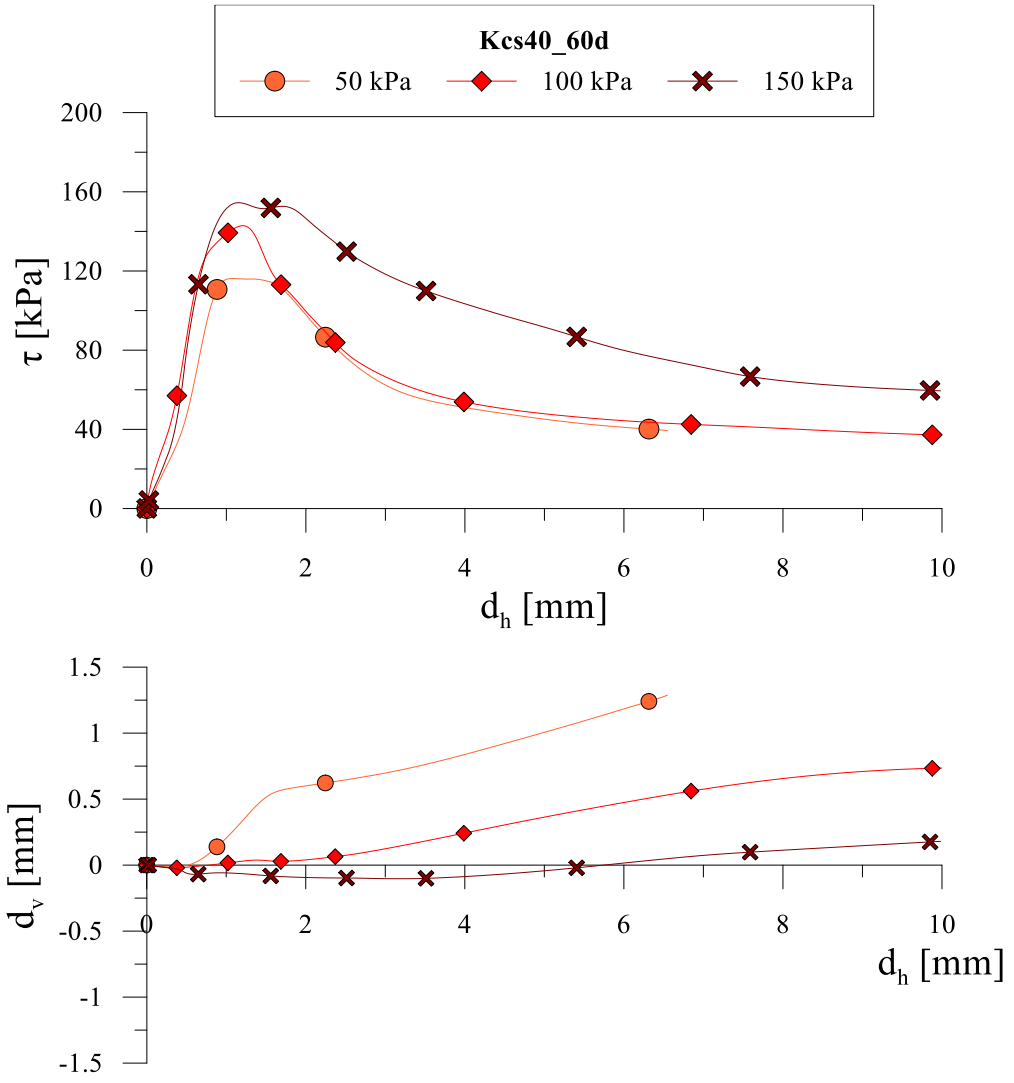
Kcs40_60d
50 kPa
100 kPa
150 kPa
τ [kPa]
200
160
120
80
40
0
0
2
4
6
8
10
d_h [mm]
d_v [mm]
1.5
1
0.5
0
-0.5
-1
-1.5
0
2
4
6
8
10
d_h [mm]

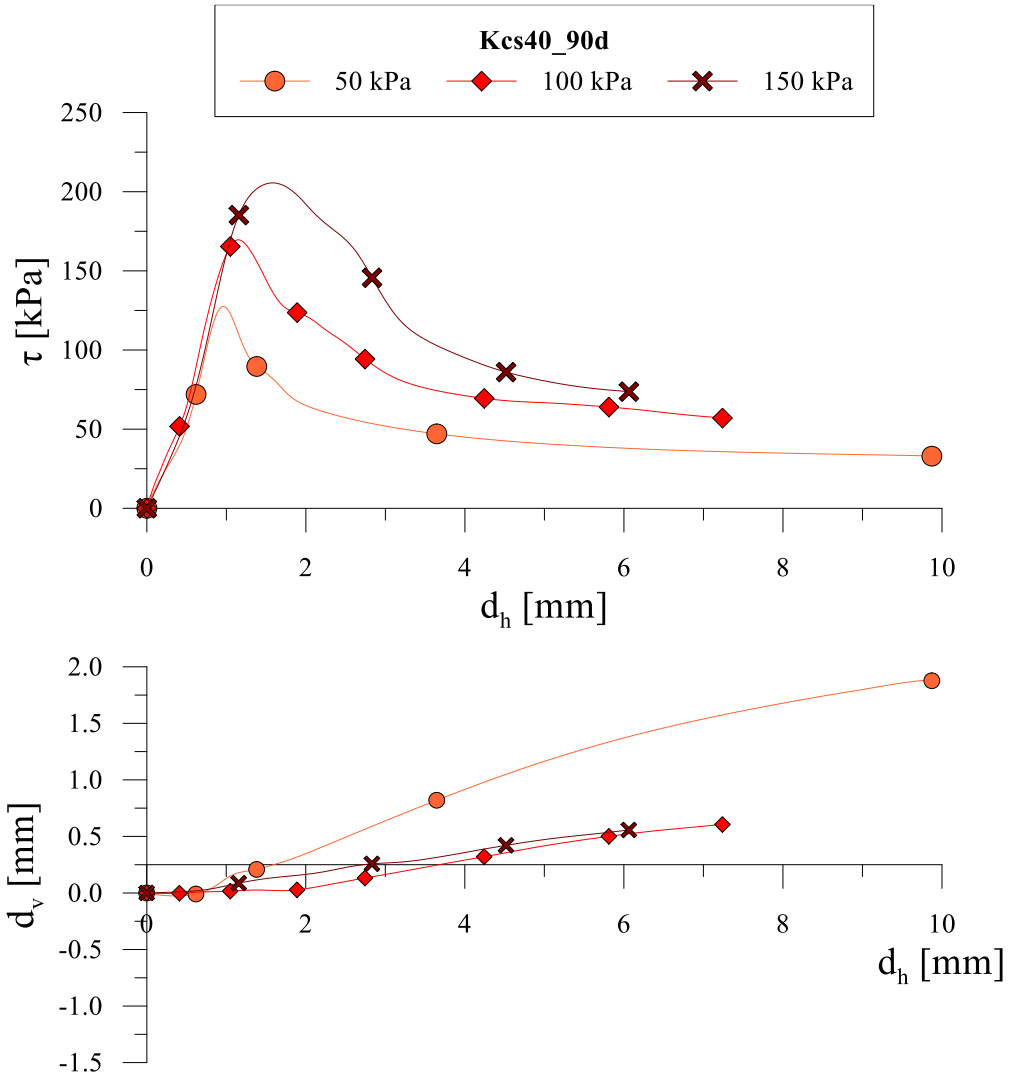
Kcs40_90d
50 kPa
100 kPa
150 kPa
τ [kPa]
250
200
150
100
50
0
0
2
4
6
8
10
d_h [mm]
d_v [mm]
2.0
1.5
1.0
0.5
0.0
-0.5
-1.0
-1.5
0
2
4
6
8
10
d_h [mm]

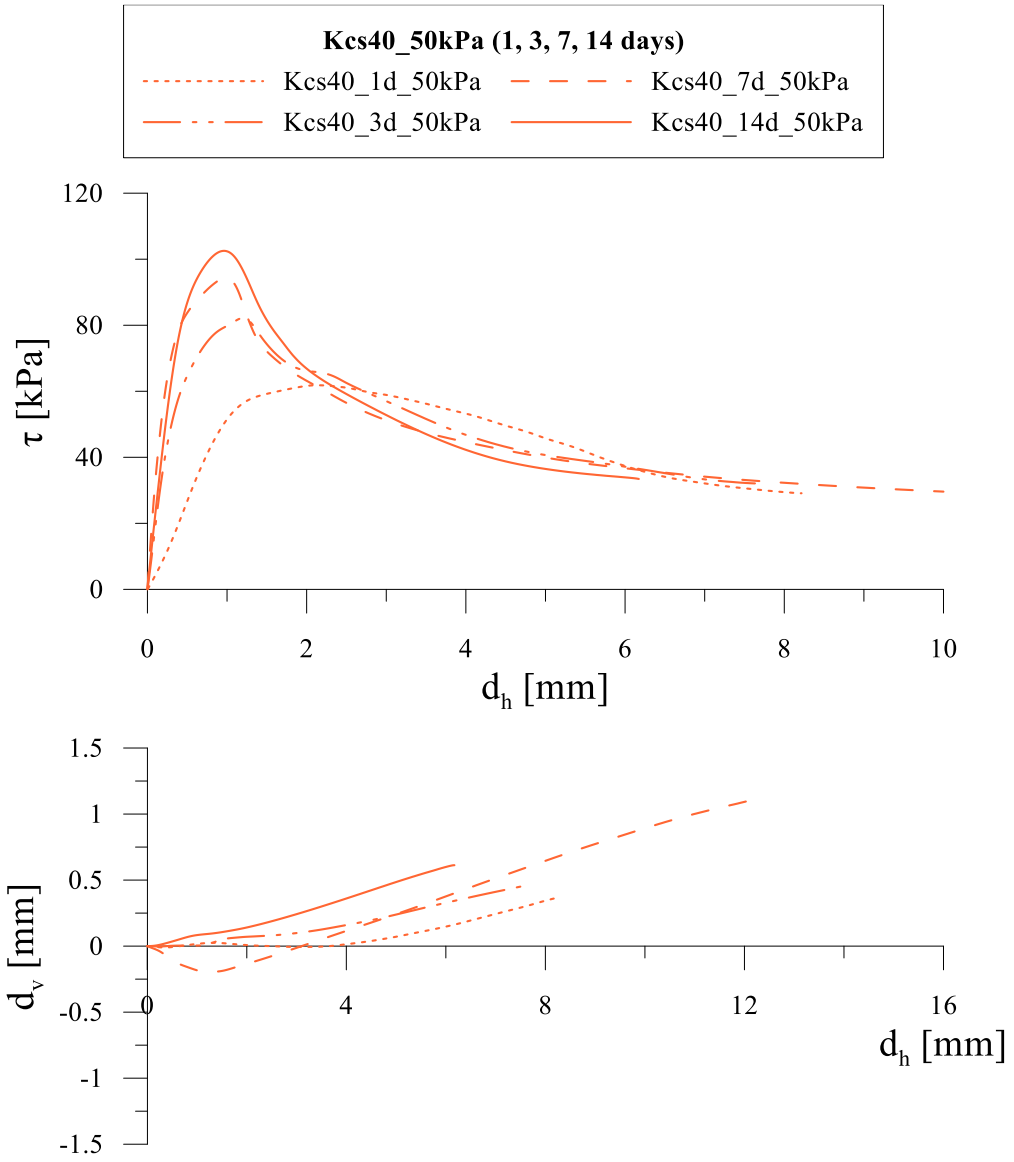
Kcs40_50kPa (1, 3, 7, 14 days)
Kcs40_1d_50kPa
Kcs40_7d_50kPa
Kcs40_3d_50kPa
Kcs40_14d_50kPa
τ [kPa]
120
80
40
0
0
2
4
6
8
10
d_h [mm]
d_v [mm]
1.5
1
0.5
0
-0.5
-1
-1.5
0
4
8
12
16
d_h [mm]

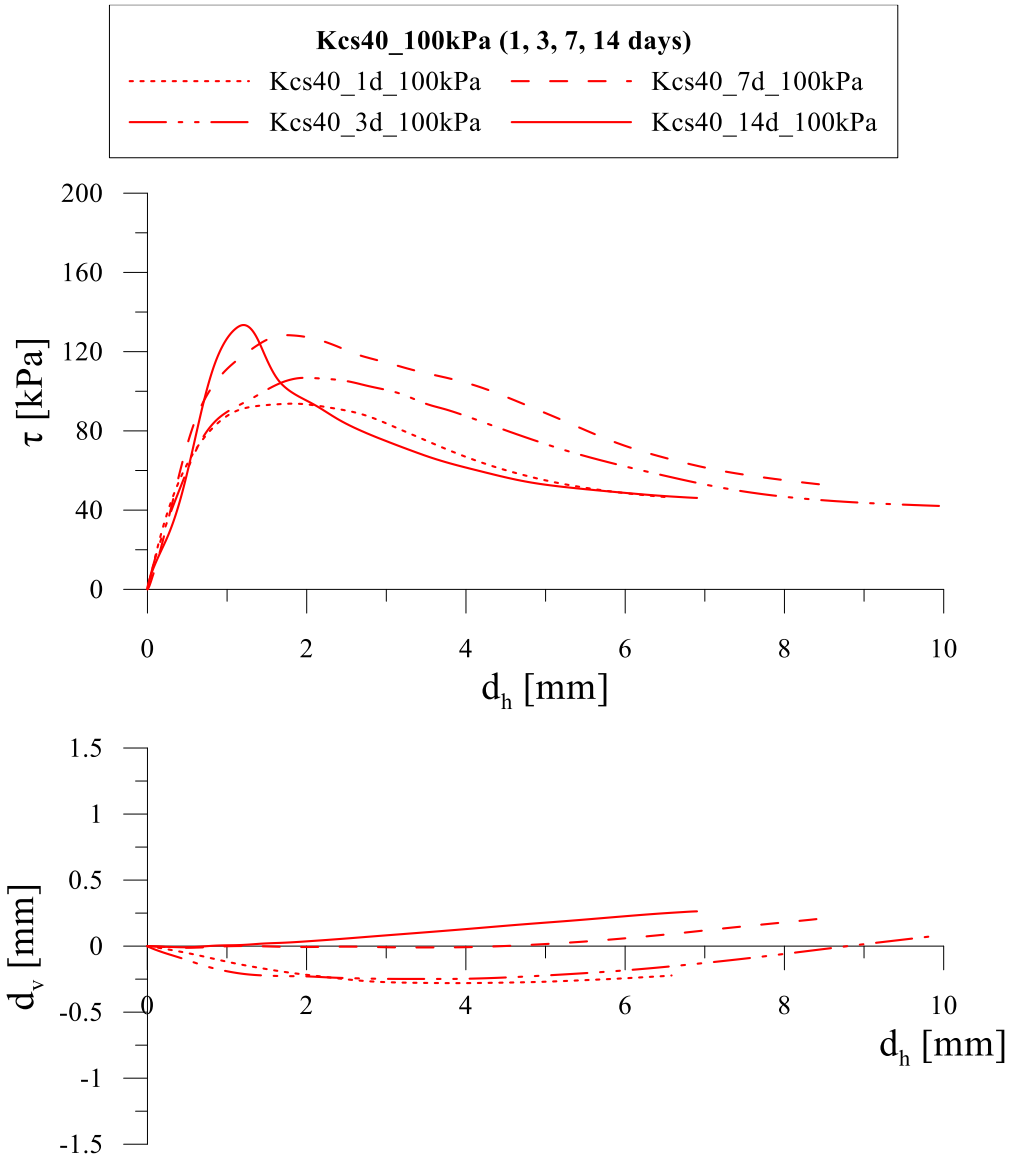
Kcs40_100kPa (1, 3, 7, 14 days)
Kcs40_1d_100kPa
Kcs40_7d_100kPa
Kcs40_3d_100kPa
Kcs40_14d_100kPa
τ [kPa]
200
160
120
80
40
0
0
2
4
6
8
10
d_h [mm]
d_v [mm]
1.5
1
0.5
0
-0.5
-1
-1.5
0
2
4
6
8
10
d_h [mm]

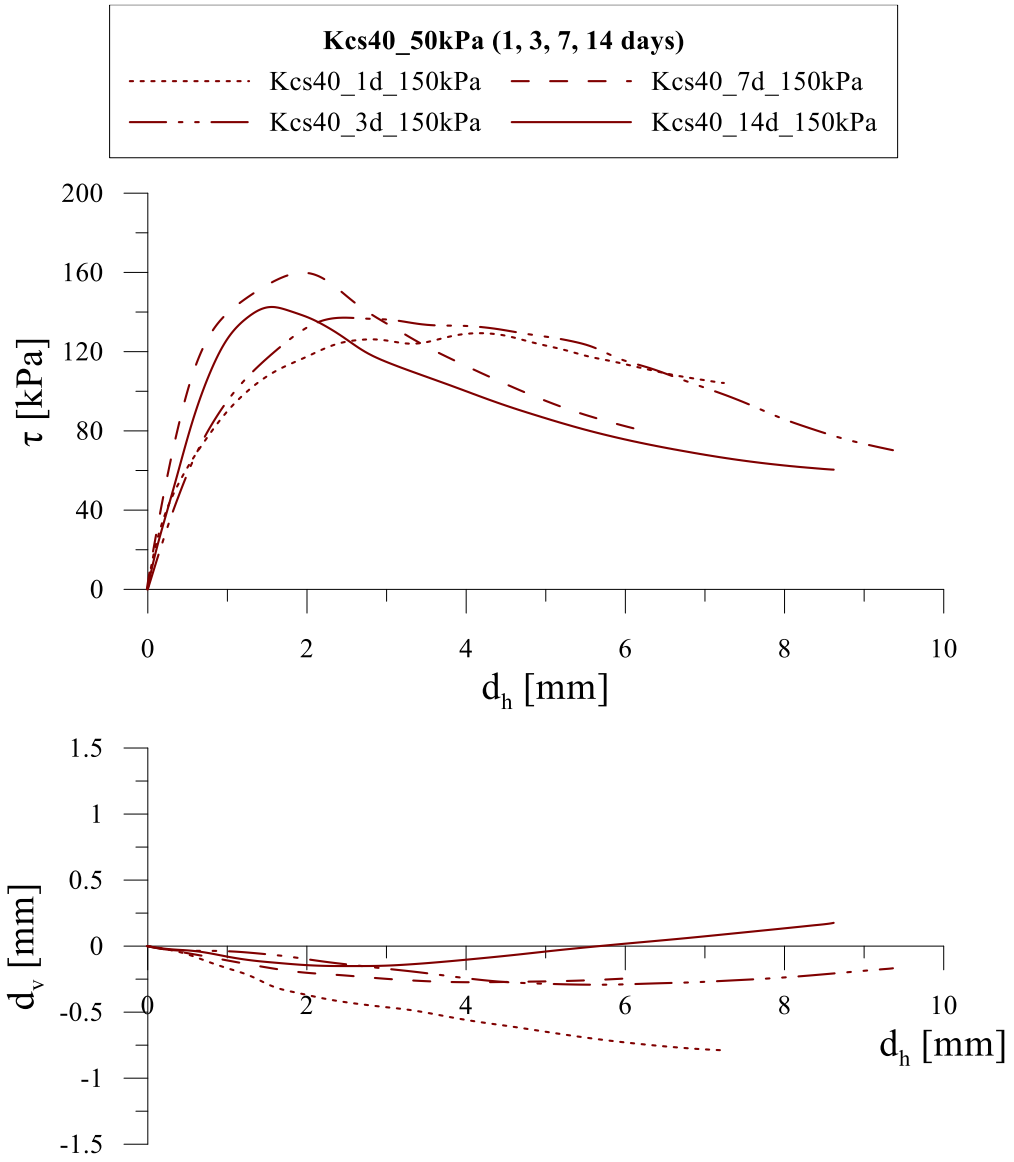
Kcs40_50kPa (1, 3, 7, 14 days)
Kcs40_1d_150kPa
Kcs40_7d_150kPa
Kcs40_3d_150kPa
Kcs40_14d_150kPa
τ [kPa]
200
160
120
80
40
0
0
2
4
6
8
10
d_h [mm]
d_v [mm]
1.5
1
0.5
0
-0.5
-1
-1.5
0
2
4
6
8
10
d_h [mm]

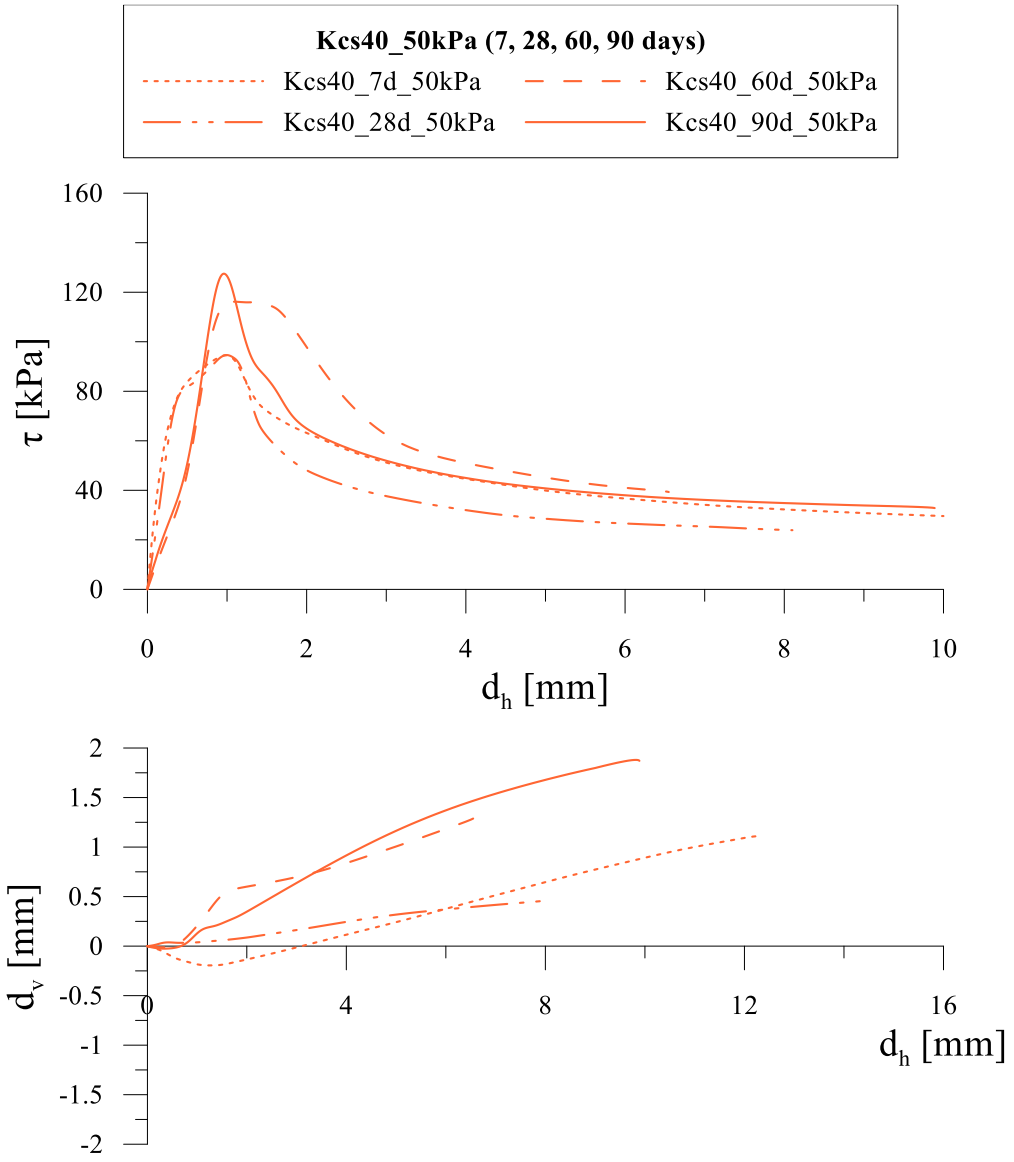
Kcs40_50kPa (7, 28, 60, 90 days)
Kcs40_7d_50kPa
Kcs40_28d_50kPa
Kcs40_60d_50kPa
Kcs40_90d_50kPa
τ [kPa]
160
120
80
40
0
0
2
4
6
8
10
d_h [mm]
d_v [mm]
2
1.5
1
0.5
0
-0.5
-1
-1.5
-2
0
4
8
12
16
d_h [mm]

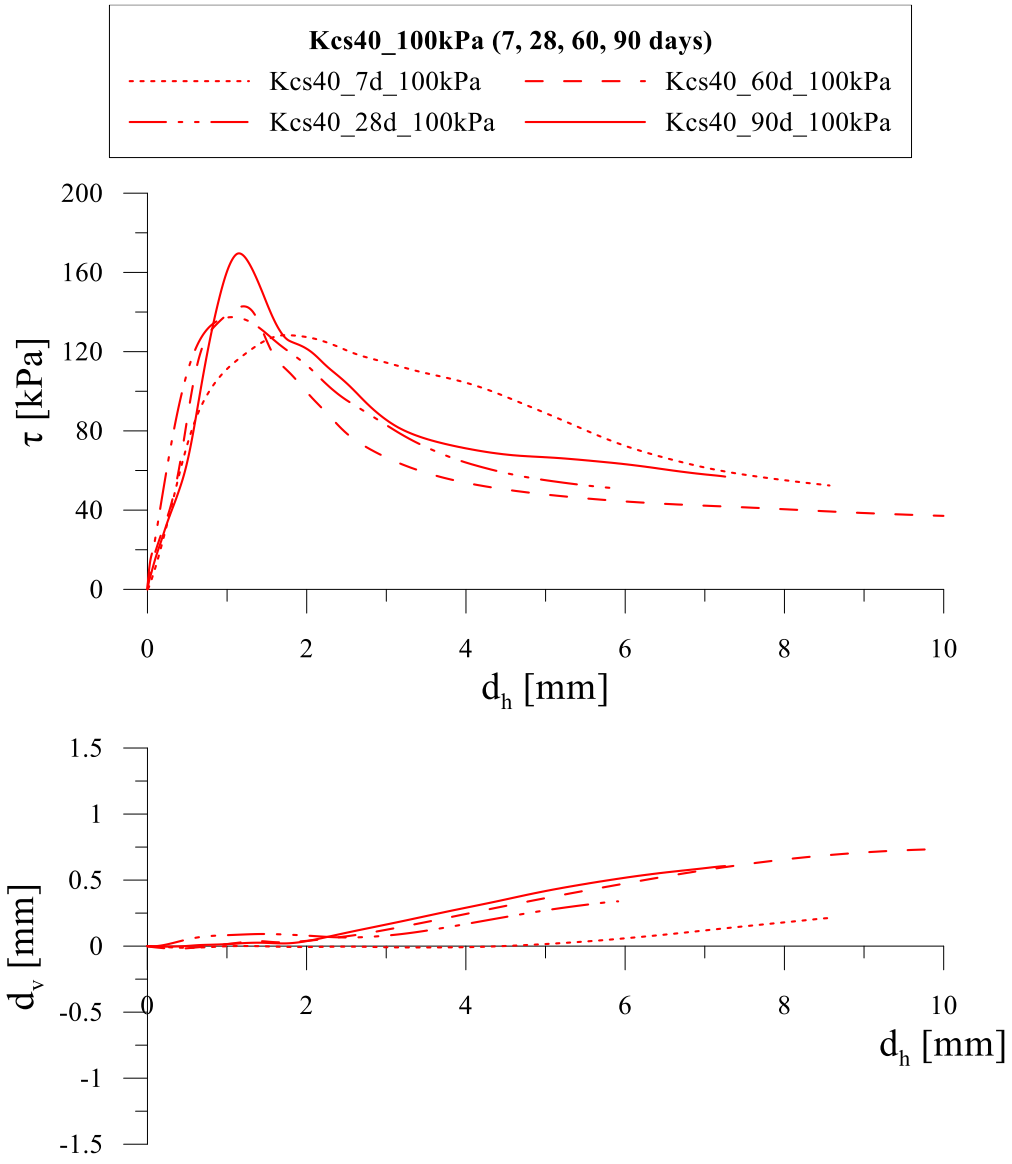
Kcs40_100kPa (7, 28, 60, 90 days)
Kcs40_7d_100kPa
Kcs40_28d_100kPa
Kcs40_60d_100kPa
Kcs40_90d_100kPa
τ [kPa]
200
160
120
80
40
0
0
2
4
6
8
10
d_h [mm]
d_v [mm]
1.5
1
0.5
0
-0.5
-1
-1.5
0
2
4
6
8
10
d_h [mm]

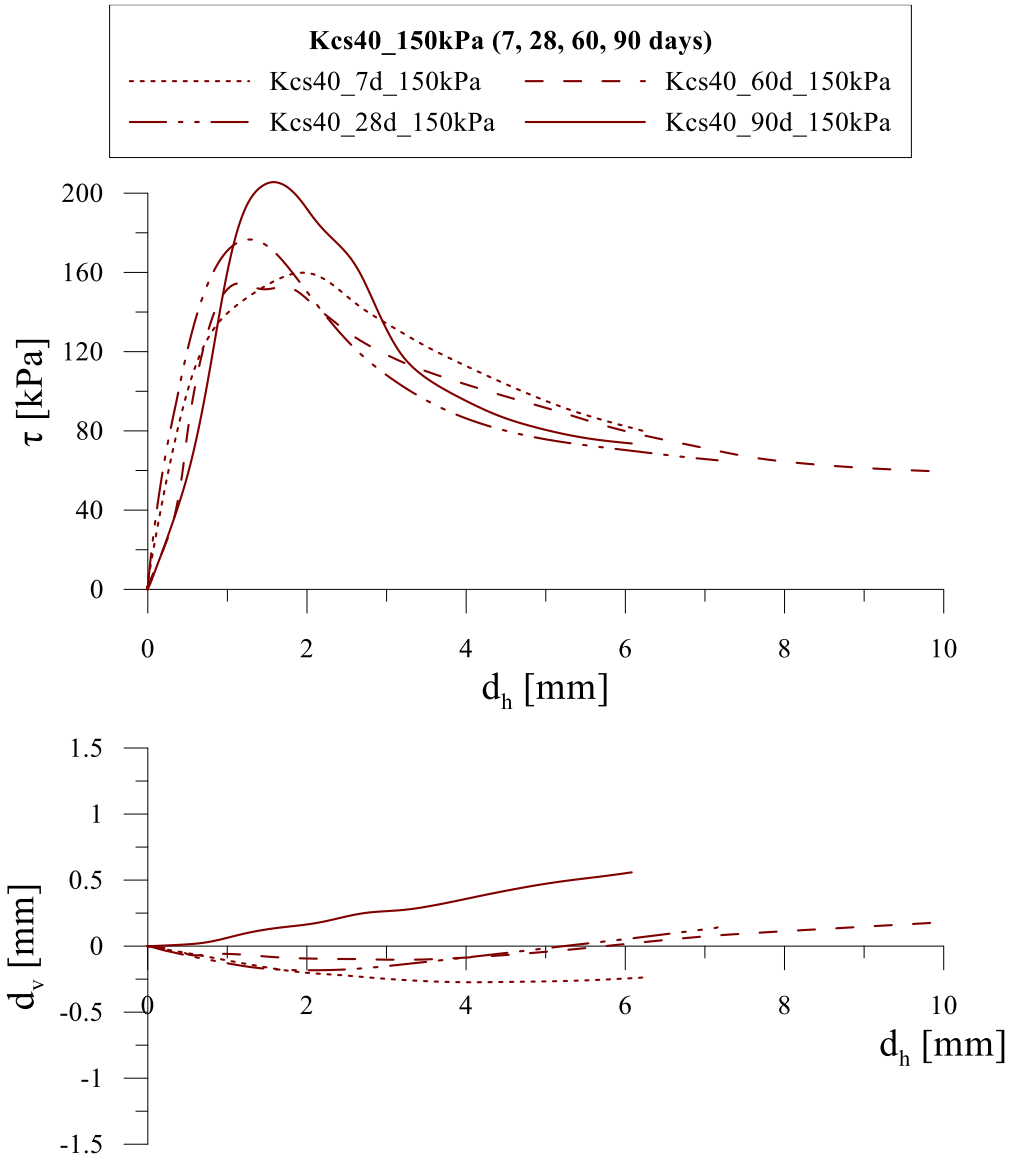
Kcs40_150kPa (7, 28, 60, 90 days)
Kcs40_7d_150kPa
Kcs40_28d_150kPa
Kcs40_60d_150kPa
Kcs40_90d_150kPa
τ [kPa]
200
160
120
80
40
0
0
2
4
6
8
10
d_h [mm]
d_v [mm]
1.5
1
0.5
0
-0.5
-1
-1.5
0
2
4
6
8
10
d_h [mm]

Oedometric tests

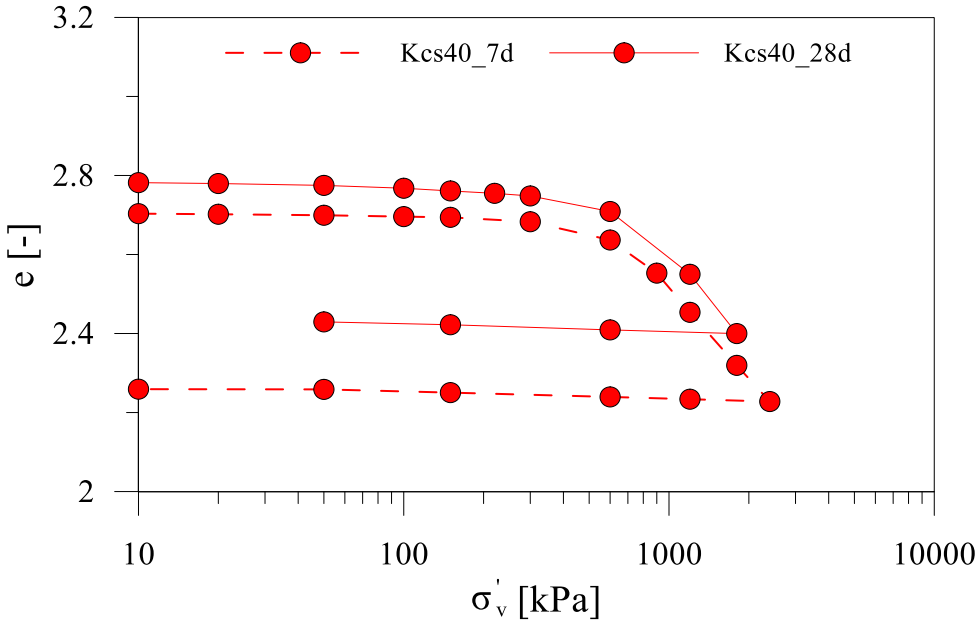

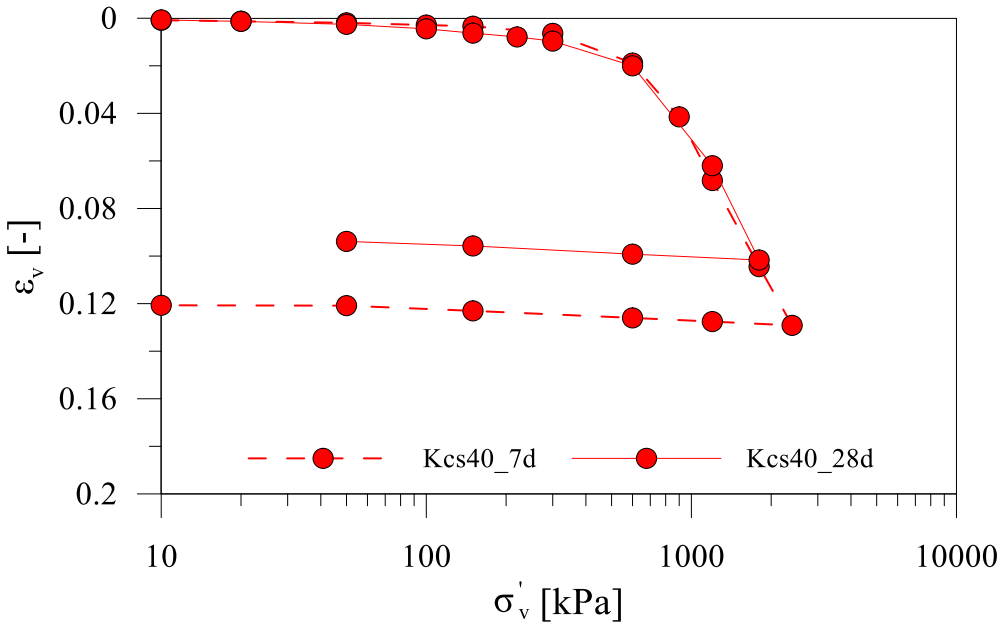

Kcs20

Direct shear tests

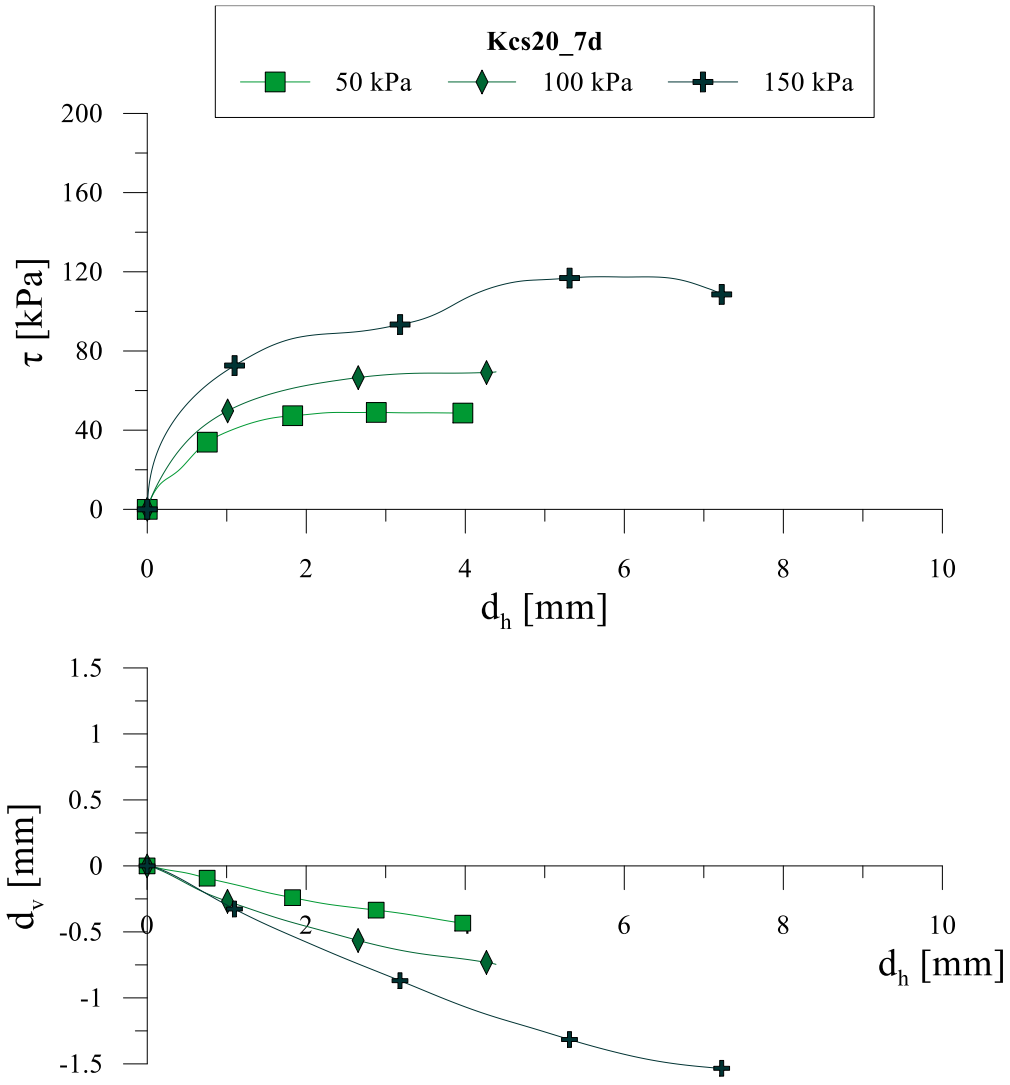

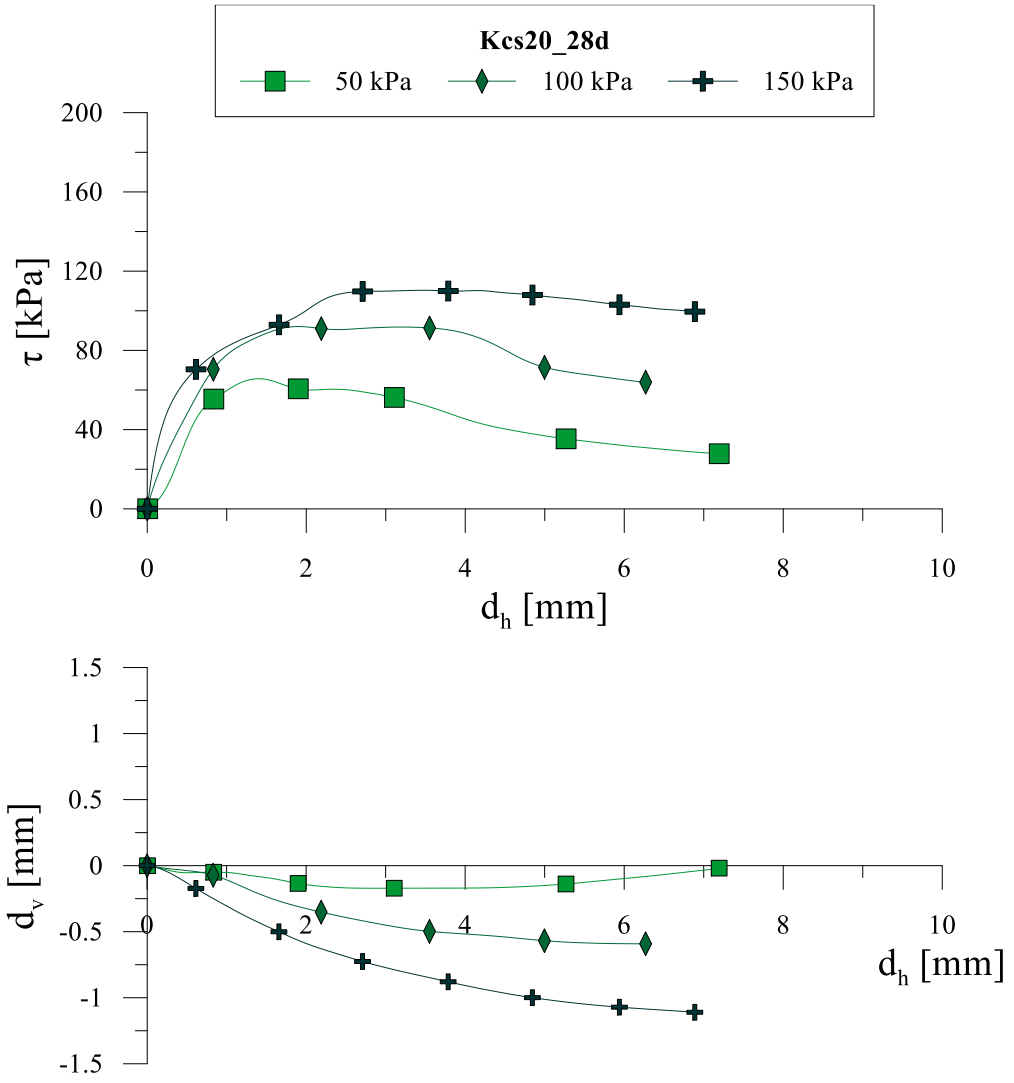
Kcs20_28d
50 kPa
100 kPa
150 kPa
τ [kPa]
200
160
120
80
40
0
0
2
4
6
8
10
d_h [mm]
d_v [mm]
1.5
1
0.5
0
-0.5
-1
-1.5
0
2
4
6
8
10
d_h [mm]

Oedometric tests

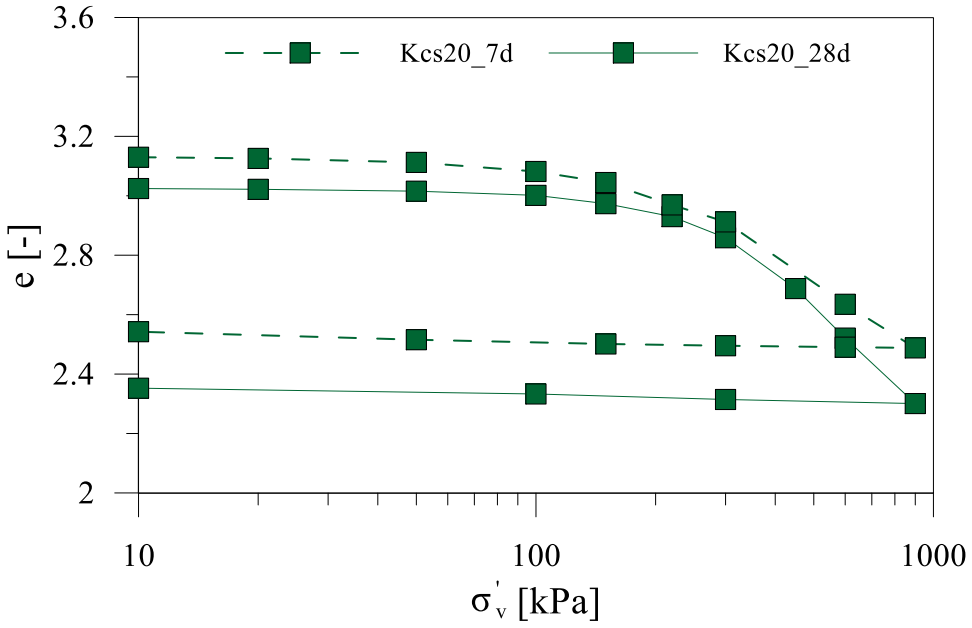

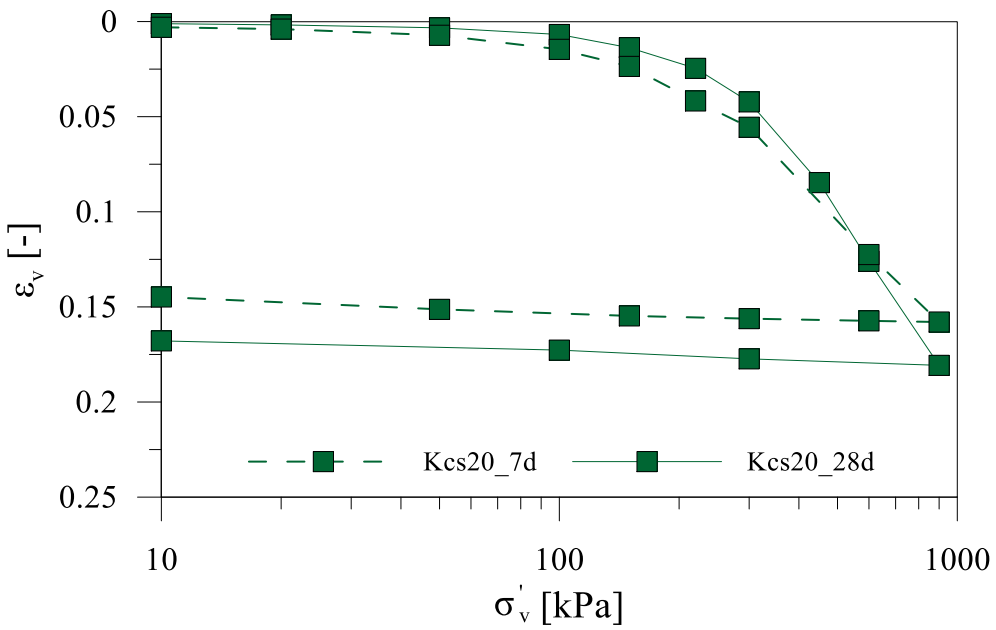

Lightweight cemented kaolin

Table C-0-2

		t [days]	γ [kN/m^3]	γ_{dry} [kN/m^3]	e	σ'_v [kPa]	τ_{max} [kPa]
K cs20 nf20	*Kcs20_nf20_7d_50kPa*	7	12.8	5.7	3.5	50	49.1
	Kcs20_nf20_7d_100kPa	7	12.3	5.5	3.8	100	71.9
	Kcs20_nf20_7d_150kPa	7	12.9	6.2	3.2	150	105.5
	Kcs20_nf20_28d_50kPa	28	13.0	5.8	3.5	50	47.8
	Kcs20_nf20_28d_100kPa	28	13.0	5.8	3.5	100	77.9
	Kcs20_nf20_28d_150kPa	28	12.5	5.6	3.6	150	101.9
	Kcs20_nf20_7d_oed	7	12.7	5.8	3.5	-	-
K cs40 nf20	*Kcs40_nf20_7d_50kPa*	7	12.6	6.0	3.3	50	69.0
	Kcs40_nf20_7d_100kPa	7	12.8	6.1	3.2	100	99.7
	Kcs40_nf20_7d_150kPa	7	12.8	6.1	3.3	150	121.1
	Kcs40_nf20_14d_50kPa	14	12.5	6.0	3.4	50	70.1
	Kcs40_nf20_14d_100kPa	14	12.8	-	-	100	100.3
	Kcs40_nf20_14d_150kPa	14	12.9	5.9	3.4	150	123.6
	Kcs40_nf20_28d_50kPa	28	12.5	6.1	3.3	50	83.2
	Kcs40_nf20_28d_100kPa	28	13.0	6.2	3.2	100	106.2
	Kcs40_nf40_28d_150kPa	28	13.0	-	-	150	127.2
K cs20 nf40	*Kcs20_nf20_7d_50kPa*	7	10.2	4.7	4.6	50	36.6
	Kcs20_nf20_7d_100kPa	7	10.2	4.4	4.9	100	62.5
	Kcs20_nf20_7d_150kPa	7	10.4	4.5	4.8	150	86.4
	Kcs20_nf20_28d_50kPa	28	10.2	4.5	4.8	50	47.5
	Kcs20_nf20_28d_100kPa	28	10.2	4.5	4.8	100	58.3
	Kcs20_nf20_28d_150kPa	28	10.4	4.3	5.1	150	92.9
	Kcs20_nf40_14d_oed	14	10.4	4.7	4.5	-	-
	Kcs20_nf40_28d_oed	28	10.4	4.7	4.6	-	-
K cs40 nf40	*Kcs40_nf40_1d_50kPa*	1	10.3	4.8	4.4	50	45.5
	Kcs40_nf40_1d_100kPa	1	10.0	4.6	4.6	100	64.7
	Kcs40_nf40_3d_50kPa	3	10.5	4.8	4.5	50	44.5
	Kcs40_nf40_3d_100kPa	3	10.6	4.7	4.6	100	65.9
	Kcs40_nf40_3d_150kPa	3	10.5	4.7	4.5	150	90.8
	Kcs40_nf40_7d_50kPa	7	10.1	4.7	4.5	50	46.3
	Kcs40_nf40_7d_100kPa	7	10.7	4.9	4.3	100	77.7
	Kcs40_nf40_7d_150kPa	7	10.8	5.3	3.9	150	94.9
	Kcs40_nf40_14d_50kPa	14	10.4	4.9	4.3	50	52.3
	Kcs40_nf40_14d_100kPa	14	10.0	4.7	4.5	100	72.2
	Kcs40_nf40_28d_50kPa	28	10.3	5.0	4.2	50	60.3
	Kcs40_nf40_28d_100kPa	28	10.6	5.0	4.2	100	75.3
	Kcs40_nf40_28d_150kPa	28	10.0	-	-	150	104.1
	Kcs40_nf40_60d_50kPa	60	10.8	5.0	4.2	50	70.7
	Kcs40_nf40_60d_100kPa	60	10.8	5.1	4.1	100	82.4
	Kcs40_nf40_90d_50kPa	90	10.3	5.1	4.1	50	71.2
	Kcs40_nf40_90d_100kPa	90	10.7	4.8	4.4	100	95.4
	Kcs40_nf40_90d_150kPa	90	10.9	-	-	150	107.1
	Kcs40_nf40_7d_oed	7	10.2	5.0	4.2	-	-
	Kcs40_nf40_14d_oed	14	10.3	5.1	4.1	-	-
	Kcs40_nf40_28d_oed	28	10.2	5.0	4.2	-	-

Kcs40nf20

Direct shear tests

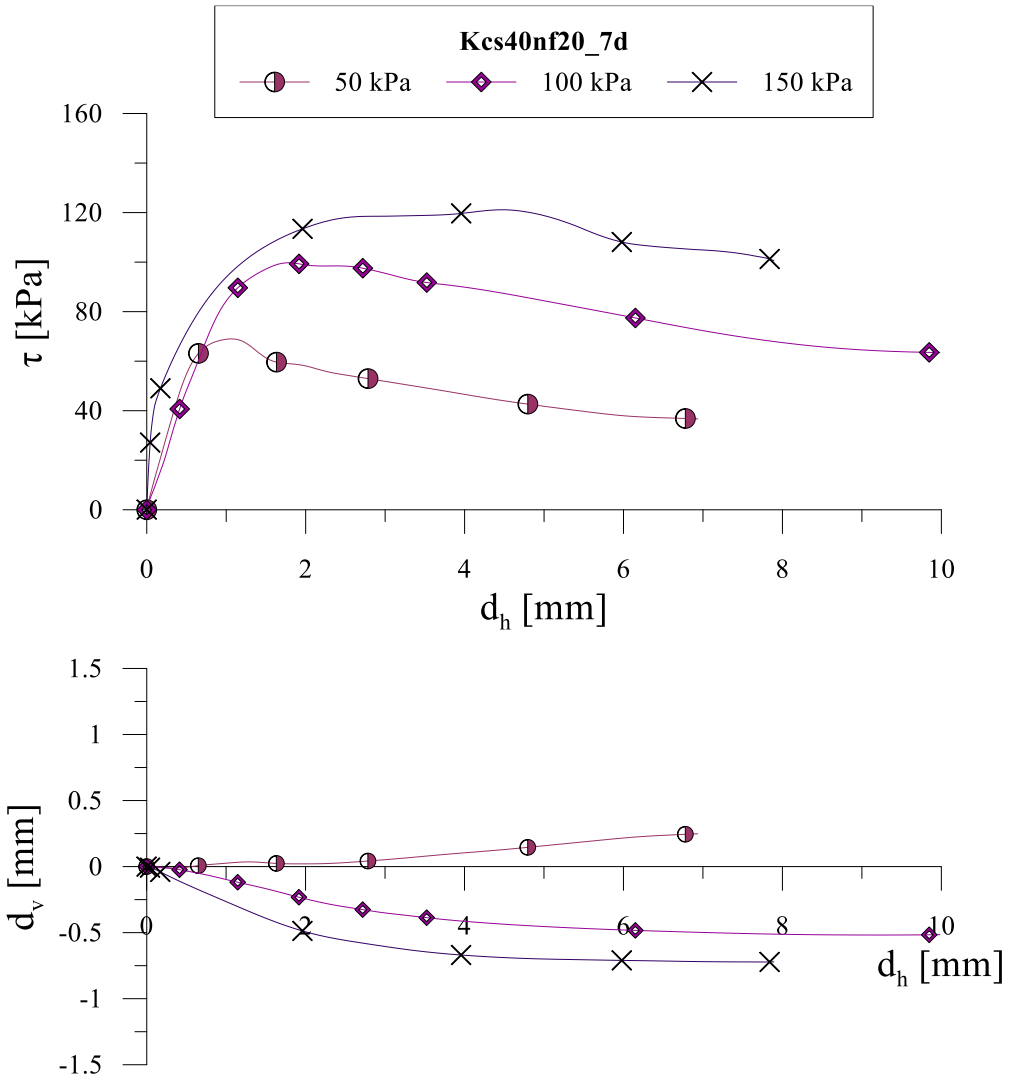

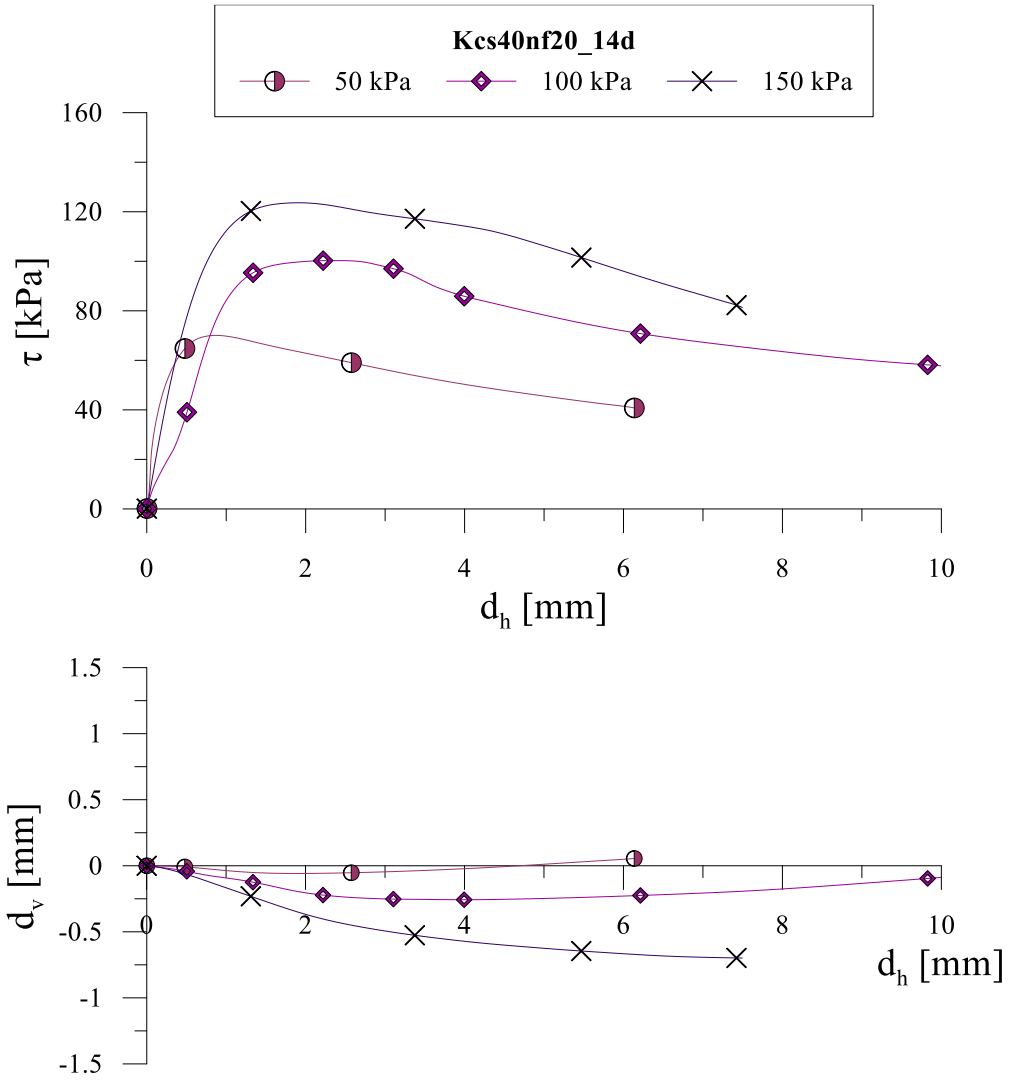
Kcs40nf20_14d
50 kPa
100 kPa
150 kPa
τ [kPa]
160
120
80
40
0
0
2
4
6
8
10
d_h [mm]
d_v [mm]
1.5
1
0.5
0
-0.5
-1
-1.5
0
2
4
6
8
10
d_h [mm]

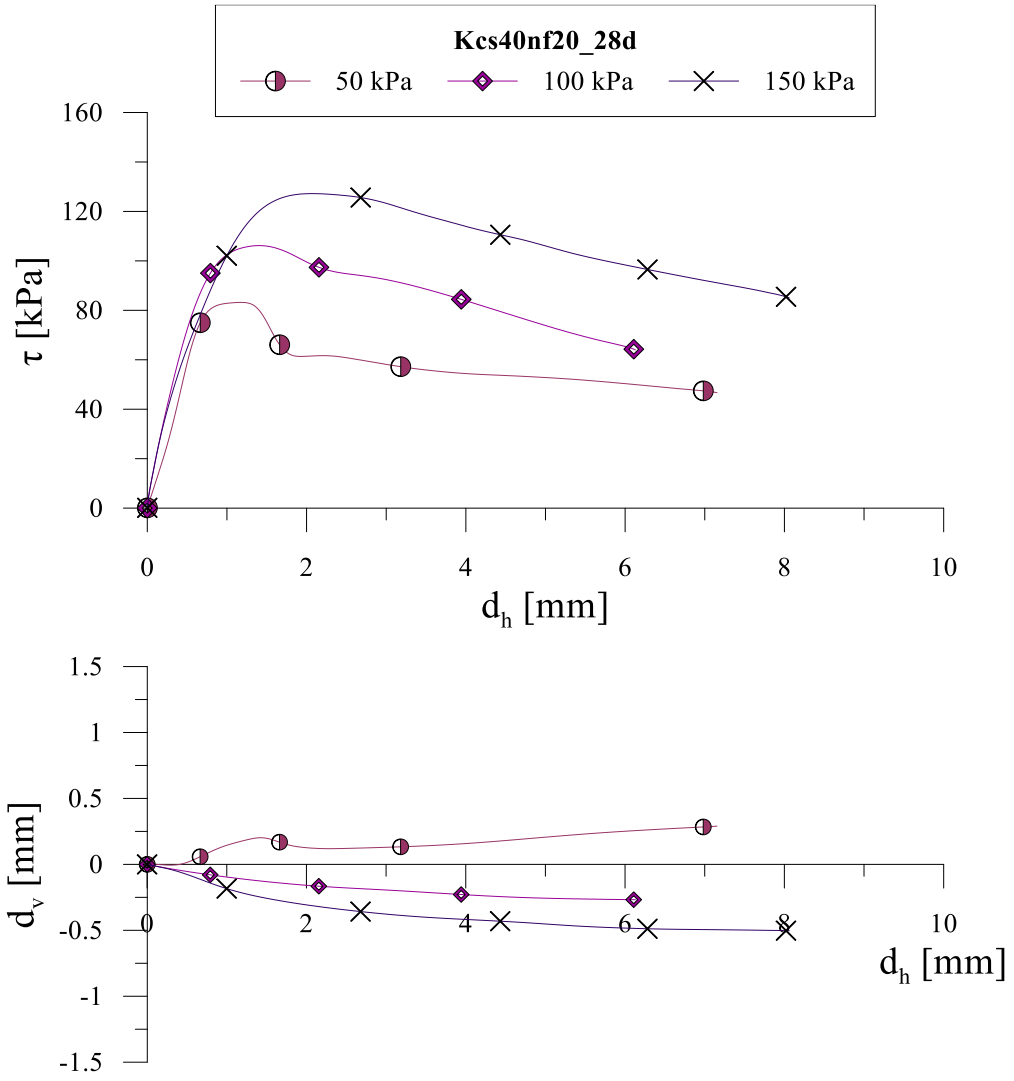
Kcs40nf20_28d
50 kPa
100 kPa
150 kPa
τ [kPa]
160
120
80
40
0
0
2
4
6
8
10
d_h [mm]
d_v [mm]
1.5
1
0.5
0
-0.5
-1
-1.5
0
2
4
6
8
10
d_h [mm]

Kcs40nf40

Direct shear tests

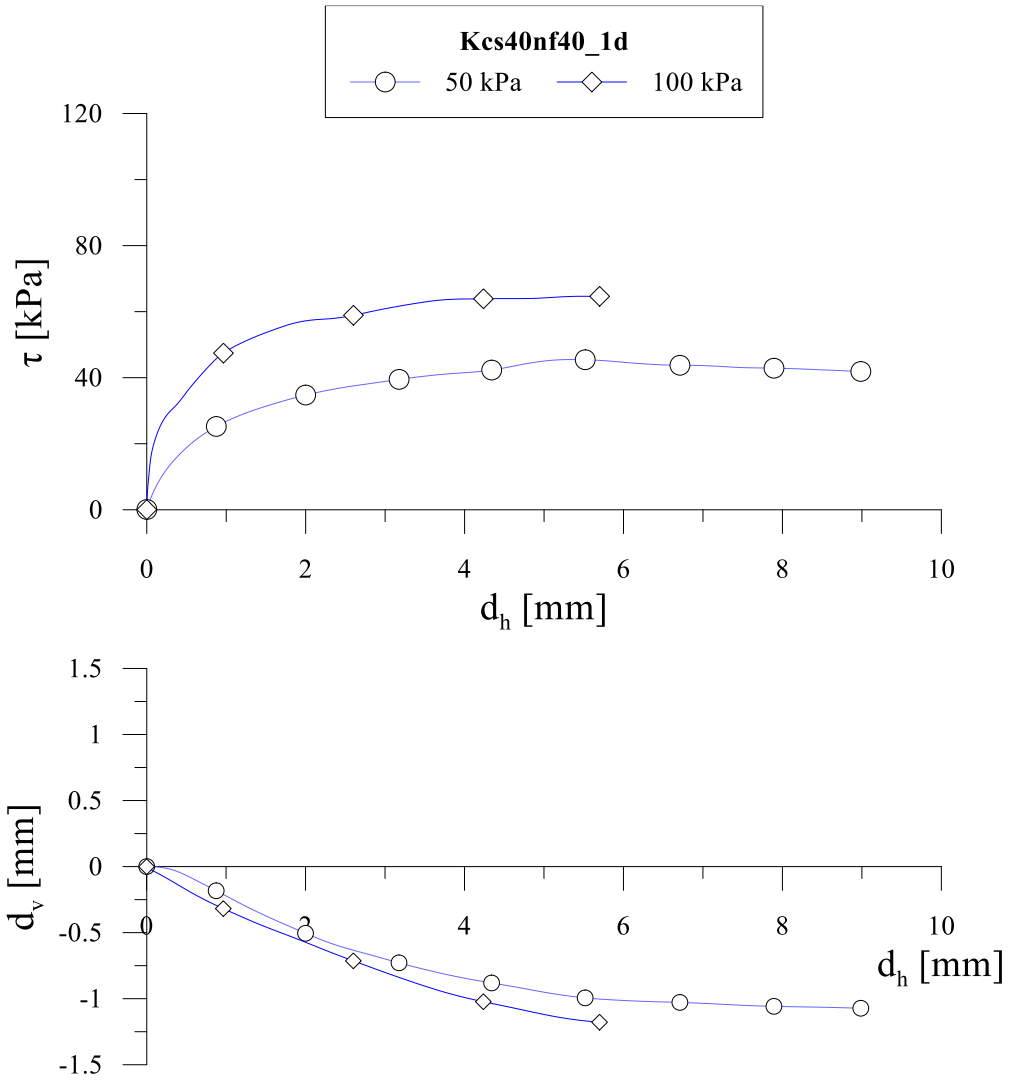

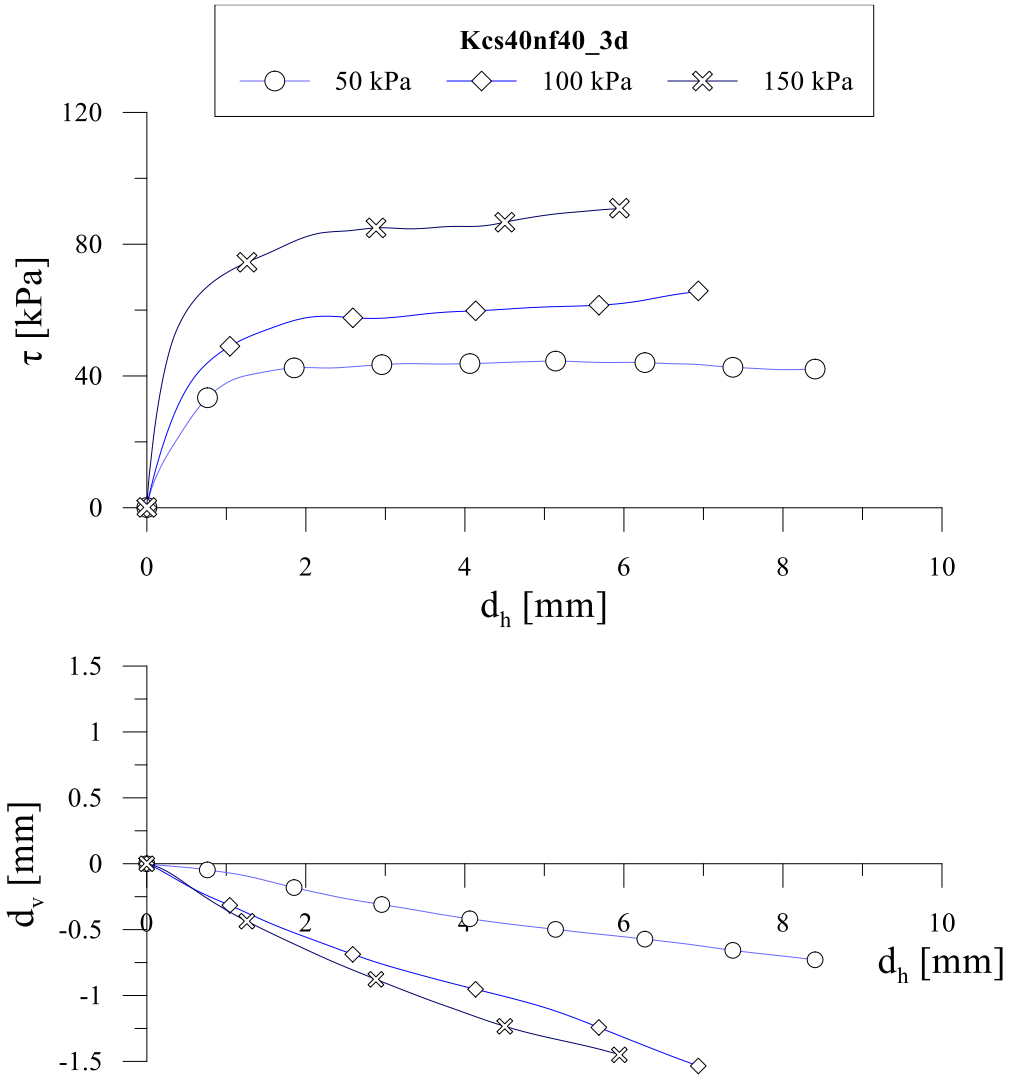
Kcs40nf40_3d
50 kPa
100 kPa
150 kPa
120
80
40
0
τ [kPa]
0
2
4
6
8
10
d_h [mm]
1.5
1
0.5
0
-0.5
-1
-1.5
d_v [mm]
0
2
4
6
8
10
d_h [mm]

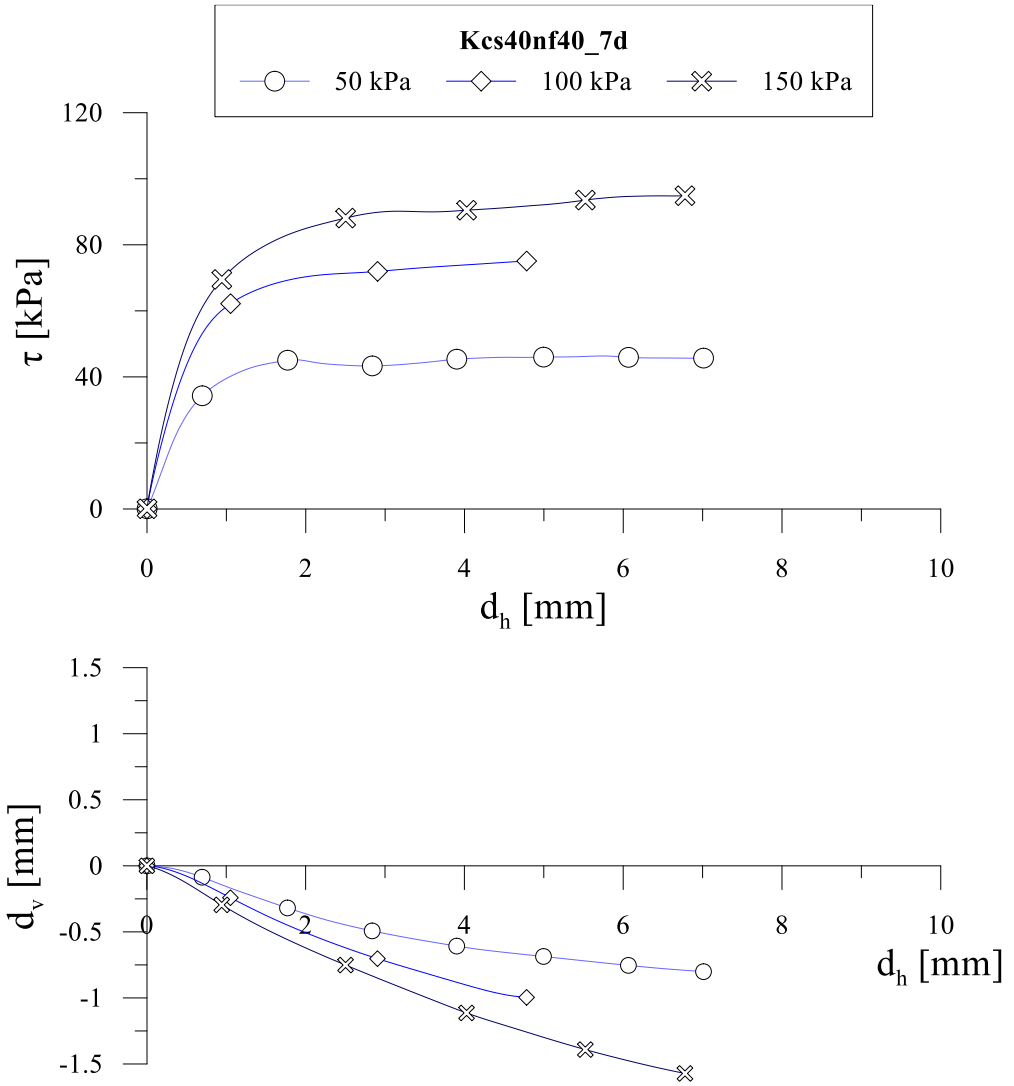
Kcs40nf40_7d
50 kPa
100 kPa
150 kPa
τ [kPa]
120
80
40
0
0
2
4
6
8
10
d_h [mm]
d_v [mm]
1.5
1
0.5
0
-0.5
-1
-1.5
0
2
4
6
8
10
d_h [mm]

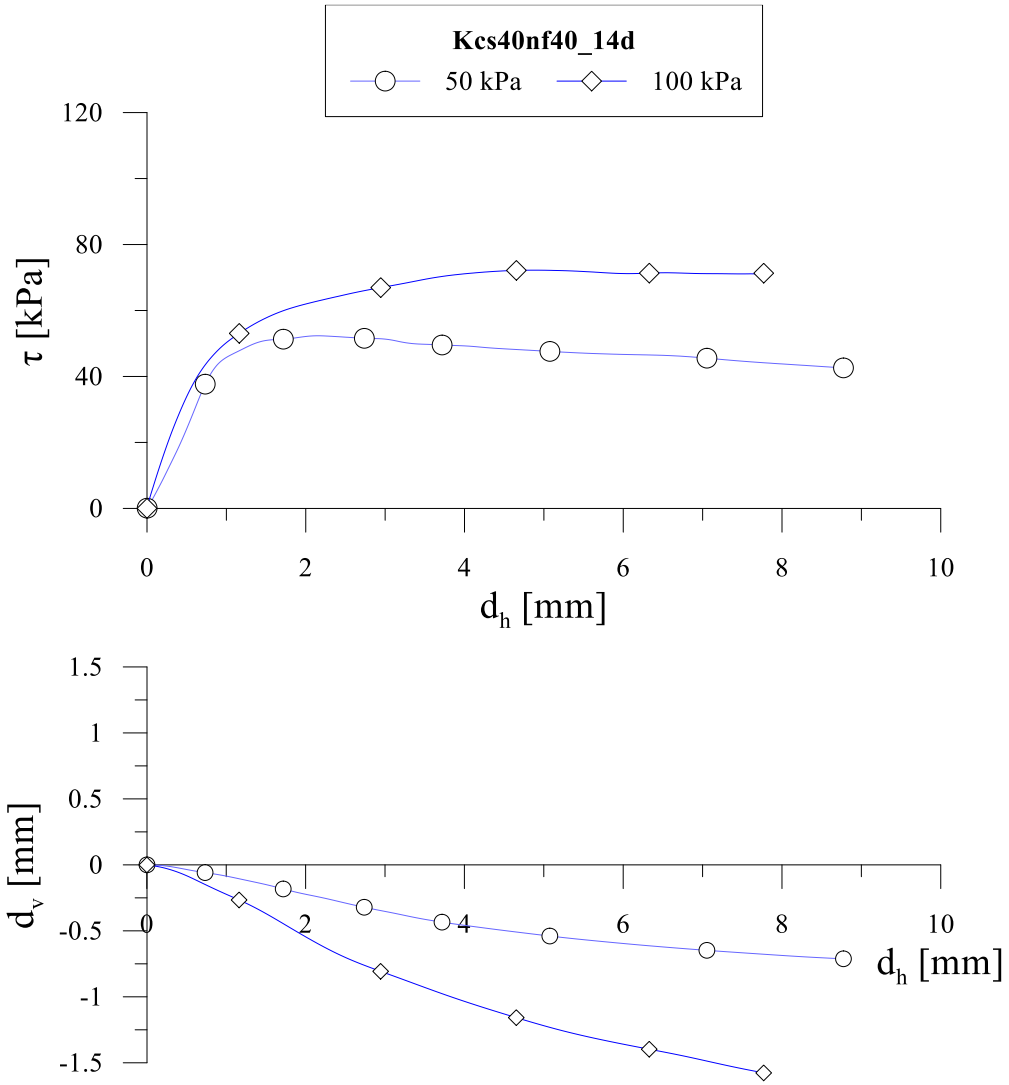
Kcs40nf40_14d
50 kPa
100 kPa
τ [kPa]
120
80
40
0
0
2
4
6
8
10
d_h [mm]
d_v [mm]
1.5
1
0.5
0
-0.5
-1
-1.5
0
2
4
6
8
10
d_h [mm]

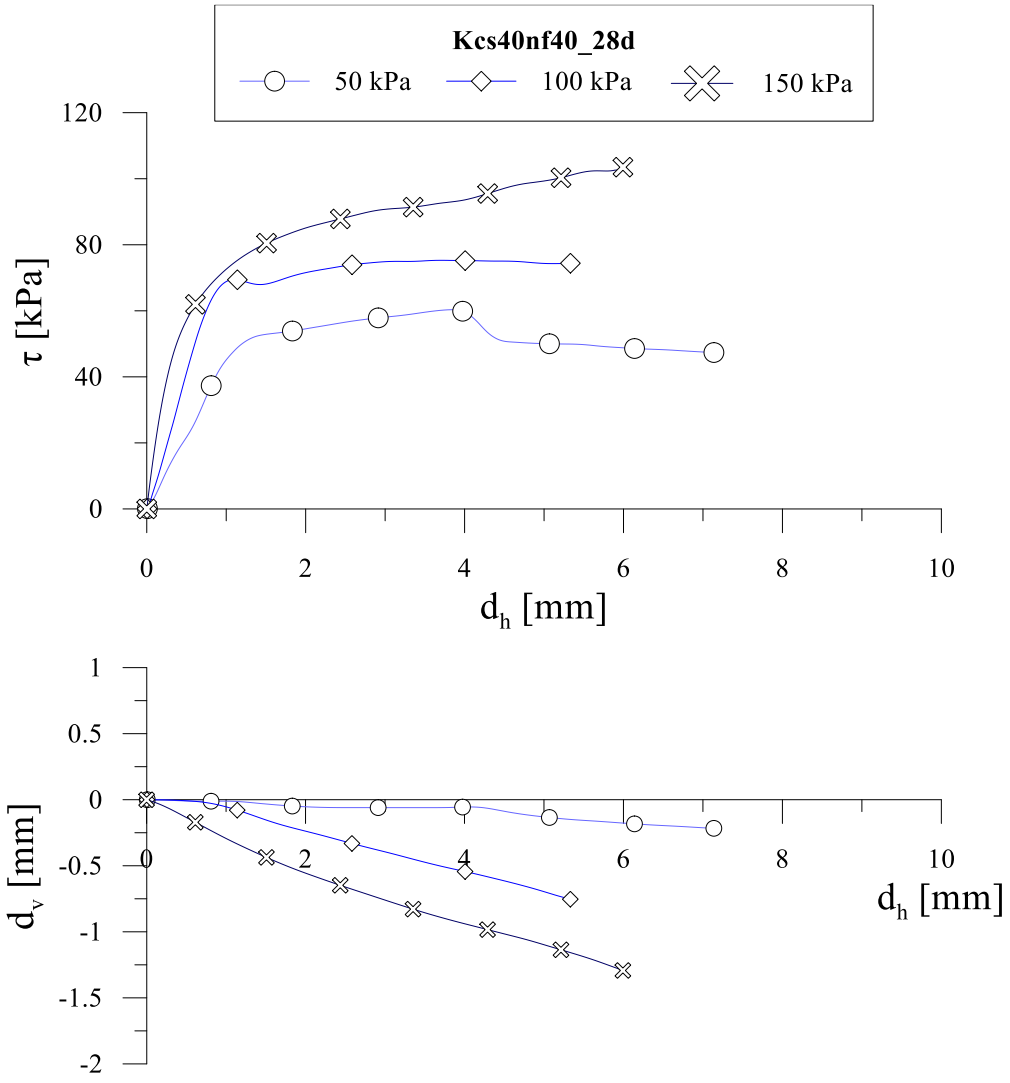
Kcs40nf40_28d
50 kPa
100 kPa
150 kPa
τ [kPa]
120
80
40
0
0
2
4
6
8
10
d_h [mm]
d_v [mm]
1
0.5
0
-0.5
-1
-1.5
-2
0
2
4
6
8
10
d_h [mm]

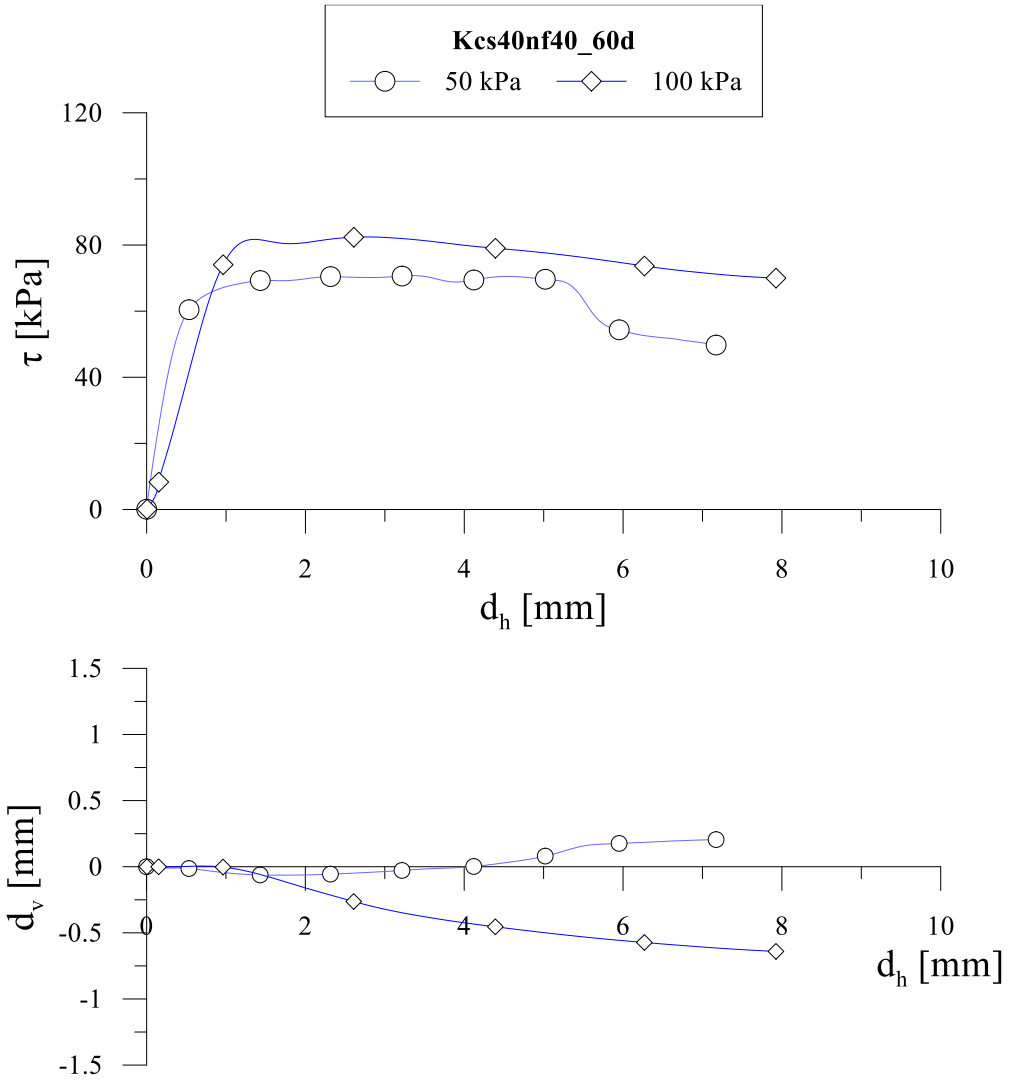
Kcs40nf40_60d
50 kPa
100 kPa
τ [kPa]
120
80
40
0
0
2
4
6
8
10
d_h [mm]
d_v [mm]
1.5
1
0.5
0
-0.5
-1
-1.5
0
2
4
6
8
10
d_h [mm]

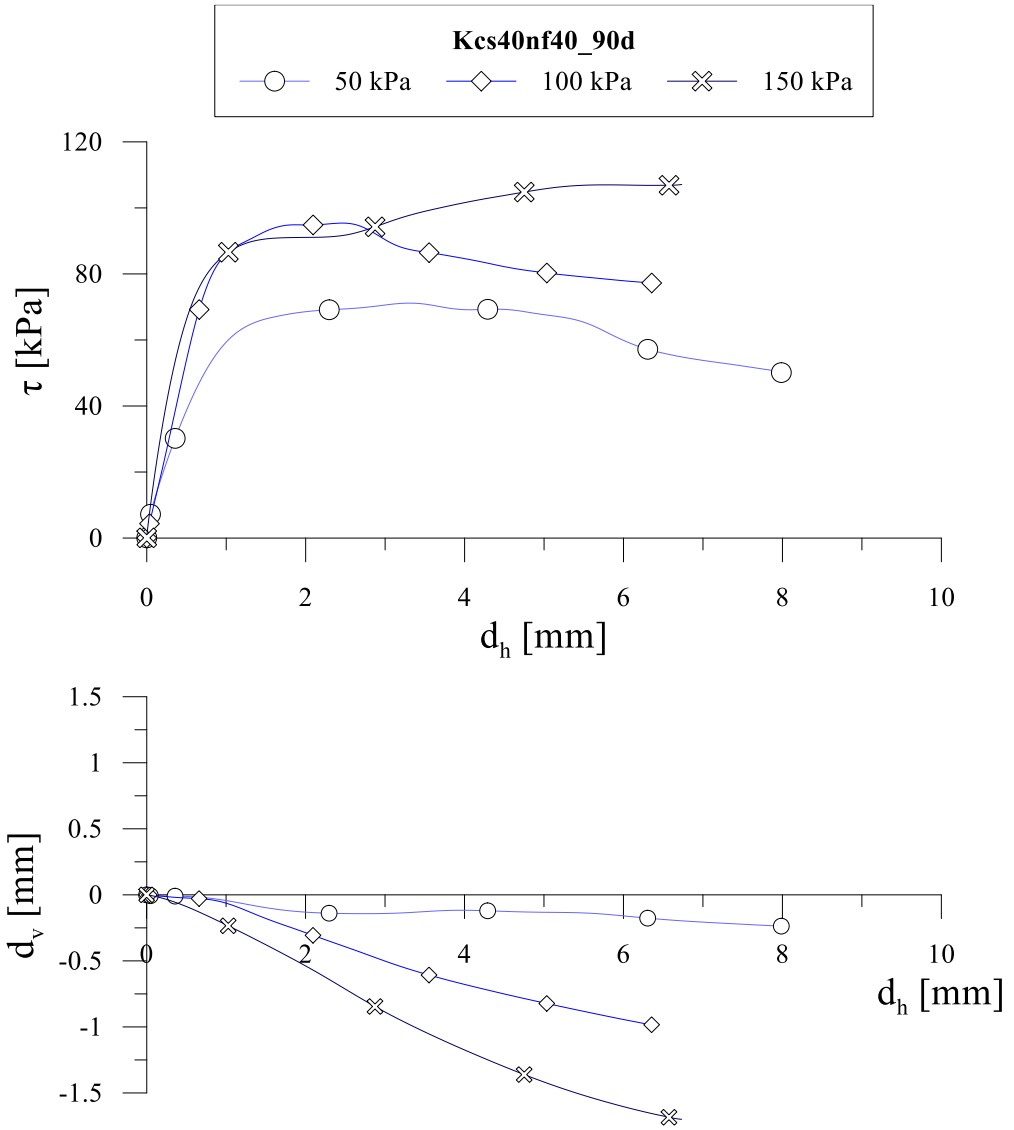
Kcs40nf40_90d
50 kPa
100 kPa
150 kPa
τ [kPa]
120
80
40
0
0
2
4
6
8
10
d_h [mm]
d_v [mm]
1.5
1
0.5
0
-0.5
-1
-1.5
0
2
4
6
8
10
d_h [mm]

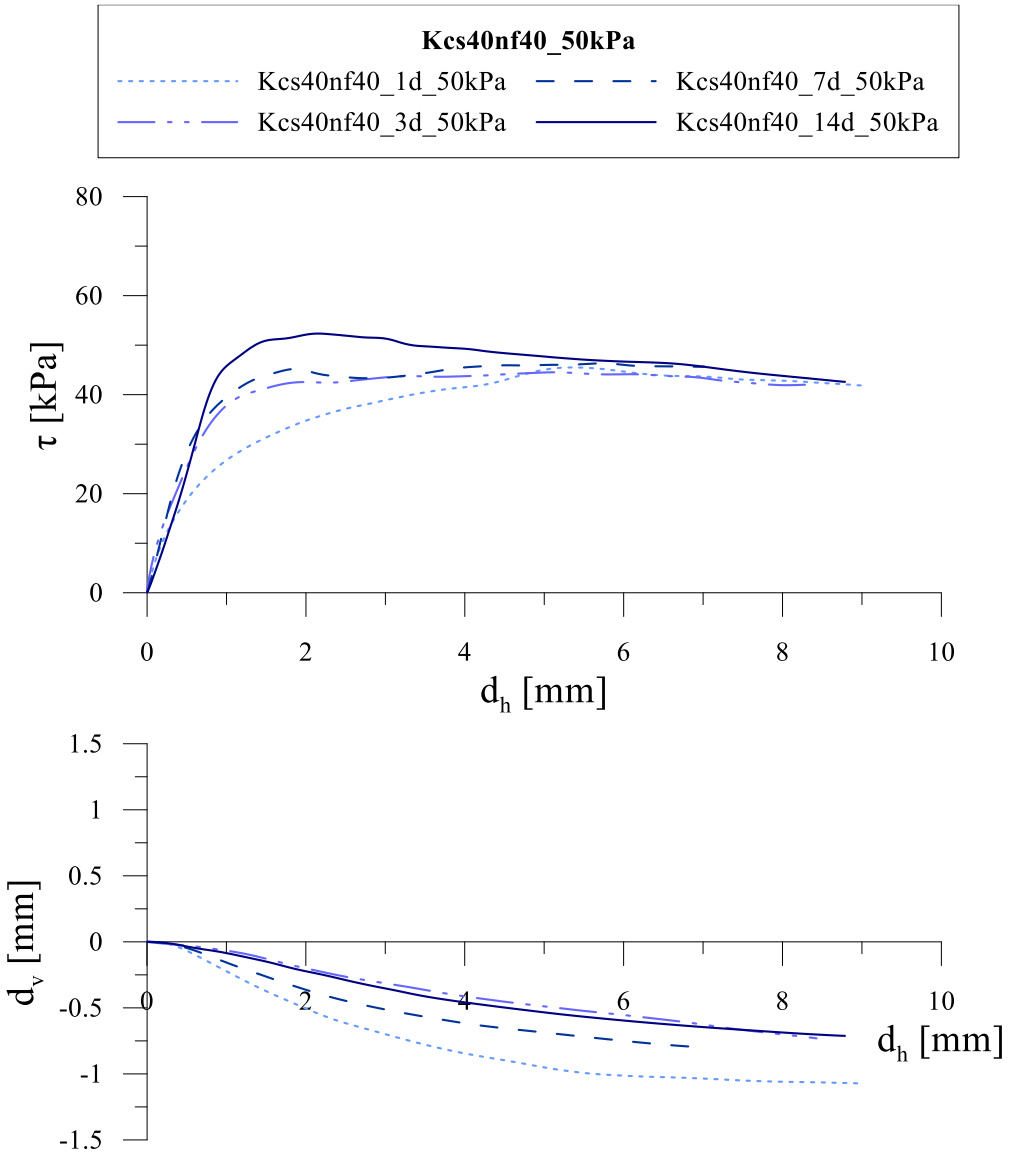
Kcs40nf40_50kPa
Kcs40nf40_1d_50kPa
Kcs40nf40_3d_50kPa
Kcs40nf40_7d_50kPa
Kcs40nf40_14d_50kPa
τ [kPa]
d_h [mm]
d_v [mm]
d_h [mm]

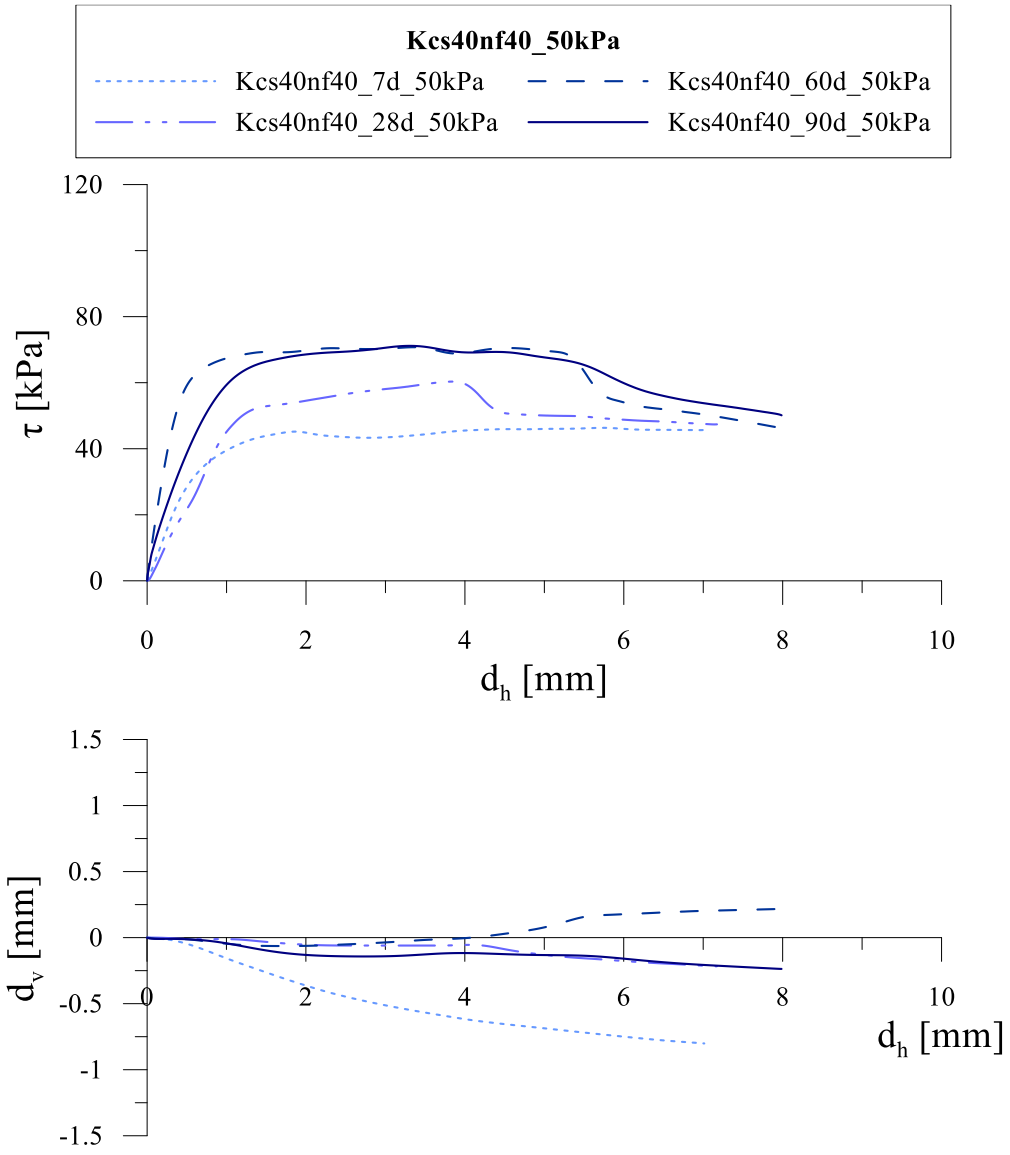
Kcs40nf40_50kPa
Kcs40nf40_7d_50kPa
Kcs40nf40_28d_50kPa
Kcs40nf40_60d_50kPa
Kcs40nf40_90d_50kPa
τ [kPa]
120
80
40
0
0
2
4
6
8
10
d_h [mm]
d_v [mm]
1.5
1
0.5
0
-0.5
-1
-1.5
0
2
4
6
8
10
d_h [mm]

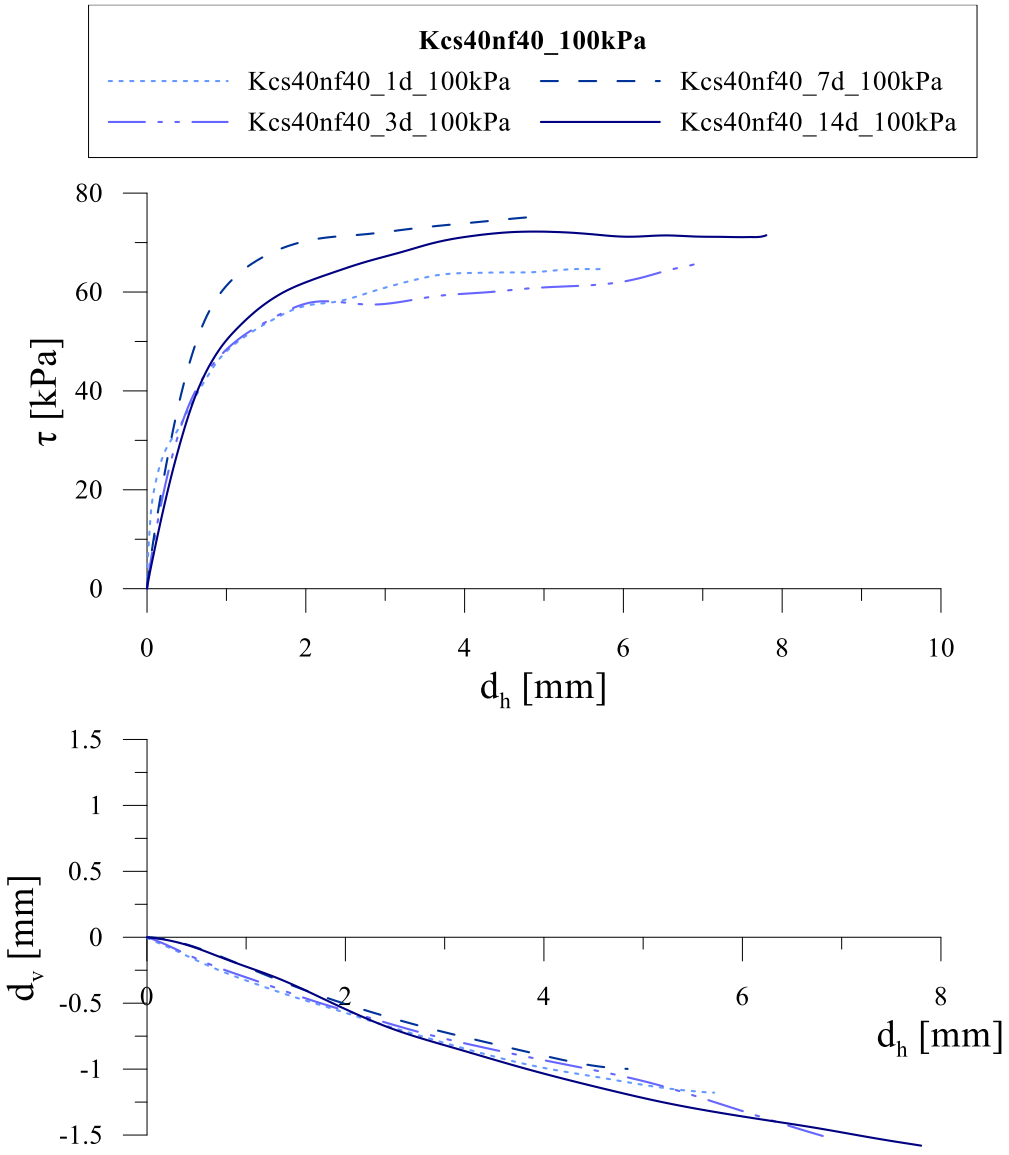
Kcs40nf40_100kPa
Kcs40nf40_1d_100kPa
Kcs40nf40_3d_100kPa
Kcs40nf40_7d_100kPa
Kcs40nf40_14d_100kPa
τ [kPa]
d_h [mm]
d_v [mm]
d_h [mm]

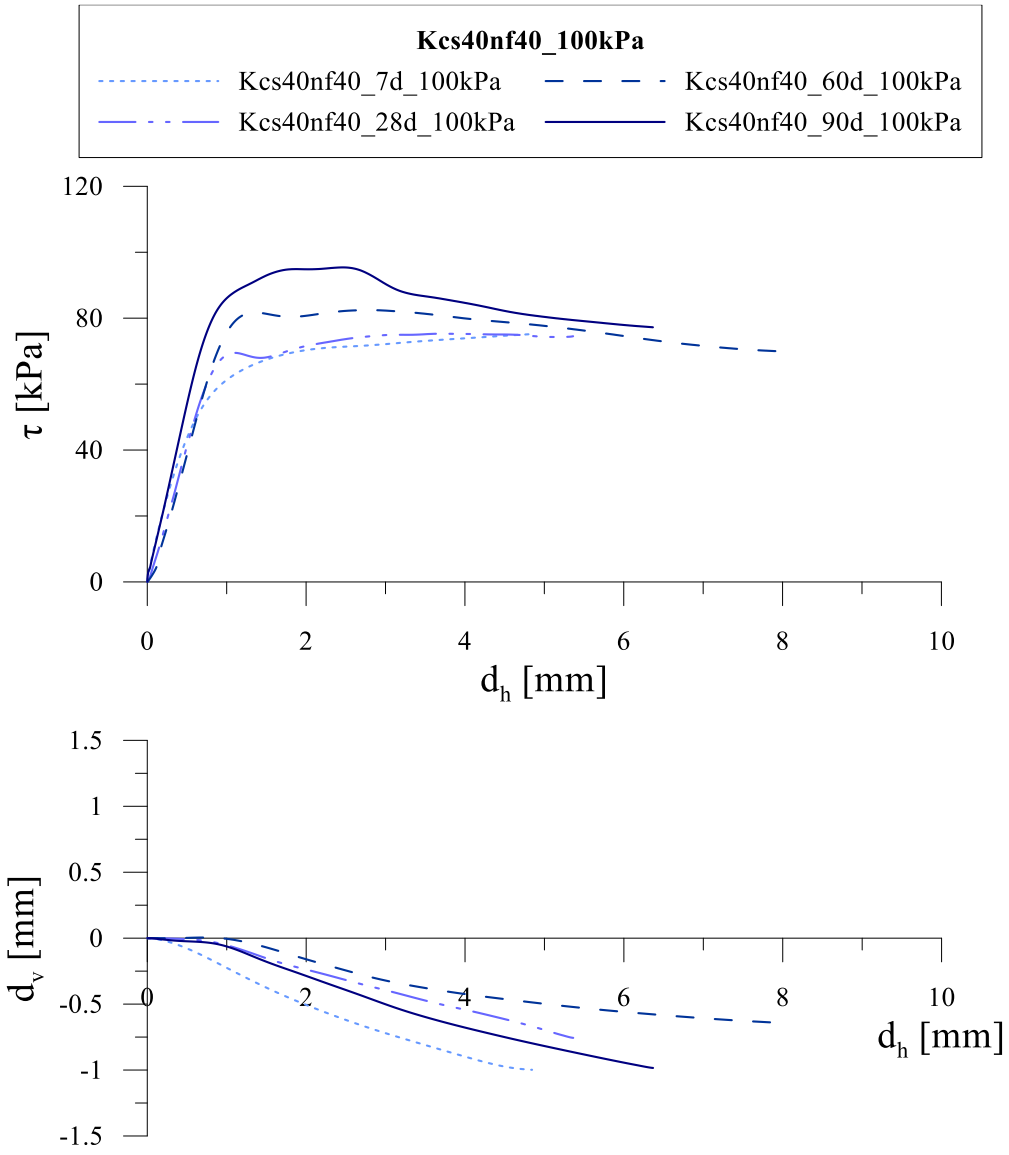
Kcs40nf40_100kPa
Kcs40nf40_7d_100kPa
Kcs40nf40_60d_100kPa
Kcs40nf40_28d_100kPa
Kcs40nf40_90d_100kPa
120
80
40
0
τ [kPa]
0
2
4
6
8
10
d_h [mm]
1.5
1
0.5
0
-0.5
-1
-1.5
d_v [mm]
0
2
4
6
8
10
d_h [mm]

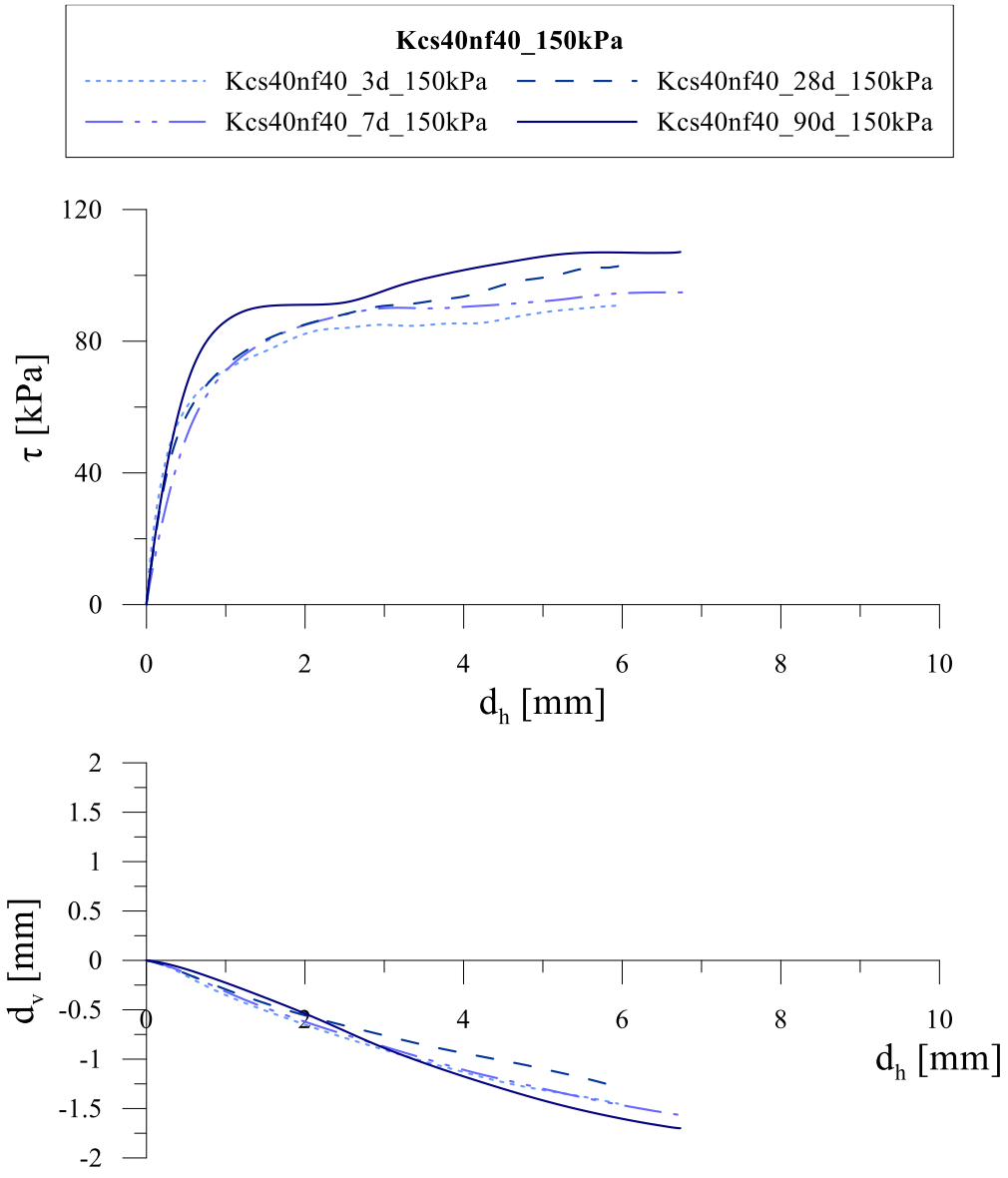
Kcs40nf40_150kPa
Kcs40nf40_3d_150kPa
Kcs40nf40_28d_150kPa
Kcs40nf40_7d_150kPa
Kcs40nf40_90d_150kPa
τ [kPa]
120
80
40
0
0
2
4
6
8
10
d_h [mm]
d_v [mm]
2
1.5
1
0.5
0
-0.5
-1
-1.5
-2
0
2
4
6
8
10
d_h [mm]

Kcs20nf20

Direct shear tests

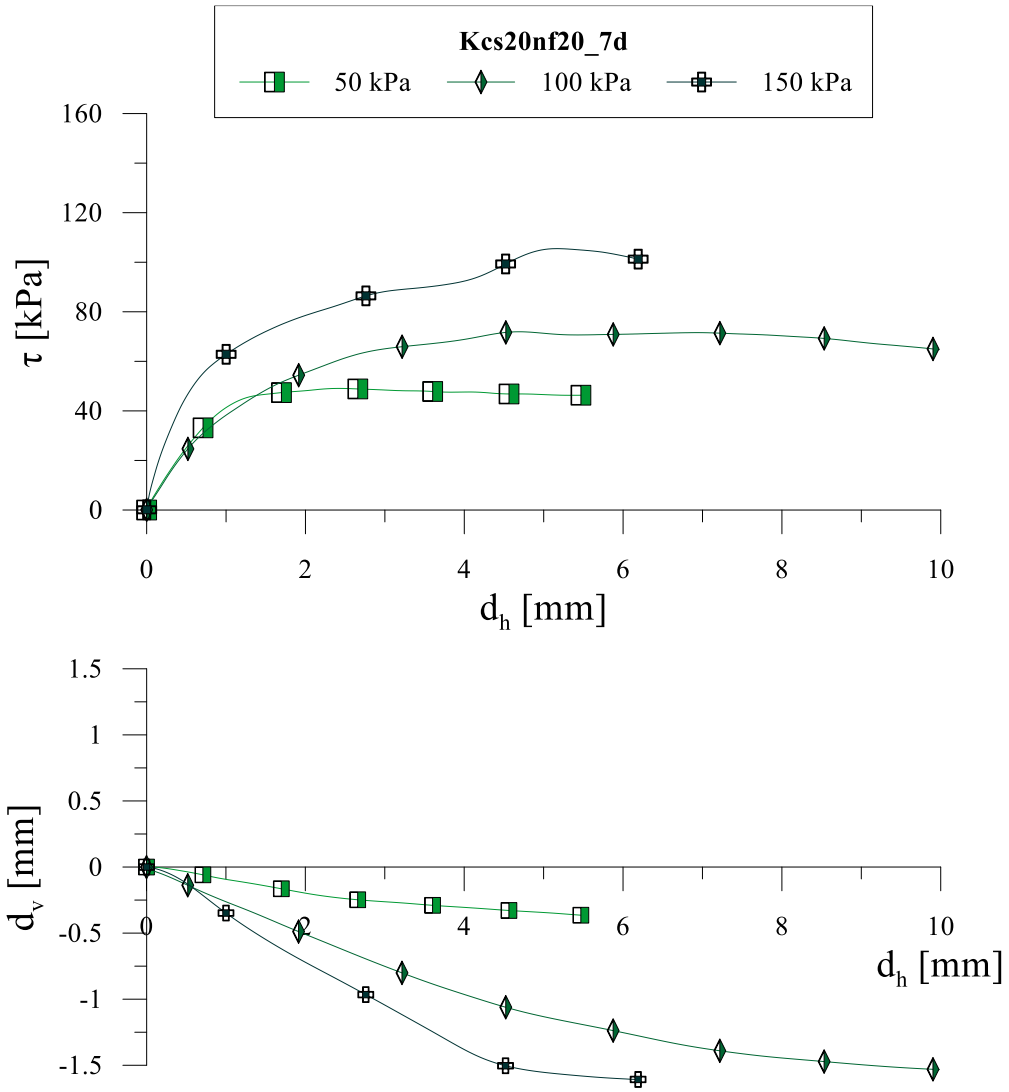

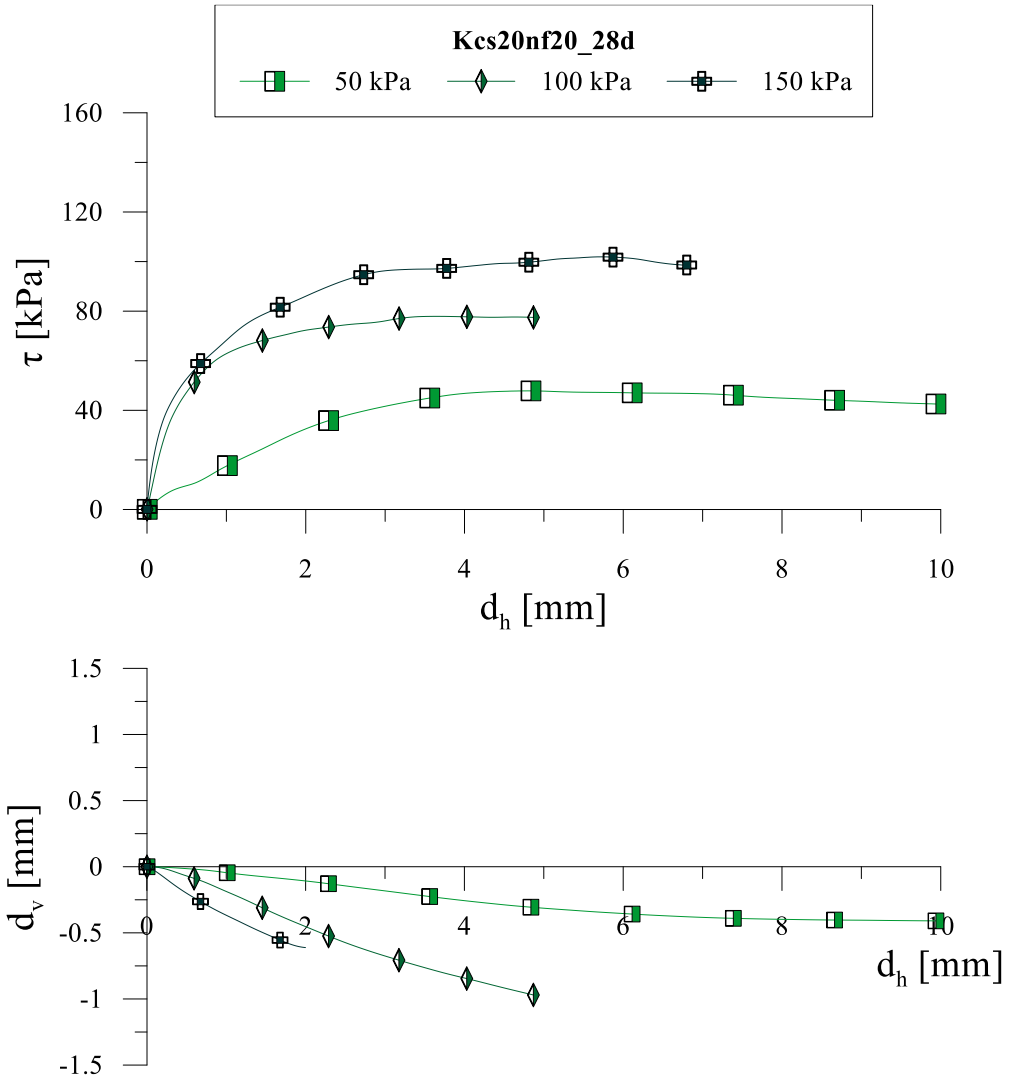

*Vertical displacements of Kcs20nf20_28d_150kPa are truncated at a horizontal displacement of 2 mm due to an problem occurred on vertical transducer.

Kcs20nf40

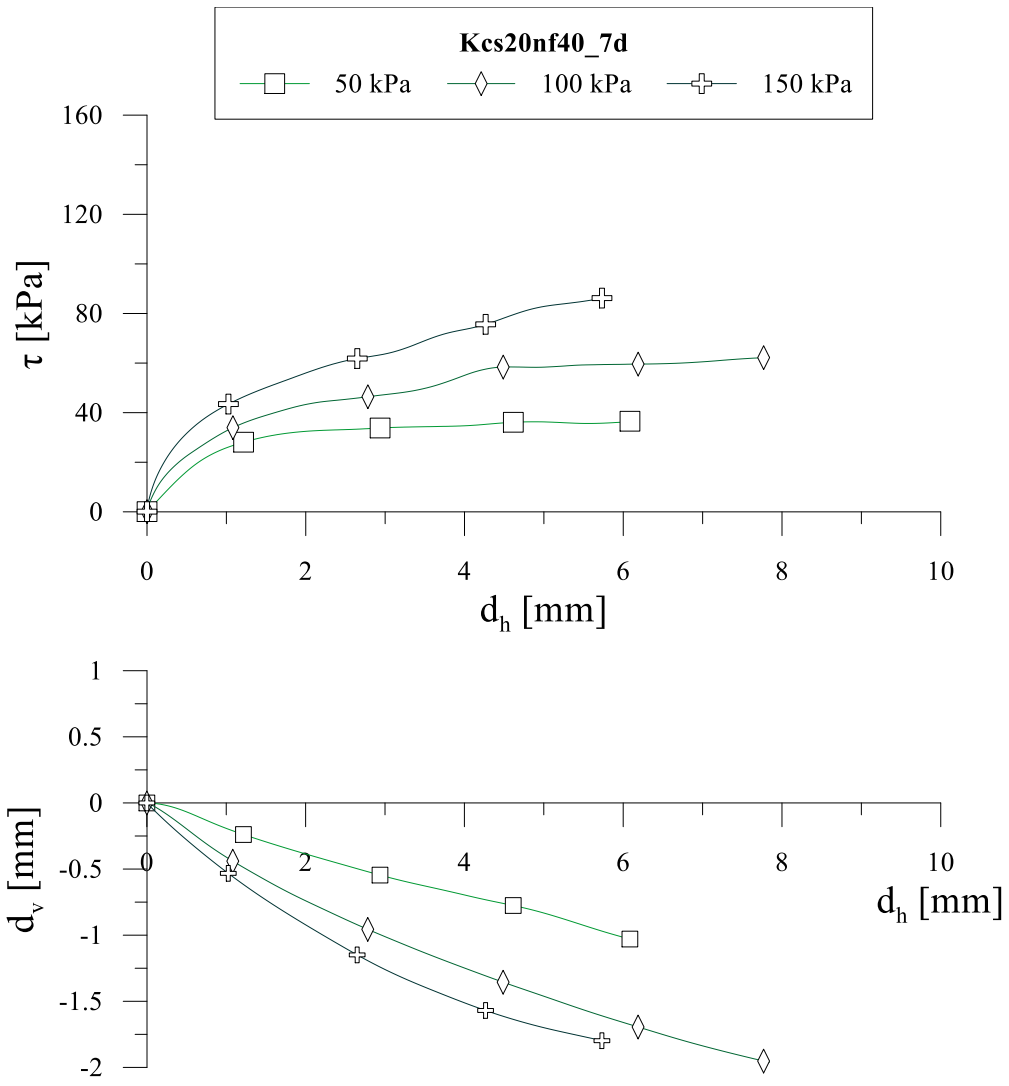
Kcs20nf40_7d
50 kPa
100 kPa
150 kPa
τ [kPa]
160
120
80
40
0
0
2
4
6
8
10
d_h [mm]
d_v [mm]
1
0.5
0
-0.5
-1
-1.5
-2
0
2
4
6
8
10
d_h [mm]

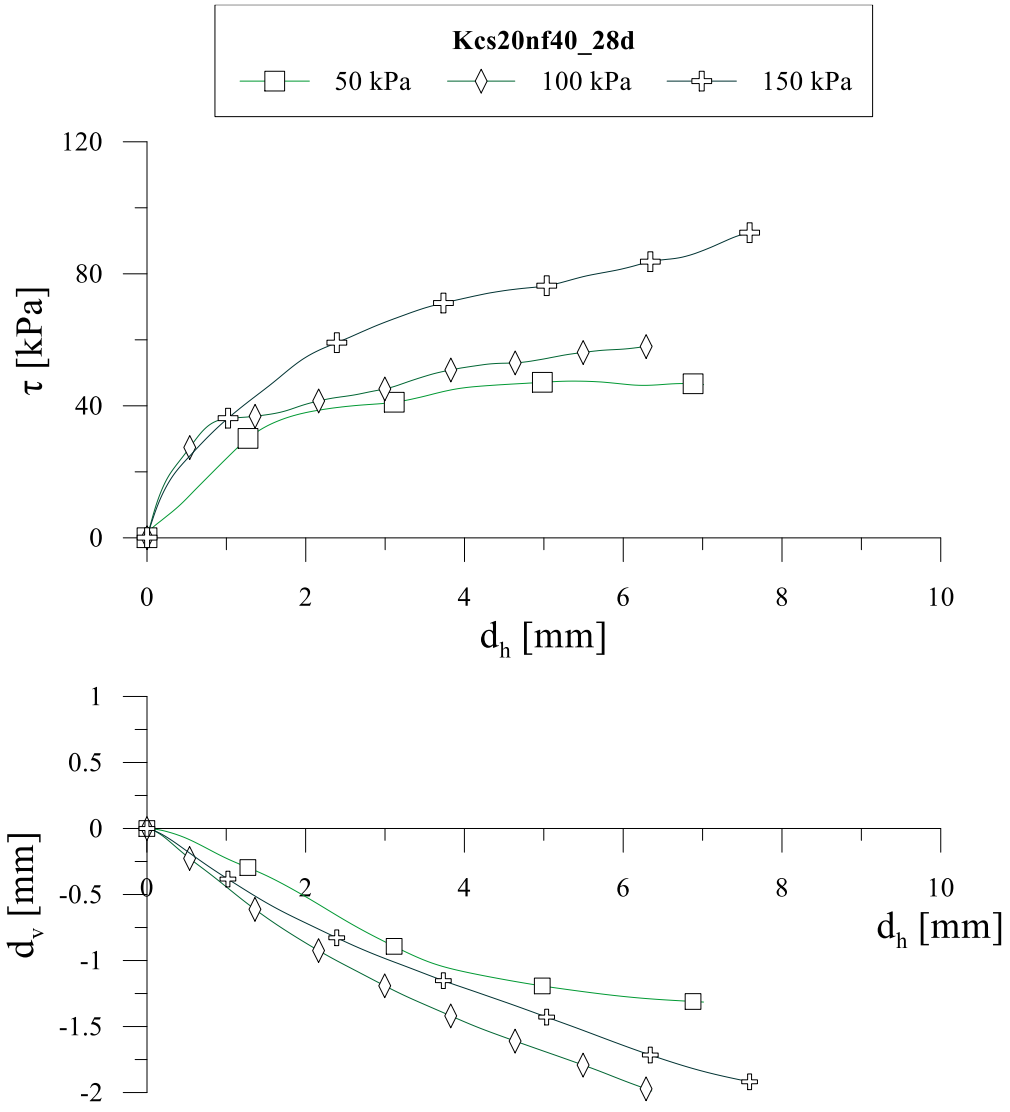
Kcs20nf40_28d
50 kPa
100 kPa
150 kPa
τ [kPa]
120
80
40
0
0
2
4
6
8
10
d_h [mm]
d_v [mm]
1
0.5
0
-0.5
-1
-1.5
-2
0
2
4
6
8
10
d_h [mm]

Oedometric tests on lightweight cemented kaolin

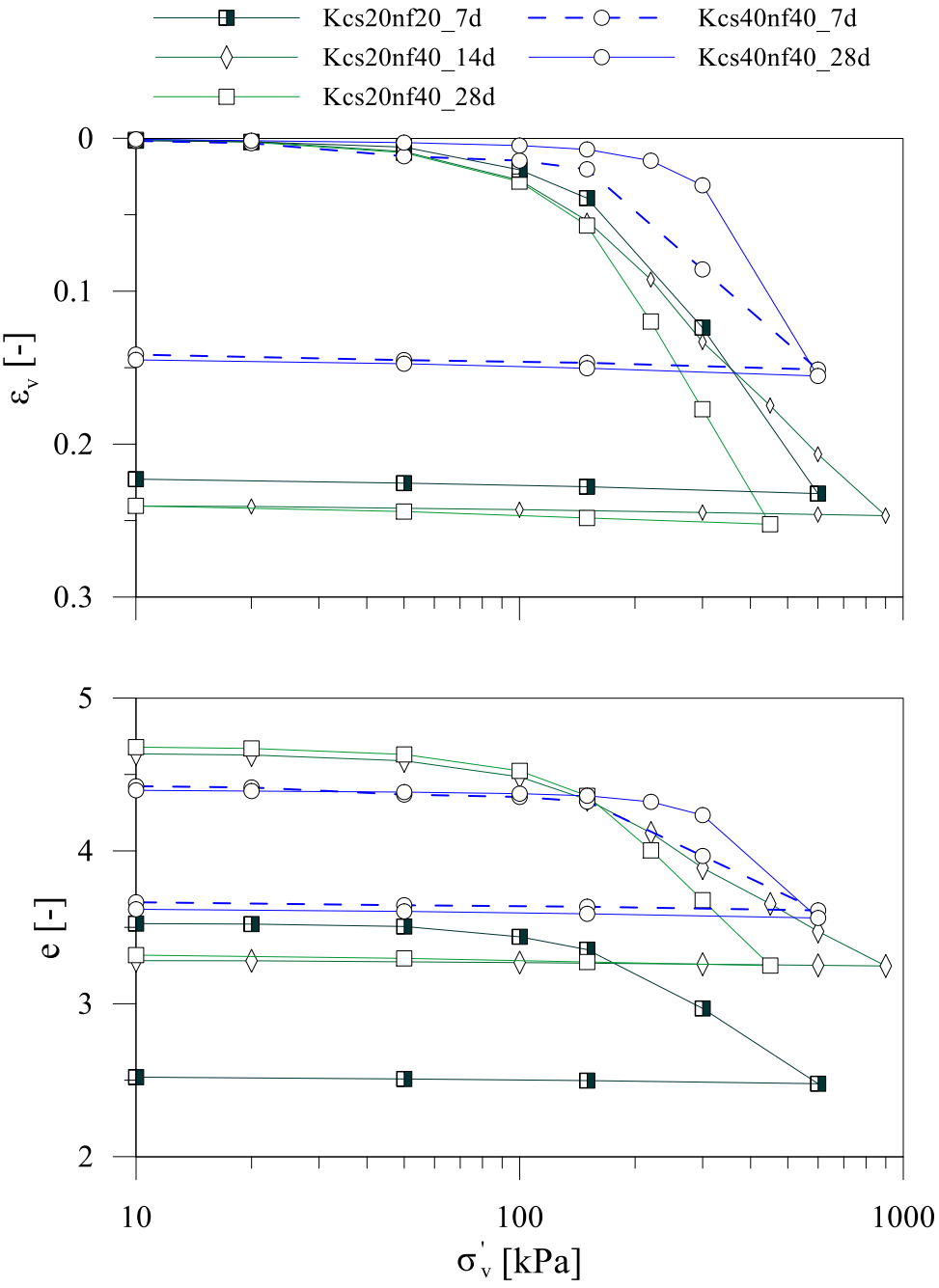

Caposele soil

Table C-0-3.

		t [days]	γ [kN/m^3]	γ_{dry} [kN/m^3]	e	σ'_v [kPa]	τ_{max} [kPa]
C cs40	*Ccs40_7d_50kPa*	7	14.5	7.6	2.6	50	82
	Ccs40_7d_150kPa	7	14.6	7.6	2.6	150	148
	Ccs40_28d_50kPa	28	14.6	7.5	2.7	50	96
	Ccs40_28d_150kPa	28	14.8	7.6	2.6	150	163
	Ccs40_7d_oed	7	14.9	7.6	2.6	-	-
	Ccs40_28d_oed	28	13.9	7.6	2.6	-	-
C cs40 nf20	*Ccs40nf20_7d_50kPa*	7	12.2	6.0	3.6	50	41
	Ccs40nf20_7d_150kPa	7	12.2	6.2	3.4	150	107
	Ccs40nf20_28d_100kPa	28	12.0	6.2	3.4	50	77
	Ccs40nf20_28d_150kPa	28	12.0	6.1	3.5	150	123
	Ccs40nf20_28d_oed	28	12.4	6.5	3.2	-	-
C cs40 nf40	*Ccs40nf40_7d_50kPa*	7	10.5	5.3	4.2	50	36
	Ccs40nf40_7d_150kPa	7	10.6	5.1	4.4	150	91
	Ccs40nf40_28d_100kPa	28	9.2	4.5	5.1	50	41
	Ccs40nf40_28d_150kPa	28	10.5	5.2	4.3	150	93
	Ccs40nf40_7d_oed	7	10.0	10.0	4.7	-	-
	Ccs40nf40_28d_oed	28	9.7	9.7	4.6	-	-

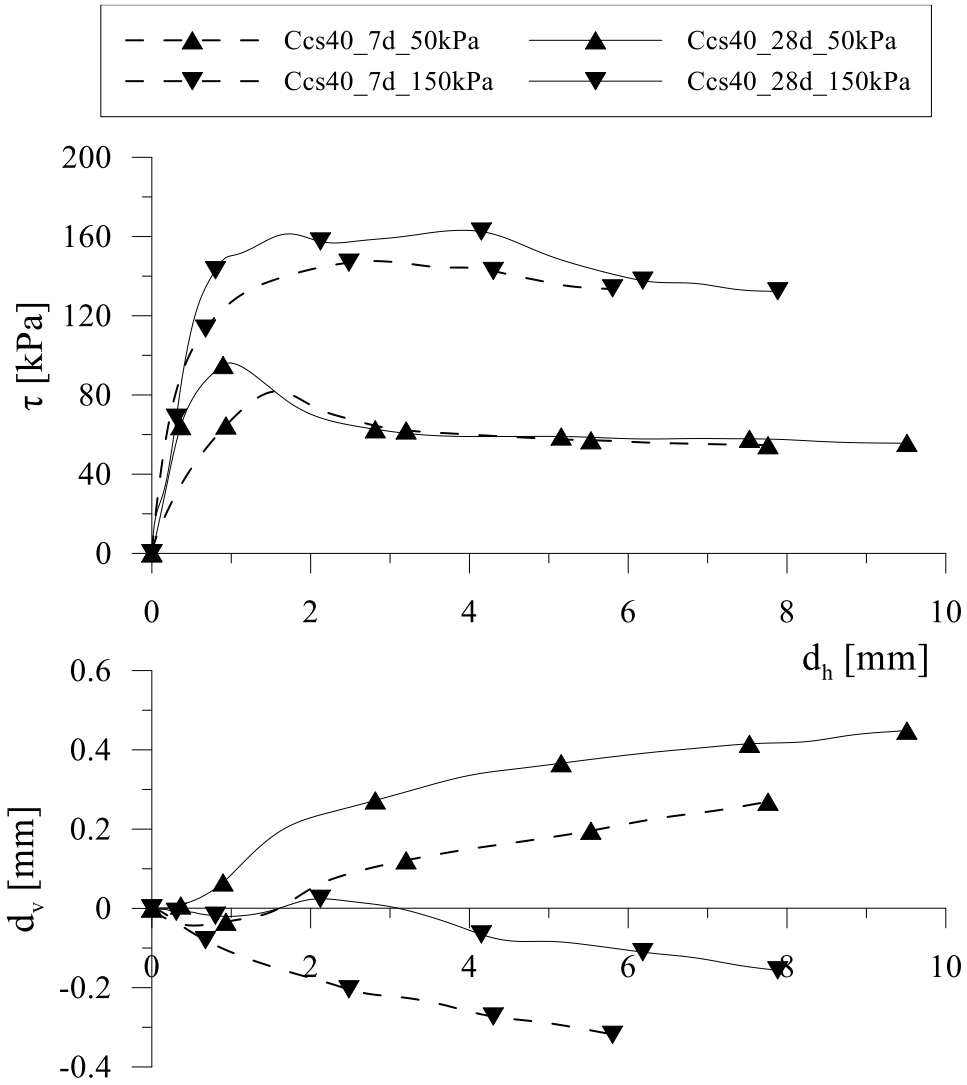
Ccs40_7d_50kPa
Ccs40_28d_50kPa
Ccs40_7d_150kPa
Ccs40_28d_150kPa
τ [kPa]
200
160
120
80
40
0
0
2
4
6
8
10
d_h [mm]
d_v [mm]
0.6
0.4
0.2
0
-0.2
-0.4

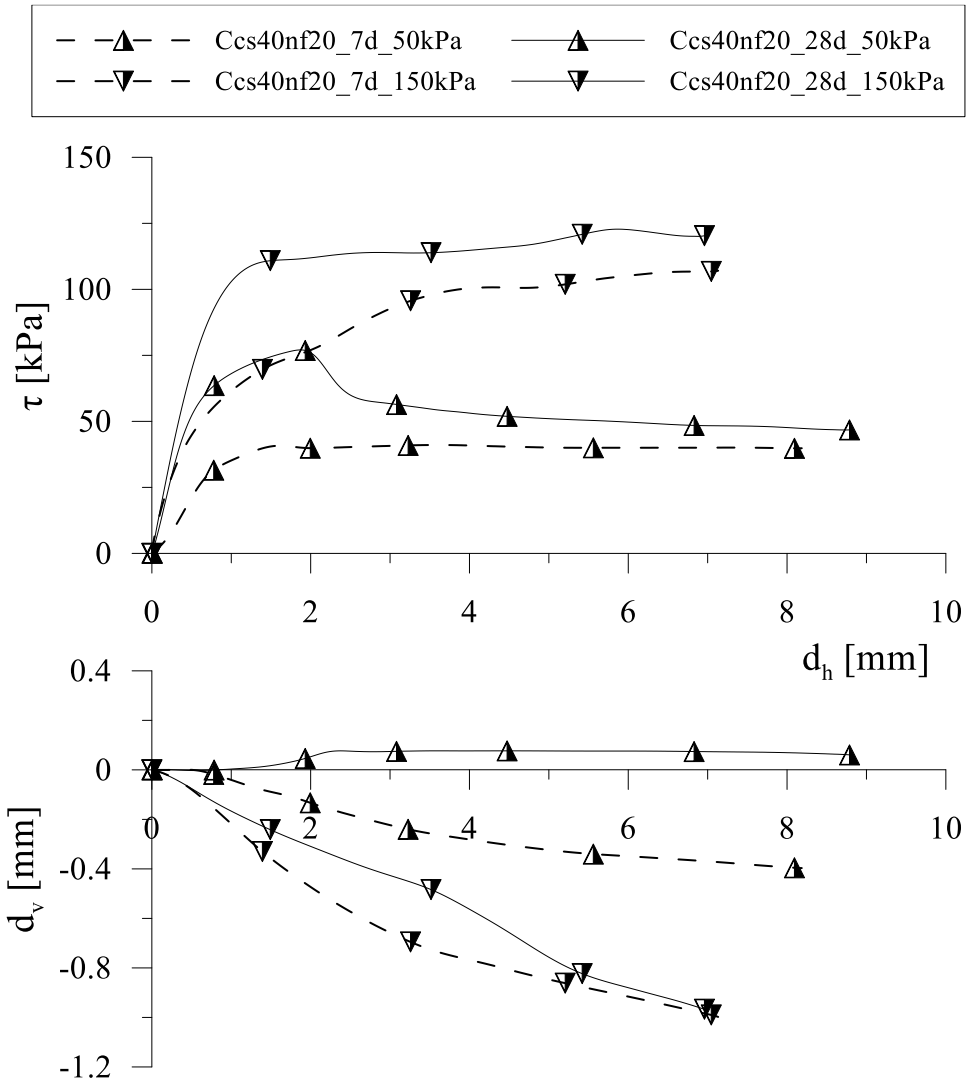
Ccs40nf20_7d_50kPa
Ccs40nf20_28d_50kPa
Ccs40nf20_7d_150kPa
Ccs40nf20_28d_150kPa
τ [kPa]
150
100
50
0
0
2
4
6
8
10
d_h [mm]
d_v [mm]
0.4
0
-0.4
-0.8
-1.2

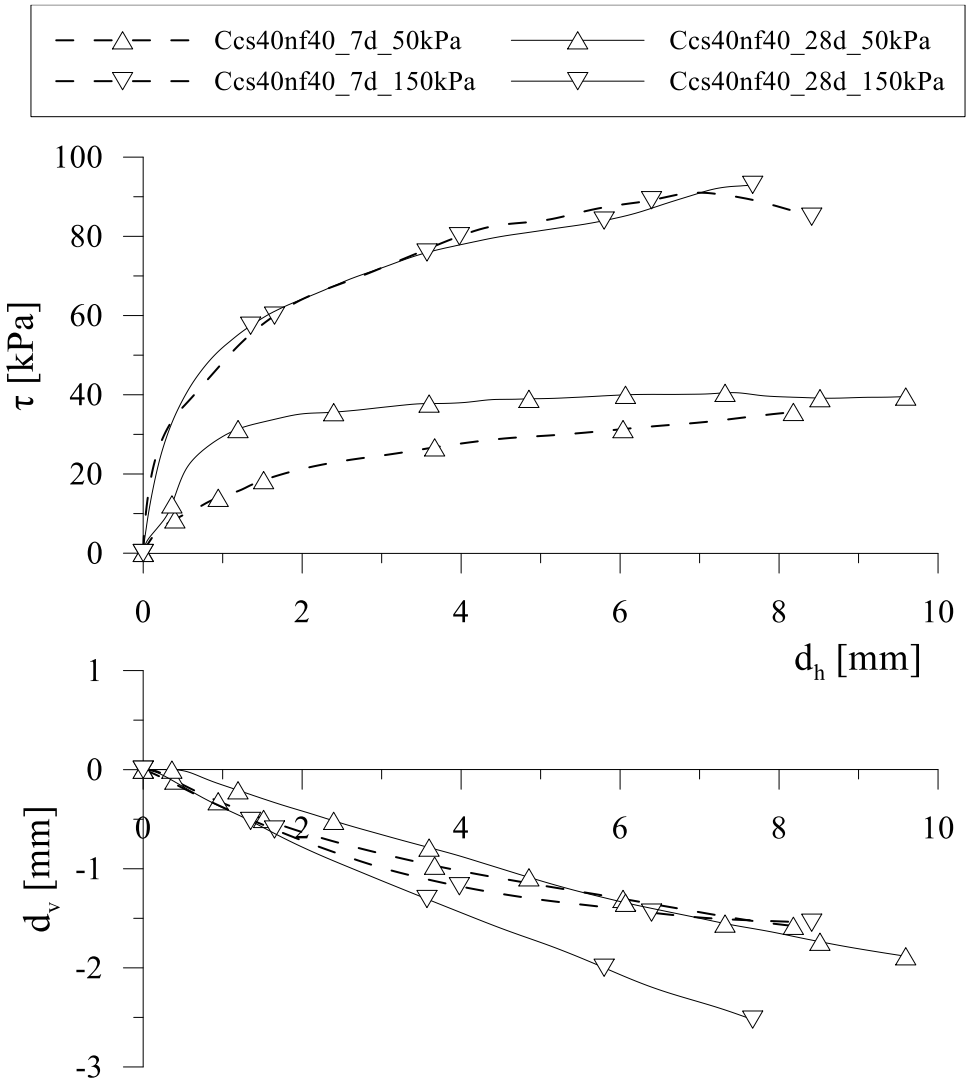
Ccs40nf40_7d_50kPa
Ccs40nf40_28d_50kPa
Ccs40nf40_7d_150kPa
Ccs40nf40_28d_150kPa
τ [kPa]
100
80
60
40
20
0
0
2
4
6
8
10
d_h [mm]
d_v [mm]
1
0
-1
-2
-3

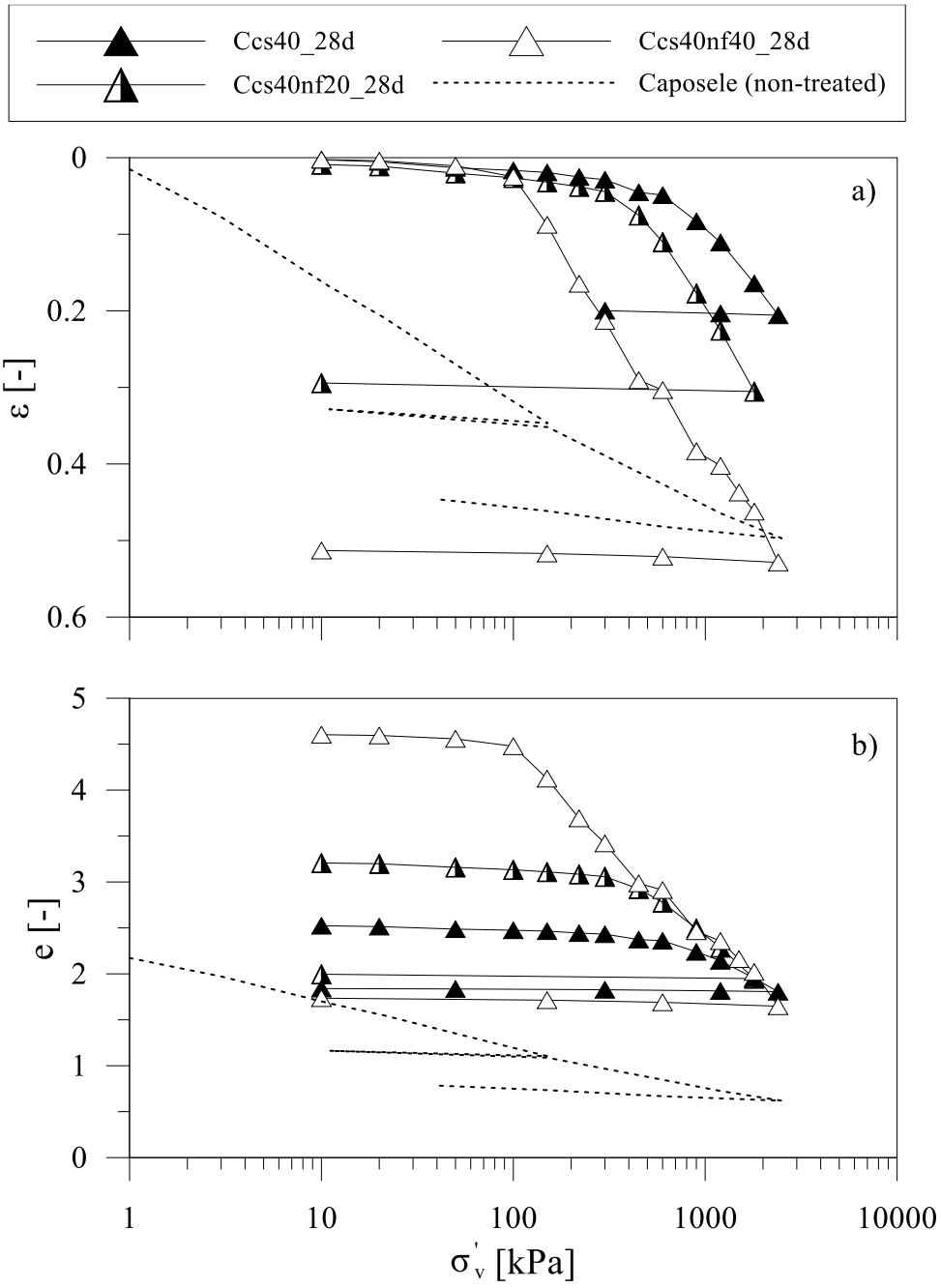
Ccs40_28d
Ccs40nf40_28d
Ccs40nf20_28d
Caposele (non-treated)
a)
b)
ε [-]
e [-]
0
0.2
0.4
0.6
5
4
3
2
1
0
1
10
100
1000
10000
σ'v [kPa]

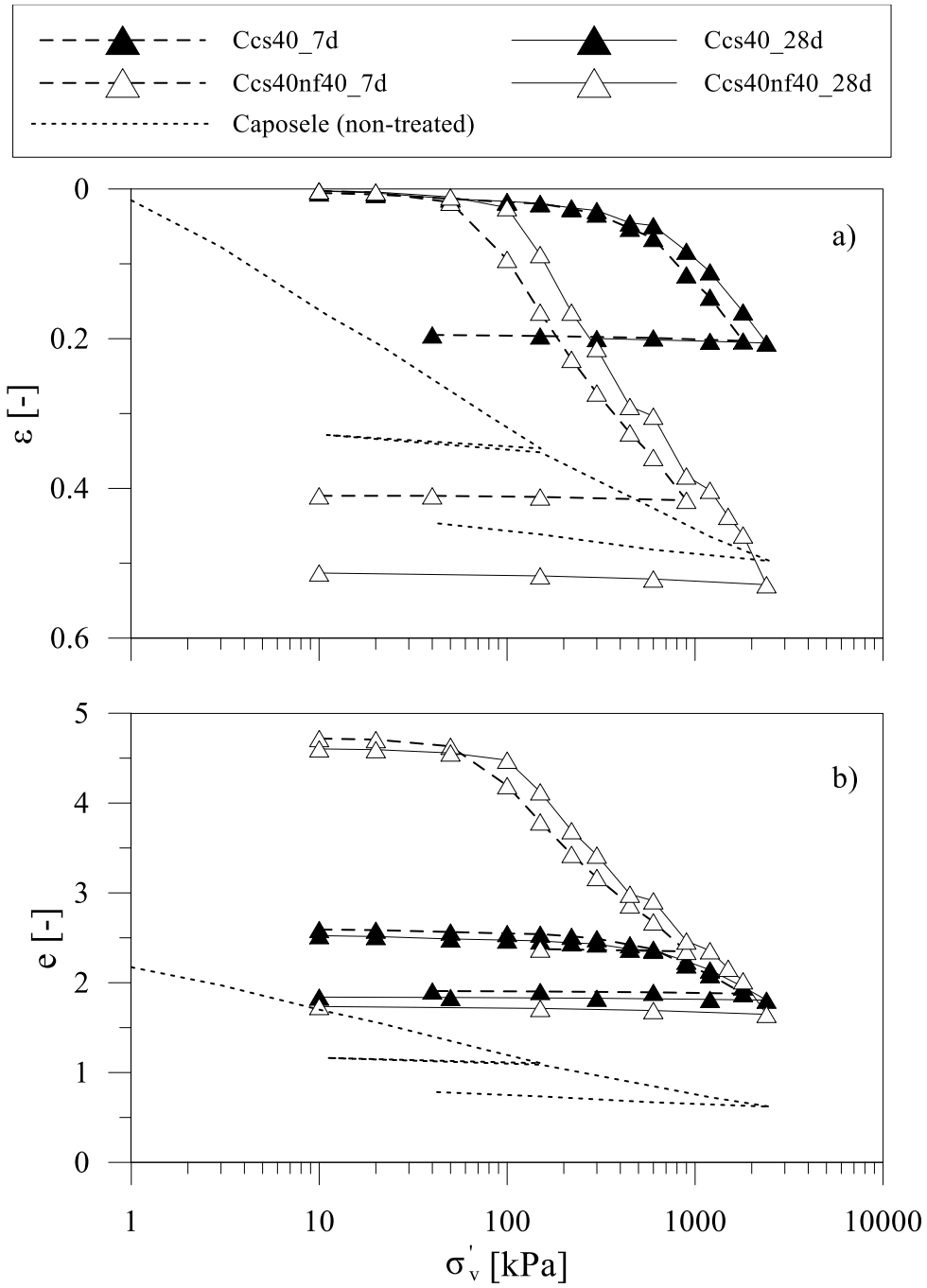
Ccs40_7d
Ccs40_28d
Ccs40nf40_7d
Ccs40nf40_28d
Caposele (non-treated)
a)
ε [-]
0
0.2
0.4
0.6
b)
e [-]
5
4
3
2
1
0
1
10
100
1000
10000
σ'v [kPa]